

University of Groningen

The X-Shooter spectral library and application to stellar population in galaxies

Chen, Yanping

IMPORTANT NOTE: You are advised to consult the publisher's version (publisher's PDF) if you wish to cite from it. Please check the document version below.

Document Version

Publisher's PDF, also known as Version of record

Publication date:

2013

[Link to publication in University of Groningen/UMCG research database](#)

Citation for published version (APA):

Chen, Y. (2013). *The X-Shooter spectral library and application to stellar population in galaxies*. s.n.

Copyright

Other than for strictly personal use, it is not permitted to download or to forward/distribute the text or part of it without the consent of the author(s) and/or copyright holder(s), unless the work is under an open content license (like Creative Commons).

The publication may also be distributed here under the terms of Article 25fa of the Dutch Copyright Act, indicated by the "Taverne" license. More information can be found on the University of Groningen website: <https://www.rug.nl/library/open-access/self-archiving-pure/taverne-amendment>.

Take-down policy

If you believe that this document breaches copyright please contact us providing details, and we will remove access to the work immediately and investigate your claim.

Downloaded from the University of Groningen/UMCG research database (Pure): <http://www.rug.nl/research/portal>. For technical reasons the number of authors shown on this cover page is limited to 10 maximum.



rijksuniversiteit
groningen

The X-Shooter Spectral Library and Application to Stellar Population in Galaxies

Proefschrift

ter verkrijging van het doctoraat in de
Wiskunde en Natuurwetenschappen
aan de Rijksuniversiteit Groningen
op gezag van de
Rector Magnificus, dr. E. Sterken,
in het openbaar te verdedigen op
maandag 11 november 2013
om 11:00 uur

door

Yanping Chen

geboren op 21 augustus 1979
te Hebei, China

Promotores: Prof. dr. S.C. Trager
Prof. dr. R.F. Peletier

Beoordelingscommissie: Prof. dr. J.M. van der Hulst
Prof. dr. M. Salaris
Dr. Ph. Prugniel

ISBN: 978-90-367-6502-2 Printed version
ISBN: 978-90-367-6503-9 Electronic version

COVER: Designed by Yanping Chen and Yunhee Choi

Front: Spectra of warm stars from the X-Shooter spectral library over the background of the Hubble Ultra Deep Field.

Image Credit: NASA; ESA; G. Illingworth, D. Magee, and P. Oesch, University of California, Santa Cruz; R. Bouwens, Leiden University; and the HUDF09 Team

Back: Bicycles we used everyday in Groningen.

PRINTED BY: NetzoDruk Groningen b.v., The Netherlands.

Contents

1	Introduction	1
1.1	Stellar populations	1
1.1.1	Absorption-line indices	3
1.1.2	Full-spectrum fitting	4
1.2	Stellar spectral libraries	5
1.3	X-Shooter	6
1.3.1	Basic data reduction process	6
1.4	This thesis	9
1.4.1	Outline of this thesis	10
	Bibliography	11
2	The X-Shooter Spectral Library (XSL) – I. DR1	15
2.1	Introduction	15
2.2	Sample selection and observation	17
2.2.1	Observations	18
2.3	Data reduction	20
2.3.1	Difficulties encountered and proposed solutions	20
2.3.2	Saturation	26
2.4	Telluric correction	28
2.4.1	The telluric library	30
2.4.2	Final telluric correction	33
2.5	Flux calibration	43
2.5.1	Construction of the extinction curve	43
2.5.2	Construction of the response curve	43
2.5.3	Flux calibration of individual frames	44
2.5.4	Final flux calibration	46
2.5.5	ADC issue in the UVB arm	46
2.6	Quality checks	46
2.6.1	Spectral resolution	46
2.6.2	Arm combination	47
2.6.3	Photometric comparison	47
2.6.4	Comparison with literature spectra	53
2.7	Summary	61
	Appendix 2.A Pipeline reduction tips	62

Appendix 2.B	Log of telluric standard stars	63
Appendix 2.C	The first-year XSL sample	68
	Bibliography	76
3	Stellar Population Models with XSL in the Optical	81
3.1	Introduction	81
3.2	Atmospheric parameters of XSL DRI	83
3.2.1	Fitting strategy for warm stars	83
3.2.2	Fitting strategy for cool stars	83
3.2.3	Quality of the derived parameters	83
3.3	The models	85
3.3.1	Spectral synthesis	85
3.3.2	Stellar spectral library	86
3.3.3	The initial mass function	88
3.3.4	Isochrones	88
3.4	Results	89
3.4.1	Spectral energy distributions	89
3.4.2	Broad-band colors	97
3.4.3	Line-strength indices	102
3.5	IMF effects on the SEDs	105
3.6	Fitting Globular Cluster spectra	106
3.7	Summary	110
Appendix 3.A	Stellar atmospheric parameters of XSL	110
	Bibliography	115
4	The Initial Mass Function Of Intermediate-Mass Early-Type Galaxies	119
4.1	Introduction	119
4.2	Data	121
4.2.1	The Galaxy Sample	121
4.2.2	Data Reduction	123
4.3	Absorption line indices	124
4.3.1	Variations of the model spectra with changing IMF	125
4.3.2	Index definitions	126
4.3.3	Correction for velocity dispersion broadening	127
4.3.4	Comparison with the literature	128
4.4	Results	130
4.5	Discussion	133
4.6	Summary and Conclusion	135
	Bibliography	136

5	Conclusions and Outlook	139
5.1	Summary of main results	139
5.1.1	The new X-Shooter stellar spectral library	139
5.1.2	Stellar population models with XSL in the optical	140
5.1.3	Determining the masses of distant galaxies	141
5.2	Future outlook	142
5.2.1	Fundamental parameters of nuclear clusters	142
5.2.2	XSL and stellar population models with XSL	145
	Nederlandse samenvatting	149
	Summary	153
	Acknowledgements	157

INTRODUCTION

We are living in a universe which contains various shining stellar systems. When people see light from these stellar systems, they ask themselves, “how do these systems form and what happened when they formed?” The answers lie in the light, but sometimes not that straightforwardly. Some nearby galaxies or stellar clusters can be investigated star by star. But for compact or remote stellar systems that cannot be resolved into individual stars, we have to resort to special tools in order to decode the evolutionary history hidden in their integrated light.

1.1 Stellar populations

Galaxies are made up of stars, and the light from a galaxy and many of its properties, like its color, depend on the properties of its stars. A stellar population is a group of stars within a galaxy that resembles each other in spatial distribution, chemical composition or age. Different stellar populations can be used as tracers of the evolutionary history of stellar systems.

A major tool in the study of galaxy evolution is stellar population synthesis, which seeks to model the spectral and photometric properties of a galaxy with a suitable combination of stars of different types (e.g., Tinsley 1980). In this scheme, one starts with a knowledge of stellar evolution and then builds a model for the galaxy’s spectrum or photometric properties with physical input parameters, such as the initial mass function (IMF), star formation history, and chemical abundance patterns (Worthey et al. 1994). Substantial progress was made in stellar evolution theory in the 1980s and 1990s, which paved the way for modeling the spectral energy distributions (SEDs) of galaxies (e.g., Charlot & Bruzual 1991; Worthey et al. 1994; Vazdekis 1999).

Galaxies usually contain a mixture of stellar populations of various ages and chemical compositions. The simplest model of a stellar population assumes that all the stars making up a galaxy or cluster are coeval and that they share the same elemental abundances. Such a group of stars is commonly known as a single stellar population (SSP).

There are in general three primary ingredients when constructing modern stellar population models: stellar isochrones or tracks as the backbone for representing the

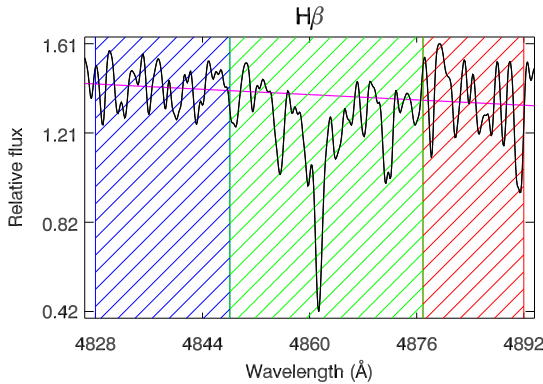


Figure 1.1: Example of an absorption-line index definition of $H\beta$, where the pseudo-continuum $C(\lambda)$ (magenta line) is defined by the blue and red side-bands; the central feature is defined by the green bandpass.

evolution of the interiors of the stars in a stellar system; an IMF to populate the mass or light distribution of stars along the isochrones; and a stellar library that offers detailed spectral lines and colors of individual stars with sensible stellar atmospheric parameters.

SSP models predict SEDs by integrating stellar spectra along theoretical isochrones, where stellar spectra are collected from a stellar library that consists of observations of real stars or of artificial spectra calculated using model atmospheres (e.g. Fioc & Rocca-Volmerange 1997; Vazdekis 1999; Leitherer et al. 1999; Bruzual & Charlot 2003; Vazdekis et al. 2003; Le Borgne et al. 2004; Maraston 2005; Vazdekis et al. 2010; Conroy & van Dokkum 2012). The SED of an SSP is obtained by

$$S_{\lambda}(t, Z) = \int_{m_a}^{m_b} S_{\lambda}(m, t, Z) \psi(m, t) F_X(m, t, Z) dm \quad (1.1)$$

where $S_{\lambda}(m, t, Z)$ is the spectrum of stars with given mass m , age t and metallicity Z , $F_X(m, t, Z)$ is the light-weighted flux in a certain normalized wavelength band X , $\psi(m, t)$ is the mass distribution inferred from the IMF according to the star formation history extracted from the isochrone, and m_a and m_b are the minimum and maximum masses of stars sharing the same age and metallicity, respectively.

With the model SEDs and observations, it should be straightforward to extract the evolutionary history, such as age, metallicity, and chemical abundance ratios, from stellar systems. However, the reality is more complicated, because SEDs respond to different parameters in degenerate ways, i.e. old metal-poor models have similar shapes as young metal-rich models. This age-metallicity degeneracy (e.g., Faber 1972, 1973; O’Connell 1980; Worthey 1994) is more obvious when analyzing colors or low-resolution spectra (see, Vazdekis 1999; Schiavon et al. 2002). Stellar population analyses must therefore take this degeneracy into account when interpreting the evolutionary histories from the integrated light of stellar systems.

There are two popular methods for studying stellar populations: analyzing line-strength indices and full-spectrum fitting. We now discuss these two methods in turn.

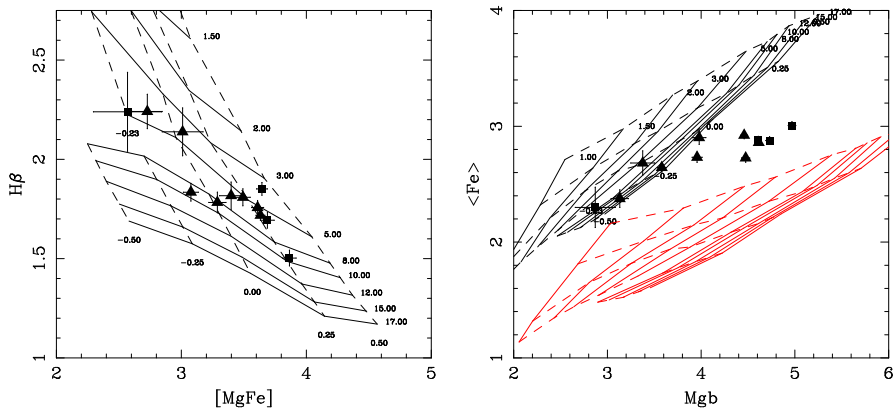


Figure 1.2: Illustration of stellar population models compared with Coma early-type galaxies using indices from Trager et al. (2008). The grids are calculated based on models by Worthey et al. (1994). Solid lines indicate same ages (in Gyr) and dashed lines indicate same metallicities (in $[Z/H]$), triangles and squares denote early-type galaxies. In the left panel, the indices $H\beta$ and $[Mg/Fe]$ are used to break the degeneracy of age and metallicity. In the right panel Mgb and $\langle Fe \rangle$ are used to indicate α -enhancement, lower red grids are models with α -enhancement $[E/Fe] = +0.3$, and black grids are models with solar metallicity pattern $[E/Fe] = 0.0$. This approach is good for old stellar populations.

1.1.1 Absorption-line indices

The traditional method of breaking the degeneracy between age and metallicity in old stellar populations is to resort to diagnostics of individual stellar absorption line features – spectral indices.

The line-strength indices are defined either via the classical expression for an equivalent width,

$$EW_{\lambda} = \int_{\lambda_1}^{\lambda_2} (1 - S(\lambda)/C(\lambda)) d\lambda, \quad (1.2)$$

or in terms of magnitudes,

$$I_{\lambda}(\text{mag}) = -2.5 \times \log_{10} \left[\left(\frac{1}{\lambda_2 - \lambda_1} \right) \int_{\lambda_1}^{\lambda_2} S(\lambda)/C(\lambda) d\lambda \right], \quad (1.3)$$

where $S(\lambda)$ is the observed flux per unit wavelength and $C(\lambda)$ is the pseudo-continuum defined by adjacent flux levels, and λ_1 and λ_2 are the wavelength limits of the central feature bandpass. Figure 1.1 illustrates a typical index definition, here for $H\beta$. The Lick/IDS system (Burstein et al. 1984; Worthey et al. 1994; Trager et al. 1998) is the most widely used index system. This system consists of 25 indices, defined on low-resolution spectra, each of which has a central bandpass and two pseudo-continuum bands.

Worthey et al. (1994) investigated a number of spectral indices and identified the hydrogen Balmer absorption-line indices as sensitive age indicators, while recognizing

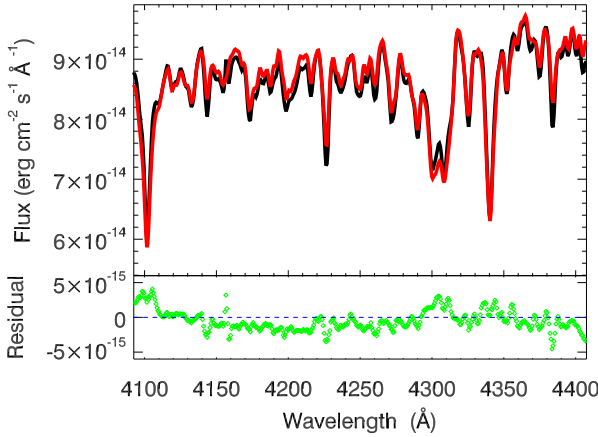


Figure 1.3: Example of full-spectrum fitting for NGC 2808, see Chapter 3 for details. The upper panel shows the observation (black) and the best fit (red); the lower panel shows the residual between the data and best-fit template.

other metal-line indices such as Fe4668, Fe5270, Fe5335 as sensitive-metallicity indicators. This concept was later developed and applied to estimate the age, metallicity and chemical abundances in old early-type galaxies (e.g., Peletier 1989; González 1993; Trager et al. 2000a,b; Kuntschner et al. 2006; Trager et al. 2008, and many others). Figure 1.2 shows an example of SSP models of line-strength indices compared with Coma early-type galaxies (Trager et al. 2008). After the Lick/IDS system was set up, more indices were independently defined and developed (e.g., Rose et al. 1994; Cenarro et al. 2001; Serven et al. 2005). Line-strength indices generally have been excellent tools for the study of stellar populations.

1.1.2 Full-spectrum fitting

Due to the availability of high-quality observations and model spectra, full-spectrum fitting has become a popular method for decoding the evolutionary histories from integrated light (e.g., Vazdekis 1999; Cid Fernandes et al. 2005; Ocvirk et al. 2006; Sarzi et al. 2006; Koleva et al. 2008). This method uses all of the stellar features contained in the integrated spectrum, and fits the entire optical spectrum with models that allow for variations in (at least) age and total metallicity. Obviously, full-spectrum fitting requires high S/N and a wide wavelength coverage to recover the complex star formation histories of stellar systems (Ocvirk et al. 2006; Tojeiro et al. 2007). In this technique, one fits the observation with the template spectra to minimize template-mismatch errors, which is also useful for extracting gas kinematics or deriving emission-corrected line-strengths indices (e.g., Sarzi et al. 2006, GANDALF).

Figure 1.3 shows an example of how the evolutionary history and kinematic profiles can be simultaneously extracted from the integrated spectrum with full-spectrum fitting. We perform the fit on flux-calibrated spectrum of NGC 2808 using the XBK models from Chapter 3 over the wavelength range 3360–5450 Å. The observations and models are first convolved to the same instrumental resolution, and the fit is then performed with each template model spectrum. The age, metallicity and kinematic pro-

files of a stellar system are obtained from the template giving the lowest χ^2 value.

1.2 Stellar spectral libraries

A stellar library is one of the most important ingredients in stellar population models. A stellar library is a collection of spectra from various stars with different spectral types but sharing the same wavelength range and resolution. Stellar libraries can be built from theoretical atmospheres (e.g., Kurucz 1993; Hauschildt et al. 1997; Coelho et al. 2005; Martins et al. 2005; Munari et al. 2005; Coelho et al. 2007; Gustafsson et al. 2008; Allard et al. 2011) or from empirical observations (e.g., Worthey & Ottaviani 1997; Pickles 1998; Prugniel & Soubiran 2001, 2004; Cenarro et al. 2003; Prugniel et al. 2007; Le Borgne et al. 2003; Sánchez-Blázquez et al. 2006; Gregg et al. 2006). Both theoretical and empirical libraries have improved dramatically in recent years. However, there is no single spectral library, whether theoretical or empirical, that covers the entire range of parameter space (effective temperature, T_{eff} , gravity, $\log g$, and metallicity, $[\text{Fe}/\text{H}]$) that is necessary for constructing SSP models. Whether one should choose a theoretical or an empirical library in creating stellar population models is a subject of debate (Coelho et al. 2005), since both have their own benefits and drawbacks (e.g., Conroy 2013).

Theoretical libraries are advantageous for their high resolution, wide wavelength coverage, availability of non-solar abundance patterns, and the fact that they are not subject to observational limitations such as extinction and atmospheric absorption. Since they rely on model atmospheres, which are subject to systematic uncertainties, theoretical libraries sometimes have a hard time reproducing certain atomic or molecular lines. To compute a reliable, high-resolution theoretical library for a large range of stellar parameters and a wide wavelength coverage, reliable lists of atomic and molecular line opacities are required. However, even recently, models still fail to reproduce lines in ultra-violet high-resolution spectra of the Sun due to incomplete atomic line lists (Kurucz 2011). In addition, reproducing molecular lines in cooler stars is a challenging task, because reliable molecular line lists are not yet complete (e.g., Coelho et al. 2005; Kurucz 2011; Conroy 2013). Detailed and more complete line lists are required to improve the spectral features in theoretical libraries (Kurucz 2011).

Empirical libraries do not suffer from unreliable spectral features, but their incomplete coverage of parameter space (T_{eff} , $\log g$ and $[\text{Fe}/\text{H}]$) hinders their capability to reproduce spectral features in giant elliptical galaxies (e.g., Peletier 1989; Worthey et al. 1992). The fact that most of the empirical libraries are compiled from samples of stars in the solar neighborhood has long been a limitation of empirical libraries. Empirical libraries with different resolution and wavelength coverage have been published in the last two decades. In the optical, there are (among others) the Lick/IDS (Worthey & Ottaviani 1997), Pickles (1998), MILES (Sánchez-Blázquez et al. 2006), ELODIE (Prugniel & Soubiran 2001, 2004; Prugniel et al. 2007), STELIB (Le Borgne et al. 2003), and NGSL (Gregg et al. 2006) libraries. Stellar libraries in the near-IR are smaller, but pioneering work has been done by Lançon & Rocca-Volmerange (1992); Lançon & Wood (2000); Lançon & Mouhcine (2002) (LW2000, LM2002), Mármol-Queraltó et al. (2008),

and Rayner et al. (2009, IRTF-SpeX). However, a spectral library with continuous wavelength coverage at moderate resolution is still missing.

1.3 X-Shooter

X-Shooter (Figure 1.4) is a high-efficiency, ground-based, single-target echelle spectrograph of the ESO Very Large Telescope (VLT) (Vernet et al. 2011). It was built by a consortium of 11 institutes in Denmark, France, Italy and the Netherlands, together with ESO. This instrument consists of a central backbone that supports three prism-cross-dispersed spectrographs in different wavelength ranges, namely the UV-Blue (UVB), Visible (VIS) and Near-infrared (NIR) arms. A slit wheel equipped with $11''$ -long slits of different widths is located at the entrance of each spectrograph. One of the unique capabilities of X-Shooter is that it collects spectra over the entire wavelength range ($\lambda\lambda$ 3000–25000 Å) simultaneously. It operates at intermediate resolutions ($R = 4000$ –14000) depending on wavelength and slit width. We refer to Vernet et al. (2011) for a detailed description of the resolution of X-Shooter. The spectral format of X-Shooter is fixed. The whole spectral range is covered by 12 orders in the UVB, 15 in the VIS, and 16 in the NIR. Figure 1.5 shows typical raw echelle spectra taken by X-Shooter.

1.3.1 Basic data reduction process

The basic CCD image reduction process includes bias and dark subtraction, flat-fielding and wavelength calibration. A bias image is obtained with the shutter closed and with a zero-second exposure, and shows the electronic noise of the camera as well as possible systematics. A dark image is similar to a bias, but with some non-zero exposure time. A flat-field image is used to correct for pixel-to-pixel variations in the CCD response and the non-homogeneous illumination by the telescope. It can be obtained either by an evenly illuminated screen or a twilight sky. Wavelength calibration is usually performed after or simultaneously with geometric corrections. To do this, a ThAr lamp giving emission lines is used for X-Shooter in the UVB and VIS arms. One can perform the wavelength calibration by making models or by cross correlating the observations with the lamp image. The more lamp lines one has, the better the wavelength calibration will be.

The X-Shooter pipeline is used to generate two-dimensional spectra of the observed object, an example of which is shown in Figure 1.6. In order to build a spectral library from these two-dimensional spectra, the following steps are then necessary:

- Optimal extraction of one-dimensional spectra from the two-dimensional spectra
- Telluric correction
- Flux calibration
- Rest-frame shifting

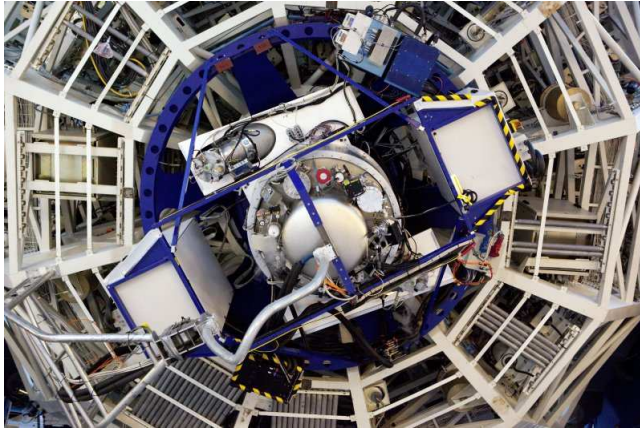


Figure 1.4: A view of X-Shooter from Vernet et al. (2011).

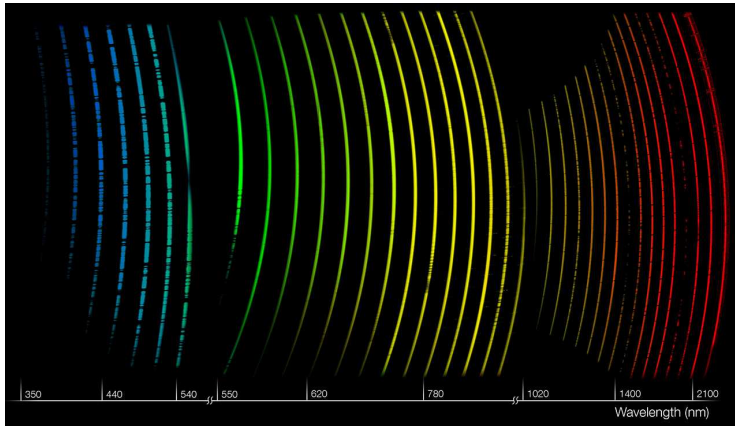


Figure 1.5: An illustration of echelle spectra taken by X-Shooter in three arms at one shot (by ESO). The rainbow colors applied to the spectra indicate X-Shooter's wide spectral coverage and are meant for illustrative purposes only.

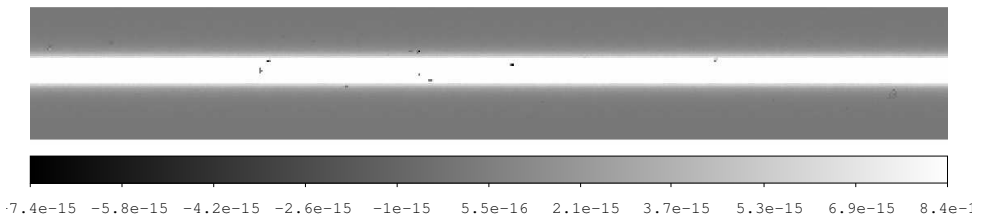


Figure 1.6: An example of a two-dimensional spectrum of a flux standard star observed in the staring mode.

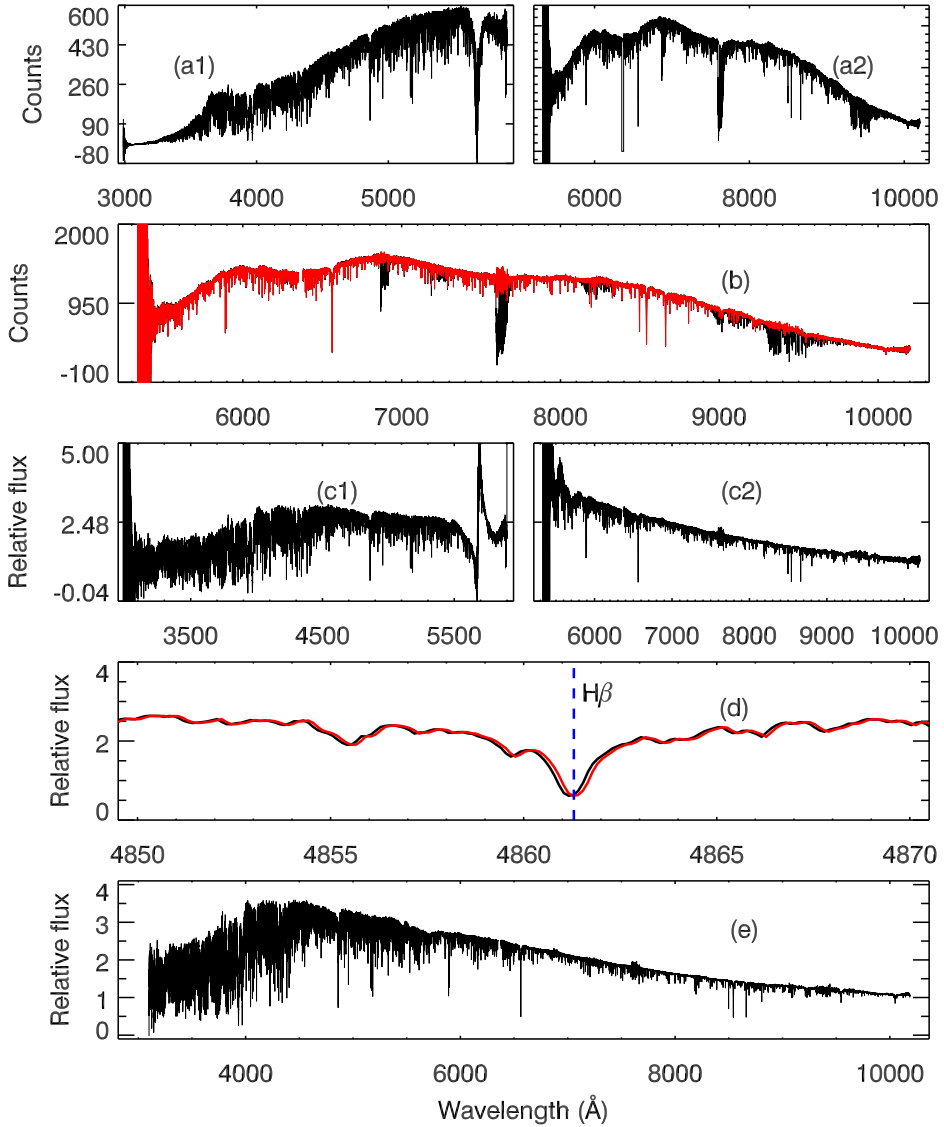


Figure 1.7: An example of the data reduction steps after pipeline extraction for HD217877 (F8V). Panels (a1) and (a2) show the one-dimensional spectrum extracted from the two-dimensional spectrum in the UVB arm and from the VIS arm, respectively. Panel (b) shows the comparison between before (black) and after (red) telluric correction. Panels (c1) and (c2) show flux-calibrated one-dimensional spectra in the UVB (left) and VIS (right) arms. Panel (d) shows spectra in the UVB arm before (black) and after (red) rest-frame shifting, compared with the laboratory $H\beta$ line (blue). Panel (e) shows the final arm-merged, telluric-corrected, and flux-calibrated one-dimensional spectrum of HD217877.

- Arm combination

Figure 1.7 demonstrates how the spectra change after application of each of the steps listed above. Here we take HD217877 (F8V) as an example. One-dimensional spectra are extracted with our optimal extraction script (inspired by Horne 1986) from the UVB and VIS arms as shown in panels (a1) and (a2). The relative transmission of the instrumental is clearly seen. In the UVB arm, the bump around 3700 Å is due to the two flat-field lamps used in the UVB arm; features around 5600–5800 Å are due to the dichroic used to split the beam between the UVB and VIS arms. In the VIS arm, the maximum instrumental efficiency occurs around 7000–8000 Å. Panel (b) shows telluric features in the VIS arm and we see that important spectral features are contaminated by atmospheric absorption. A successful telluric correction procedure will recover these spectral features. Flux calibration is performed for the spectra of each arm and the resulting flux-calibrated spectra are shown in panels (c1) and (c2). The dichroic features are more obvious in the flux-calibrated spectra both in the UVB and VIS arms. If we are lucky, these features can be removed in the arm-merged final spectrum. Using theoretical stellar templates, we shift the observed spectra to rest-frame wavelengths. Panel (d) shows the H_{β} line sitting exactly at the correct wavelength after rest-frame shifting. We finally show the arm-merged, telluric-corrected, and flux-calibrated one-dimensional spectrum of HD217877 in panel (e), which can then be used as an input for our stellar library.

1.4 This thesis

Decoding the evolutionary history of stellar systems from their integrated light is an important goal in modern astronomy. The wavelength region around 5000 Å has traditionally been popular since the Lick/IDS index system had been set up. Later, it was realized that important features in the red, such as the CaII triplet and NaI 8200, can also be useful diagnostics of metallicity (Armandroff & Zinn 1988; Cenarro et al. 2008; Foster et al. 2009) and for determining dwarf-to-giant ratios (e.g. Faber & French 1980; Conroy & van Dokkum 2012; Spiniello et al. 2012). Using those red features may give better constraints on the interpretation of stellar populations of stellar systems. In order to have a wider wavelength coverage that includes these important red features, several empirical stellar libraries have been combined in stellar population models. Vazdekis et al. (2012) combined MILES (Sánchez-Blázquez et al. 2006), and the CaT library (Cenarro et al. 2001) with Indo-U.S. (Valdes et al. 2004) to build the MIUSCAT stellar synthesis models; Conroy & van Dokkum (2012, CvD model) combined the MILES and IRTF (Rayner et al. 2009) libraries with synthetic spectra filling in the gap between these libraries. However, as libraries will have been created from data with different resolutions, parameter coverage, etc., combining these is not a straightforward process. Unavoidable systematic errors will therefore be introduced into the resulting models.

Using X-Shooter, which has a high efficiency, wide wavelength coverage, and moderate to high spectral resolution, we can build an empirical spectral library that covers the full wavelength range from near-ultraviolet to the near-infrared at a relatively high

resolution ($R \sim 7000 - 11000$). The work presented in this thesis provides the first set of results towards our goal of creating a complete spectral library containing ~ 700 stars with good parameter coverage as well as abundance pattern variations.

Stellar population models built from the new spectral library will be powerful tools to investigate the spectral features in galaxies and/or stellar clusters over a wide wavelength range simultaneously without any uncertainty from artifacts of “joined” or combined libraries. The high resolution of our models makes them particularly suited for studying small stellar systems.

1.4.1 Outline of this thesis

I begin in Chapter 2 with the crucial element for stellar populations, the new X-Shooter library (XSL), where I present the first release of XSL, containing 237 stars spanning the wavelength range 3000–10200 Å at a resolving power $R \equiv \lambda/\Delta\lambda \sim 10000$. Features of the pilot survey are described. This library has been carefully corrected for telluric absorption, flux-calibrated, and shifted to the rest frame. Spectra of stars from the UVB and VIS arms have been combined into single, broad-band (UV and optical) spectra. We also present a promising principal component analysis (PCA)-based method that I have developed and used in order to perform the telluric correction on XSL. The resulting telluric spectral library is presented in this thesis and will be useful to astronomers beyond simply performing telluric corrections for the XSL.

In Chapter 3, I present stellar population models built from XSL in the optical. Four sets of SSP SEDs have been generated and compared. Our models are robust in the sense that the effects of individual input ingredients of stellar population models can be assessed, because we can choose from two sets of isochrones and two IMFs. I test our models against three globular clusters (GCs) since they are excellent calibrators for stellar population models. Good agreement is achieved between our model interpretation of their ages and metallicities and literature values based on color-magnitude diagram (CMD) estimates. I identify a number of gravity-sensitive spectral features from our model SEDs, which can be used to trace the dwarf-to-giant ratio in stellar systems.

To determine the dwarf-to-giant ratio in galaxies beyond the Local Group, I expand the analysis in Chapter 4. Using the MIUSCAT models (Vazdekis et al. 2012) together with spectral line-strength indices, we find TiO-related line features are good indicators of the IMF slope. Among these is a particularly good spectral feature, from which we define a new index that we call “TiO+CaH”. The Salpeter IMF is likely the steepest mass function of early-type galaxies with velocity dispersion below $\sim 200 \text{ km s}^{-1}$. Non-solar chemical abundance models are required to put better constraints on the slope and shape of IMFs in galaxies.

The main results of this thesis are summarized in Chapter 5, where I also discuss the future outlook of both XSL and our stellar population models. Preliminary results from applying our models on nuclear star clusters in distant ($d > 2 \text{ Mpc}$) galaxies are also presented.

Bibliography

- Allard, F., Homeier, D., & Freytag, B. 2011, in *Astronomical Society of the Pacific Conference Series*, Vol. 448, 16th Cambridge Workshop on Cool Stars, Stellar Systems, and the Sun, ed. C. Johns-Krull, M. K. Browning, & A. A. West, 91
- Armandroff, T. E. & Zinn, R. 1988, *AJ*, 96, 92
- Bruzual, G. & Charlot, S. 2003, *MNRAS*, 344, 1000
- Burstein, D., Faber, S. M., Gaskell, C. M., & Krumm, N. 1984, *ApJ*, 287, 586
- Cenarro, A. J., Cardiel, N., Gorgas, J., et al. 2001, *MNRAS*, 326, 959
- Cenarro, A. J., Cervantes, J. L., Beasley, M. A., Marín-Franch, A., & Vazdekis, A. 2008, *ApJ*, 689, L29
- Cenarro, A. J., Gorgas, J., Vazdekis, A., Cardiel, N., & Peletier, R. F. 2003, *MNRAS*, 339, L12
- Charlot, S. & Bruzual, A. G. 1991, *ApJ*, 367, 126
- Cid Fernandes, R., Mateus, A., Sodré, L., Stasińska, G., & Gomes, J. M. 2005, *MNRAS*, 358, 363
- Coelho, P., Barbuy, B., Meléndez, J., Schiavon, R. P., & Castilho, B. V. 2005, *A&A*, 443, 735
- Coelho, P., Bruzual, G., Charlot, S., et al. 2007, *MNRAS*, 382, 498
- Conroy, C. 2013, *ARA&A*, 51, 393
- Conroy, C. & van Dokkum, P. 2012, *ApJ*, 747, 69
- Faber, S. M. 1972, *A&A*, 20, 361
- Faber, S. M. 1973, *ApJ*, 179, 731
- Faber, S. M. & French, H. B. 1980, *ApJ*, 235, 405
- Fioc, M. & Rocca-Volmerange, B. 1997, *A&A*, 326, 950
- Foster, C., Proctor, R. N., Forbes, D. A., et al. 2009, *MNRAS*, 400, 2135
- González, J. J. 1993, PhD thesis, Thesis (PH.D.)–UNIVERSITY OF CALIFORNIA, SANTA CRUZ, 1993. Source: Dissertation Abstracts International, Volume: 54-05, Section: B, page: 2551.
- Gregg, M. D., Silva, D., Rayner, J., et al. 2006, in *The 2005 HST Calibration Workshop: Hubble After the Transition to Two-Gyro Mode*, ed. A. M. Koekemoer, P. Goudfrooij, & L. L. Dressel, 209
- Gustafsson, B., Edvardsson, B., Eriksson, K., et al. 2008, *A&A*, 486, 951
- Hauschildt, P. H., Baron, E., & Allard, F. 1997, *ApJ*, 483, 390

- Horne, K. 1986, PASP, 98, 609
- Koleva, M., Prugniel, P., Ocvirk, P., Le Borgne, D., & Soubiran, C. 2008, MNRAS, 385, 1998
- Kuntschner, H., Emsellem, E., Bacon, R., et al. 2006, MNRAS, 369, 497
- Kurucz, R. 1993, ATLAS9 Stellar Atmosphere Programs and 2 km/s grid. Kurucz CD-ROM No. 13. Cambridge, Mass.: Smithsonian Astrophysical Observatory, 1993., 13
- Kurucz, R. L. 2011, Canadian Journal of Physics, 89, 417
- Lançon, A. & Mouhcine, M. 2002, A&A, 393, 167
- Lançon, A. & Rocca-Volmerange, B. 1992, A&AS, 96, 593
- Lançon, A. & Wood, P. R. 2000, A&AS, 146, 217
- Le Borgne, D., Rocca-Volmerange, B., Prugniel, P., et al. 2004, A&A, 425, 881
- Le Borgne, J.-F., Bruzual, G., Pelló, R., et al. 2003, A&A, 402, 433
- Leitherer, C., Schaerer, D., Goldader, J. D., et al. 1999, ApJS, 123, 3
- Maraston, C. 2005, MNRAS, 362, 799
- Mármol-Queraltó, E., Cardiel, N., Cenarro, A. J., et al. 2008, A&A, 489, 885
- Martins, L. P., González Delgado, R. M., Leitherer, C., Cerviño, M., & Hauschildt, P. 2005, MNRAS, 358, 49
- Munari, U., Sordo, R., Castelli, F., & Zwitter, T. 2005, A&A, 442, 1127
- O'Connell, R. W. 1980, ApJ, 236, 430
- Ocvirk, P., Pichon, C., Lançon, A., & Thiébaud, E. 2006, MNRAS, 365, 46
- Peletier, R. F. 1989, PhD thesis, University of Groningen, The Netherlands, (1989)
- Pickles, A. J. 1998, PASP, 110, 863
- Prugniel, P. & Soubiran, C. 2001, A&A, 369, 1048
- Prugniel, P. & Soubiran, C. 2004, ArXiv Astrophysics e-prints
- Prugniel, P., Soubiran, C., Koleva, M., & Le Borgne, D. 2007, ArXiv Astrophysics e-prints
- Rayner, J. T., Cushing, M. C., & Vacca, W. D. 2009, ApJS, 185, 289
- Rose, J. A., Bower, R. G., Caldwell, N., et al. 1994, AJ, 108, 2054
- Sánchez-Blázquez, P., Peletier, R. F., Jiménez-Vicente, J., et al. 2006, MNRAS, 371, 703
- Sarzi, M., Falcón-Barroso, J., Davies, R. L., et al. 2006, MNRAS, 366, 1151
- Schiavon, R. P., Faber, S. M., Castilho, B. V., & Rose, J. A. 2002, ApJ, 580, 850

- Serven, J., Worthey, G., & Briley, M. M. 2005, *ApJ*, 627, 754
- Spiniello, C., Trager, S. C., Koopmans, L. V. E., & Chen, Y. P. 2012, *ApJ*, 753, L32
- Tinsley, B. M. 1980, *Fund. Cosmic Phys.*, 5, 287
- Tojeiro, R., Heavens, A. F., Jimenez, R., & Panter, B. 2007, *MNRAS*, 381, 1252
- Trager, S. C., Faber, S. M., & Dressler, A. 2008, *MNRAS*, 386, 715
- Trager, S. C., Faber, S. M., Worthey, G., & González, J. J. 2000a, *AJ*, 120, 165
- Trager, S. C., Faber, S. M., Worthey, G., & González, J. J. 2000b, *AJ*, 119, 1645
- Trager, S. C., Worthey, G., Faber, S. M., Burstein, D., & González, J. J. 1998, *ApJS*, 116, 1
- Valdes, F., Gupta, R., Rose, J. A., Singh, H. P., & Bell, D. J. 2004, *ApJS*, 152, 251
- Vazdekis, A. 1999, *ApJ*, 513, 224
- Vazdekis, A., Cenarro, A. J., Gorgas, J., Cardiel, N., & Peletier, R. F. 2003, *MNRAS*, 340, 1317
- Vazdekis, A., Ricciardelli, E., Cenarro, A. J., et al. 2012, *MNRAS*, 424, 157
- Vazdekis, A., Sánchez-Blázquez, P., Falcón-Barroso, J., et al. 2010, *MNRAS*, 404, 1639
- Vernet, J., Dekker, H., D'Odorico, S., et al. 2011, *A&A*, 536, A105
- Worthey, G. 1994, *ApJS*, 95, 107
- Worthey, G., Faber, S. M., & González, J. J. 1992, *ApJ*, 398, 69
- Worthey, G., Faber, S. M., González, J. J., & Burstein, D. 1994, *ApJS*, 94, 687
- Worthey, G. & Ottaviani, D. L. 1997, *ApJS*, 111, 377

THE X-SHOOTER SPECTRAL LIBRARY (XSL) – I. DR1

*Yan-Ping Chen, S. C. Trager, R. F. Peletier, A. Lançon,
A. Vazdekis, Ph. Prugniel and D.R. Silva*

To be submitted to A&A

Abstract

We present the first release of XSL, the X-Shooter Spectral Library. This release contains 239 stars spanning the wavelengths 3000–10200 Å observed at a resolving power $R \equiv \lambda/\Delta\lambda \sim 10000$. The spectra were obtained at ESO's 8-m Very Large Telescope (VLT). The sample contains O – M, long-period variable (LPV), C and S stars. The spectra are flux-calibrated and telluric-corrected. We describe a new technique for the telluric correction. The wavelength coverage, spectral resolution and spectral type of this library make it well suited to stellar population synthesis of galaxies and clusters, kinematical investigation of stellar systems and studying the physics of cool stars.

2.1 Introduction

Spectral libraries play an important role in different fields of astrophysics. In particular they serve as reference for the classification and automatic analysis of large stellar spectroscopic surveys and are fundamental ingredients of the models of stellar populations used to study the evolution of galaxies.

Much of what we know about the formation, evolution, and current state of galaxies comes through studies of their starlight. In distant galaxies, where the ability to study their stellar populations star-by-star is compromised by crowding and blending due to poor resolution, we must resort to studying their integrated light. This typically means comparing colours or spectra to models of simple or composite stellar population models (e.g. Guiderdoni & Rocca-Volmerange 1987; Buzzoni et al. 1994; Worthey

et al. 1994; Leitherer et al. 1996; Fioc & Rocca-Volmerange 1997; Leitherer et al. 1999; Bruzual & Charlot 2003; Le Borgne et al. 2004; González Delgado et al. 2005; Maraston 2005; Vazdekis et al. 2010; Conroy & van Dokkum 2012). Such comparisons yield insight into a galaxy’s evolution process: stellar population analysis can reveal the detailed chemical composition and star formation history of a galaxy (e.g. González 1993; Davies et al. 1993; Trager et al. 2000; Thomas et al. 2005; Yamada et al. 2008; Koleva et al. 2013; Conroy et al. 2013).

Modern stellar population models consist of three primary ingredients (e.g. Vazdekis et al. 2010): stellar isochrones representing the location in the luminosity-effective temperature plane (and as a consequence also surface gravity-effective temperature) of stars of different masses and the same initial chemical composition and age; an initial mass function to populate the isochrones with a sensible number of stars; and a stellar library. A spectral library is a collection of stellar spectra sharing similar wavelength coverage and spectral resolution. The spectra change as a function of effective temperature (T_{eff}), gravity ($\log g$) and metallicity ($[\text{Fe}/\text{H}]$). In order to reproduce galaxy spectra as precisely as possible, one requires a comprehensive stellar spectral library that covers the entire desired parameter space of T_{eff} , $\log g$, and $[\text{Fe}/\text{H}]$. Moreover, extended wavelength coverage is strongly desirable, because different stellar phases contribute their light in different bands. For instance, cool giants contribute more light than warmer faint giant stars in the near-infrared, while in the optical, the situation is reversed (Frogel 1988; Maraston 2005). Asymptotic giant branch (AGB) stars dominate the light of intermediate-aged stellar populations in the near-infrared but are unimportant in the optical (Charlot & Bruzual 1991; Worthey et al. 1994; Maraston 1998). Detecting their presence requires *broad wavelength coverage* in both the target and model spectra.

Stellar spectral libraries can be classified into empirical and theoretical libraries, depending on how libraries are obtained. Both theoretical and empirical libraries have improved in recent years. The most widely used theoretical libraries in stellar population models are those of Kurucz (1993); Coelho et al. (2005); Martins et al. (2005); Munari et al. (2005); Coelho et al. (2007); Gustafsson et al. (2008), and Allard et al. (2011). Theoretical libraries have the advantage of (nearly) unlimited resolution and selectable abundance patterns – not only scaled-solar abundances but also non-solar patterns. Unfortunately, theoretical libraries suffer from systematic uncertainties, as they rely on model atmospheres and require a reliable list of atomic and molecular line wavelengths and opacities (Coelho et al. 2005). Empirical stellar libraries, on the other hand, have the advantage of being drawn from real, observed stars and therefore do not suffer this limitation; however they frequently have relatively low resolution (with a few exceptions; see below) and are typically unable to reproduce the indices measured in giant elliptical galaxies (Peletier 1989; Worthey et al. 1992), because they are based on local stars with Milky Way disk abundance patterns. Table 2.1 lists several previous empirical stellar libraries and their principal features. In the optical, there are the (among others) Lick/IDS (Worthey & Ottaviani 1997), MILES (Sánchez-Blázquez et al. 2006), ELODIE (Prugniel & Soubiran 2001, 2004; Prugniel et al. 2007), STELIB (Le Borgne et al. 2003), NGSL (Gregg et al. 2006), and the Pickles (1998) libraries. Building stellar libraries in the near-IR is a challenging task, but pioneering work has been done

Table 2.1: *A selection of previous empirical stellar libraries*

Library	Resolution $R=\lambda/\Delta\lambda$	Spectral range (nm)	Number of stars	Reference
STELIB	2000	320-930	249	Le Borgne et al. (2003)
ELODIE	10000	390-680	1388	Prugniel & Soubiran (2001, 2004) Prugniel et al. (2007)
INDO-US	5000	346-946	1237	Valdes et al. (2004)
MILES	2000	352-750	985	Sánchez-Blázquez et al. (2006)
IRTF-SpeX	2000	800-5000	210	Rayner et al. (2009)
NGSL	1000	167-1025	374	Gregg et al. (2006)
UVES-POP	80000	307-1030	300	Bagnulo et al. (2003)
LW2000	1100	500-2500	100	Lançon & Wood (2000)

by Lançon & Rocca-Volmerange (1992); Lançon & Wood (2000); Lançon & Mouhcine (2002) (LW2000, LM2002), Mármol-Queraltó et al. (2008), and Rayner et al. (2009, IRTF-SpeX). However, spectral libraries with extended wavelength coverage at moderate resolution are still largely missing.

With the ability of the high efficiency, broad wavelength coverage, and high/moderate resolution of the X-Shooter spectrograph at ESO's VLT (Vernet et al. 2011), we can now fill the gap between high-resolution theoretical stellar libraries and low-resolution empirical stellar libraries. To this end, we have been developing the X-Shooter Spectral Library (XSL, PI: Trager), a survey of $\gtrsim 700$ stars covering the entire Hertzsprung–Russell (HR) diagram, including both cool (M dwarfs, M giants, C stars, long-period variables, etc.) and hot stars (up to late O stars), with wavelength coverage from 300–2480 nm – i.e., the entire near-ultraviolet (NUV) to near-infrared (NIR) range – at $R \sim 8000$ –11000.

Here we present the first two of six periods of XSL data (from ESO Periods 84 and 85). We concentrate in this paper on the NUV–optical data (3000–10200 Å) from the UVB and VIS arms of X-Shooter and leave the NIR arm data for a forthcoming paper.

2.2 Sample selection and observation

XSL targets are selected from several empirical stellar libraries as well as supplementary literature sources. We take stars from Lick/IDS, MILES, and NGSL to cover T_{eff} , $\log g$, and $[\text{Fe}/\text{H}]$ as uniformly as possible. However, these libraries mostly lack the cool, bright stars which are important in the near-infrared. For this purpose we select AGB and long-period variable (LPV) stars from LW2000 and IRTF-SpeX with declination $< 35^\circ$ marked M, C or S-stars. LPV stars are also collected from the LMC (Hughes & Wood 1990) and the SMC (Cioni et al. 2003). Red supergiant stars are taken from the lists of LW2000 and Levesque et al. (2005, 2007). To cover metal-rich stars with abundances similar to giant elliptical galaxies, we also include Galactic Bulge giants from the samples of Blanco et al. (1984) and Groenewegen & Blommaert (2005).

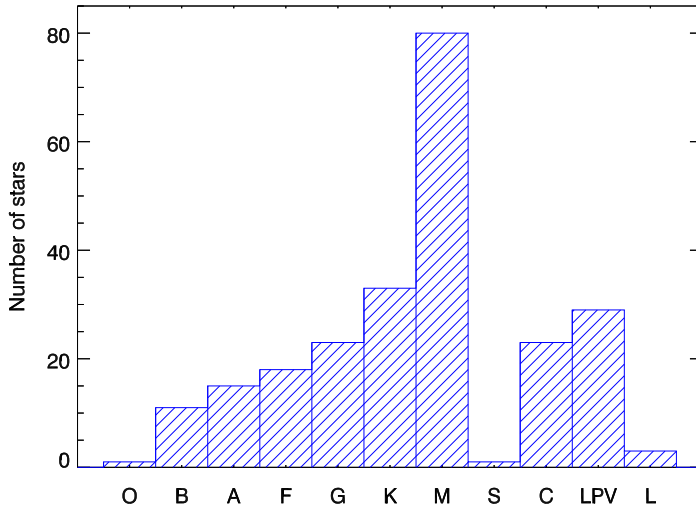


Figure 2.1: Distribution of spectral types in XSL observed in Periods 84 and 85 (excluding telluric calibrators). Spectral types were retrieved from SIMBAD or based on educated guesses from the source libraries or atmospheric parameters.

As of the end of March 2011, 258 observations of 240 individual stars from the XSL input catalog had been completed. Figure 2.1 shows the distribution of stellar types of these XSL stars. In Figure 2.2 we show those sample stars with calculated stellar parameters in an HR diagram; these parameters were computed using ULySS (Koleva et al. 2009; Wu et al. 2011) and will be described in more detail in a forthcoming paper.

2.2.1 Observations

The observations described here were carried out in Periods 84 and 85 using X-Shooter. X-Shooter was built by a consortium of 11 institutes in Denmark, France, Italy and the Netherlands, together with ESO. It is a single-target echelle spectrograph, which maximizes the sensitivity over a broad wavelength by splitting the spectra into three different arms (UVB, VIS and NIR). X-Shooter works at high/intermediate resolutions, depending on wavelength and slit width, of $R = 4000 - 14000$. A unique capability of X-Shooter is that it collects spectra in the wavelength range from the near-ultraviolet to the near-infrared through its three arms simultaneously. This property is extremely useful for observing variable stars, especially very cool stars – like AGB stars – whose spectra may vary substantially during their pulsation cycles.

X-Shooter offers multiple spectroscopic observation modes; we used the longslit SLIT mode for all observations. Three observing strategies are supported in SLIT mode:

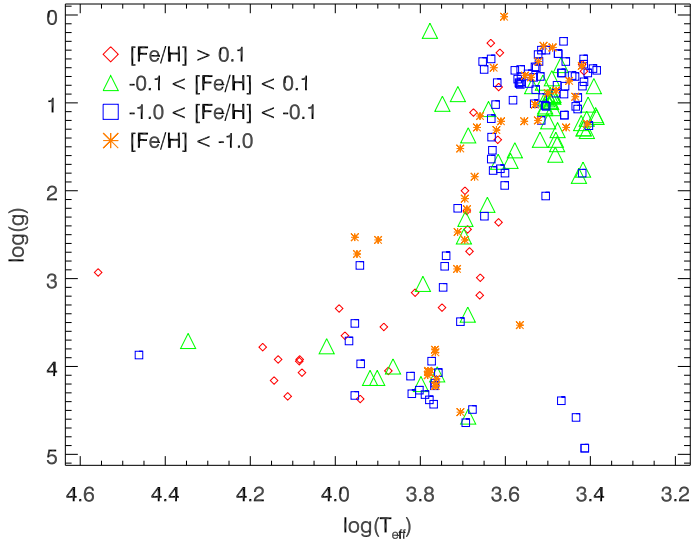


Figure 2.2: HR diagram of the 219 XSL stars (O–M, LPV, S) with calculated T_{eff} , $\log g$ and $[Fe/H]$, where $[Fe/H]$ is presented in different colours.

classical “staring” observations, A–B “nodding” along the slit for improved sky subtraction, and on–off target–sky switching (“offset”). Almost all XSL stars were observed in nodding mode with a narrow slit, yielding an intermediate resolving power of ~ 10000 and good sky subtraction; and nearly all were also observed in staring mode with a wide slit for flux calibration. The observed modes used, slit widths, and CCD readout modes are detailed in Table 2.2. Wide-slit observations were carried out (except on the brightest stars, for which no wide-slit observations were made since they would saturate the detectors) just before nodding observations. CCD binning and readout speeds were altered depending on the brightness of a given target: faint stars ($K \geq 8$ or $V \geq 10$) were generally observed binned in the VIS arm and observed non-binned in the UVB arm with slow readout speeds in nodding-mode. Fast readout speeds were used for brighter stars (Table 2.2¹).

Along with the program stars, we observed hot stars (mostly B-type) to use as telluric standard stars. These were observed using the same narrow-slit setup to preserve the spectral resolution. Flux standard stars taken as part of the normal ESO X-Shooter calibration program were collected from the archive; these were observed using a wide slit ($5.0'' \times 11''$) to sample as much of the total flux as possible.

¹See http://www.hq.eso.org/sci/facilities/paranal/instruments/xshooter/doc/VLT-MAN-ESO-14650-4942_P91P92.pdf for more information

Table 2.2: X-Shooter observing modes for XSL in Periods 84 and 85

Mode	Arm	Slit	λ (nm)	R	Readout (bright)	Readout (faint)
Nod	UVB	0.''5 \times 11''	300–600	9100	400k/1pt/hg	100k/1pt/hg
Nod	VIS	0.''7 \times 11''	600–1020	11000	400k/1pt/hg	100k/1pt/hg/2 \times 2
Nod	NIR	0.''6 \times 11''	1000–2480	8100		
Stare (P84)	UVB	5'' \times 11''	300–600		100k/1pt/hg/2 \times 2	100k/1pt/hg/2 \times 2
Stare (P85)	UVB				400k/1pt/hg	100k/1pt/hg
Stare (P84)	VIS	5'' \times 11''	600–1020		100k/1pt/hg/2 \times 2	100k/1pt/hg/2 \times 2
Stare (P85)	VIS				400k/1pt/hg	100k/1pt/hg
Stare	NIR	5'' \times 11''	1000–2480			

2.3 Data reduction

Basic data reduction was performed with the public release of the X-Shooter pipeline version 1.5.0, following the standard steps described in the X-Shooter pipeline manual² up to the production of 2D spectra, including bias and/or dark correction, flat-fielding, geometric correction, wavelength calibration and sometimes sky subtraction. A master bias constructed from a set of at least five exposures was used to remove the bias level of the CCD and to correct for large-scale electronic noise patterns. A master flat field constructed from a set of at least five exposures was used to correct the pixel-to-pixel variations in the CCD response and the non-homogeneous illumination by the telescope. Wavelength and spatial scale calibration are performed with observations of a Th-Ar lamp in the UVB and VIS arm.

2.3.1 Difficulties encountered and proposed solutions

A number of issues were discovered during the pipeline reduction process which required further processing steps. We give details about the most significant of these steps here.

ISSUES WITH NODDING MODE OBSERVATIONS

Most spectra were reduced using the pipeline recipes corresponding to the observation mode used: spectra observed in staring mode were reduced by the pipeline recipe "xsh_scired_slit_stare", and spectra observed in nodding mode were reduced by the pipeline recipe "xsh_scired_slit_nod". However, in the case of nodding-mode observations, occasionally the first exposure in an A–B pair was centered in the slit and the "throw" to the B image (which is fixed angular difference plus a random extra "jitter") was large enough to put the star at the end or even off of the slit in the B image (we show an example in Fig. 2.3). In these cases, we reduce the well-centered slit in "offset" mode using the second frame as the "sky" frame. This does an excellent job of sky subtraction for these frames, but it means the effective exposure time for these stars is half that anticipated.

²See <http://www.eso.org/sci/software/pipelines/>

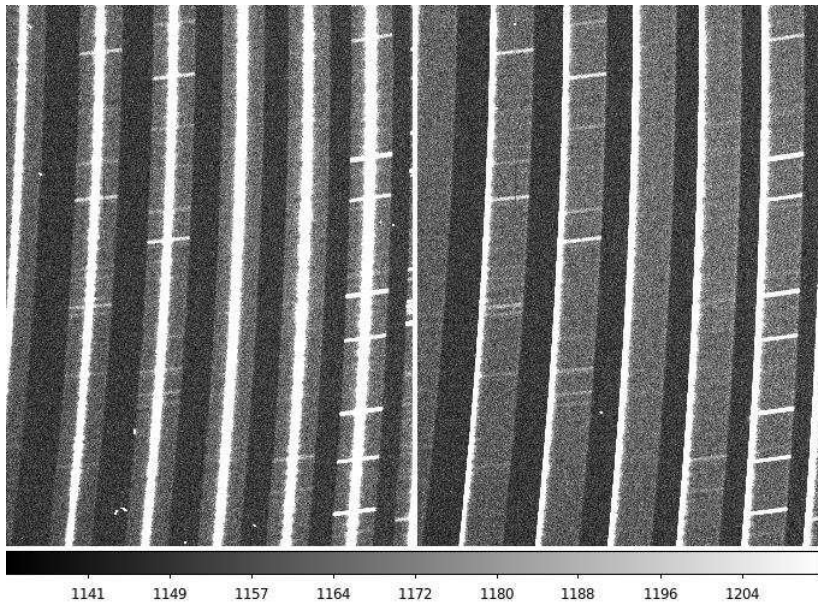


Figure 2.3: Data observed in nodding mode in the VIS arm. Here the star is sitting in the center of the slit in the first exposure (left panel) while the star is almost out of the slit in the second exposure (right panel).

BACKGROUND SUBTRACTION ISSUES IN UVB SPECTRA

When the sky lines are very weak in stare mode – often the case in short-exposure frames, especially in the UVB arm – the background model constructed by the pipeline can fail catastrophically, particularly if weak pattern noise is not properly subtracted by the master bias. Figure 2.4 illustrates an extreme case of this: the left-hand panel is the observed star, and the right-hand panel is the background modeled by the pipeline, in which the modeling has clearly failed. In such cases, we turn off sky subtraction in the pipeline. Instead, we estimate the sky using pixels on either side of the stellar spectrum in the rectified 2D spectra of each spectrograph order, as would be done for observations in stare mode.

The final sky-subtracted 1D spectrum is derived by subtracting the 1D sky spectrum from the 1D spectrum. In Figure 2.5 we show a comparison of the two methods, showing that the in-place background estimation gives a clear improvement.

EXTRA COSMIC RAY CLEANING

The X-Shooter pipeline (ver. 1.5.0) removes the cosmic ray hits (CRHs) for multiple-input images ($n \geq 3$), e.g., in nodding and offset modes, by computing a median of these images and applying a sigma-clipping. If only two raw images are input, as is the case for most of our nodding and offset mode exposures, proper CRH cleaning is

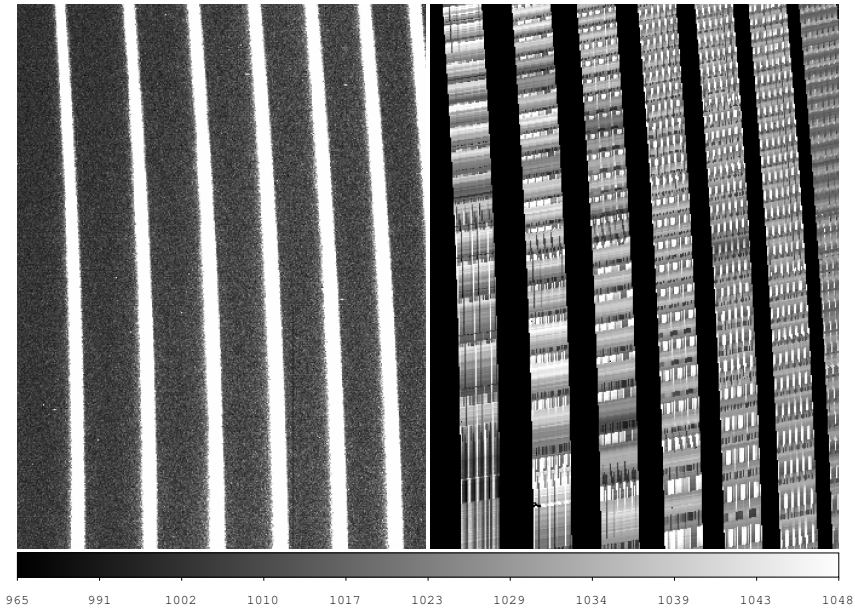


Figure 2.4: Example of background (“sky”) modeled by the pipeline from data observed in stare mode in the UVB arm, in which sky lines are nearly absent. Left panel: original raw frame; right panel: sky frame generated by the pipeline scaled to the same intensity as the left panel. Note the very poor background model.

not performed by the pipeline. This becomes an issue when a CRH in image “A” is sitting on the same position as the star in image “B”; this results in an artificial emission or absorption line in the final 1D spectrum. We present the case of exposures of the star [M2002] SMC 55188 in the VIS arm in Figure 2.6 (a) to illustrate the problem. We see an artificial feature around 1004 nm caused by the CRH in the original “B” frame, (Figure 2.6 (b)), which creates an artificial feature in the 2D image. To correct this problem, we use the algorithm of van Dokkum (2001, as implemented in the IDL code “*la_cosmic.pro*”) to clean the raw image before running the pipeline. The CRH-corrected images are then run through the pipeline before extracting the 1D spectrum (Figure 2.6 (a)). CRH pre-cleaning is used whenever strong CRHs are found to corrupt the 1D spectra.

BAD COLUMNS

We have found that the bad pixel maps produced by and used in the pipeline reduction recipes do not always produce a complete list of bad pixels. In particular, a few bad columns in the VIS arm improperly mapped in the pipeline disrupt the object spectra in order 26, at 635–638 nm. Figure 2.7 shows these bad columns in the raw frame and the final 2D spectrum. These bad columns are difficult to correct effectively in the raw

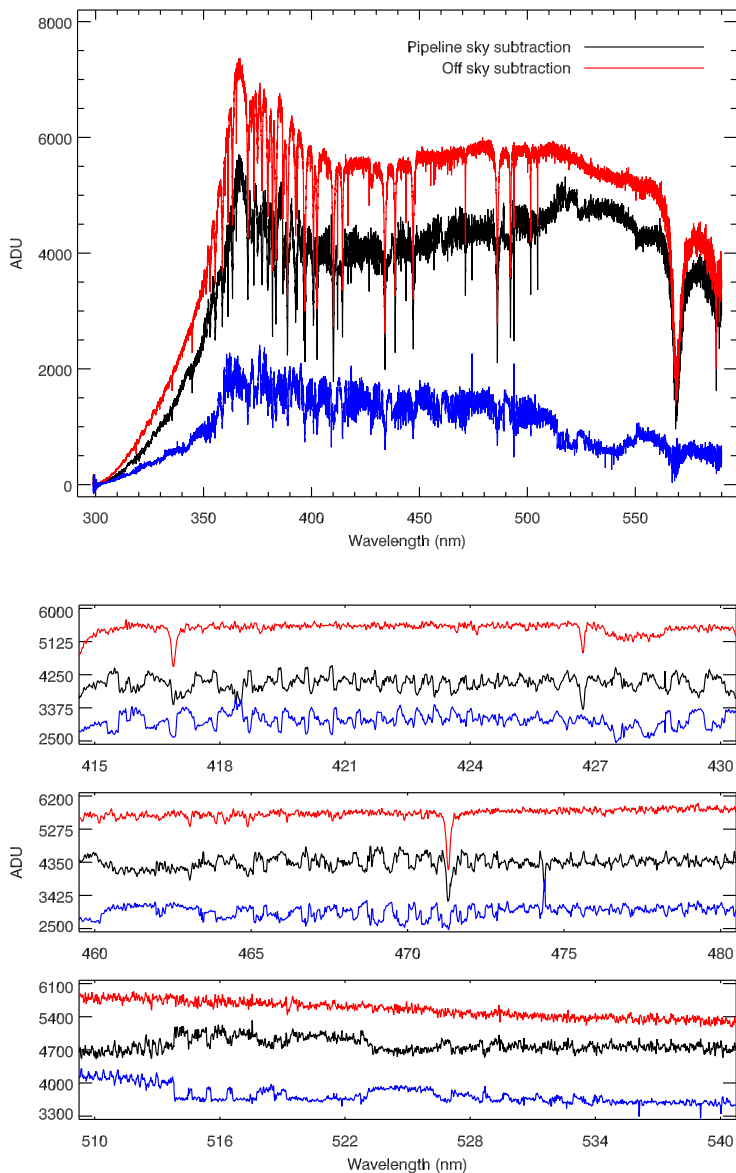


Figure 2.5: Extracted 1D spectra from the UVB arm, using the pipeline sky model (black) and using a background extracted directly from the observation (red), when the sky emission lines are weak (or not observed). The blue spectrum shows the difference between the two methods. In the right panels, we zoom into three small wavelength regions, so that the sky modeling errors of the pipeline are clear.

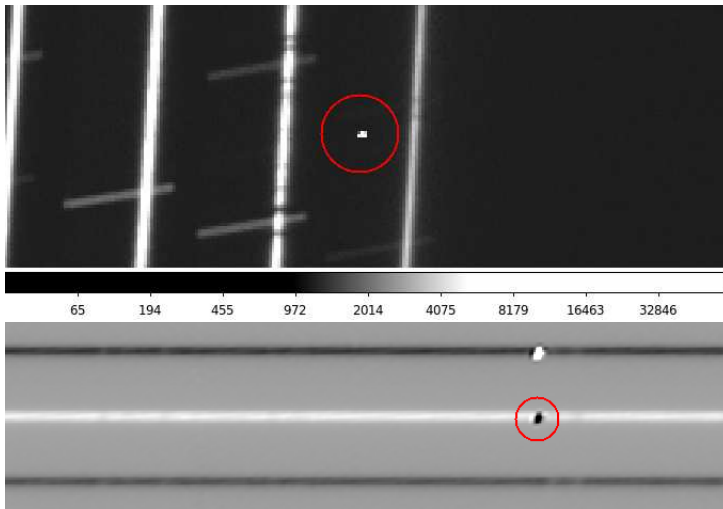
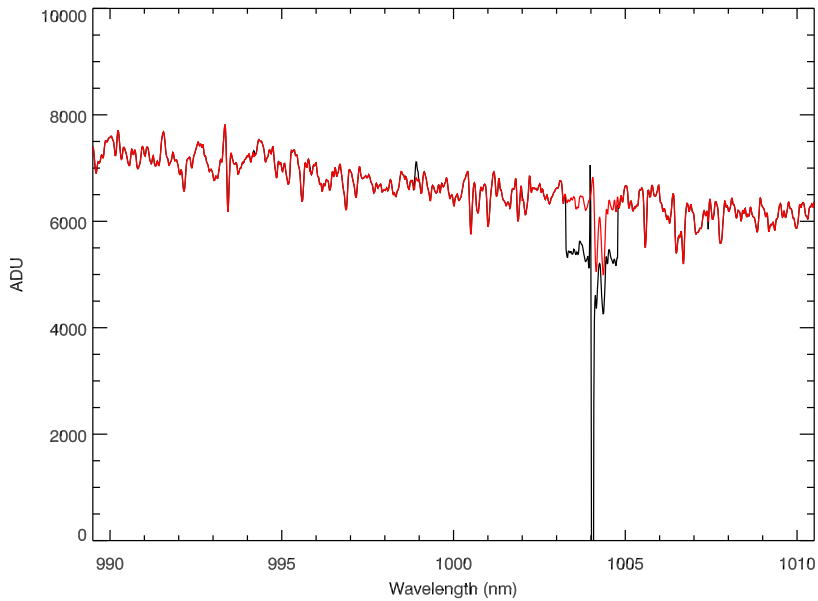


Figure 2.6: Panel (a): Black: extracted 1D spectrum from the pipeline; red: extracted 1D spectra after raw frames corrected using the algorithm of van Dokkum (2001). Panel (b): raw image of “B” frame zoomed in on the CRH feature (red circle). Panel (c): pipeline-corrected 2D spectrum zoomed in on the CRH feature (red circle).

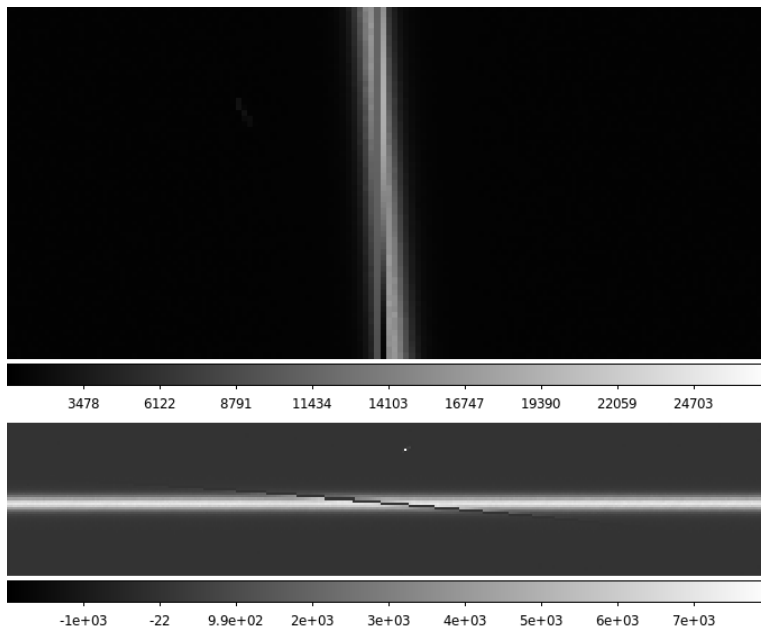


Figure 2.7: *Upper panel: raw image of the telluric standard star Hip024505 zoomed into a region of bad columns in the VIS arm. Lower panel: corresponding final, pipeline-corrected 2D spectrum of this star.*

spectra and make it difficult to reconstruct the profile of the star in this region. Moreover, due to instrumental flexure, these bad columns can affect different exposures at slightly different wavelengths. In the current version of the spectral library, we have set the fluxes to zero from 635.1 nm to the end of order 26 in the final reduced 2D order-by-order frames.

EXTRACTION OF 1D SPECTRA FROM PIPELINE-CORRECTED 2D IMAGES

After the pipeline reduction and our further modifications, we extract a one-dimensional spectrum from the pipeline-corrected flat-fielded, wavelength and geometrically-corrected single-order 2D spectra using our own IDL weighted extraction code, inspired by the prescription of Horne (1986). There are in total three extensions for each order in the pipeline-produced 2D spectra: the first is the flux in counts, the second is the error, and the third is the quality, which corresponds to the bad pixel mask. We make use of the third extension as the first guess for a bad pixel mask, and the second extension as the square root of each pixel's variance. With 2 to 20 iterations, the bad pixel mask is improved and most of the CRHs or bad pixels are masked. Spectra from each order are then extracted and merged using a variance-weighted mean of each wavelength in the overlapping regions.

The extraction aperture was set to a fixed width of $4''9$ (in narrow-slit observations)

or $10''.9$ (in wide-slit observations) in the optimal-extraction code. However, if significant CRHs or other problems remain within the nominal extraction aperture the final 2D frame, the extraction aperture was modified to exclude these regions.

We show a G2 star, HD17072, observed in the UVB arm in Figure 2.8 to illustrate this process. We note that the orange order between 355 and 370 nm shows noisy features. However, the larger errors in this region yield lower weights compared with the green order in the overlap region. These features therefore do not appear in the final merged spectrum (thin black line).

2.3.2 Saturation

In these first two periods, saturation was a common problem, as our sample contained variable stars near X-Shooter’s bright target limit (and our exposure times were, in the absence of accurate light curves, determined for the *mean* stellar brightnesses). Given the large total number of frames in these periods (1847 for the 258 observations, including NIR arm spectra), an automated saturation-detection scheme was required. Uncorrected CRHs and bad pixels appear as (nearly) saturated pixels, so a scheme had to be developed to decide which frames were strongly saturated and had to be thrown away. Every raw frame was transformed using the following rules. In the UVB and VIS arm images, pixels with counts ≥ 65000 are set to “1”, which means “saturated”; all others are set to “0”, which means “good”³. Truly saturated frames typically have saturated pixels clustered together in individual orders. We sum each transformed binary “good”/“saturated” image along the wavelength direction for a better visualization of the saturation. We show an example of a typical saturated raw frame in Figure 2.9. Here saturated pixels are accumulated along the orders, showing sharp features. Raw frames with such features are considered to be “saturated” and removed from the library. In the end, 173 (9.3%) of 1847 extracted spectra were found to be “saturated” and removed.

³In the NIR arm, due to the different readout scheme of these detectors, pixels with counts ≤ 0 or ≥ 42000 are set to “1”.

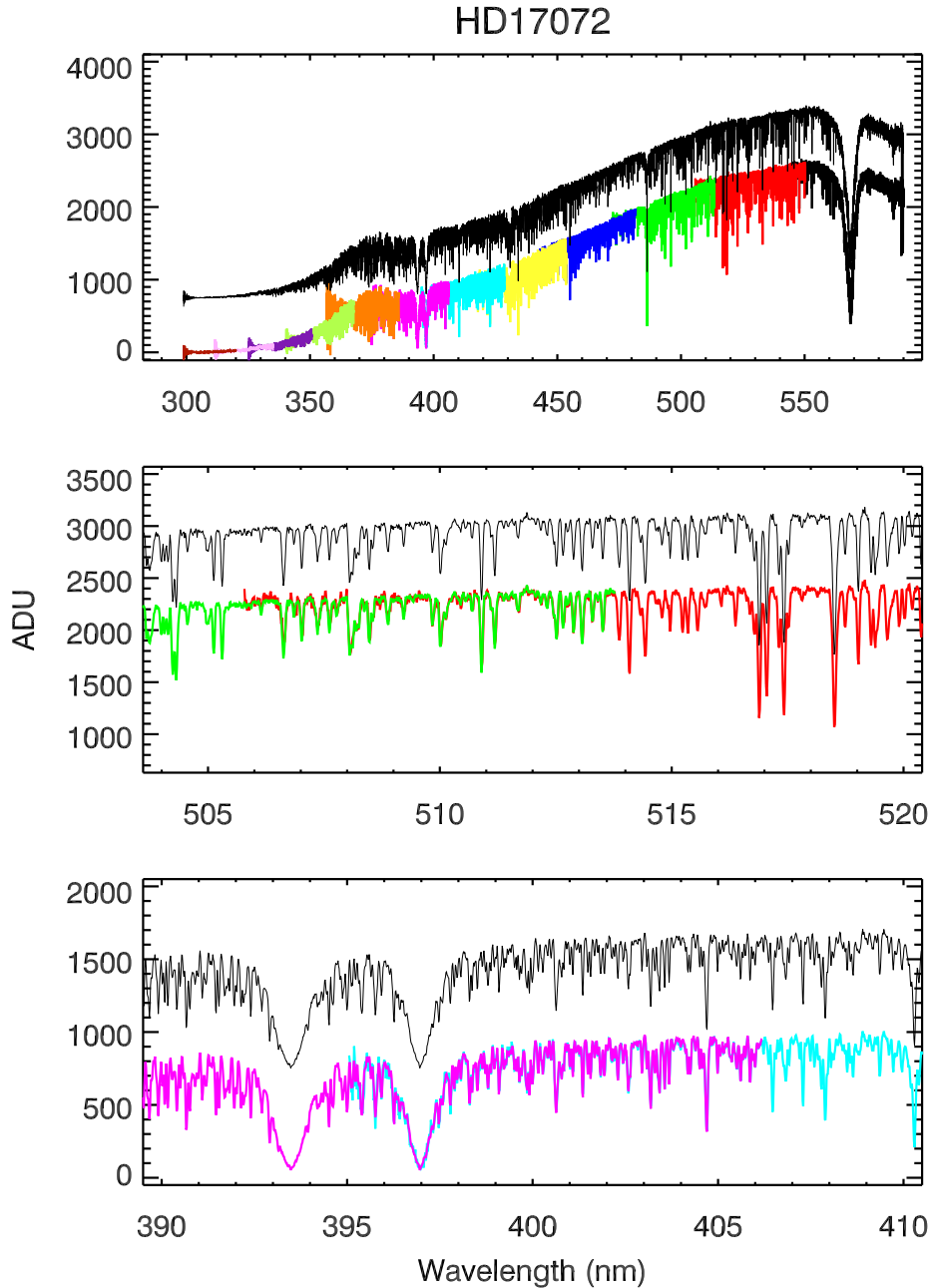


Figure 2.8: Order-by-order 1D spectrum extraction for the G2 star HD17072 in the UVB arm, without flux calibration. Different colours correspond to different orders. The continuous black spectrum is the combined spectrum, offset for clarity. In the middle and bottom panels, we zoom in on two wavelength regions, 504–520 nm and 390–410 nm where orders overlap, to see the extraction and combination process in detail.

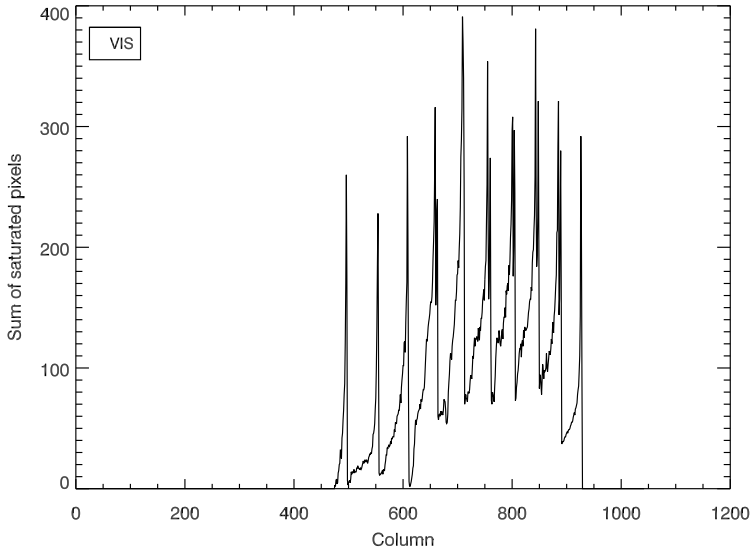


Figure 2.9: A saturated raw VIS arm frame after transformation of counts to a binary “good pixel”/“saturated pixel” basis, and summed along the wavelength direction. Note the sharp features with values in excess of 200, indicative of saturation due to overexposure. See text for details.

2.4 Telluric correction

Ground-based spectroscopy is always subject to contamination from the Earth’s atmosphere. The sky subtraction described in Sec. 2.3.1 corrects for the additive component of this contamination, leaving the multiplicative effects of absorption and diffusion. In the visible and NIR portions of the spectrum, water vapour, molecular oxygen, carbon-dioxide and methane generate strong absorption features. Absorption features that originate in the Earth’s atmosphere are referred to as telluric features. Correction for telluric contamination, therefore, is important for the XSL spectra in the VIS and NIR arms. The correction for the continuous component of atmospheric extinction is discussed in Sec. 2.5.1.

In general, if we knew how much light was absorbed by the Earth’s atmosphere in a certain wavelength region, we could “recover” the fluxes in that region by dividing the known absorbed fraction. This requires a telluric template, determined either by modeling the atmosphere by a radiative transfer code such as ATRAN (Lord 1992) and LBLRTM⁴, or by observations of ideally featureless stars (in practice typically hot stars, whose only features are hydrogen and/or helium lines). Although radiative transfer codes have shown to be promising (Seifahrt et al. 2010) to remove the atmospheric

⁴See http://rtweb.aer.com/lblrtm_description.html

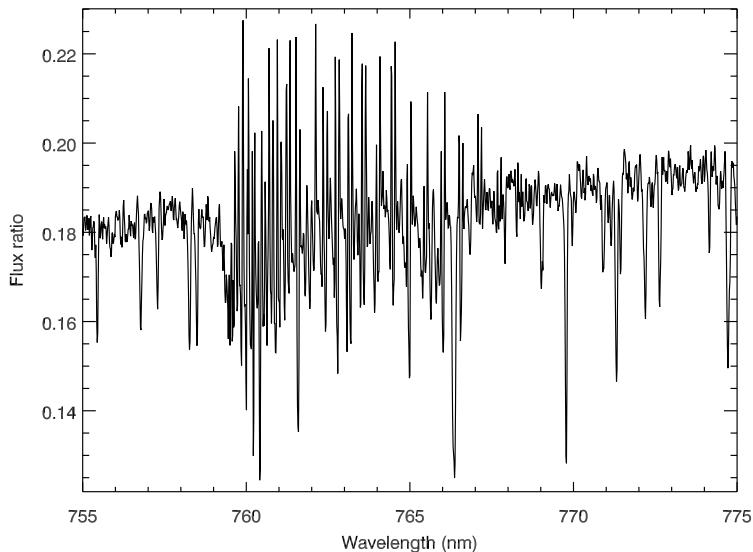


Figure 2.10: Ratio of counts between CI* NGC 6522 ARP 4329 and the closest (in elapsed time) telluric standard star Hip094378, zoomed in the ‘A’ band in the VIS arm.

absorption, particularly at high spectral resolution in the NIR, this method requires as input a molecular line database and a model atmosphere based on meteorological data. Because we have thousands of spectra taken at different airmasses, pressures and humidities, this method is currently computationally too expensive.

Instead, we use telluric standard star observations taken as part of the standard X-Shooter calibration plan directly after each of our science observations as a basis for telluric correction of our data. The narrow-slit settings are used for the telluric standard observations, to match the highest resolution of our science observations.

We find that the telluric absorption lines change strength on timescales shorter than the “long” exposure time (≥ 90 seconds) of faint XSL stars and the total overhead time of ~ 900 seconds, resulting in an imperfect telluric correction. In addition, small changes in spectral resolution and wavelength zero-point occur even between successive observations. Figure 2.10 shows the ratio of counts between a science object (CI* NGC 6522 ARP 4329, an M star in the Galactic bulge) and the telluric standard star (Hip094378, a B2V star) observed 37 minutes later. The ratio shows that the closest telluric standard spectrum does not give a satisfactory solution for the atmospheric transmission.

To optimize the telluric correction, we have built a library of telluric spectra, in which the hot stars were first carefully wavelength- (re)calibrated. The final library is a large collection of different atmospheric transmissions used to correct the telluric absorption features in the XSL spectra, as described below. We note that in this paper

Table 2.3: *The input stars for the VIS-arm telluric library*

Name	RA (J2000.0)	DEC (J2000.0)	Exp. time (s)	airmass	Sp. type	shift (kms ⁻¹)
Hip088947	18:09:22.50	-36:40:20.2	12.50	1.771	B1II	-3.21
Hip089086	18:10:55.37	-33:47:58.4	12.50	2.505	B1V	-1.77
Hip091038	18:34:15.92	-04:48:48.7	12.50	1.063	B1V	-5.65
...

we only discuss the correction of the VIS arm spectra, as the UVB spectra do not require telluric line correction, and we will discuss the NIR spectra in another paper.

2.4.1 The telluric library

We have collected 178 VIS arm spectra of telluric standard stars with spectral type A, B and G in Periods 84 and 85. The data were reduced identically to the program spectra. As the G stars are much cooler and have more lines than A and B stars, we have not used them to build our telluric templates. Moreover, 22 out of 175 spectra of A and B had strong intrinsic emission lines and have not been used either. Table 2.3 lists the 152 telluric standard stars (and the airmass at which they were observed) used in the telluric library.

IDENTIFICATION OF ATMOSPHERIC TRANSMISSION FEATURES

The goal of building the telluric library is to produce a collection of empirical atmospheric transmission spectra to use as a basis for correcting the telluric absorption in the science spectra. To accomplish this, the main telluric features in the observed telluric standard spectra must be separated from the intrinsic features of these hot stars.

In order to extract the atmospheric transmission from the 1D spectrum of a hot star, we need to identify the intrinsic spectral features of the star. We use synthetic spectra from model atmospheres drawn from the POLLUX database⁵ (Palacios et al. 2010) for stars with effective temperatures 10000–15000 K, and synthetic spectra from Munari et al. (2005) for stars with effective temperatures 15000–27000 K. We use the full-spectral-fitting program pPXF (Cappellari & Emsellem 2004) to fit the hot star's intrinsic features with the synthetic spectra. We choose a sub-sample of templates from the collection of synthetic spectra according to the spectral type of each telluric standard star.

Pixels fit "well" by the model template are marked as intrinsic features of the hot stars, while any others are marked as contaminated by telluric features. It is not always straightforward to recognize which pixel belongs to the star itself or is affected by the atmosphere especially when the atmospheric features are superimposed on the hydrogen Paschen absorption lines of the hot stars, i.e., in the wavelength region $\sim 8900 - 9800 \text{ \AA}$. Furthermore, some lines affected by non-local thermodynamic equilibrium (NLTE) effects are not perfectly reproduced by the LTE POLLUX and Munari

⁵<http://pollux.graal.univ-montp2.fr/>

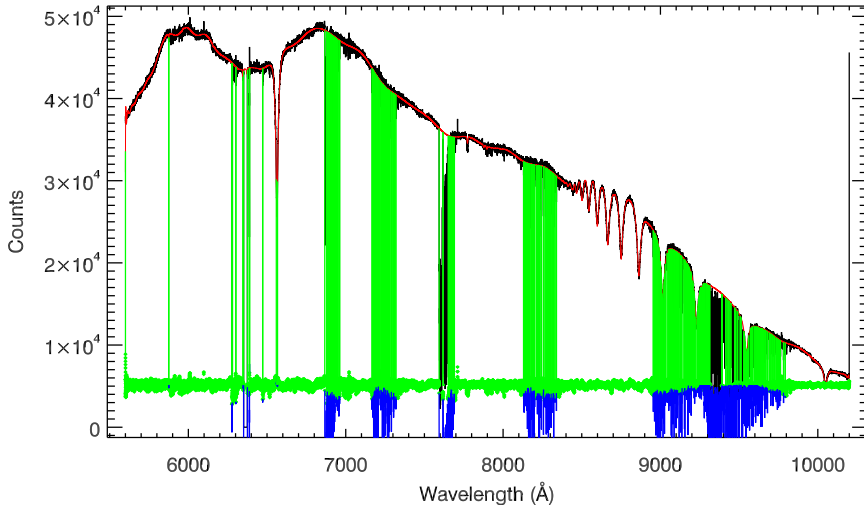


Figure 2.11: Extraction of the telluric absorption from the B8V star Hip012389. The black spectrum is the original 1D spectrum (without telluric or flux calibration). This spectrum is fit by the synthetic LTE spectrum from a model atmosphere in the pixels outside of the vertical green lines. The red spectrum represents this fit. The lower part of the plot shows the residuals from the best fit: green points represent regions of intrinsic stellar absorption, while blue points are (almost) the telluric absorption spectrum. We note that the residual between the best fit and the data is scaled to the view level. It is therefore not surprising that some features are below zero.

models. To separate the pixels containing telluric features from those containing intrinsic stellar features, at least two iterations are necessary. In the first iteration, we define strong hydrogen absorption regions uncontaminated by telluric absorption, and fit these with the model synthetic spectrum and a moderate-order multiplicative polynomial. Because some parts of the $H\alpha$ line (λ 6562.8 Å) are affected by NLTE (Thurl et al. 2006), and occasionally the core is filled by weak absorption, this line can be very hard to reproduce by the models based on LTE. We therefore mask the core of the $H\alpha$ line – roughly ± 4 Å around the line center – and after the fit replace this region with the same wavelength region of the fitted model. Residuals from this first iteration are assumed to represent the noise of each pixel. Pixels deviating by more than 3–5 standard deviations from this first fit are mostly telluric absorption features and are masked from the fit in the next step.

In the second iteration, the fit is performed with a high-order multiplicative polynomial, and we are able to match in detail the continuum of the hot star. A B8V star is shown in Figure 2.11 to illustrate the fitting process in this iteration. Subsequent iterations were occasionally necessary to improve the final fit. The telluric features were then extracted by dividing the original 1D telluric standard star spectrum by the best fit of the final iteration.

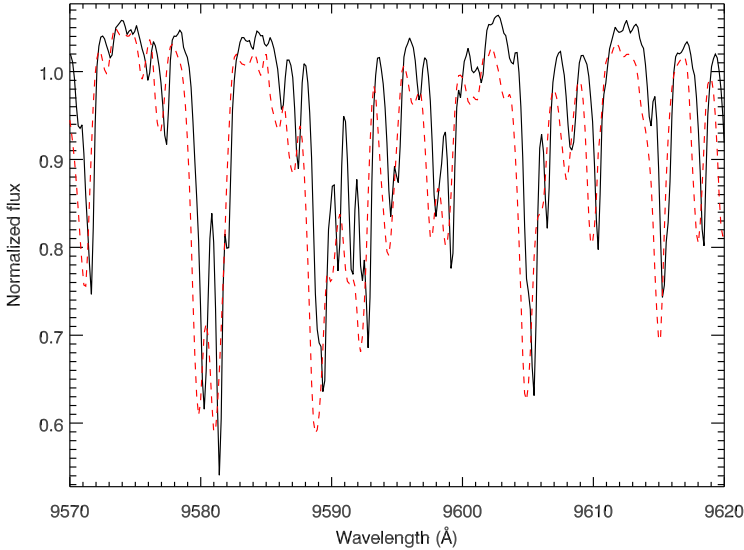


Figure 2.12: Two normalized telluric standard stars, Hip026545 (black line) and Hip012389 (red dashed line), zoomed into the wavelength region 9570–9620 Å, showing the impact of the flexure of the X-Shooter backbone on the wavelength calibration. The wavelength shift is roughly 2 pixels between these two spectra, or $\approx 10 \text{ km s}^{-1}$.

We call the telluric features extracted by this process the “raw transmission spectra”, as there are several steps required before the telluric library is ready to be used. The quality of the raw transmission spectra depends on the templates of the hot stars and the signal-to-noise of the original X-Shooter spectra, as well as the multiplicative polynomial used in the fitting.

ABSOLUTE WAVELENGTH CALIBRATION AND SPECTRAL CLEANING

To build the telluric library, all the telluric features in different standard stars must be at exactly the same wavelengths. We find that the wavelengths for the same telluric feature are slightly shifted in different spectra, due to the flexure and imperfect rotation of the X-Shooter backbone. In Figure 2.12 we show an example of this shift, which is equivalent to $\approx 10 \text{ km s}^{-1}$ in this case. We therefore require an extra wavelength calibration step for each raw transmission spectrum.

Although we do not use theoretical atmospheric transmission spectra to correct our spectra for telluric absorption, we use them as references for the final wavelength calibration. We use a high-resolution ($R \sim 60000$) model transmission spectrum computed for us by J. Vinther from the ESO Sky Model Calculator⁶ as a template to cross-correlate

⁶<http://www.eso.org/observing/etc/bin/gen/form?INS.MODE=swspectr+INS.NAME=SKYCALC>

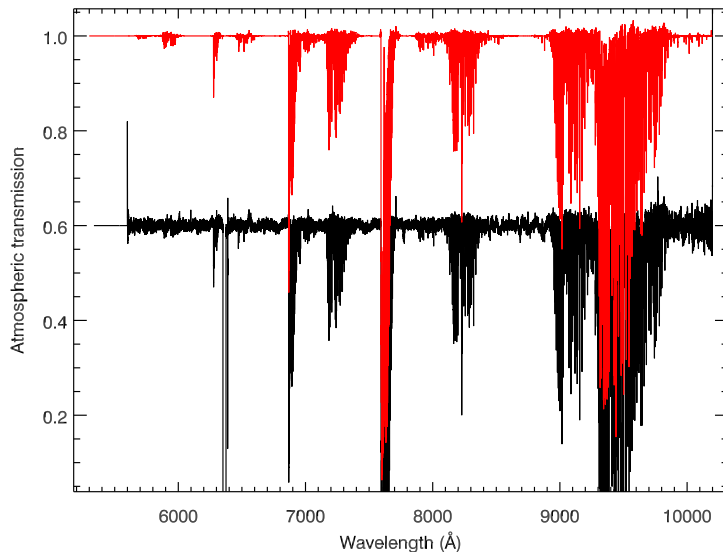


Figure 2.13: *Extracted raw transmission spectrum from the B8V telluric standard star Hip012389 (black) and the shifted, cleaned “final” transmission spectrum from this star (red). The raw transmission spectrum has been offset for clarity.*

and correct the small residual wavelength offsets in the raw transmission spectra. The corrections for each raw transmission spectrum are listed in the last column of Table 2.3; see Appendix 2.B for details and the complete list.

The extracted transmission spectra are inevitably influenced by the signal-to-noise ratios of the original spectra (and any remaining bad pixels). To reduce the influence on the final telluric-corrected spectra, especially those pixels which are not contaminated by telluric features, we “clean” the shifted transmission spectra based on the model transmission template. Pixels with values which deviate more than 10 sigma from the template are set to unity, so as not to introduce noise or artificial features into the telluric-corrected science spectra. Figure 2.13 shows the raw transmission spectrum (in black) and shifted, cleaned transmission spectrum (in red) extracted from the telluric standard star Hip012389.

After carefully checking the quality of the output transmission spectra, the telluric library is ready to be used, with 152 final transmission spectra.

2.4.2 Final telluric correction

Once the telluric library is available, we can perform the telluric correction on the science spectra. The simplest process would be to divide a science spectrum by the temporally-closest transmission spectrum. An improvement is obtained by exploiting

the variety of telluric absorption properties present in our large telluric library. A combination of telluric templates can provide a better estimate of the telluric absorption in a given science exposure than the one telluric standard observed closest in time (Chen et al. 2011).

The key to our telluric correction method, like producing the telluric library itself, is determining the underlying stellar spectrum. A quick glance at the extracted 1D spectra shows that it is easier to define the continua of warm stars than cool stars, such as M-type giants and dwarfs, carbon stars or LPVs. We therefore classify the science spectra according to their spectral types into two groups: those that have easily-determined continua, O to K stars, and the cooler stars, which do not. For warm stars we estimate the atmospheric transmission using the optimization algorithm described below, making use of the original science spectra; for the cooler star we simply use the temporally-closest transmission spectrum from the telluric library.

RECONSTRUCTING TELLURIC ABSORPTION WITH PRINCIPAL COMPONENT ANALYSIS

Algorithms that estimate the telluric absorption by seeking the best linear combination of the 152 templates of the telluric library seemingly succeed (i.e. they produce a result that passes eye inspection), but they are dangerous: this linear problem is ill-conditioned. There are not 152 meaningful degrees of freedom in this problem. In more physical terms, there are not 152 fundamental Earth-atmospheric parameters that produce differences between transmission curves larger than the amplitude of the noise in the XSL data. The consequence is that the linear combination coefficients derived from a standard linear-optimization algorithm are determined to a large extent by the noise in the spectra, rather than by the telluric features of interest (see Ocvirk et al. 2006, for further explanations in a conceptually similar context). Details of the science spectrum that are not telluric features may be erased. To avoid this issue, one needs to remove items from the telluric library until the linear problem is well behaved. But which ones? We use principal component analysis (PCA) to circumvent this problem.

PCA reveals the internal structure of a data set in a way that best explains the variance in the data. It is widely used in analyzing multi-dimensional data sets. In data reduction applications, PCA has been used for sky subtraction by Wild & Hewett (2005) and Sharp & Parkinson (2010). Inspired by this idea, we have developed a method to determine the telluric correction for our (warm) program stars. The algorithm (Wild & Hewett 2005) is to determine the basis vectors from those pixels which vary most in the spectra of the telluric library. The amplitudes given by the projection of these basis vectors onto each science spectrum are used to reconstruct the telluric features in the science spectrum. Telluric correction is then a straightforward division of science spectrum by the projected telluric spectrum.

PCA components The telluric library contains 152 spectra, each with a length of 43615 pixels. Standard PCA analysis would imply the requirement of diagonalizing a 43615×43615 matrix, which is computationally expensive. Instead, we assume that \mathbf{X}

is the matrix that we built based on the telluric library, with the mean subtracted from each individual spectrum. The covariance matrix C for computing the eigenvectors then can be written as

$$C = \frac{1}{N} \mathbf{X}^\dagger \mathbf{X}, \quad (2.1)$$

where \mathbf{X}^\dagger is the transpose of the matrix \mathbf{X} and N is the number of objects, here 152. The eigenvectors \mathbf{u}_i then can be solved from the equation

$$C \mathbf{u}_i = \lambda_i \mathbf{u}_i, \quad (2.2)$$

where λ_i is the eigenvalue associated with \mathbf{u}_i . If we expand the Equation 2.2, and multiply by \mathbf{X} on both sides, we have

$$\frac{1}{N} \mathbf{X} \mathbf{X}^\dagger \mathbf{X} \mathbf{u}_i = \lambda_i \mathbf{X} \mathbf{u}_i. \quad (2.3)$$

Equation 2.3 has the same set of eigenvalues as Equation 2.2 for the vector $\mathbf{v}_i = \mathbf{X} \mathbf{u}_i$. The dimension of the array $\mathbf{X} \mathbf{X}^\dagger$ is much smaller – 152×152 – than in the standard formulation, dramatically reducing the computing time. When the temporary eigenvector \mathbf{v}_i is derived, we can derive the original eigenvector \mathbf{u}_i . We wrote our own IDL PCA code following the above algorithm and performed the PCA on our 152 telluric library spectra. The extracted 152 eigenvectors or principal components are then ready to be used to reconstruct the telluric features in the science objects.

Figure 2.14 shows the first six principal components from the bottom to top. The first two components have a clear physical meaning: the first component shows the mean spectrum of the telluric library, while the second component appears to separate most of the water vapour features (seen “in absorption”) from O_2 features (seen “in emission”).

Reconstructing the telluric absorption spectra Two steps remain before we can obtain the final estimate of the telluric absorption in a science spectrum. First we must normalize the science spectra. Second, we have to correct the wavelength offset of the telluric features in the observed spectra (due to instrument flexure) from the more-accurate wavelengths of the telluric library spectra. The resulting telluric absorption spectrum is used to correct the science spectrum. In this procedure, any intrinsic absorption or emission features should not be removed from the science spectra. An accurate estimation of the stellar continuum is therefore required. We recall that we only perform the PCA reconstruction for the spectra of warm stars.

To normalize a science spectrum, we need to determine its continuum. We have developed an IDL code that determines an approximate continuum for a (warm) star. The code seeks the strong intrinsic features (e.g. H_α , H_β , CaII triplet etc.) from a line list ⁷ according to the radial velocity given by ULYSS and defines them as nodes. We flag pixels between those nodes which have a second derivative greater than zero and replace them by a linear interpolation between the nearest unflagged pixels. By this

⁷http://physics.nist.gov/PhysRefData/ASD/lines_form.html

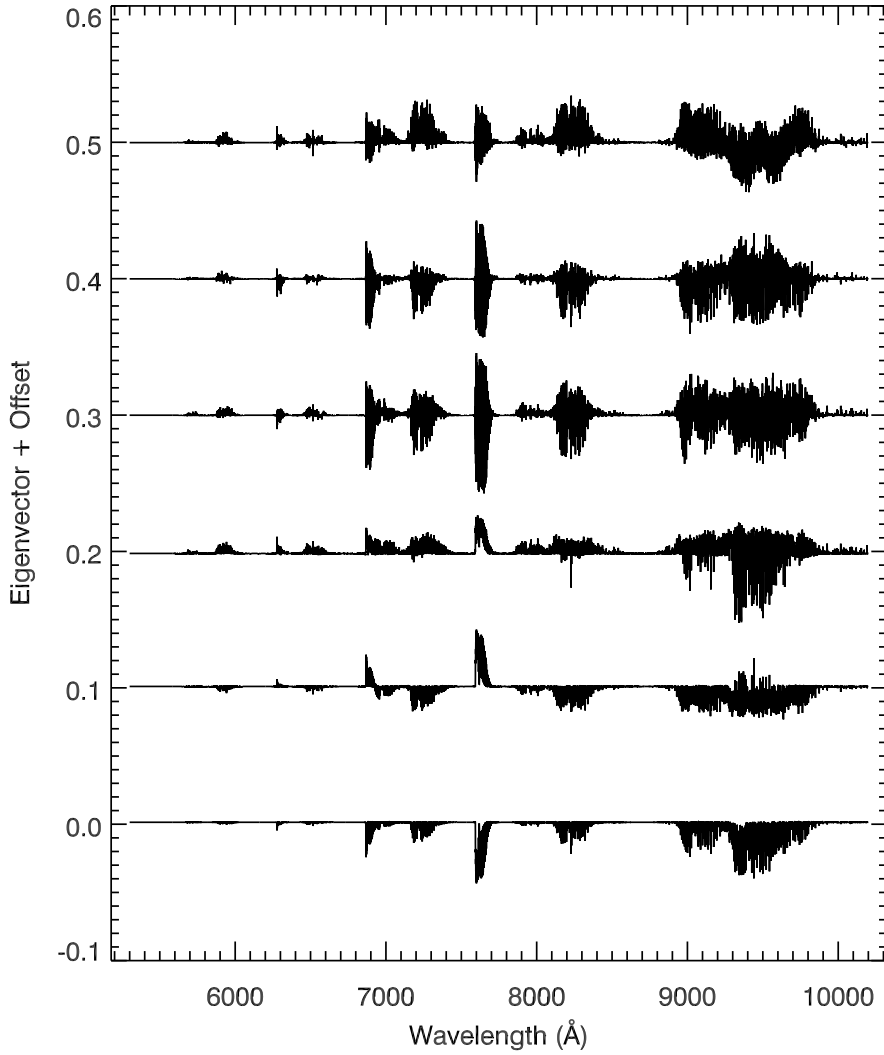


Figure 2.14: The first six principal components of the telluric library. The eigenvalues decrease from the bottom to the top of this figure (i.e., the first – largest – eigenvector is the lowest). The eigenvectors have been offset for display purposes.

process, weak and narrow lines are rejected, since we only care about a rough continuum. Usually around three to five iterations are used to find the local continuum between two nodes. Once the continuum of a spectrum has been found, the science spectrum is easily normalized by dividing the continuum before finding the PCA components.

We use pPXF to determine any residual wavelength shift in the telluric lines of the normalized science spectrum, taking the first principal component as a template. The shift is applied to the PCA components, thus avoiding unnecessary rebinning of the science spectrum.

For wide slit observations, pPXF also determines an adequate broadening function for the lines of the telluric library. The principal components are then convolved with this function before they are used. We note that smoothed PCA components are not precisely the PCA components of a smoothed telluric library. After a few tests, smoothing first was judged too computationally expensive for our current purpose, considering that the wide slit observations are used only to correct the high resolution observations for slit losses.

We finally project the mean-subtracted, normalized science spectrum onto the modified principal components and sum these projections. The final estimate of the transmission is derived by the combination of 40 principal components with the amplitudes resulting from the projection. However, stars with weak emission lines or with a high density of lines present a challenge, and for these stars we use only 20 components to avoid affecting their intrinsic features by mistake. Once the reconstructions have been constructed, the telluric correction can be performed by dividing the normalized spectra by the reconstructed transmission. The final telluric corrected spectra are then derived by multiplying the resulting spectra by the continuum.

We show the original 1D spectra of HD 164257 (A0V), HD 193896 (G5IIIa), and HD 79349 (K7IV) and their telluric-corrected versions in Figure 2.15, 2.16 and 2.17, respectively. We find that the telluric correction by the PCA reconstruction has done a reasonable job both for the early-type stars and some late-type stars. In general, this method works better for stars with simpler continua and high signal-to-noise ratios. Occasionally, division by almost zero produces artificial spikes like those seen at 7600 Å in Figure 2.16 or at 9300 – 9400 Å in Figure 2.17. When these occur, we flag the pixels incorrectly reconstructed and set them equal to zero in the final telluric-corrected spectra.

TELLURIC CORRECTION FOR COOL STARS

The PCA method requires an accurate representation of the stellar continuum to work correctly. It is difficult to trace the continua of cool stars. For instance, carbon stars have strong and sharp molecular bands. One therefore has to trace each absorption bandhead, which can be difficult because some molecular bands occur exactly at the same wavelengths as the telluric absorption regions. In this case, we use the temporally-closest transmission spectrum from the telluric library.

As in the warm stars, we must correct residual wavelength calibration errors and match the line broadening of the science and the temporally-closest transmission be-

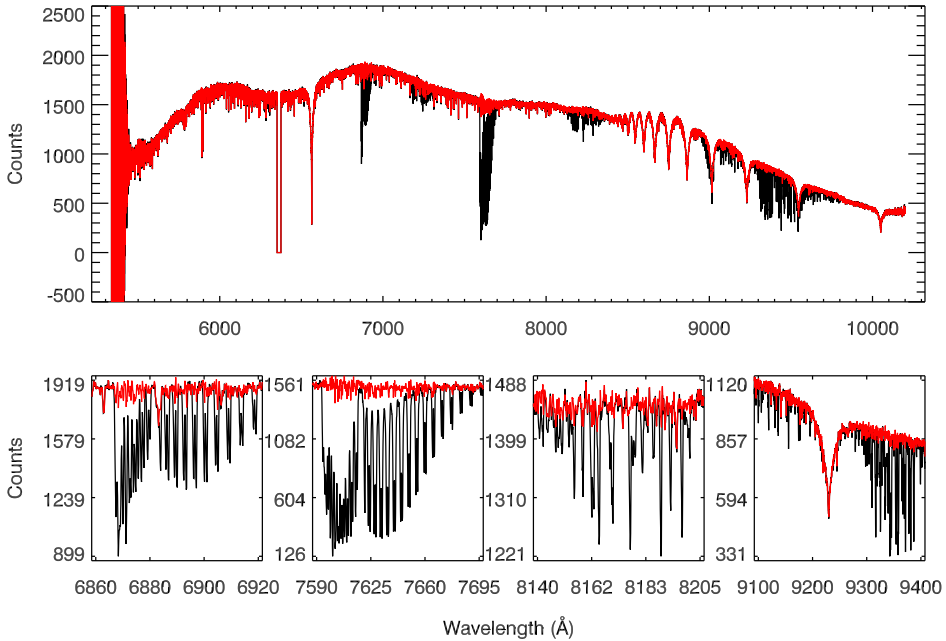


Figure 2.15: Spectrum of HD 164257 (A0) before (black) and after (red) telluric correction in the VIS arm, using the PCA reconstruction method described in the text. The lower panel shows four zoomed-in regions to show the corrections in detail.

fore dividing. We calculate these corrections as described above, using the wavelength range of the atmospheric “A” band of O_2 . The “A” band is chosen because it is the strongest telluric absorption feature in the VIS arm spectra and is easily distinguished from other molecular species. The telluric correction is then made by directly dividing the science spectrum by this modified transmission spectrum.

There is the risk that by using the closest telluric absorption spectrum one may over- or underestimate the real telluric spectrum of the science object. In the case that the exposure time of the science object is short and the accompanying telluric standard star spectrum is therefore very close in time to the science object, this method does a better job to preserve the intrinsic features of the stars than the PCA method for cool stars. We show an example of the telluric correction made by both methods on an LPV star OGLEII DIA BUL-SC1 235 in Figure 2.18. To make sure where the molecular bands should be, we use an NGSL star HD175865 (thick green spectrum) with similar temperature as a comparison, which has no telluric contamination. The PCA reconstruction method, as shown in the blue spectrum, does not reproduce the molecular bands properly. The correction by the closest transmission spectrum, although not

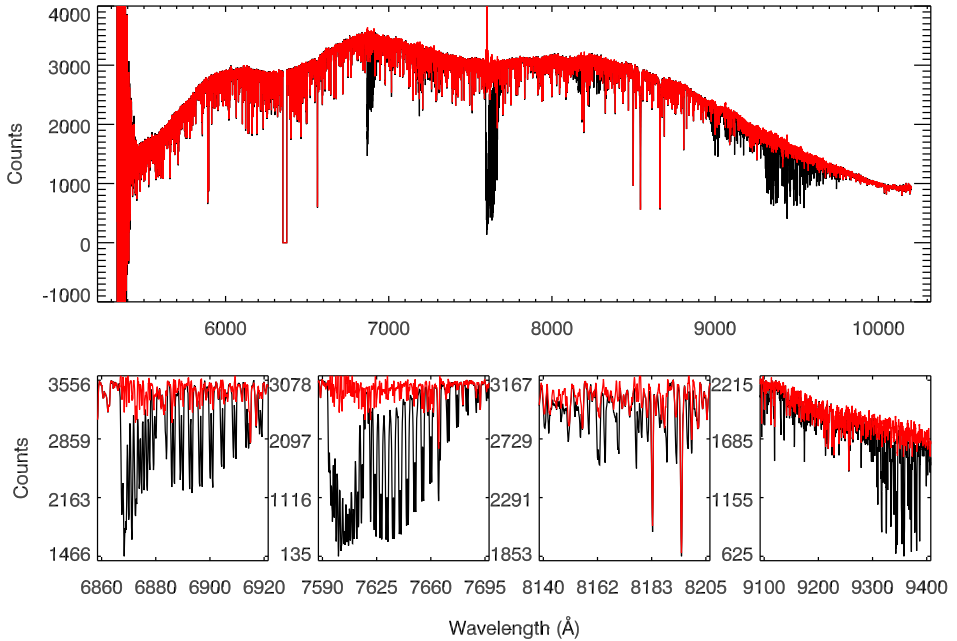


Figure 2.16: Spectrum of HD 193896 (G5IIIa) before (black) and after (red) telluric correction in the VIS arm, using the PCA reconstruction method described in the text. The lower panel shows four zoomed-in regions to show the corrections in detail. Artificial spikes around 7600 Å are the residuals after telluric correction.

perfect, is closer to the intrinsic features of the star, as we can distinguish the molecular bands clearly.

We use this method on all carbon stars, LPV stars, and most of the cool M stars. We remind the reader that the method (using the closest transmission spectrum) for cool stars may not be the final, best solution for these stars, but we use it in the absence of accurate spectral models of these (molecule-rich and typically variable) stars.

COMPARISON OF THE TWO METHODS OF TELLURIC CORRECTION FOR WARM STARS

To test the PCA reconstruction method, we compare the results with a simple correction using the closest telluric absorption spectra on warm stars. In Figure 2.19 we show the telluric correction achieved by our two methods for the G3V star G169-28. We zoom into the atmospheric “A” band for a fair comparison. It is clear that the PCA reconstruction (blue spectrum) does a better job than the temporally-closest telluric absorption

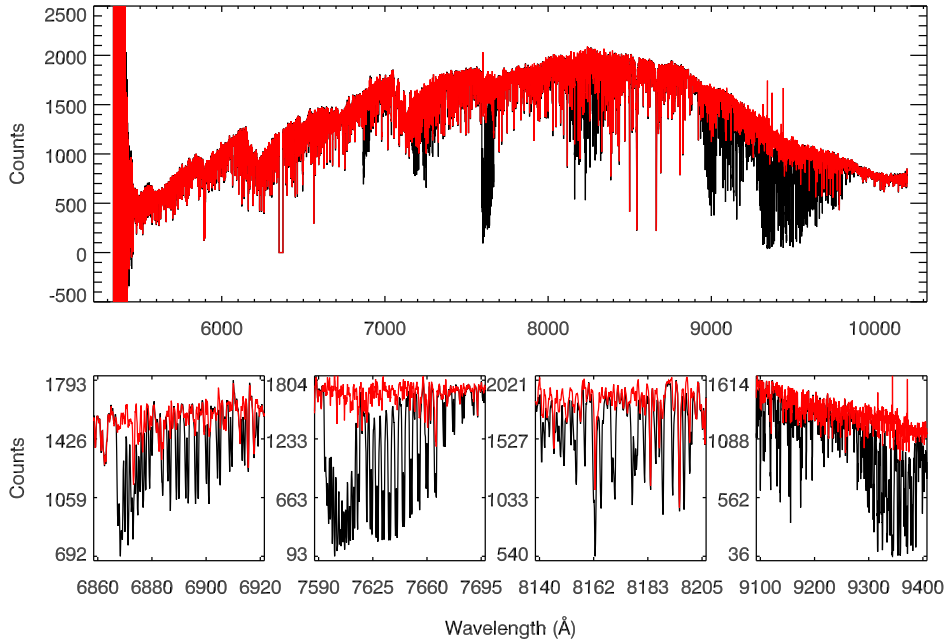


Figure 2.17: Spectrum of HD 79349 (K7IV) before (black) and after (red) telluric correction in the VIS arm, using the PCA reconstruction method described in the text. The lower panel shows four zoomed-in regions to show the corrections in detail. Artificial spikes around 9350 Å are the residuals after telluric correction.

spectrum in at least this warm star. Again, whether we use the PCA reconstruction method to perform the telluric correction depends on whether we can determine an accurate representation of a star's continuum.

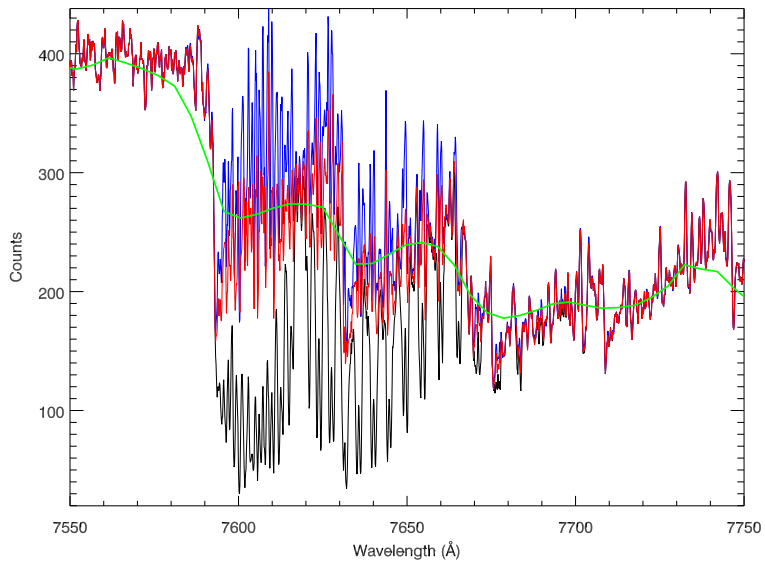


Figure 2.18: *Telluric correction by two different methods for the cool bulge LPV star OGLEII DIA BUL-SC1 235. The black line is the original 1D extracted spectrum, and the blue and red lines are the spectrum after correction by the PCA reconstruction and the temporally-closest telluric absorption spectrum, respectively. The green spectrum is an M5III star with a similar temperature, HD175865, taken from NGSL as a comparison.*

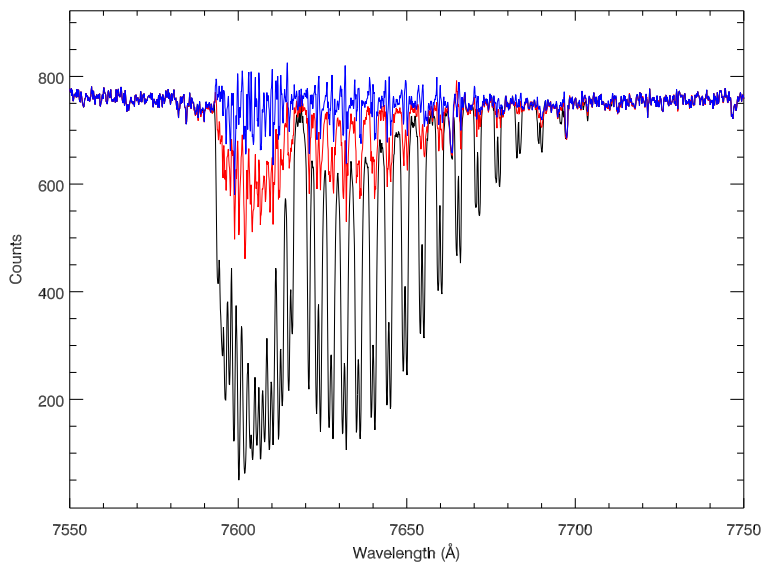


Figure 2.19: Telluric correction by the PCA reconstruction and temporally-closest telluric absorption methods on the G3V star G169-28. Symbols and wavelength ranges are the same as in Figure 2.18.

2.5 Flux calibration

In order to perform a reliable flux calibration, we observed several spectrophotometric standards (BD+17 4708, GD 71, GD 153, EG 274, Feige 110, LTT 3218 and LTT 7987) with a wide slit ($5'' \times 11''$) in “stare” mode at different airmasses. All flux standard stars used here were observed with the readout mode “100k/1pt/hg”. The median signal to noise ratio of the flux standards (44 spectra in the UVB arm and 43 spectra in the VIS arm) spanned the range between 100 and 800 .

2.5.1 Construction of the extinction curve

To reconstruct the intrinsic flux and spectral shape, it is important to correct the spectra for atmospheric extinction. We start from the basic assumption that the atmospheric (extinction curve) and instrumental (response curve) properties are uncorrelated. Determining the extinction curve then can be simply done by assuming the extinction curve does not change with time.

We reduced and extracted the spectra of flux standard stars with the same set of master bias and master flat field in each arm. Telluric correction was performed in the VIS arm for each flux standard. The spectra of the standards were compared with the flux tables of the appropriate stars from the CALSPEC HST database (Bohlin 2007)⁸. By running IRAF .standard and using the Paranal extinction curve (Patat et al. 2011) as a first guess, we derived the extinction curve for our X-Shooter observations in the UVB and VIS arms.

The extinction curve of the XSL in Period 84 and 85 is shown in Figure 2.20, where the Paranal extinction curve (Patat et al. 2011) is shown for a reference comparison (black line). We find that the inferred extinction curve is very similar to that given by Patat et al. (2011), with only a slightly steeper extinction coefficient in the red.

2.5.2 Construction of the response curve

We create our response curves as follows. First, for a given science spectrum we reduce its flux standard star with the same set of master bias and master flat field as used for the science observation and extract the 1D spectrum. For the VIS arm spectra, we perform the telluric correction on the 1D spectrum of the flux standard. Second, the airmass of the flux standard is used to derive the atmospheric extinction using the XSL extinction curve. Third, the 1D spectrum of the flux standard is corrected by $F' = F_{ADU} / t_{exp} \times AtmExt$, where F_{ADU} is the original 1D spectrum, t_{exp} is the exposure time of the flux standard and $AtmExt$ is the derived extinction term. We compare this corrected 1D spectrum with its flux table from the CALSPEC HST database. The final response curve is derived by fitting a spline to the ratio between the reformed 1D flux standard spectrum and the corresponding flux table.

Because the flat field and bias of X-Shooter are not stable, at least in the Period 84 and 85, the response curve derived from each flux standard can vary by around 5%. We show the averaged response curve in the UVB and VIS arm, respectively, in Figure 2.21

⁸<http://www.stsci.edu/hst/observatory/cdbs/calspec.html>

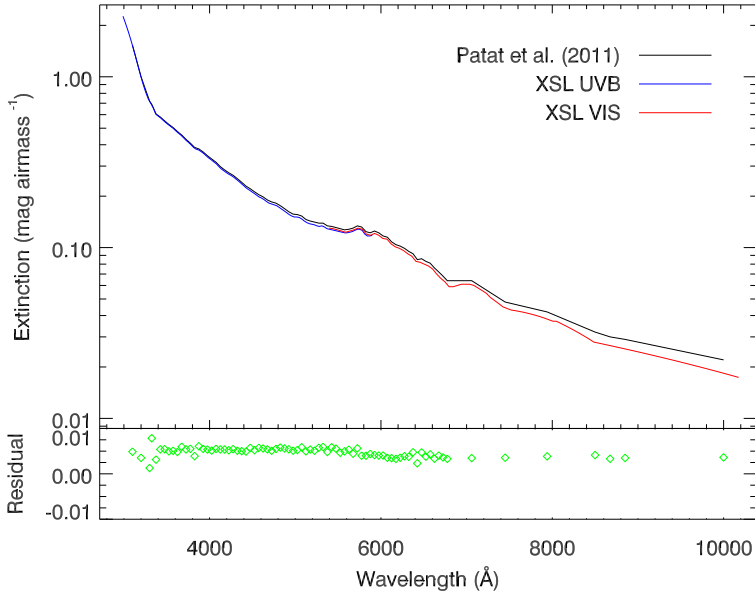


Figure 2.20: Extinction curve for the XSL in the UVB arm (red line) and the VIS arm (blue line). The Paranal extinction by Patat et al. (2011) is shown as the black line for comparison. Lower panel shows the residual between XSL and Patat et al. (2011) which is calculated by the IRAF standard procedure and applied to derive the XSL extinction.

to illustrate the overall response of the instrument. The sharp feature around 3700 Å in the top plot is due to the two flat field lamps used in the UVB arm. We note that there is a strong feature beyond $\lambda\lambda$ 5500 Å in the UVB arm (top panel). This is due to the dichroic used to split the beam between the UVB and VIS arms. This feature is also seen in the VIS arm before $\lambda\lambda$ 5800 Å (lower panel in Figure 2.21).

2.5.3 Flux calibration of individual frames

We note that the dichroic features do not always appear in the same position in the extracted 1D spectra, and therefore it is difficult to totally remove those features in our final flux-calibrated spectra. To minimize the influence of the dichroic, we choose the time closest observation of a certain flux standard star as the corresponding flux standard for each science observation. The chosen flux standard is reduced and extracted as described above. If the binning of the science observation is different from the selected flux standard, we rebin the selected flux standard first.

For each science spectrum, we generated its response curve following the procedure described above. The flux-calibrated science spectrum is derived using the formula

$$F_{cal,s}(\lambda) = \frac{F_{ADU,s}(\lambda) / t_{exp}^s}{Respon \times AtmExt_s}, \quad (2.4)$$

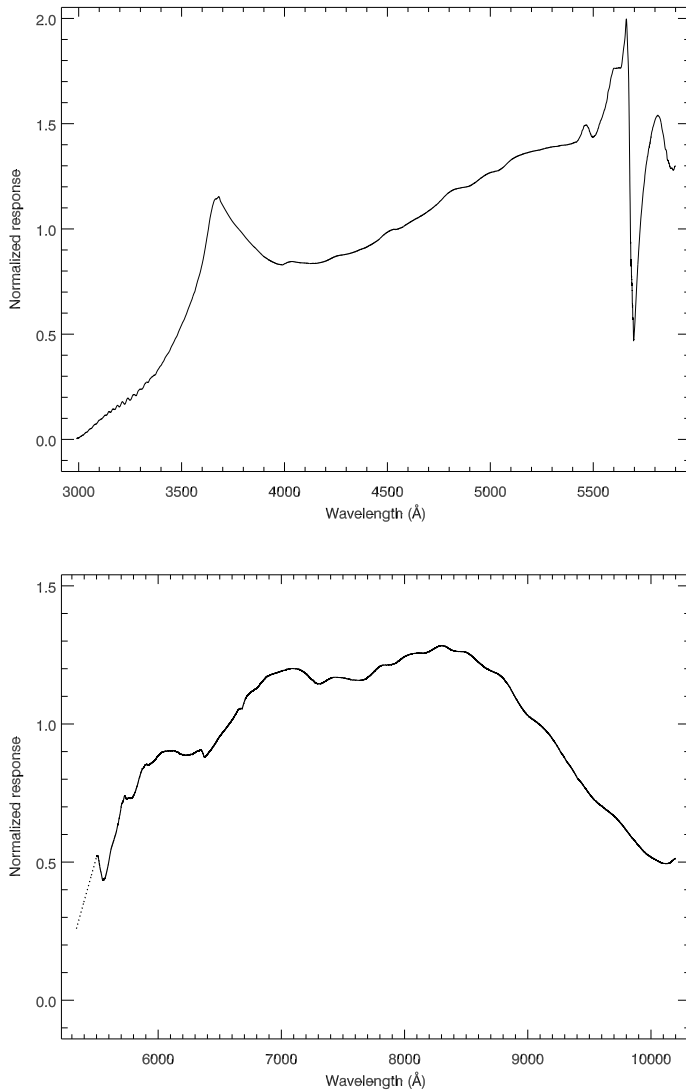


Figure 2.21: Averaged response curves in the UVB (upper panel) and VIS arm (lower panel). The dotted line in the VIS arm indicates low signal to noise region, which is interpolated for display purpose. Dichroic features are shown in both UVB and VIS arms around 5600 – 5800 Å.

where $F_{ADU,s}$ is the 1D spectrum of the science object, t_{exp}^s is the exposure time of the science object, $Respon$ is the derived response curve, and $AtmExt_s$ is the extinction term calculated from the airmass and the extinction curve of XSL. We perform the flux calibration process on both narrow slit and wide slit observations.

2.5.4 Final flux calibration

A final flux calibration is carried at the narrow-slit observations using the shape of wide slit observations to avoid flux losses. To do this, we seek the flux-calibrated narrow-slit spectrum for its corresponding wide-slit companion. For those whose wide-slit observation is available, we run pPXF to shift and broaden the narrow-slit spectrum. The flux correction is performed by multiplying the narrow-slit spectrum by the second order polynomial determined by pPXF. For the narrow-slit spectra whose corresponding wide-slit spectrum are not available, because of saturation, we leave their flux as in the previous step (individual flux calibration). We note that stars without wide-slit flux correction may be missing flux, especially in the UVB arm.

2.5.5 ADC issue in the UVB arm

Some of our data, especially narrow-slit observations in the UVB arm observed from 18 July 2010 to 2 August 2010, are influenced by a failure of the Atmospheric Dispersion Compensator (ADC). To correct for this ADC issue we perform the following steps. First, we run pPXF to determine the possible shift and broadening between the narrow- and wide-slit observations. Second, we convolve the narrow-slit observation to the same resolution and wavelength range as the wide-slit according to the first step. Third, we smooth the wide-slit observation and wide-slit-like narrow slit spectrum, respectively, with a boxcar size of 500 pixels to avoid possible noise features. The final compensation curve is given by the ratio of smoothed versions of the wide- and narrow-slit observations. Once the compensation curve is derived, we multiply it to the original narrow-slit spectrum to perform the flux calibration.

2.6 Quality checks

2.6.1 Spectral resolution

We now determine the line-spread function (LSF) of our X-Shooter spectra to accurately measure the spectral resolution and confirm the wavelength calibration of our observations. We fit the spectra of our F, G, K stars (212 spectra) using the synthetic library of Coelho et al. (2005) as templates. To determine the LSF, we use the function ULY_LSF from ULYSS, which minimizes the difference between the observed spectra and a parametric model by full-spectrum fitting (Koleva et al. 2008, 2009). The fit is performed in wavelength intervals of 200 Å spaced by 60 Å.

Figure 2.22 shows the LSF for the F, G, K stars from XSL in the UVB (upper panels) and VIS (lower panels) arm, respectively. In each arm, we estimate the mean instrumental velocity dispersion (σ) and residual shift (ν) using the IDL procedure

BIWEIGHT_MEAN. The mean difference of the residual velocity in the UVB arm spans the range between -2.6 and $+2.3 \text{ km s}^{-1}$. This may be due to the imperfect wavelength calibration. We find that the wavelength solution is very good in the VIS arm (upper panel in the lower plot).

The instrumental velocity dispersion in the UVB arm ranges from 13.3 to 18.1 km s^{-1} , corresponding to a resolution $R = 9584 - 7033$. The fitted instrumental resolution in km s^{-1} is given by

$$\sigma_{\text{UVB}} = 15.625 - 0.0026 \times (\lambda - 4300) \text{ (km s}^{-1}\text{)}, \quad (2.5)$$

with λ in \AA . In the VIS arm, the instrumental variation is constant at $\sigma_{\text{VIS}} = 11.62 \text{ km s}^{-1}$ (i.e. $R = 10986$), very close to the stated resolution $R = 11000$.

2.6.2 Arm combination

After carefully checking the resolution and flux calibration of our sample, we shift every spectra to rest frame using the synthetic libraries of Coelho et al. (2005); Palacios et al. (2010), and Allard et al. (2011) as templates. The second wavelength calibration in the UVB arm is carefully performed to correct the small shifts shown in the upper panel of Figure 2.22. Multiple observations of the same non-variable star are combined in the same arm. Multiple observations of the same variable star are kept as different spectra. We merge multiple UVB and VIS arm spectra of each star into a single spectrum using the overlapped region, mostly from 5420 to 5650 \AA . Some of the spectra have the dichroic features slightly shifted in wavelength, and in this case we shift the overlapped regions accordingly. The merged spectra of each star are carefully checked and evaluated to maintain the appropriate spectral shape.

2.6.3 Photometric comparison

We have calculated synthetic colours on the Johnson-Cousins *UVBRI* and Sloan Digital Sky Survey (SDSS) systems for our XSL stars, and compared them with published values to check the reliability of our flux calibration.

A number of studies have discussed the response functions required to reproduce the standard Johnson-Cousins *UVBRI* photometric system (Johnson et al. 1966; Cousins 1971, 1973; Landolt 1973, 1983; Bessell 1990), those which reproduce the observations most accurately are likely to be the work by Bessell (1990); Fukugita et al. (1995). We therefore use the response functions from Bessell (1990) for the *UVBRI* system. The SDSS response functions (Fukugita et al. 1996) without atmosphere are adopted here to calculate the colours through the $u' g' r' i' z'$ filters. We show the normalized *UBVRI* (solid lines) and SDSS (dotted lines) response functions in Figure 2.23.

We have calculated the synthetic $B - V$, $U - B$, $R - I$ and $V - I$ colours of the XSL sample. The synthetic magnitude of the Johnson-Cousins system is given by

$$M_X = -2.5 \times \log_{10} \left[\frac{\int \lambda f_\lambda(\lambda) R_X(\lambda) d\lambda}{\int \lambda f_\lambda^{\text{Vega}}(\lambda) R_X(\lambda) d\lambda} \right] + C_X, \quad (2.6)$$

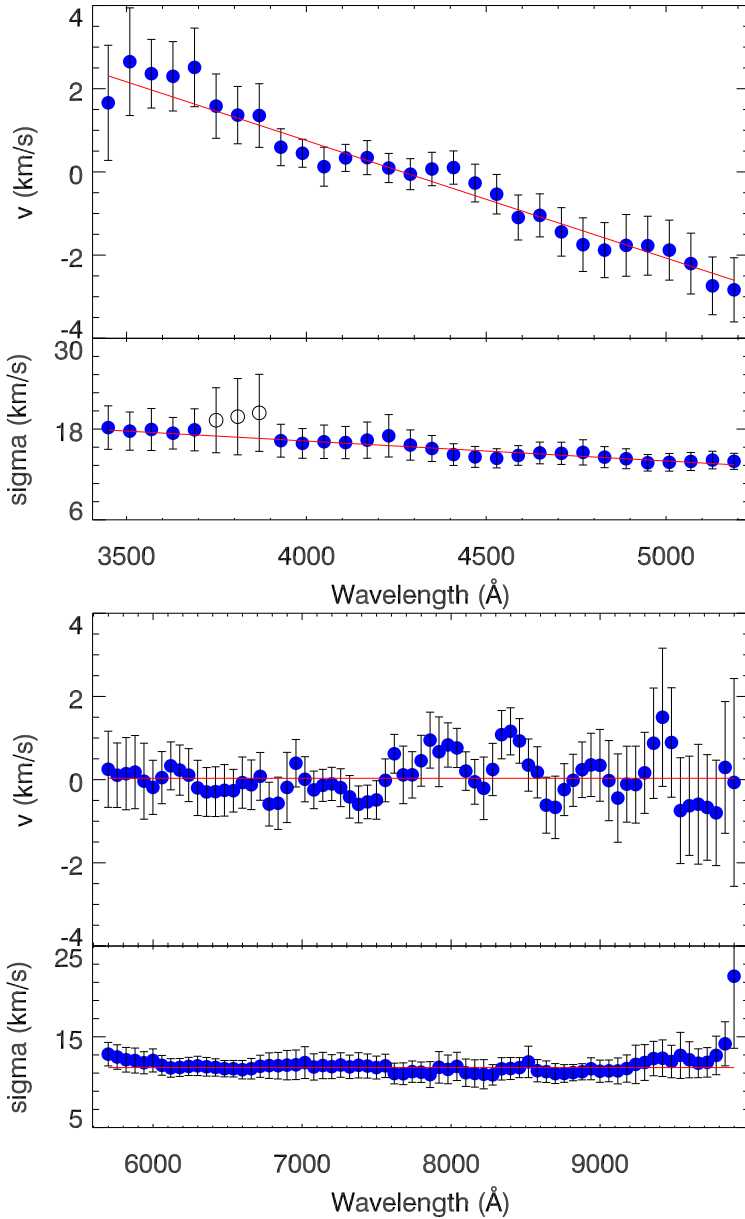


Figure 2.22: Averaged line-spread function for the FGK stars (212 spectra) in the UVB (upper panel) and VIS (lower panel) arms. In each arm, the top panel shows the residual shift of the spectra (blue dots). The bottom panel shows the detected instrumental velocity dispersion. A simple first order polynomial fitting (red lines) of the line-spread function are marked in each panels. The error bars are the standard deviation in each wavelength bin. The three open circles show the region where two different flat field lamps are used in the UVB arm, which may result in larger uncertainties.

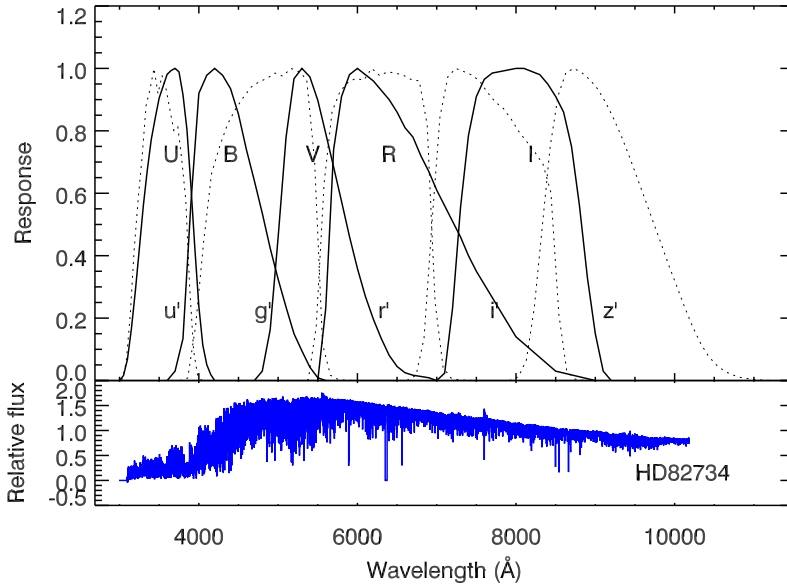


Figure 2.23: Upper panel: response functions of UBVR filters (solid lines) and the Monitor Telescope u' , g' , r' , i' , z' filters (dotted lines). Both systems are normalized to 1. Bottom panel: a typical XSL spectrum of HD82734 (K0III) for comparison.

Table 2.4: The mean offsets and rms of the synthetic colour comparison between the XSL and the Bright Star Catalogue.

	(B-V)	(U-B)
Offset	-0.024	0.016
rms	0.058	0.080

where X can be any of the U, B, V, R, I filters, $R_X(\lambda)$ is the response function of the filter X , C_X is the X magnitude of Vega, and f_λ and $f_\lambda^{\text{Vega}}(\lambda)$ are the flux densities of the object and Vega, respectively.

In order to check the colours, we compare our calculation with the the colours from NGSL library (Gregg et al. 2006) and the Bright Star Catalogue by Hoffleit et al. (1983); Hoffleit & Jaschek (1991). There are in total 78 stars in common with the NGSL library which have $B - V$ colour extracted from SIMBAD⁹. Figure 2.24 illustrates the $B - V$ colour comparison between NGSL and XSL, where the residuals represent the XSL minus NGSL. We find good agreement with a mean offset of -0.01 and an rms scatter of 0.07 mag.

To further check the flux calibration over whole wavelength range (the UVB and

⁹<http://archive.stsci.edu/prepds/stisngsl/>

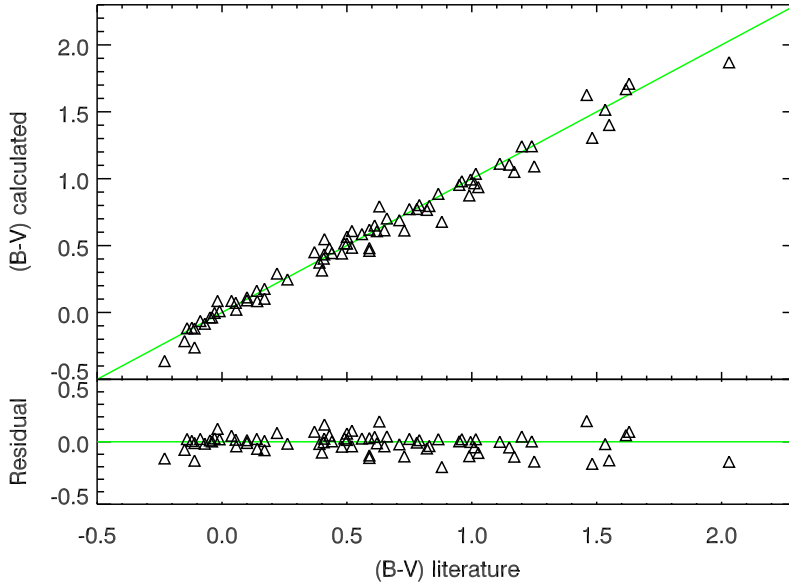


Figure 2.24: Comparison of synthetic $(B - V)$ colour between XSL and NGSL. The one-to-one relation is indicated by the green line in the upper panel. The residuals in the lower panel are calculated as $(B - V)_{\text{XSL}} - (B - V)_{\text{NGSL}}$.

VIS arm), we also compare our colours with the published $U - B$ and $B - V$ colours from the Bright Star Catalogue. There are in total 54 stars in common. We show the comparison in Figure 2.25. The XSL stars with flux losses are marked as blue squares. The star which has around 0.3 magnitude difference between literature and measured $U - B$ is a variable star HD170756, which has big literature $U - B$ scatter (~ 0.5 mag) as well. The mean offsets and rms scatter measured from each colour is summarized in Table 2.4. The large scatter in the $U - B$ residual is partly due to variable stars (e.g. HD170756, with $U - B$ literature value around 0.2), and partly due to the low signal-to-noise region in the U band. The outliers in the $B - V$ residual panel are mainly from the flux losses in the B band, in the UVB arm, as discussed in Sec. 2.5.4.

The SDSS $u' - g'$, $g' - r'$ and $r' - i'$ colours as another flux reference are calculated following the definition of AB magnitudes:

$$M_{\text{AB}} = -2.5 \times \log_{10}[f_{\nu}^{\text{eff}}] - 48.6, \quad (2.7)$$

where $f_{\nu}^{\text{eff}} = \frac{\int d\nu f_{\nu} R_{\nu}}{\int d\nu R_{\nu}}$ (see Fukugita et al. 1995, for details). Since there are few literature stars which have the SDSS colours in common with our sample, we use the model colours computed by Lenz et al. (1998) as a quick check. Models with $\log g = 4.5$ and $\log g = 2.5$ are chosen to represent the main sequence and giants, respectively. Three metallicities $[M/H] = -2.0, 0$, and 1.0 are used to diagnose the metallicity range of the

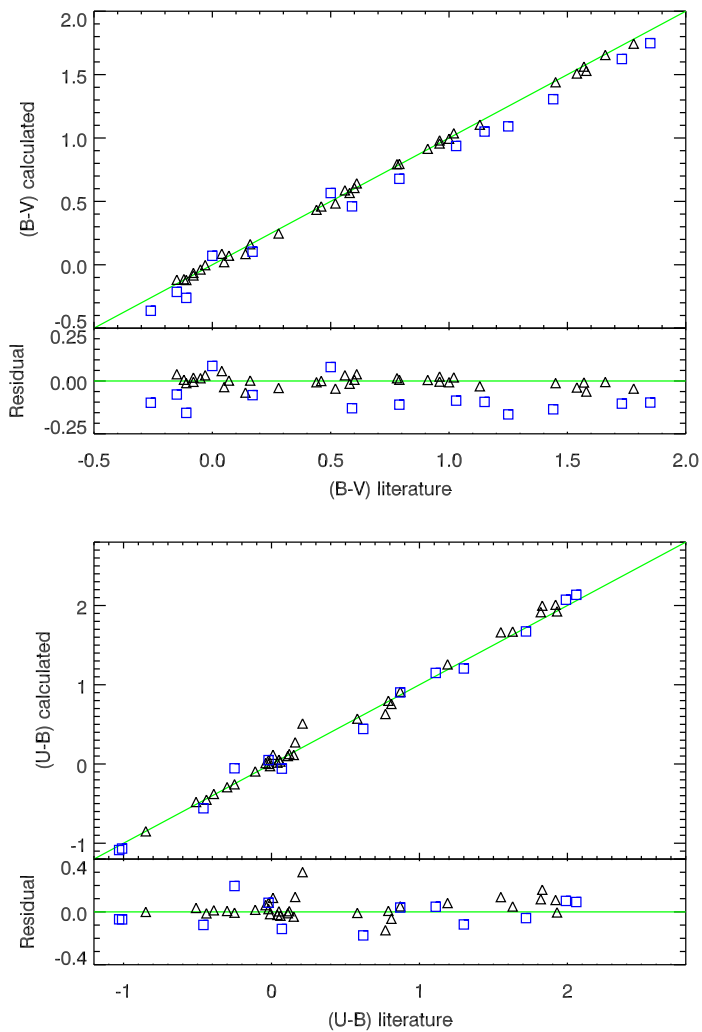


Figure 2.25: Comparison of synthetic $(B - V)$ and $(U - B)$ colours between XSL and the Bright Star Catalogue. The residuals are calculated similarly as in Figure 2.24. Blue squares indicate those stars which likely have flux losses.

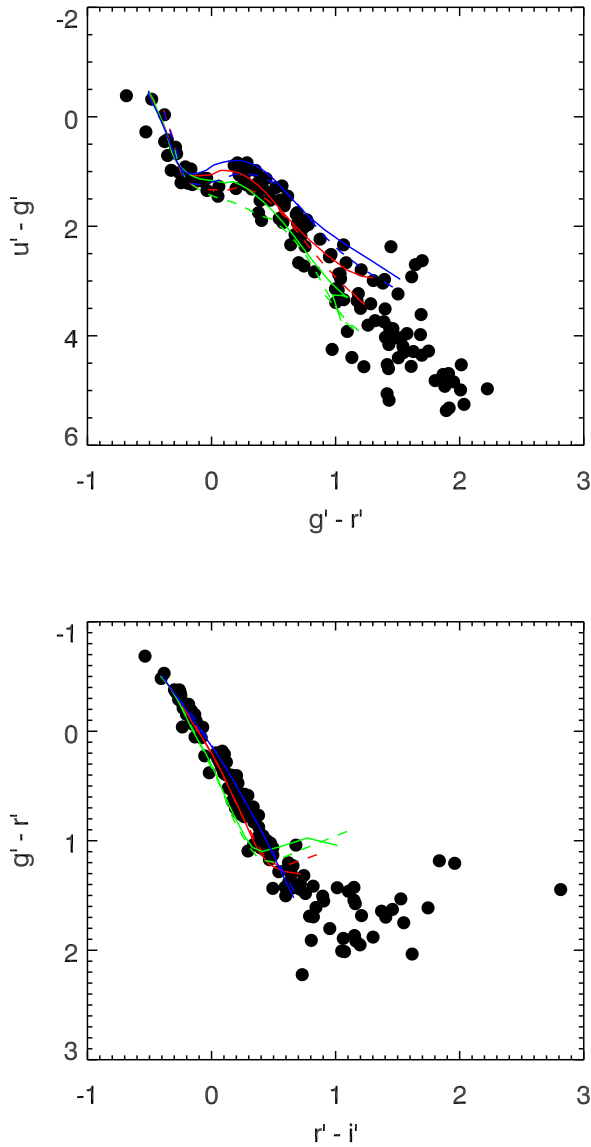


Figure 2.26: Synthetic SDSS colours of the XSL sample (black dots) compared with synthetic model colours by Lenz et al. (1998). Only three metallicities are shown in for the model colours: $[M/H] = -2.0$ (blue lines), 0.0 (red lines) and $+1.0$ (green lines). Solid lines indicate models with $\log g = 4.5$ and dashed lines indicate models with $\log g = 2.5$.

XSL sample. Figure 2.26 shows the $u' - g'$ vs $g' - r'$ colours and $r' - i'$ vs $g' - r'$ colours for the XSL sample compared with model colours. In general the agreement between the model and data is very good. The coolest model from Lenz et al. has $T_{\text{eff}} = 3500$ K, significantly warmer than the coolest XSL stars, and so the reddest model colours will not be as red as the reddest XSL stars.

2.6.4 Comparison with literature spectra

Since our sample is selected from different literature sources, it is interesting to compare the XSL spectra with spectra of the same stars in other libraries. The first year of XSL has 78 stars in common with NGSL, 40 stars in common with MILES, 34 stars in common with ELODIE, 26 stars in common with IRTE, and 25 stars in common with CaT (Cenarro et al. 2001).

We show several examples of the spectral slope comparison between XSL, NGSL, MILES and CaT in Figures 2.27, 2.28, and 2.29. With the higher resolution data of XSL, we can resolve spectral features in detail. We see in general that the flux calibration of XSL agrees well with MILES and NGSL, with the occasional exception of the very red part of the MILES spectra for HD27295 because of the second-order problem of some MILES stars (see Figure 2.27 and the discussion in Sec. 4.3 of Sánchez-Blázquez et al. 2006). Further, the comparison with the CaT library shows that library is not telluric corrected (Cenarro et al. 2001) as seen from the features around 9000 Å in Figures 2.27 and 2.28.

As a further check on the quality of XSL, we compare our spectra with two higher-resolution spectral libraries: UVES POP (Bagnulo et al. 2003) and ELODIE¹⁰ (Prugniel & Soubiran 2001, 2004; Prugniel et al. 2007). To make this comparison we first smooth the UVES POP and ELODIE spectra to the resolution of the XSL spectra and then use pPXF to match the continua and velocity zero points, masking bad pixels when necessary. Figures 2.30–2.33 show the results of these comparisons. The typical residual between XSL and UVES POP is 2–4%; the typical residual between XSL and ELODIE is 2–6%. We find very good agreement in the line shapes and depths between XSL and the two higher-resolution libraries, for both warm and cool stars. This gives us confidence that the XSL spectra will be a useful basis for moderate-resolution studies of both stars and composite stellar populations.

¹⁰Note that we use the high-resolution version of the ELODIE library with $R \sim 42000$ for this comparison.

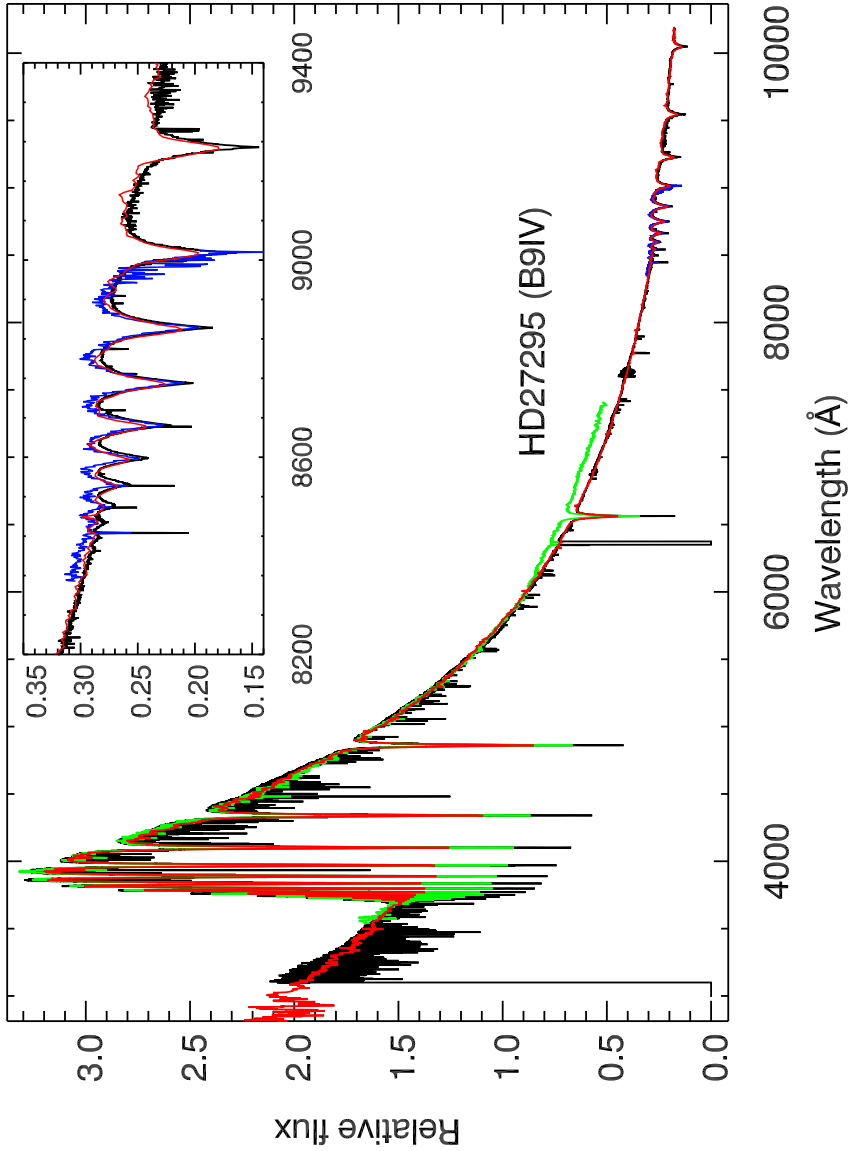


Figure 2.27: Spectra of HD27295 from XSL (black), MILES (green), NGSL (red), and CaT (blue). The sub-windows show the comparison in detail in a zoomed-in region for telluric correction comparison.

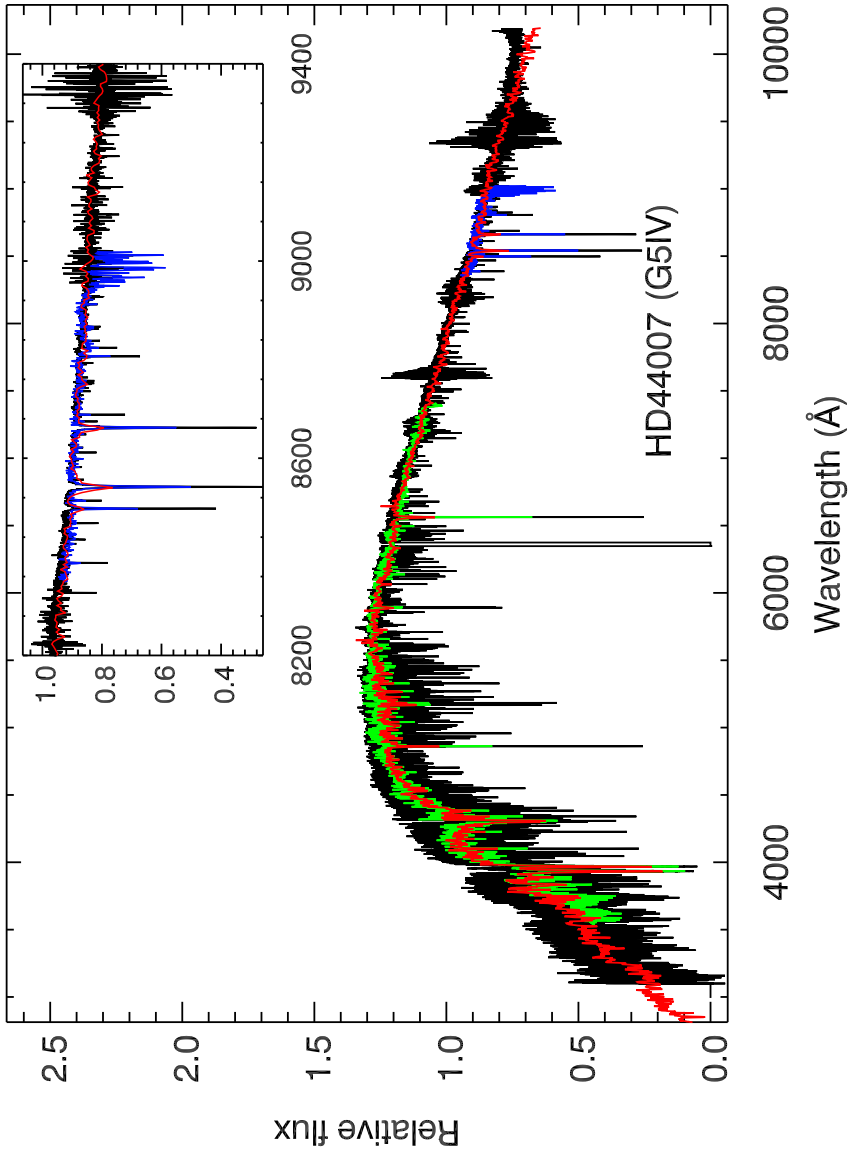


Figure 2.28: Spectra of HD44007 from different spectral libraries. Symbols are as in Figure 2.27.

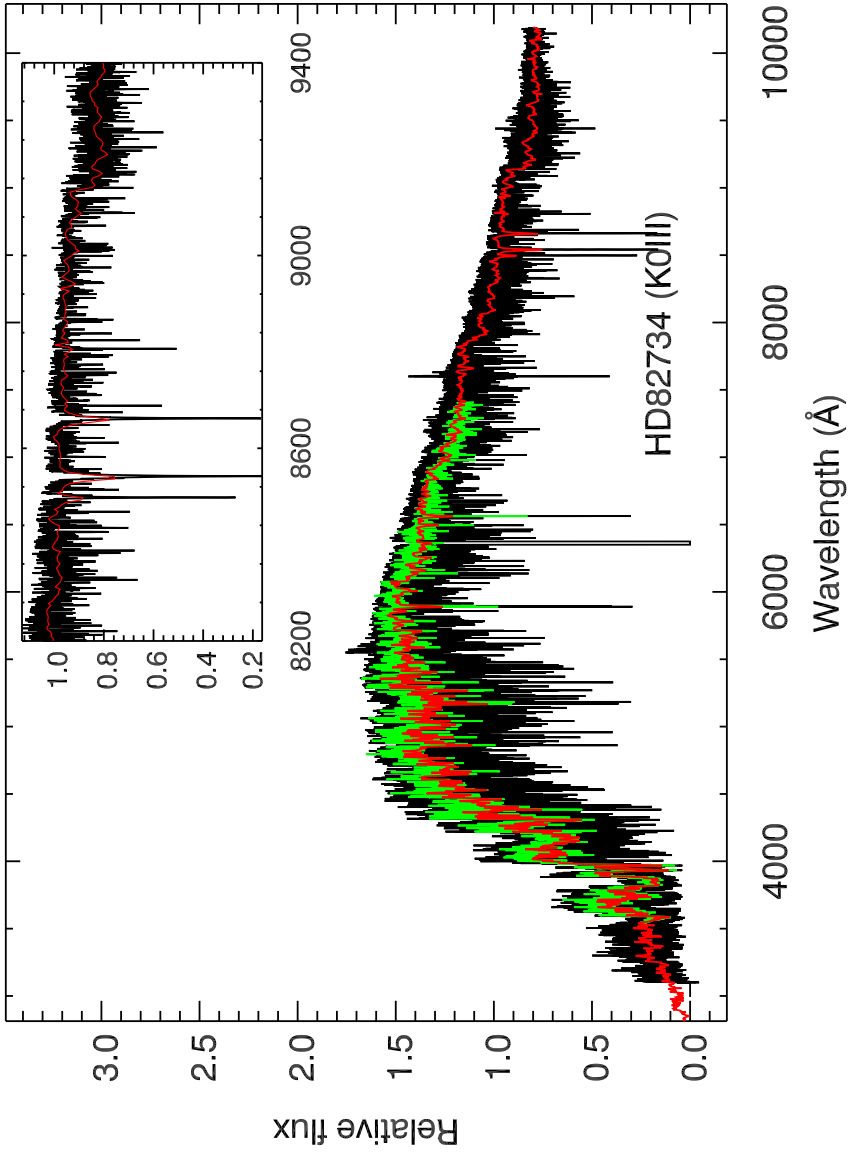


Figure 2.29: Spectra of HD82734 from different spectral libraries. Symbols are as in Figure 2.27.

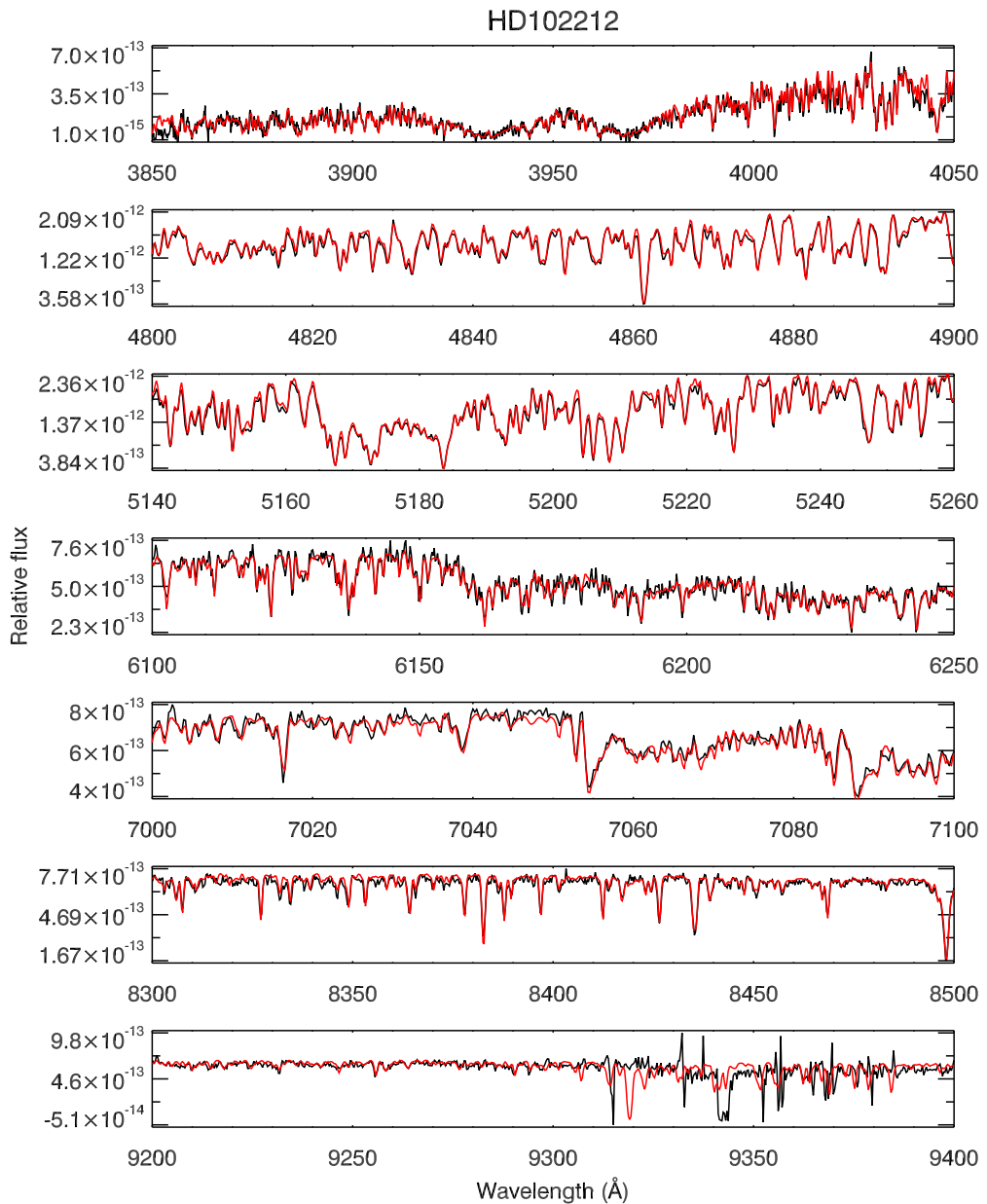


Figure 2.30: Detailed spectral line comparison between XSL (black) and UVESPOP (red) of HD102212 (M1III), where the UVESPOP spectrum is smoothed to the resolution of XSL. The XSL spectrum around 9350 Å is heavily contaminated by telluric features, and therefore the stellar features are difficult to recover.

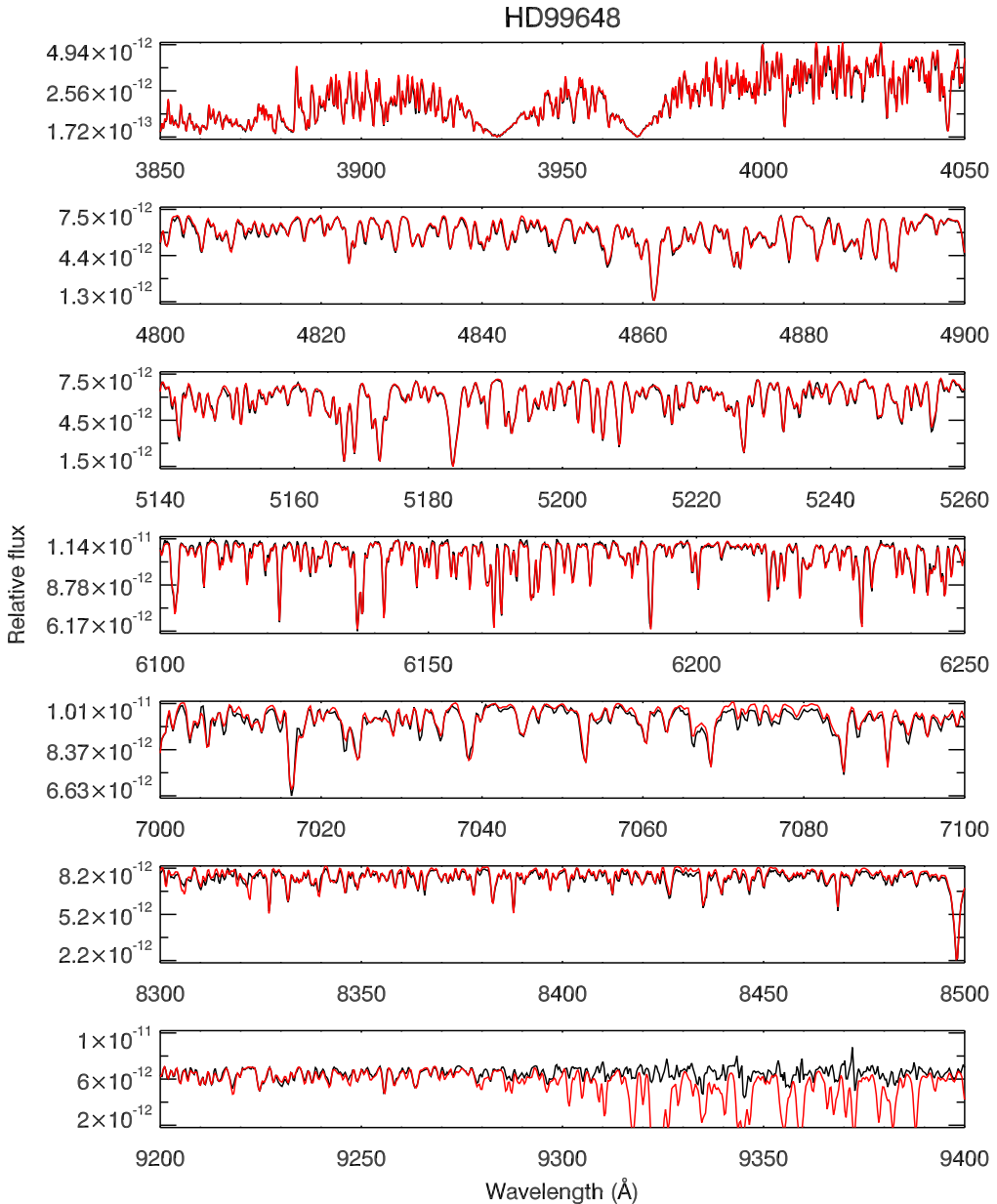


Figure 2.31: Detailed spectral line comparison between XSL (black) and UVESPOP (red) of HD99648 (G8Iab), where the UVESPOP spectrum is smoothed to the resolution of XSL. Telluric features are clearly seen in the UVESPOP spectrum, especially around 9300–9400 Å.

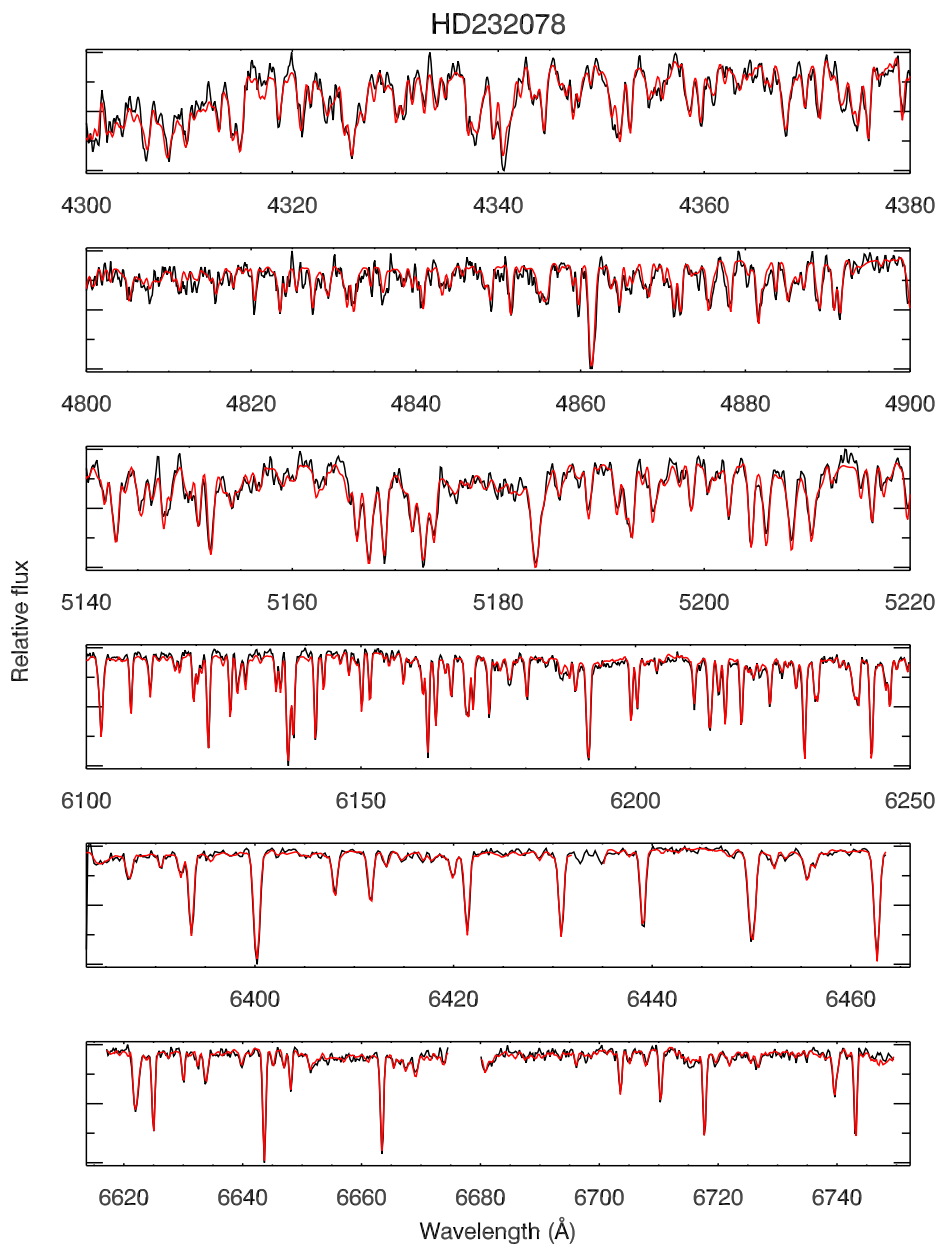


Figure 2.32: Detailed spectral line comparison between XSL (black) and ELODIE (red) of HD232078 (K3IIp), where the ELODIE spectrum is smoothed to the resolution of XSL. The gap in the two bottom panels represents bad pixels in ELODIE.

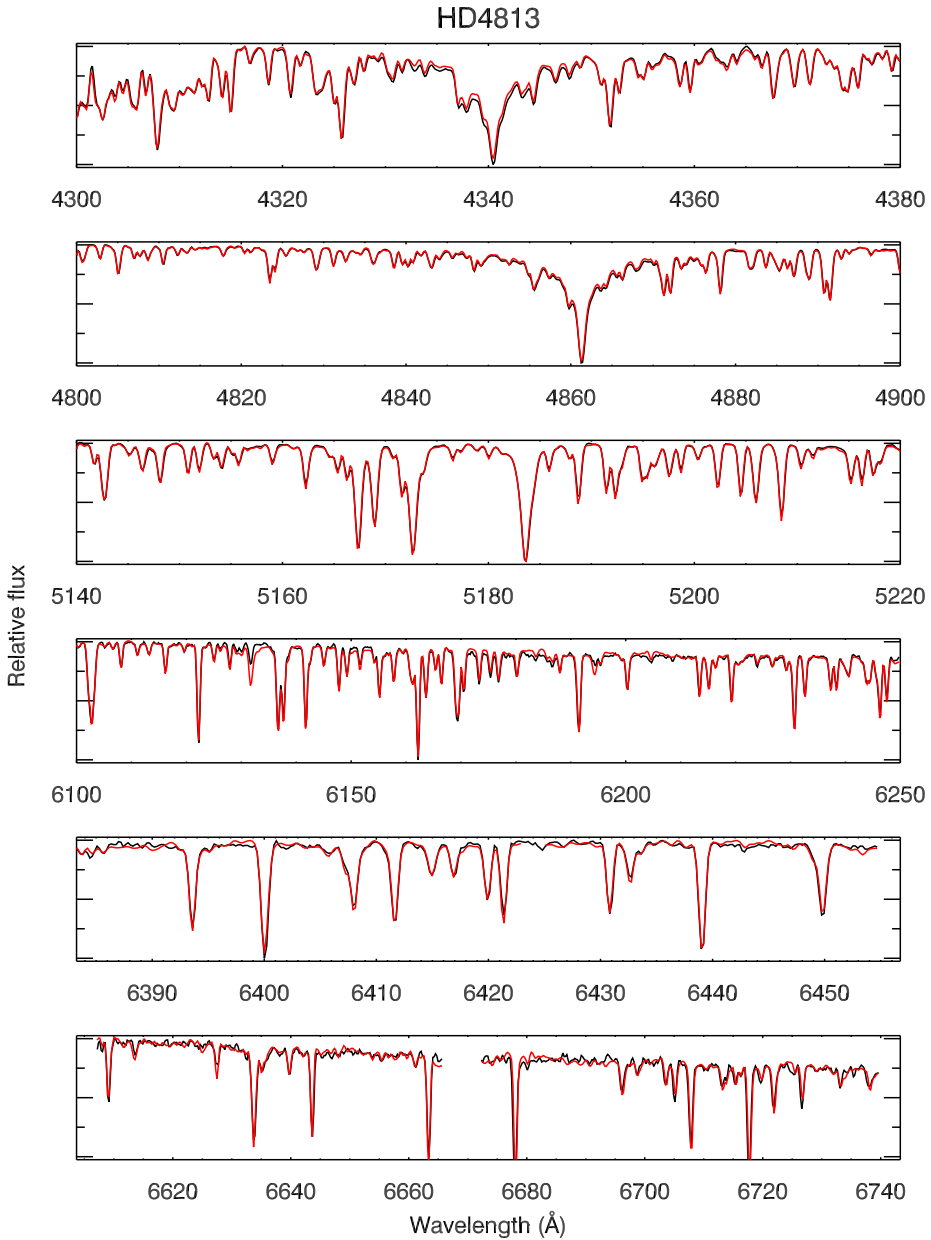


Figure 2.33: Detailed spectral line comparison between XSL (black) and ELODIE (red) of HD4813 (F7IV-V), where the ELODIE spectrum is smoothed to the resolution of XSL. The gap in the two bottom panels represents bad pixels in ELODIE.

2.7 Summary

We are building a new, moderate-resolution stellar spectral library, the X-Shooter Spectral Library (XSL). The pilot survey (this work) contains 237 unique stars covering the spectral range $\lambda\lambda$ 3100 – 10185 Å at a resolution $R \sim 10000$. We have identified a number of issues with the X-Shooter pipeline and presented our solutions. A telluric library is built for telluric correction of the XSL data using a PCA-based method. Flux and wavelength calibration are carefully performed and are shown to be consistent with published spectra. XSL is still under construction and the final database will contain more than 600 stars. XSL will provide a vital tool for extragalactic astronomers to extract even more information from their observations than previously possible, and will provide stellar astronomers with a world-leading panchromatic spectral library for further studies of a wide range of stellar types.

Acknowledgments

We thank our collaborators on XSL, A. Gonneau, S. Meneses-Goytia, A.J. Cenarro, J. Falcón-Barroso, E. Mármol-Queraltó, P. Sánchez-Blázquez, C.J. Walcher, P. Hauschildt and M. Koleva. We thank also B. Davies and G. Zhang for useful discussions. We would also like to extend our great thanks to V. Manieri, A. Modigliani, J. Vernet, and the ESO staff for their help during the XSL observations and reduction process. This research used the POLLUX database (<http://pollux.graal.univ-montp2.fr>) operated at LUPM (Université Montpellier II - CNRS, France with the support of the PNPS and INSU. This work has been supported by the Programa Nacional de Astronomía y Astrofísica of MINECO, under grant AYA2010-21322-C03-02.

Appendix 2.A Pipeline reduction tips

For the data reduction by X-Shooter pipeline, we need prepare the necessary raw science data, calibration data and reference frames. Therefore a full set of raw data are required from the ESO archive: bias/dark, flat field (for the UVB arm, Q-lamps and D-lamps; for the NIR arm ON and OFF mode), order-definition, multi-pinhole arc lamp for determining the 2D transformation and format-check frames to find solution of order locations and wavelength calibration, flexure compensation (AFC) frames to compute the instrument flexures and optimize the wavelength solution.

Here we use the physical mode of X-Shooter pipeline version v1.5.0 to reduce our raw data, according to the X-Shooter Pipeline User Manual (Issue 10.0, pipeline v1.5.0, 28 of 182), the reduction chain for “physical” mode for calib slit data is as following:

```

esorex xsh_lingain xsh_lingain.sof
esorex xsh_mbias xsh_mbias.sof
esorex xsh_mdark xsh_mdark.sof
esorex xsh_predict xsh_predict.sof
esorex xsh_orderpos xsh_orderpos.sof
esorex xsh_mflat xsh_mflat.sof
esorex xsh_2dmap xsh_2dmap.sof
esorex xsh_flexcomp xsh_flexcomp.sof
esorex xsh_wavecals xsh_wavecals.sof
esorex xsh_respon_slit_stare xsh_respon_slit_stare.sof
esorex xsh_respon_slit_offset xsh_respon_slit_offset.sof
esorex xsh_scired_slit_stare xsh_scired_slit_stare.sof
esorex xsh_scired_slit_offset xsh_scired_slit_offset.sof
esorex xsh_scired_slit_nod xsh_scired_slit_nod.sof

```

Although it is encouraged to use Reflex reducing the raw data, we find it is more handy only using the pipeline itself and writing the wrapper by our own code. For doing this, we need the following set of raw frames to put as the input list for the “set-of-frames” (SOF) requested by the pipeline.

Bias frame: observing time closest to the science object, the same arm and readout mode as the science object. Keywords in the fits file header of the raw data to check: “HIERARCH ESO DPR TYPE” = “BIAS”, “HIERARCH ESO DET READ CLOCK”(readout mode), “HIERARCH ESO SEQ ARM” (observing arm). For each group of bias, 5 raw frames are needed.

Dark frame: observing time equal to the science object, the same arm, exposure time and readout mode as the science object. Keywords in the fits file header of the raw data to check: "HIERARCH ESO DPR TYPE"="DARK", "HIERARCH ESO SEQ ARM" (observing arm), "EXPTIME" (equal to the object's exposure time). For each group of dark, 3 raw frames are needed.

Flat frame: observing time closest to the science object, the same arm, slit width and readout mode as the science object. Keywords in the fits file header of the raw data to check: "HIERARCH ESO DPR TYPE" = "LAMP,FLAT" for the VIS and NIR arm; "HIERARCH ESO DPR TYPE" = "LAMP,QFLAT" and "HIERARCH ESO DPR TYPE" = "LAMP,DFLAT" for the UVB arm; "HIERARCH ESO DPR TECH" = "ECHELLE,SLIT" and "IMAGE" for the NIR arm; "HIERARCH ESO DET READ CLOCK" (readout mode), "HIERARCH ESO SEQ ARM" (observing arm), "HIERARCH ESO INS OPTIi NAME" (i=3, 4, 5, same as the science object.) For each group of flat field, 5 raw frames are needed for the VIS arm and 10 raw frames are needed for the UVB and NIR arms.

Order-definition: observing time closest to the science object, readout mode with binning 1×1 , the same arm as the science object. Keywords in the fits file header of the raw data to check: "HIERARCH ESO DPR TYPE" = "LAMP,ORDERDEF" for the VIS and NIR arm "HIERARCH ESO DPR TYPE" = "LAMP,DORDERDEF" for the UVB arm, "HIERARCH ESO DET READ CLOCK" = "400k/1pt/lg", "HIERARCH ESO DPR TECH" = "ECHELLE,PINHOLE" and "IMAGE" for the NIR arm; "HIERARCH ESO SEQ ARM" (observing arm).

Multi-pinhole arc lamp: observing time closest to the science object, readout mode with binning 1×1 for the UVB and VIS arm, the same arm as the science object. Keywords in the fits file header of the raw data to check: "HIERARCH ESO DPR TYPE" = "LAMP,WAVE"; "HIERARCH ESO DPR TECH" = "ECHELLE,MULTI-PINHOLE" for the UVB and VIS arm, pair multi-pinhole arc lampes which has "HIERARCH ESO DPR TECH" = "ECHELLE,MULTI-PINHOLE" and "IMAGE" for the NIR arm.

AFC frame: observing time closest to the science object, readout mode with keywords "AFC" for the UVB and VIS arm, the same arm and object name as the science object. Keywords in the fits file header of the raw data to check: "HIERARCH ESO DPR TYPE" = "LAMP,AFC", "HIERARCH ESO INS OPTIi NAME" = "Pin_0.5" (i=3, 4, 5), "HIERARCH ESO OBS NAME" (same as in science object), "HIERARCH ESO DET READ CLOCK" = "400k/1pt/lg/AFC" for the UVB and VIS arm, "HIERARCH ESO SEQ ARM" (observing arm).

Since all our data were observed in the "Slit" mode, most of the raw files should have keyword "HIERARCH ESO INS OPTI2 NAME" = "SLOT" in their header. An SOF file is and ASCII files which lists the necessary frames and their corresponding category, see 2 for details.

Appendix 2.B Log of telluric standard stars

We present the observation log of telluric standard stars in the VIS arm used to create the telluric library in Table 2.5. In this table, the last column is the shift (in kms^{-1}) which is used to achieve the absolute wavelength calibration. Note the intent here is

only to make sure that every telluric feature is consistent in all the standard stars.

Table 2.5: *The input stars for the VIS-arm telluric library*

Name	RA (J2000.0)	DEC (J2000.0)	Exp. time (s)	airmass	Sp. type	Shift (kms ⁻¹)
Hip088947	18:09:22.50	-36:40:20.2	12.50	1.771	B1II	-3.21
Hip089086	18:10:55.37	-33:47:58.4	12.50	2.505	B1V	-1.77
Hip091038	18:34:15.92	-04:48:48.7	12.50	1.063	B1V	-5.65
Hip026766	05:41:08.17	-03:37:56.6	12.50	1.137	B2	-7.03
Hip047963	09:46:30.35	-44:45:19.7	1.25	1.385	B2.5IV	0.06
Hip030660	06:26:34.44	-04:35:49.4	1.25	1.366	B2.5V	-2.74
Hip087314	17:50:28.43	-53:36:43.9	12.50	2.064	B2/B3Vnn	-5.01
Hip087505	17:52:43.70	-38:38:32.5	12.50	1.452	B2II	-5.81
Hip054082	11:03:60.00	-57:57:20.4	12.50	1.202	B2III	-1.11
Hip039691	08:06:41.64	-48:29:49.8	1.25	1.255	B2IV	-8.61
Hip092470	18:50:41.35	-47:46:46.3	1.25	1.631	B2IV	-0.14
Hip055667	11:24:21.90	-42:40:08.4	12.50	1.060	B2IV-V	-0.62
Hip007873	01:41:17.45	-75:39:47.8	1.25	1.805	B2V	2.38
Hip025751	05:29:54.81	-06:42:28.8	1.25	1.510	B2V	0.33
Hip025869	05:31:20.90	-68:56:11.3	1.25	1.785	B2V	-3.61
Hip072518	14:49:36.95	-26:17:11.7	12.50	1.803	B2V	-0.84
Hip045044	09:10:28.60	-14:15:22.2	12.50	1.484	B3/B4V	-6.47
Hip100556	20:23:26.26	-58:34:14.9	12.50	1.527	B3II/III	-3.47
Hip088702	18:06:29.55	-50:28:39.3	12.50	2.341	B3III	-2.86
Hip049076	10:00:58.61	-47:26:30.3	12.50	2.434	B3IV	1.19
Hip044509	09:04:05.79	-20:37:09.5	1.25	1.316	B3IV/V	0.16
Hip014898	03:12:15.40	-05:11:38.9	1.25	1.004	B3V	-5.69
Hip021575	04:37:54.40	-49:37:38.2	1.25	1.190	B3V	-0.47
Hip026581	05:39:02.42	-45:47:06.2	5.00	1.069	B3V	-3.02
Hip027937	05:54:41.16	-62:38:09.5	12.50	2.107	B3V	-3.43
Hip041823	08:31:36.75	-68:52:54.4	1.25	1.657	B3V	-4.32
Hip052977	10:50:12.88	-61:38:02.2	12.50	1.366	B3V	-1.08
Hip067969	13:55:09.92	-56:53:45.2	1.25	1.987	B3V	-5.01
Hip074110	15:08:45.18	-32:59:59.8	1.25	1.322	B3V	-0.98
Hip108022	21:53:03.84	-12:50:24.8	12.50	1.581	B3Ve	-7.32
Hip108022	21:53:03.85	-12:50:24.8	12.50	1.575	B3Ve	-4.00
Hip087928	17:57:42.72	-03:04:18.0	12.50	2.163	B4III	-3.05
Hip098960	20:05:32.00	-25:01:30.5	12.50	1.011	B4III	-3.47
Hip093225	18:59:23.81	-39:20:31.7	12.50	1.214	B4V	-6.26
Hip093225	18:59:23.81	-01:40:04.3	6.00	1.219	B4V	-7.08
Hip028064	05:56:00.60	-01:40:04.5	12.50	1.385	B5	-5.95
Hip036235	07:27:42.88	-28:38:22.0	1.25	1.451	B5	-1.07
Hip080371	16:24:21.29	-45:14:06.2	12.50	1.624	B5III	-3.54
Hip089224	18:12:29.27	-54:58:57.5	12.50	1.578	B5III	-5.85
Hip022840	04:54:50.75	-59:11:24.6	1.25	1.381	B5V	-3.09
Hip026405	05:37:14.57	-72:14:31.6	1.25	1.121	B5V	-4.14
Hip026405	05:37:14.59	-33:03:26.9	1.25	1.442	B5V	-0.05
Hip027303	05:47:04.59	-33:03:26.9	4.00	1.009	B5V	-5.22
Hip045145	09:11:52.98	-01:20:45.1	5.00	1.720	B5V	-3.29
Hip047495	09:40:56.20	-37:31:26.4	12.50	1.250	B5V	-5.31
Hip051934	10:36:32.69	-37:31:25.6	12.50	1.312	B5V	-5.42
Hip054006	11:02:54.65	-37:31:25.6	12.50	1.978	B5V	-2.66
Hip085885	17:33:05.94	-04:31:08.9	15.00	1.042	B5V	-1.30
Hip085885	17:33:05.94	-04:31:08.9	30.00	1.044	B5V	-1.06
Hip093836	19:06:35.14	-04:31:10.0	6.00	1.383	B5V	-4.32
Hip094378	19:12:34.41	-36:33:50.6	12.50	1.026	B5V	-0.26
Hip094378	19:12:34.54	-21:57:58.0	12.50	1.204	B5V	-5.04

Table 2.5 – Continued

Name	RA (J2000.0)	DEC (J2000.0)	Exp. time (s)	airmass	Sp. type	Shift (km s^{-1})
Hip094378	19:12:34.54	-49:01:07.6	1.25	1.210	B5V	-3.55
Hip096840	19:41:05.58	-66:54:04.3	12.50	1.685	B5V	-3.91
Hip096840	19:41:05.59	-34:45:16.8	12.50	1.392	B5V	-3.94
Hip096840	19:41:05.59	-30:56:30.4	6.00	1.559	B5V	-2.85
Hip105164	21:18:11.11	-30:56:28.6	1.25	1.127	B5V	-3.86
Hip105164	21:18:11.12	-35:40:08.8	12.50	1.142	B5V	-4.48
Hip105164	21:18:11.14	-50:00:15.4	12.50	1.066	B5V	-4.04
Hip029464	06:12:29.10	-66:50:52.6	1.25	1.041	B5Vn	-5.97
Hip009534	02:02:35.30	-09:43:54.7	1.25	1.005	B6V	-5.83
Hip025903	05:31:43.77	-00:40:43.6	12.50	1.676	B6V	-1.96
Hip027534	05:49:53.39	-56:08:04.8	5.00	1.537	B6V	-5.88
Hip039640	08:06:03.25	-56:08:00.6	25.00	1.450	B6V	-6.55
Hip089960	18:21:16.39	-13:21:10.3	12.50	1.009	B6V	-0.65
Hip089960	18:21:16.42	-71:14:01.8	12.50	1.118	B6V	-4.14
Hip088309	18:02:05.22	-49:50:11.6	12.50	2.313	B7II	-3.18
Hip013327	02:51:29.62	-68:48:42.9	12.50	2.284	B7V	-1.54
Hip013327	02:51:29.69	-68:48:42.9	1.25	1.302	B7V	-2.83
Hip013327	02:51:29.70	-68:48:41.5	1.25	1.336	B7V	-2.55
Hip020789	04:27:17.50	-68:48:41.8	0.70	1.627	B7V	-8.90
Hip046848	09:32:48.00	-68:48:41.2	45.00	1.410	B7V	-4.89
Hip063465	13:00:16.95	-68:48:41.0	1.25	1.403	B7V	-4.25
Hip003541	00:45:12.93	-41:42:09.0	1.25	1.504	B8	-3.61
Hip015378	03:18:19.78	-63:47:18.5	1.25	1.389	B8	0.65
Hip024632	05:17:05.35	-37:20:36.0	1.25	2.009	B8	-4.67
Hip028697	06:03:33.96	-37:20:35.6	1.25	1.976	B8	2.37
Hip086954	17:46:07.38	-37:20:36.2	12.50	1.169	B8	-2.06
Hip087290	17:50:09.32	-37:20:35.3	20.00	1.558	B8	-2.24
Hip092409	18:49:54.81	-72:24:43.2	1.25	1.421	B8	1.45
Hip094526	19:14:19.27	-72:24:43.8	1.25	1.796	B8	1.68
Hip025098	05:22:21.98	-64:16:54.9	1.25	1.617	B8.5V	-2.55
Hip025098	05:22:22.29	-40:42:27.7	12.50	1.432	B8.5V	-0.05
Hip038184	07:49:28.84	-31:39:14.4	12.50	1.216	B8/B9II	-7.36
Hip102376	20:44:36.29	-64:06:43.7	1.25	1.659	B8/B9IV	-3.39
Hip009022	01:56:09.32	-64:45:58.9	1.25	1.105	B8/B9V	-1.44
Hip021599	04:38:12.84	-24:51:06.0	1.25	1.413	B8/B9V	-2.39
Hip021599	04:38:12.84	-46:25:39.4	1.25	1.448	B8/B9V	-1.44
Hip021599	04:38:13.12	-34:47:11.5	1.25	1.426	B8/B9V	-1.22
Hip021599	04:38:13.14	-30:28:24.3	1.25	1.402	B8/B9V	0.94
Hip021599	04:38:13.17	-50:49:19.3	1.25	1.517	B8/B9V	-2.02
Hip021599	04:38:13.20	-03:59:32.8	1.25	1.562	B8/B9V	-2.85
Hip038584	07:54:02.32	-04:34:34.4	12.50	1.257	B8II	0.27
Hip060771	12:27:24.61	-38:27:48.2	12.50	1.291	B8IV	0.98
Hip092989	18:56:40.41	-38:27:46.9	7.00	1.025	B8IVs...	-7.22
Hip092989	18:56:40.41	-58:24:33.5	7.00	1.032	B8IVs...	-3.91
Hip092989	18:56:40.43	-58:24:33.8	12.50	1.025	B8IVs...	-3.77
Hip092989	18:56:40.44	-17:27:20.6	7.00	1.047	B8IVs...	-5.58
Hip008485	01:49:22.04	-42:22:56.5	1.25	1.572	B8V	-1.66
Hip008485	01:49:22.41	-09:34:11.0	1.25	1.567	B8V	-2.08
Hip012389	02:39:31.74	-26:56:35.4	1.25	1.663	B8V	1.23
Hip026545	05:38:43.56	-48:10:37.7	12.50	1.259	B8V	-8.88
Hip032348	06:45:07.21	-01:36:33.8	1.25	1.061	B8V	-7.62
Hip052160	10:39:22.85	-18:50:10.5	1.25	2.135	B8V	-2.64
Hip057451	11:46:36.39	-51:28:19.4	12.50	2.054	B8V	-4.74

Table 2.5 – Continued

Name	RA (J2000.0)	DEC (J2000.0)	Exp. time (s)	airmass	Sp. type	Shift (kms^{-1})
Hip062448	12:47:53.53	-44:43:05.9	12.50	1.064	B8V	-8.02
Hip066454	13:37:23.41	-42:01:43.9	1.25	1.274	B8V	-4.26
Hip070243	14:22:19.68	-42:01:43.9	12.50	1.417	B8V	-7.21
Hip101552	20:34:47.32	-42:01:38.6	12.50	1.008	B8V	-4.07
Hip092159	18:46:59.89	-37:32:54.4	1.25	1.660	B8Vn...	-4.19
Hip003082	00:39:09.58	-10:18:40.8	25.00	1.112	B9	-3.05
Hip005387	01:08:55.92	-14:03:22.7	1.25	1.532	B9	-2.43
Hip012392	02:39:34.78	-47:50:53.0	25.00	1.273	B9	-2.43
Hip022914	04:55:52.25	-47:50:53.0	1.25	1.310	B9	-4.08
Hip045252	09:13:22.91	-33:24:03.5	12.50	1.199	B9	-4.76
Hip045252	09:13:22.91	-71:39:29.1	25.00	1.201	B9	-6.54
Hip086960	17:46:10.99	05:39:29.7	12.50	1.159	B9	-7.29
Hip087807	17:56:15.09	-04:34:34.4	12.50	1.073	B9	-6.61
Hip101607	20:35:29.69	06:56:50.5	12.50	1.790	B9	-0.86
Hip108127	21:54:21.92	12:45:05.1	12.50	1.900	B9	-1.88
Hip112376	22:45:38.09	03:37:51.5	25.00	1.163	B9	-1.51
Hip003356	00:42:42.84	-38:27:48.2	12.50	1.087	B9.5V	-3.00
Hip003356	00:42:42.85	-38:27:46.9	1.25	1.165	B9.5V	-1.99
Hip031589	06:36:40.05	-58:24:33.5	1.25	1.278	B9.5V	-1.44
Hip031589	06:36:40.10	-58:24:33.8	1.25	1.414	B9.5V	-1.57
Hip072154	14:45:30.23	00:43:03.0	6.00	1.303	B9.5V	-5.15
Hip104297	21:07:44.72	-17:27:20.6	12.50	1.067	B9.5V	-3.64
Hip106243	21:31:09.68	12:08:13.1	12.50	1.253	B9.5V	-4.59
Hip108875	22:03:19.08	11:23:12.7	12.50	1.539	B9.5V	-3.79
Hip025555	05:27:45.59	15:52:26.2	12.50	1.903	B9.5Vn	-6.22
Hip092963	18:53:07.86	01:45:21.0	12.50	2.582	B9III	-2.67
Hip050200	10:14:53.80	-42:22:56.5	12.50	1.068	B9IV	-7.72
Hip001191	00:14:54.60	-09:34:11.0	12.50	1.078	B9V	-2.80
Hip024505	05:15:24.30	-26:56:35.4	1.00	1.015	B9V	-3.10
Hip030591	06:25:43.76	-48:10:37.7	12.50	1.808	B9V	-5.05
Hip038280	07:50:34.28	-01:36:33.8	28.00	2.317	B9V	-5.92
Hip041399	08:26:43.89	-18:50:10.5	32.00	1.779	B9V	-8.23
Hip058859	12:04:16.56	-51:28:19.4	12.50	1.123	B9V	-8.19
Hip062483	12:48:16.27	-44:43:05.9	12.50	1.080	B9V	-8.00
Hip087054	17:47:18.94	-42:01:43.9	12.50	2.166	B9V	-1.98
Hip087054	17:47:18.94	-42:01:43.9	50.00	2.191	B9V	-1.62
Hip087054	17:47:20.11	-42:01:38.6	40.00	1.745	B9V	-2.54
Hip091286	18:37:12.69	11:25:16.8	12.50	1.479	B9V	-4.94
Hip092188	18:47:19.02	-37:32:54.4	1.25	1.469	B9V	-1.03
Hip108058	21:53:36.06	-10:18:40.8	1.25	1.781	B9V	1.47
Hip110573	22:24:00.57	15:16:53.8	12.50	1.315	B9V	-4.47
Hip112542	22:47:42.85	-14:03:22.7	12.50	1.019	B9V	-4.85
Hip113821	23:02:56.79	-47:50:53.0	12.50	1.693	B9V	-4.08
Hip113821	23:02:56.79	-47:50:53.0	12.50	1.693	B9V	-8.9
Hip006751	01:26:53.63	03:32:08.2	1.25	1.145	B9V+...	-0.12
Hip026796	05:41:27.01	-33:24:03.5	12.50	1.729	A0V	-2.67
Hip017543	03:45:23.32	-71:39:29.1	1.25	1.480	Ap...	-1.65

Appendix 2.C The first-year XSL sample

Our telluric-corrected, flux-calibrated, UVB- and VIS-arm-merged spectral library contains 246 spectra of 237 individual stars covering the wavelength from 3100 – 10185 Å. Table 2.6 lists the object name of XSL sample, the observation Modified Julian Date (MJD) and the airmass of the observation, and the star’s spectral type. When the merged spectrum of a certain star is combined from different observations, the MJD and airmass of the first observation are taken for this star.

Typical XSL spectra in the OBAFGKM sequence are shown in Figure 2.34. We show an M star sequence in Figure 2.35 to illustrate our collection of these cool stars. Other cool stars such as LPV, C, S, and L stars are shown in Figure 2.36.

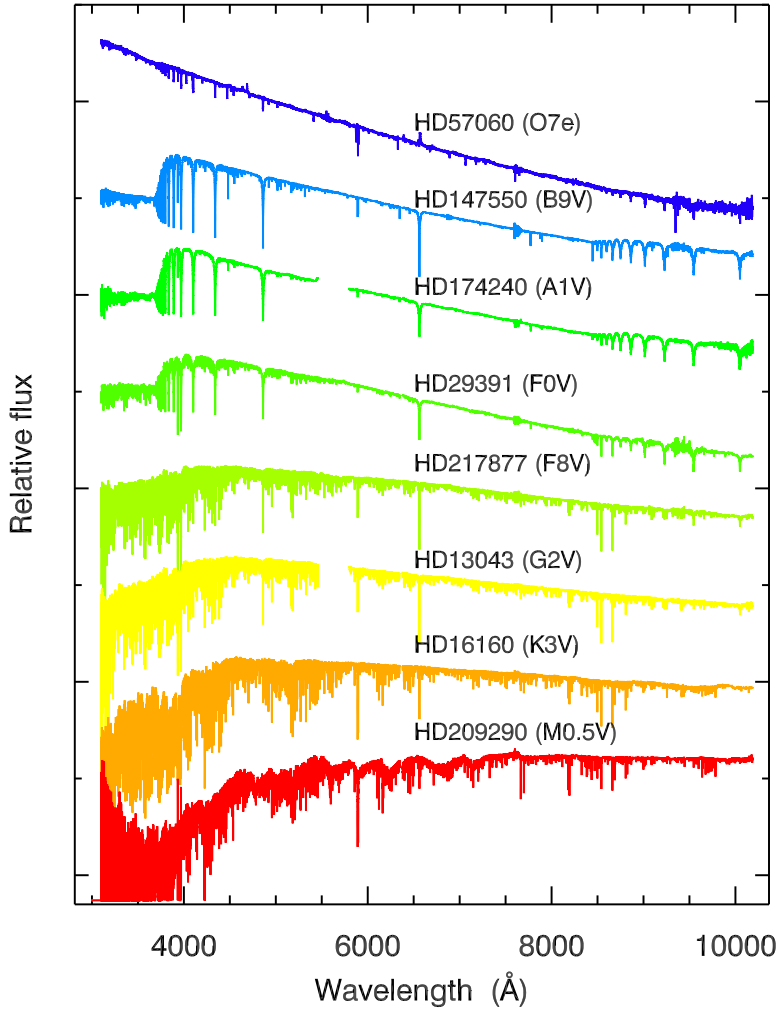


Figure 2.34: OBAFGKM sequence of the XSL sample in $\log(F_\lambda)$. Gaps around 5700 \AA indicate strong dichroic features between the UVB and VIS arms.

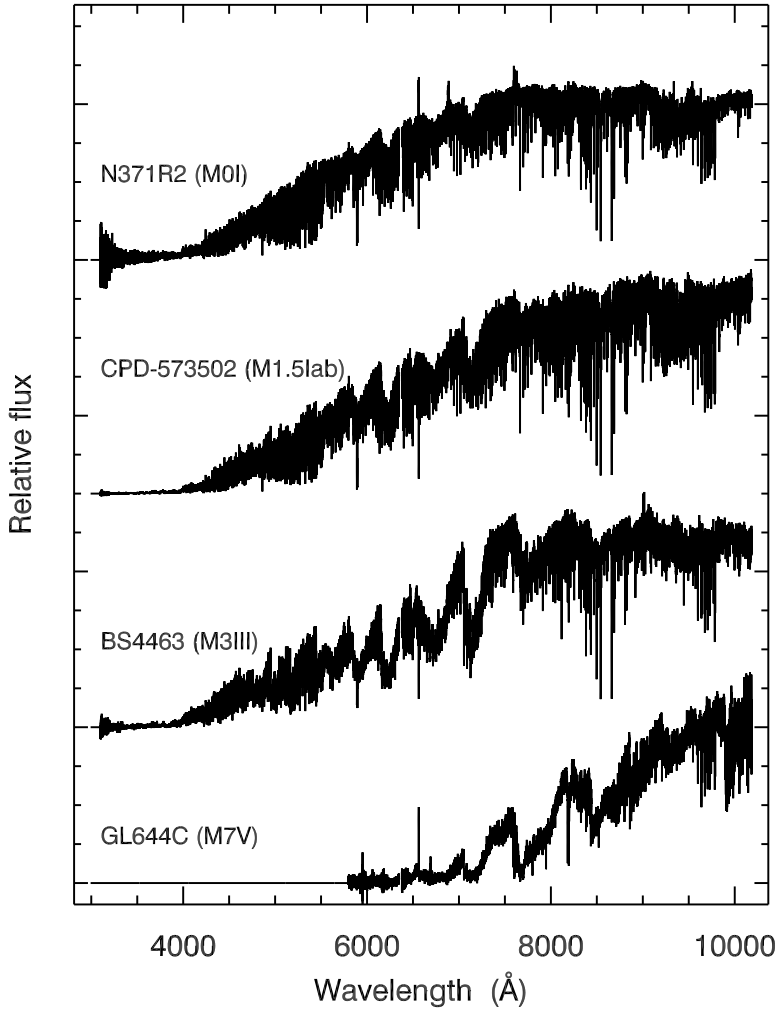


Figure 2.35: Sequence of M stars sorted by spectral type. Flat regions in the star GL644C indicates spectrum in very low signal-to-noise ratios regions.

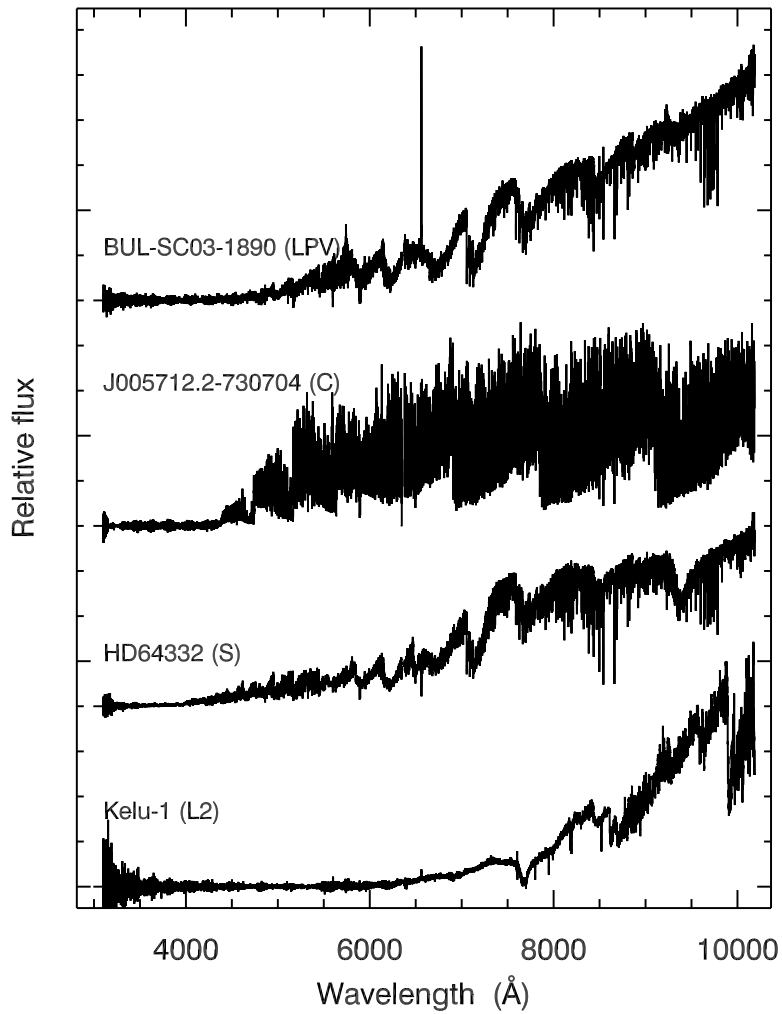


Figure 2.36: A sample of LPV, C, S, and L stars in the XSL.

Table 2.6: *The XSL first-year sample*

Star name	RA (J2000)	DEC (J2000)	MJD	airmass	Sp. type
HD57060	07:18:40.42	-24:33:30.3	55235.123	1.001	O7e...
HD34816	05:19:34.56	-13:10:37.1	55467.375	1.030	B0.5IV
HD96446	11:06:05.46	-59:56:57.4	55200.329	1.249	B2IIIp
HD224926	00:01:49.31	-03:01:41.4	55112.998	1.800	B7III-IV
HD34797	05:19:18.50	-18:30:36.2	55235.059	1.016	B8/B9IV:
HD196426	20:37:18.56	00:05:47.4	55408.257	1.184	B8IIIp
HD358	00:08:23.37	29:05:23.9	55113.051	2.290	B8IVmnp...
HD128801	14:38:48.31	07:54:38.8	55438.003	1.863	B9
HD163641	17:56:56.19	06:29:14.9	55457.080	1.719	B9III
HD175640	18:56:22.83	-01:48:00.5	55410.231	1.394	B9III
HD27295	04:19:26.26	21:08:30.7	55178.202	1.535	B9IV
HD147550	16:22:39.12	-02:04:48.0	55438.045	1.371	B9V
HD164257	18:00:07.38	06:33:11.6	55412.087	1.170	A0
HD194453	20:25:25.55	06:38:28.9	55408.227	1.206	A0
HD204041	21:25:51.81	00:32:02.0	55407.283	1.159	A1IV
HD72968	08:35:28.43	-07:58:57.1	55596.333	1.715	A1spe...
HD174240	18:49:37.33	00:50:08.6	55395.199	1.144	A1V
HD2857	00:31:53.12	-05:15:45.6	55113.031	1.593	A2
HD193281	20:20:27.96	-29:11:47.2	55408.204	1.008	A2III
HD190073	20:03:02.67	05:44:15.6	55409.239	1.281	A2IVe
HD28978	04:34:08.15	05:34:04.5	55162.115	1.366	A2Vs
HD38237	05:44:30.49	04:20:19.4	55461.293	1.812	A3
HD163346	17:55:37.73	02:04:28.7	55457.067	1.502	A3
HD174966	18:53:08.01	01:45:17.8	55395.206	1.162	A3
HD18769	03:01:54.19	26:27:41.4	55162.107	1.631	A3m
HD19445	03:08:25.44	26:19:39.4	55162.076	1.786	A4p
HD172230	18:38:55.10	06:16:12.6	55395.185	1.194	A5
HD16031	02:34:10.97	-12:23:07.4	55162.043	1.141	F0V
HD29391	04:37:36.33	-02:28:26.8	55178.218	1.150	F0V
HD284248	04:14:35.76	22:20:58.4	55162.098	1.820	F2
HD167278	18:14:33.84	00:10:32.3	55457.088	1.536	F2
HD205202	21:33:03.06	30:21:32.7	55407.255	1.753	F2
HD170756	18:30:16.41	21:51:58.8	55466.019	1.627	F4Ibvpv
G029-023	23:19:40.78	03:22:13.2	55410.325	1.142	F5
HD61064	07:37:16.58	-04:06:42.2	55507.355	1.086	F6III
HD160365	17:38:57.93	13:19:42.6	55357.219	1.268	F6III
HD196892	20:40:49.62	-18:47:37.5	55408.269	1.093	F6V
HD4813	00:50:07.37	-10:38:44.2	55150.032	1.076	F7IV-V
HD19019	03:03:50.92	06:07:57.6	55162.090	1.228	F8
G20-15	17:47:28.23	-08:46:54.3	55395.121	1.040	F8
HD175805	18:56:58.28	02:27:41.1	55410.240	1.532	F8
G188-22	21:43:57.03	27:23:19.7	55407.260	1.632	F8
HD217877	23:03:57.54	-04:47:44.2	55409.294	1.063	F8V
HD52298	06:57:45.19	-52:38:58.8	55461.322	1.599	F8VFe-1CH-0.5
HD157089	17:21:07.03	01:26:34.8	55357.209	1.114	F9V
HD45282	06:26:40.97	03:25:28.0	55240.162	1.377	G0
HD161770	17:47:46.13	-09:36:22.8	55357.241	1.044	G0
HD188262	19:53:46.06	16:46:39.5	55409.213	1.406	G0
HD200081	21:01:22.56	-02:30:51.5	55407.276	1.156	G0
G187-40	21:21:58.02	27:27:09.1	55408.249	1.643	G0
HD52973	07:04:06.57	20:34:13.9	55586.103	1.481	G0Ibv
HD216219	22:50:52.22	18:00:05.1	55409.283	1.360	G0IIp
HD39587	05:54:22.88	20:16:34.4	55586.086	1.415	G0VCH+M

Table 2.6 – Continued

Star name	RA (J2000)	DEC (J2000)	MJD	airmass	Sp. type
HD345957	20:10:48.17	23:57:53.6	55409.228	1.617	G0Vw
HD13043	02:07:33.87	-00:37:09.0	55408.305	1.515	G2V
HD17072	02:40:39.63	-69:13:57.0	55119.138	1.544	G2w...
HD163810	17:58:38.36	-13:05:57.5	55458.134	2.180	G3V
G169-28	16:50:11.45	22:18:43.8	55412.049	1.476	G3V
HD8724	01:26:17.73	17:07:31.3	55176.050	1.348	G5
HD204155	21:26:43.19	05:26:25.3	55407.293	1.243	G5
HD179821	19:13:58.77	00:07:30.3	55409.186	1.156	G5Ia
HD193896	20:23:00.98	-09:39:19.2	55408.215	1.050	G5IIIa
HD6229	01:03:36.45	23:46:02.9	55110.154	1.582	G5IIIw
HD18907	03:01:37.64	-28:05:34.9	55119.194	1.065	G5IV
HD44007	06:18:48.82	-14:50:43.8	55240.154	1.188	G5IV:w...
HD99648	11:27:56.18	02:51:19.2	55589.263	1.207	G8Iab
HD83212	09:36:20.10	-20:53:15.3	55637.158	1.039	G8IIIw...
HD201626	21:09:59.36	26:36:52.7	55408.238	1.608	G9p
PHS2008-RGB512	05:10:56.70	-71:11:33.7	55408.389	1.829	K
PHS2008-RGB522	05:11:22.08	-71:07:26.3	55439.349	1.640	K
PHS2008-RGB533	05:13:12.29	-71:18:00.9	55429.347	1.765	K
HD37828	05:40:54.72	-11:12:04.3	55224.081	1.028	K0
HD173158	18:43:45.43	05:44:11.9	55395.191	1.192	K0
HD93813	10:49:37.60	-16:11:34.8	55636.021	1.530	K0/K1III
HD179870	19:13:53.72	09:01:57.5	55409.181	1.252	K0IIb
HD82734	09:33:12.65	-21:06:55.8	55591.360	1.332	K0III
HD170820	18:32:13.32	-19:07:26.0	55410.215	1.251	K0III
HD33299	05:10:35.03	30:47:48.9	55235.009	1.776	K1Ib
HD1638	00:20:28.09	-30:33:21.3	55113.011	1.482	K1III
HD165438	18:06:15.38	-04:45:07.5	55413.094	1.068	K1IV
HD190404	20:03:51.51	23:20:14.8	55409.223	1.594	K1V
HD25329	04:03:16.46	35:16:08.0	55162.166	2.003	K1V..
HD50877	06:54:07.95	-24:11:04.4	55474.372	1.092	K2.5Iab
HD63302	07:47:38.86	-15:59:26.9	55636.136	1.200	K2Iab
HD19787	03:11:37.92	19:43:35.8	55180.073	1.416	K2III
HD37763	05:31:52.48	-76:20:26.5	55465.180	2.323	K2III
HD175545	18:55:51.65	-00:44:24.9	55395.216	1.157	K2III
HD31421	04:56:22.28	13:30:52.3	55202.058	1.348	K2IIIb
BS4432	11:30:18.90	-03:00:16.1	55589.274	1.126	K3.5III
HD81797	09:27:35.30	-08:39:31.3	55586.119	1.443	K3II-III
HD65354	07:57:02.76	-34:22:43.3	55475.363	1.294	K3III
HD232078	19:38:12.22	16:48:23.1	55409.207	1.424	K3IIp
HD165195	18:04:40.12	03:46:41.5	55413.083	1.137	K3p
HD16160	02:36:06.01	06:53:24.9	55162.057	1.279	K3V
HD160346	17:39:16.90	03:33:15.6	55357.231	1.141	K3V
HD52005	07:00:15.96	16:04:41.8	55508.364	1.319	K4Iab
HD74088	08:38:27.66	-62:50:36.4	55475.373	1.579	K4III
BS4104	10:27:09.23	-31:04:02.0	55636.211	1.068	K4III
BS3923	09:54:52.27	-19:00:34.9	55636.202	1.107	K5III
HD114960	13:13:57.71	01:27:22.2	55405.029	1.640	K5III
SMC052334	01:01:53.23	-71:52:14.7	55110.146	1.502	K7
HD79349	09:11:43.22	-48:46:21.5	55590.362	1.433	K7IV
J004950.3-731116	00:49:49.43	-73:11:14.6	55110.112	1.579	M
J005059.4-731914	00:50:58.98	-73:19:10.7	55110.185	1.511	M
J005101.9-731607	00:51:01.67	-73:16:04.2	55110.205	1.512	M
J005304.7-730409	00:53:05.39	-73:04:06.6	55115.305	1.713	M
J005314.8-730601	00:53:15.29	-73:05:58.7	55115.330	1.812	M

Table 2.6 – Continued

Star name	RA (J2000)	DEC (J2000)	MJD	airmass	Sp. type
J005332.4-730501	00:53:33.26	-73:04:56.0	55115.351	1.912	M
J005622.2-730334	00:56:22.16	-73:03:32.8	55114.097	1.592	M
J005714.4-730121	00:57:13.86	-73:01:19.9	55112.091	1.620	M
SHV0503595	05:03:41.55	-69:15:10.8	55407.408	1.691	M
SHV0503595	05:03:41.62	-69:15:12.3	55142.208	1.465	M
SHV0506368	05:06:27.17	-68:12:02.5	55407.425	1.607	M
SHV0506368	05:06:27.28	-68:12:01.1	55119.267	1.452	M
SHV0515461	05:15:26.61	-69:15:03.7	55142.260	1.411	M
SHV0523357	05:23:14.75	-69:17:53.0	55142.347	1.445	M
SHV0525543	05:25:32.27	-69:24:08.2	55226.161	1.534	M
SHV0526364	05:26:12.71	-69:34:09.4	55226.173	1.573	M
SHV0533015	05:32:11.26	-71:58:47.6	55226.211	1.750	M
SgrI55	17:59:29.38	-29:03:19.7	55412.062	1.007	M
SgrI11	17:59:55.94	-28:53:25.3	55412.075	1.003	M
SgrI117	18:00:45.85	-29:11:02.7	55412.097	1.009	M
Arp4329	18:03:28.67	-29:58:40.9	55397.246	1.307	M
OGLE-433669	18:03:37.02	-29:54:20.3	55393.139	1.005	M
OGLE-3733C3	18:35:18.24	-34:28:08.2	55356.397	1.416	M
OGLE-3267C3	18:35:21.81	-34:29:11.6	55356.174	1.124	M
OGLE-3690C7	18:35:28.12	-34:44:09.5	55393.051	1.204	M
OGLE-650C2	18:35:56.96	-34:34:47.4	55355.405	1.448	M
HD209290	22:02:10.09	01:23:56.5	55408.282	1.128	M0.5V
UCrt	11:12:45.34	-07:17:57.0	55351.955	1.047	M0e
SMC046662	00:59:34.43	-72:04:04.3	55110.135	1.520	M0I
N371R20	01:00:40.95	-72:10:34.4	55119.129	1.500	M0I
CD-603636	11:36:34.43	-61:36:36.1	55586.131	2.036	M0Iab
LMC170452	05:38:15.64	-69:10:12.0	55392.410	2.082	M1.5I
HD35601	05:27:10.32	29:55:13.4	55599.068	1.749	M1.5Ia0-Ia...
CPD-573502	10:35:43.85	-58:14:39.5	55636.220	1.260	M1.5Iab
CD-603621	11:35:45.09	-61:34:37.2	55231.372	1.312	M1.5Iab:
LMC162635	05:35:23.83	-69:04:01.6	55439.392	1.513	M1I
HD98817	11:21:38.55	-60:59:28.4	55637.058	1.487	M1Iab
BS4517	11:45:51.51	06:31:42.5	55636.036	2.512	M1III
LMC148035	05:30:35.52	-68:59:19.3	55240.041	1.399	M2.5I
CD-314916	07:41:02.72	-31:40:55.5	55177.322	1.023	M2.5Iab:
CD-314916	07:41:02.82	-31:40:56.8	55297.039	1.103	M2.5Iab:
CMCar	09:47:56.14	-67:27:05.5	55393.012	2.256	M2e
SMC083593	01:30:33.24	-73:18:40.6	55112.099	1.670	M2I
LMC158646	05:33:51.87	-69:11:13.5	55429.415	1.524	M2I
HV2360	05:12:45.85	-67:19:36.3	55119.290	1.400	M2Ia
HD39801	05:55:10.30	07:24:26.0	55116.342	1.223	M2Iab:
LMC150040	05:31:09.25	-67:25:52.4	55240.049	1.367	M3-M4
LMC168757	05:37:36.46	-69:29:21.8	55439.401	1.505	M3?m4I...
SMC055188	01:03:01.89	-72:01:51.4	55110.127	1.536	M3.5I
HD101712	11:41:49.72	-63:24:50.0	55314.209	1.518	M3Iab
HD101712	11:41:49.76	-63:24:50.2	55393.029	1.699	M3Iab
BS4463	11:35:12.90	-47:22:21.5	55621.115	1.337	M3III
HV2255	04:57:42.41	-70:08:49.6	55119.204	1.663	M4
HV2255	04:57:42.54	-70:08:50.1	55408.372	1.855	M4
SHV0549503	05:49:13.02	-70:42:38.3	55116.358	1.445	M4
B86-133	18:03:45.69	-30:03:00.6	55397.279	1.560	M4
RCha	08:21:46.27	-76:21:16.4	55636.163	1.727	M4.5e
EVCar	10:20:21.74	-60:27:12.5	55636.193	1.265	M4.5Ia
LMC143035	05:29:03.34	-69:06:42.5	55240.032	1.400	M4I

Table 2.6 – Continued

Star name	RA (J2000)	DEC (J2000)	MJD	airmass	Sp. type
J18025277-2954335	18:02:53.12	-29:54:33.5	55439.209	2.297	M5
J18040638-3010497	18:04:06.59	-30:10:47.7	55393.174	1.032	M5
HV2446	05:20:01.50	-67:34:39.4	55142.305	1.368	M5e
SHV0452361	04:52:25.92	-68:34:37.2	55119.228	1.532	M6
SHV0452361	04:52:26.09	-68:34:38.2	55407.386	1.747	M6
SHV0501215	05:01:14.85	-67:56:59.5	55407.392	1.740	M6
SHV0501215	05:01:14.97	-67:56:58.7	55119.237	1.512	M6
SHV0510004	05:09:40.07	-69:24:15.2	55423.393	1.595	M6
SHV0510004	05:09:40.24	-69:24:14.6	55119.276	1.465	M6
SHV0518570	05:18:36.24	-69:19:03.6	55142.292	1.405	M6
SHV0543367	05:43:07.62	-69:56:42.8	55237.063	1.425	M6
BUL-SC01-1821	18:02:12.94	-30:02:12.1	55439.189	1.896	M6
J18032525-2959483	18:03:25.44	-29:59:47.3	55397.236	1.249	M6
J18042244-3000534	18:04:22.68	-30:00:51.2	55393.181	1.042	M6
J18024611-3004509	18:02:46.42	-30:04:50.3	55439.201	2.110	M6.5
J18034305-3007541	18:03:43.30	-30:07:53.9	55397.285	1.621	M6.5
J18042719-3002575	18:04:27.41	-30:02:57.4	55463.155	2.589	M6.5
GL866	22:38:35.40	-15:17:37.4	55408.291	1.015	M6(M7e?)
SHV0606101	06:05:09.86	-72:40:32.9	55240.141	1.592	M7
J18024572-3001120	18:02:46.00	-30:01:11.6	55439.195	1.994	M7
GL644C	16:55:34.84	-08:23:51.7	55395.113	1.064	M7V
GL752B	19:16:57.96	05:08:58.6	55409.200	1.244	M8V
WXPsc	01:06:26.05	12:35:52.8	55110.161	1.301	M9
J18042265-2954518	18:04:22.85	-29:54:49.9	55393.189	1.056	M9
LHS2065	08:53:36.00	-03:29:36.2	55297.058	1.115	M9.0V
LHS2065	08:53:36.02	-03:29:36.9	55297.070	1.142	M9.0V
IRAS15060+0947	15:08:25.98	09:36:17.1	55414.019	1.328	M9III
IRAS14303-1042	14:33:00.13	-10:56:04.0	55437.994	1.455	Me
SHV0522380	05:22:18.23	-69:10:09.3	55142.330	1.421	Ms
SHV0529467	05:29:22.95	-69:36:11.8	55226.200	1.664	Ms
HD64332	07:53:05.54	-11:37:27.5	55637.148	1.287	S
J004900.4-732224	00:48:59.58	-73:22:22.7	55110.075	1.674	C
J004932.4-731753	00:49:32.01	-73:17:51.6	55110.090	1.631	C
J005307.8-730747	00:53:06.95	-73:07:45.2	55116.118	1.544	C
J005422.8-730105	00:54:22.14	-73:01:05.1	55119.075	1.608	C
J005531.0-731018	00:55:30.23	-73:10:17.8	55119.091	1.578	C
J005638.9-730452	00:56:38.55	-73:04:51.0	55114.119	1.553	C
J005644.8-731436	00:56:44.26	-73:14:32.2	55119.110	1.551	C
J005700.7-730751	00:57:00.00	-73:07:50.0	55111.071	1.689	C
J005712.2-730704	00:57:11.63	-73:07:03.5	55111.082	1.656	C
J005716.5-731052	00:57:16.02	-73:10:52.1	55111.112	1.583	C
J010031.5-730724	01:00:30.96	-73:07:21.0	55111.124	1.564	C
SHV0504353	05:03:55.38	-71:22:20.1	55119.256	1.545	C
SHV0518222	05:16:49.12	-75:00:21.3	55142.277	1.566	C
SHV0520505	05:20:15.06	-70:47:23.5	55142.315	1.450	C
SHV0525478	05:25:28.40	-69:07:11.1	55142.363	1.464	C
SHV0528537	05:28:28.10	-69:49:00.0	55226.189	1.626	C
SHV0536139	05:35:43.10	-70:14:15.3	55226.227	1.778	C
HD70138	08:19:43.34	-18:15:52.8	55596.299	1.371	C
HD76221	08:55:23.04	17:13:50.7	55558.359	1.457	C
YHya	09:51:03.96	-23:01:02.4	55636.181	1.056	C
TCae	04:47:18.70	-36:12:34.0	55142.193	1.105	CII
RUPup	08:07:29.96	-22:54:44.9	55636.150	1.180	CNv...
BUL-SC26-0532	17:47:42.54	-35:19:57.1	55375.341	1.684	LPV

Table 2.6 – Continued

Star name	RA (J2000)	DEC (J2000)	MJD	airmass	Sp. type
BUL-SC15-1379	17:48:25.24	-23:15:35.0	55395.128	1.003	LPV
BUL-SC15-2106	17:48:30.58	-23:05:23.0	55395.137	1.007	LPV
BUL-SC41-3443	17:52:14.09	-32:46:33.2	55375.356	1.852	LPV
BUL-SC41-3304	17:52:26.08	-32:49:07.5	55375.368	2.052	LPV
BUL-SC03-3941	17:53:32.66	-29:57:10.7	55395.145	1.014	LPV
BUL-SC24-0989	17:53:39.58	-33:06:02.7	55375.384	2.389	LPV
BUL-SC03-1890	17:53:45.40	-30:11:50.4	55438.057	1.053	LPV
BUL-SC03-8195	17:53:57.29	-29:31:41.1	55438.069	1.076	LPV
BUL-SC04-9008	17:54:28.10	-29:15:45.3	55439.130	1.337	LPV
BUL-SC04-4628	17:54:33.60	-29:44:03.0	55439.124	1.300	LPV
BUL-SC04-1709	17:54:49.28	-30:00:30.0	55439.136	1.373	LPV
BUL-SC22-1319	17:57:10.38	-31:02:16.0	55439.141	1.401	LPV
BUL-SC30-0707	18:01:46.26	-29:11:16.3	55412.103	1.012	LPV
BUL-SC01-0235	18:02:12.79	-30:22:32.4	55412.109	1.019	LPV
BUL-SC33-4149	18:05:39.56	-28:30:26.4	55408.120	1.014	LPV
BUL-SC36-2158	18:05:52.82	-28:11:34.9	55408.126	1.020	LPV
BUL-SC33-0357	18:05:56.47	-29:16:35.9	55408.140	1.039	LPV
BUL-SC19-2302	18:07:35.39	-27:15:33.0	55408.145	1.045	LPV
BUL-SC06-2525	18:07:51.46	-31:48:59.8	55408.155	1.068	LPV
BUL-SC19-2332	18:07:57.92	-27:15:50.7	55408.161	1.077	LPV
BUL-SC06-2997	18:08:07.85	-31:42:00.6	55408.173	1.112	LPV
BUL-SC19-2948	18:08:16.42	-27:08:51.9	55408.180	1.130	LPV
BUL-SC06-1799	18:08:32.44	-32:01:52.1	55408.190	1.167	LPV
BUL-SC16-1428	18:10:29.74	-26:28:58.7	55397.171	1.033	LPV
BUL-SC17-1595	18:11:33.72	-26:22:06.5	55397.165	1.024	LPV
BUL-SC13-0324	18:16:47.68	-24:20:32.3	55465.151	2.509	LPV
BUL-SC13-1542	18:17:06.70	-23:59:35.8	55466.138	2.234	LPV
BUL-SC08-1687	18:23:20.45	-21:35:53.7	55410.210	1.246	LPV
Kelu-1	13:05:40.17	-25:41:04.9	55352.154	1.264	L2
J15065441+1321060	15:06:54.42	13:21:05.4	55438.015	1.931	L3
J22244381-0158521	22:24:44.20	-01:59:05.7	55409.257	1.087	L4.5

Bibliography

- Allard, F., Homeier, D., & Freytag, B. 2011, in *Astronomical Society of the Pacific Conference Series*, Vol. 448, 16th Cambridge Workshop on Cool Stars, Stellar Systems, and the Sun, ed. C. Johns-Krull, M. K. Browning, & A. A. West, 91
- Bagnulo, S., Jehin, E., Ledoux, C., et al. 2003, *The Messenger*, 114, 10
- Bessell, M. S. 1990, *PASP*, 102, 1181
- Blanco, V. M., McCarthy, M. F., & Blanco, B. M. 1984, *AJ*, 89, 636
- Bohlin, R. C. 2007, in *Astronomical Society of the Pacific Conference Series*, Vol. 364, *The Future of Photometric, Spectrophotometric and Polarimetric Standardization*, ed. C. Sterken, 315
- Bruzual, G. & Charlot, S. 2003, *MNRAS*, 344, 1000

- Buzzoni, A., Mantegazza, L., & Gariboldi, G. 1994, *AJ*, 107, 513
- Cappellari, M. & Emsellem, E. 2004, *PASP*, 116, 138
- Cenarro, A. J., Cardiel, N., Gorgas, J., et al. 2001, *MNRAS*, 326, 959
- Charlot, S. & Bruzual, A. G. 1991, *ApJ*, 367, 126
- Chen, Y., Trager, S., Peletier, R., & Lançon, A. 2011, *Journal of Physics Conference Series*, 328, 012023
- Cioni, M.-R. L., Blommaert, J. A. D. L., Groenewegen, M. A. T., et al. 2003, *A&A*, 406, 51
- Coelho, P., Barbuy, B., Meléndez, J., Schiavon, R. P., & Castilho, B. V. 2005, *A&A*, 443, 735
- Coelho, P., Bruzual, G., Charlot, S., et al. 2007, *MNRAS*, 382, 498
- Conroy, C. & van Dokkum, P. 2012, *ApJ*, 747, 69
- Conroy, C., van Dokkum, P. G., & Graves, G. J. 2013, *ApJ*, 763, L25
- Cousins, A. W. J. 1971, *Royal Observatory Annals*, 7
- Cousins, A. W. J. 1973, *MNRAS*, 77, 223
- Davies, R. L., Sadler, E. M., & Peletier, R. F. 1993, *MNRAS*, 262, 650
- Fioc, M. & Rocca-Volmerange, B. 1997, *A&A*, 326, 950
- Frogel, J. A. 1988, *ARA&A*, 26, 51
- Fukugita, M., Ichikawa, T., Gunn, J. E., et al. 1996, *AJ*, 111, 1748
- Fukugita, M., Shimasaku, K., & Ichikawa, T. 1995, *PASP*, 107, 945
- González, J. J. 1993, PhD thesis, Thesis (PH.D.)—UNIVERSITY OF CALIFORNIA, SANTA CRUZ, 1993. Source: *Dissertation Abstracts International*, Volume: 54-05, Section: B, page: 2551.
- González Delgado, R. M., Cerviño, M., Martins, L. P., Leitherer, C., & Hauschildt, P. H. 2005, *MNRAS*, 357, 945
- Gregg, M. D., Silva, D., Rayner, J., et al. 2006, in *The 2005 HST Calibration Workshop: Hubble After the Transition to Two-Gyro Mode*, ed. A. M. Koekemoer, P. Goudfrooij, & L. L. Dressel, 209
- Groenewegen, M. A. T. & Blommaert, J. A. D. L. 2005, *A&A*, 443, 143
- Guiderdoni, B. & Rocca-Volmerange, B. 1987, *A&A*, 186, 1
- Gustafsson, B., Edvardsson, B., Eriksson, K., et al. 2008, *A&A*, 486, 951
- Hoffleit, D. & Jaschek, C. . 1991, *The Bright star catalogue*
- Hoffleit, D., Saladyga, M., & Wlasuk, P. 1983, *Bright star catalogue. Supplement*

- Horne, K. 1986, *PASP*, 98, 609
- Hughes, S. M. G. & Wood, P. R. 1990, *AJ*, 99, 784
- Johnson, H. L., Mitchell, R. I., Iriarte, B., & Wisniewski, W. Z. 1966, *Communications of the Lunar and Planetary Laboratory*, 4, 99
- Koleva, M., Bouchard, A., Prugniel, P., De Rijcke, S., & Vauglin, I. 2013, *MNRAS*, 428, 2949
- Koleva, M., Prugniel, P., Bouchard, A., & Wu, Y. 2009, *A&A*, 501, 1269
- Koleva, M., Prugniel, P., Ocvirk, P., Le Borgne, D., & Soubiran, C. 2008, *MNRAS*, 385, 1998
- Kurucz, R. 1993, *ATLAS9 Stellar Atmosphere Programs and 2 km/s grid*. Kurucz CD-ROM No. 13. Cambridge, Mass.: Smithsonian Astrophysical Observatory, 1993., 13
- Lançon, A. & Mouhcine, M. 2002, *A&A*, 393, 167
- Lançon, A. & Rocca-Volmerange, B. 1992, *A&AS*, 96, 593
- Lançon, A. & Wood, P. R. 2000, *A&AS*, 146, 217
- Landolt, A. U. 1973, *AJ*, 78, 959
- Landolt, A. U. 1983, *AJ*, 88, 439
- Le Borgne, D., Rocca-Volmerange, B., Prugniel, P., et al. 2004, *A&A*, 425, 881
- Le Borgne, J.-F., Bruzual, G., Pelló, R., et al. 2003, *A&A*, 402, 433
- Leitherer, C., Alloin, D., Fritze-v. Alvensleben, U., et al. 1996, *PASP*, 108, 996
- Leitherer, C., Schaerer, D., Goldader, J. D., et al. 1999, *ApJS*, 123, 3
- Lenz, D. D., Newberg, J., Rosner, R., Richards, G. T., & Stoughton, C. 1998, *ApJS*, 119, 121
- Levesque, E. M., Massey, P., Olsen, K. A. G., & Plez, B. 2007, *ApJ*, 667, 202
- Levesque, E. M., Massey, P., Olsen, K. A. G., et al. 2005, *ApJ*, 628, 973
- Lord, S. D. 1992, in *NASA Technical Memorandum*, Vol. 103957
- Maraston, C. 1998, *MNRAS*, 300, 872
- Maraston, C. 2005, *MNRAS*, 362, 799
- Mármol-Queraltó, E., Cardiel, N., Cenarro, A. J., et al. 2008, *A&A*, 489, 885
- Martins, L. P., González Delgado, R. M., Leitherer, C., Cerviño, M., & Hauschildt, P. 2005, *MNRAS*, 358, 49
- Munari, U., Sordo, R., Castelli, F., & Zwitter, T. 2005, *A&A*, 442, 1127

- Ocvirk, P., Pichon, C., Lançon, A., & Thiébaud, E. 2006, *MNRAS*, 365, 46
- Palacios, A., Gebran, M., Josselin, E., et al. 2010, *A&A*, 516, A13
- Patat, F., Moehler, S., O'Brien, K., et al. 2011, *A&A*, 527, A91
- Peletier, R. F. 1989, PhD thesis, University of Groningen, The Netherlands, (1989)
- Pickles, A. J. 1998, *PASP*, 110, 863
- Prugniel, P. & Soubiran, C. 2001, *A&A*, 369, 1048
- Prugniel, P. & Soubiran, C. 2004, *ArXiv Astrophysics e-prints*
- Prugniel, P., Soubiran, C., Koleva, M., & Le Borgne, D. 2007, *ArXiv Astrophysics e-prints*
- Rayner, J. T., Cushing, M. C., & Vacca, W. D. 2009, *ApJS*, 185, 289
- Sánchez-Blázquez, P., Peletier, R. F., Jiménez-Vicente, J., et al. 2006, *MNRAS*, 371, 703
- Seifahrt, A., Käufel, H. U., Zängl, G., et al. 2010, *A&A*, 524, A11
- Sharp, R. & Parkinson, H. 2010, *MNRAS*, 408, 2495
- Thomas, D., Maraston, C., Bender, R., & Mendes de Oliveira, C. 2005, *ApJ*, 621, 673
- Thurl, C., Sackett, P. D., & Hauschildt, P. H. 2006, *A&A*, 455, 315
- Trager, S. C., Faber, S. M., Worthey, G., & González, J. J. 2000, *AJ*, 119, 1645
- Valdes, F., Gupta, R., Rose, J. A., Singh, H. P., & Bell, D. J. 2004, *ApJS*, 152, 251
- van Dokkum, P. G. 2001, *PASP*, 113, 1420
- Vazdekis, A., Sánchez-Blázquez, P., Falcón-Barroso, J., et al. 2010, *MNRAS*, 404, 1639
- Vernet, J., Dekker, H., D'Odorico, S., et al. 2011, *A&A*, 536, A105
- Wild, V. & Hewett, P. C. 2005, *MNRAS*, 358, 1083
- Worthey, G., Faber, S. M., & González, J. J. 1992, *ApJ*, 398, 69
- Worthey, G., Faber, S. M., González, J. J., & Burstein, D. 1994, *ApJS*, 94, 687
- Worthey, G. & Ottaviani, D. L. 1997, *ApJS*, 111, 377
- Wu, Y., Singh, H. P., Prugniel, P., Gupta, R., & Koleva, M. 2011, *A&A*, 525, A71
- Yamada, Y., Arimoto, N., Vazdekis, A., & Peletier, R. F. 2008, *ApJ*, 674, 612

STELLAR POPULATION MODELS WITH XSL IN THE OPTICAL

Work done in collaboration with: S. Meneses-Goytia, R. F. Peletier, S. C. Trager and the X-Shooter spectral library collaboration.

Abstract

We present stellar population synthesis models using the new X-Shooter spectral library, XSL, which predicts spectral energy distributions (SEDs) at a resolution of $R \equiv \lambda/\Delta\lambda \sim 7000$, covering the wavelength range from 3100 to 10200 Å. Our models predict SEDs with metallicities $-0.7 < [\text{Fe}/\text{H}] < +0.2$ and ages from 0.1 to 15 Gyr. where SEDs with ages below 1 Gyr are only available for $0.0 \leq [\text{Fe}/\text{H}] < +0.2$. Two sets of isochrones and two initial mass functions (IMFs) are used to construct the SEDs, which enable our model to be a flexible tool for various investigations on stellar populations. In addition, both full spectrum fitting and line index investigation can be performed with our models. We have tested our models on spectra of Galactic globular clusters. Our inferred ages and metallicities of these clusters are consistent with the published values. Our models are well suited for asymptotic giant branch (AGB) dominated stellar systems and other unresolved galaxies and clusters in particular small stellar systems, because of our intermediate-resolution spectra.

3.1 Introduction

Extracting the evolution history from the integrated light of stellar systems is one of the most important goal in modern astrophysics. The technique is known as stellar population synthesis. In this technique, the integrated light of a galaxy is reproduced by combining individual stellar spectra with known physical atmospheric parameters from a stellar library constrained by know stellar evolution pathways (e.g. Tinsley 1978;

Guiderdoni & Rocca-Volmerange 1987; Buzzoni et al. 1994; Worthey et al. 1994; Leitherer et al. 1996; Fioc & Rocca-Volmerange 1997; Leitherer et al. 1999; Vazdekis 1999; Bruzual & Charlot 2003; Le Borgne et al. 2004; González Delgado et al. 2005; Maraston 2005; Vazdekis et al. 2010; Conroy & van Dokkum 2012a).

When analyzing the integrated stellar light one important problem is the degeneracy between age and metallicity (Worthey 1994). This effect is more obvious when analyzing colors or low resolution spectra (see, Vazdekis 1999; Schiavon et al. 2002a). The traditional method of breaking the degeneracy between age and metallicity in old stellar populations is to resort to diagnostics of individual stellar absorption line features – spectral indices. Widely used are the indices of the Lick/IDS system (Worthey et al. 1994; Trager et al. 1998). This system consists of 25 indices, defined on low resolution spectra, each of which has a center bandpass and two pseudo-continuum bands, all contain many overlapping absorption lines. The fact that many absorption lines affect the value of an index makes it difficult to interpret in terms of stellar populations. Models (e.g. Vazdekis 1999; Vazdekis et al. 2003; Le Borgne et al. 2004) constructed with flux calibrated spectra and relatively higher resolution are more effective in analyzing stellar populations, but, are usually subject to limited wavelength coverage because of instrumental limitations.

Although traditionally the wavelength region around 5000 Å has been popular, it turns out that some important features in the red, such as the CaII triplet and NaI 8200, are useful diagnostics of metallicity (Armandroff & Zinn 1988; Cenarro et al. 2008; Foster et al. 2009) and for determining dwarf-to-giant ratios (e.g. Faber & French 1980; Conroy & van Dokkum 2012a; Spiniello et al. 2012). In order to have wider wavelength coverage including those important red features, people have joined several empirical stellar libraries. Vazdekis et al. (2012) joined MILES (Sánchez-Blázquez et al. 2006), the CaT library (Cenarro et al. 2001) and Indo-U.S. (Valdes et al. 2004) together to build the MIUSCAT stellar synthesis models; Conroy & van Dokkum (2012a, CvD model) joined MILES and IRTF (Rayner et al. 2009) libraries together with synthetic spectra to fill the gap in between the libraries. During this process, different properties of the input libraries, such as resolution, parameter coverage, etc. make it easy for systematic errors to play a significant role in interpreting stellar populations. With the development of better instrumentation, we now have libraries with a much wider wavelength coverage and higher resolution than the spectra used to define the Lick/IDS system, which enables us to investigate the integrated galaxy light and trace individual elemental lines better.

We present here simple stellar population (SSP) SEDs constructed with the pilot data (1/3 stars of the complete library, Chen et al. 2013a) of the new X-Shooter Spectral Library (XSL) in the optical, which enables us to reproduce the integrated light of old stellar populations with ages from 0.1 Gyr to 15 Gyr in a wide spectral range (3100 to 10200 Å) at intermediate spectral resolution ($R \equiv \lambda/\Delta\lambda \sim 7000$). These models should be of particular interest for interpreting the integrated spectra of small stellar systems and for spectra gathered by modern spectroscopic surveys to determine galaxy evolutionary histories and metallicities. Furthermore, the large collection of cool giant stars from XSL make our models ideal tools for asymptotic giant branch (AGB) dominated stellar populations.

3.2 Atmospheric parameters of XSL DRI

To build the SSP models we need to have a full understanding of the physical parameters (i.e. effective temperature T_{eff} , gravity $\log g$, and metallicity $[\text{Fe}/\text{H}]$) of the spectral library. We divide the sample in warm stars (O–K types) and cool stars (M, long-period-variable (LPV), L, S types) to calculate these parameters.

3.2.1 Fitting strategy for warm stars

We determine the atmospheric parameters of the warm stars using the ULYSS package, which minimizes the difference between the observed spectra and a parametric model (Koleva et al. 2009; Wu et al. 2011) using the MILES interpolator (Prugniel et al. 2011). The XSL are degenerated to the resolution of MILES, to use some stars from that library as templates. We fit the spectrum of a single star in the UVB and VIS arm separately. The adopted parameters are taken from the fits with minimum chi-square of the UVB and VIS arm for the G and K stars. Parameters of the O, B, A, F stars are taken from the fits in the UVB arm, because the XSL spectra in the UVB arm contain more information than in the VIS arm (the peak of the blackbody appears in the UVB arm for warm stars), so that the results are more trustworthy.

3.2.2 Fitting strategy for cool stars

We estimate parameters of the cool stars using the full-spectrum-fitting package pPXF (Cappellari & Emsellem 2004) plus an interpolated theoretical grid of BT-SETTL¹ (Allard et al. 2011) models due to the limited cool star sample in the MILES interpolator. Spectra of cool stars in the VIS arm are used to perform the fit due to their lower signal-to-noise ratios in the UVB arm.

Fits are performed on the original XSL spectra with the BT-SETTL models. When a best fit is made for a certain star, the parameters of that star are derived as the sum of the weighted parameters of templates which are used to construct the best fit.

3.2.3 Quality of the derived parameters

We measure the atmospheric parameters for 218 XSL stars. As discussed in Wu et al. (2011) and Prugniel et al. (2011), the automatic determination is less reliable for the hot evolved stars ($T_{\text{eff}} \geq 10\,000$ K) and the cool stars ($T_{\text{eff}} \leq 3500$ K), and therefore it is important to critically assess our result. For 100 stars parameters from the literature are available. We carefully estimate the averaged literature parameters for each star, without using those of Prugniel & Soubiran (2001) and Koleva & Vazdekis (2012), since they were determined using the same ULYSS method and might have the same biases in the parameters. Figure 3.1 shows the residuals between our estimations and averaged literature values for T_{eff} , $\log g$, and $[\text{Fe}/\text{H}]$, where the “Residual” uncertainty is calculated as the standard deviation from different literature estimates for the same star, and the

¹<http://phoenix.ens-lyon.fr/Grids/BT-Settl/>

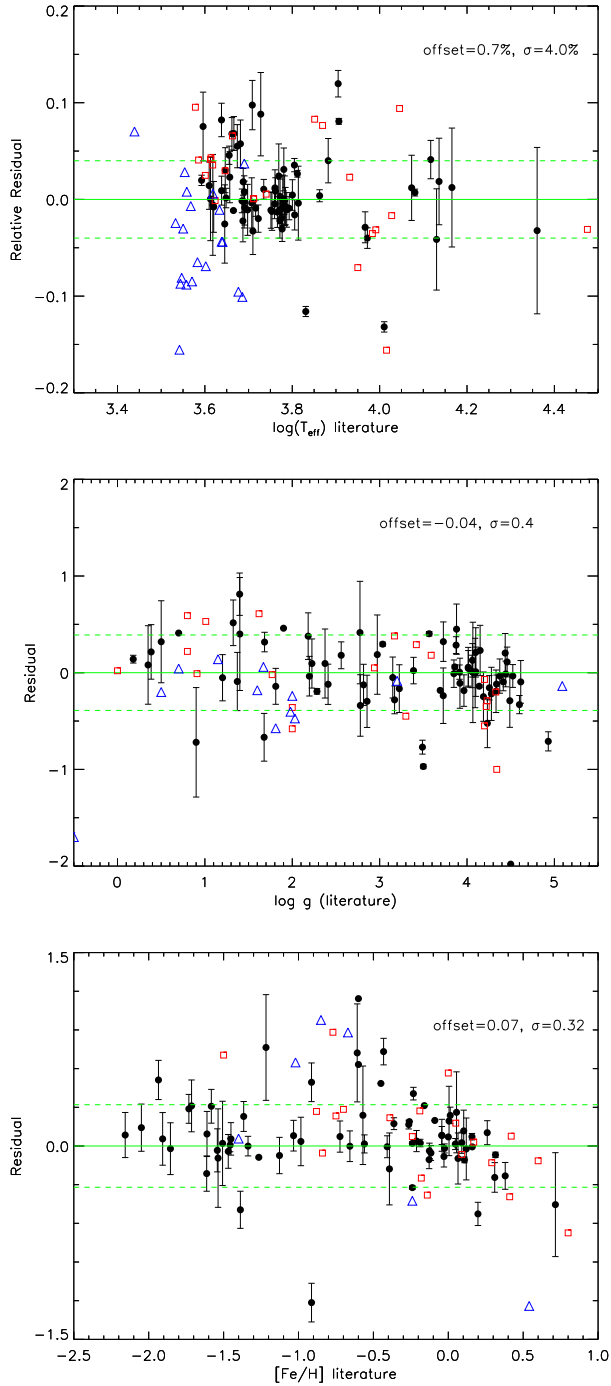


Figure 3.1: Comparison of the measured atmospheric parameters with averaged literature values, where the red squares indicate that only one set of literature values is available, and the blue triangles indicate cool stars with published literature parameters. The overall offset and 1σ standard deviation are noted in each panel for T_{eff} , $\log g$, and $[Fe/H]$.

dashed green lines indicate the overall 1σ standard deviation between the averaged literature values and our estimates. The standard deviations are 4.0% in T_{eff} , 0.4 and 0.32 dex for $\log g$ and $[\text{Fe}/\text{H}]$, respectively. Most of the outliers come from variable stars and sometimes cool stars.

The good agreement of T_{eff} and $\log g$ between our estimates and the literature values gives us confidence to adopt the estimated T_{eff} and $\log g$ for those stars without any published atmospheric parameters (most of them are cool stars). Determining the metallicity of cool stars is a difficult task. On one hand, more than half of the cool stars in our sample are variable stars, and on the other hand, metallicities are notoriously hard to measure for cool stars, which are dominated by molecular lines (e.g. Leggett et al. 2001; Rice et al. 2010; Bonnefoy et al. 2013, and references therein). The metallicities of stars in Magellanic Cloud are constrained by comparing the measured value with values of $[\text{Fe}/\text{H}]$ inferred from color-magnitude diagram (CMD)-based estimates (Geisler et al. 1997; Geisler & Sarajedini 1999; Piatti 2012; Piatti et al. 2012). We keep our measured $[\text{Fe}/\text{H}]$ when the value is consistent with CMD-based estimates; and adopt the $[\text{Fe}/\text{H}]$ given by Piatti (2012) and Piatti et al. (2012) when our measurement is not consistent with their work. Metallicities of red giants from the Galactic Bulge are assumed to have the mean $[\text{Fe}/\text{H}] = -0.21$ (Ramírez et al. 2000). Metallicities of LPVs are adopted as 0.0 since they belong to the Galactic disk.

3.3 The models

3.3.1 Spectral synthesis

The SSP spectral synthesis is obtained using

$$S_{\lambda}(t, [\text{Fe}/\text{H}]) = \int_{m_a}^{m_b} S_{\lambda}(m, t, [\text{Fe}/\text{H}]) \psi(m, t) F_X(m, t, [\text{Fe}/\text{H}]) dm \quad (3.1)$$

where $S_{\lambda}(m, t, [\text{Fe}/\text{H}])$ is the spectrum of stars with given mass m , age t and metallicity $[\text{Fe}/\text{H}]$, $F_X(m, t, [\text{Fe}/\text{H}])$ is the light weighted flux at a certain normalized wavelength band X , $\psi(m, t)$ is the mass distribution inferred from the IMF according to the star formation history extracted from the isochrone, m_a and m_b are the minimum and maximum mass of stars sharing the same age and metallicity, respectively. Here we assume $[\text{Fe}/\text{H}] = [\text{Z}/\text{Z}_{\odot}] = \log(\text{Z}/\text{Z}_{\odot})$, and we normalize our spectra in the V band.

We recall the three primary ingredients for constructing the SSP SEDs: isochrone, IMF, and a spectral library. To build the model SEDs, we need the spectra of stars with atmospheric parameters requested by the isochrones. It is rare that the input empirical spectral library has even one star with exactly the desired set of parameters. When the atmospheric parameters (T_{eff} , $\log g$, and $[\text{Fe}/\text{H}]$) of stars from a spectral library are available, we can create the required spectrum by interpolating in the library. In order to create spectra of stars with arbitrary stellar parameters, we make use of an interpolation technique similar to that of Vazdekis et al. (2003).

The interpolation technique we adopt works by first considering only those spectra within a certain stellar parameter range of the desired value. The size of this stellar

Table 3.1: *SSP models constructed in this work*

Models	Isochrones	IMF	Spectral library
XMSa	Marigo et al. (2008)	Salpeter (1955)	XSL DRI
XMKr	Marigo et al. (2008)	Kroupa (2001)	XSL DRI
XBSa	BaSTI (Pietrinferni et al. 2004)	Salpeter (1955)	XSL DRI
XBKr	BaSTI (Pietrinferni et al. 2004)	Kroupa (2001)	XSL DRI

parameter “box” is inversely proportional to the density of stars found around the target value, to ensure that enough stars are available for the interpolation. However, the minimum size of the box is limited to the typical uncertainties of the parameters of the template library. Once the size of the parameter box is determined, it is subsequently divided into eight cubes of different sizes that have the given point as an inner corner. The stars within each cube are then combined into a single spectrum, resulting in eight different spectra with parameter values that bracket the target value. This minimizes the errors due to the lack of stars in certain regions of the distribution of stars. Finally, these eight spectra are combined to obtain the final spectrum with the desired stellar parameters.

We will analyze four sets of models in this work, as shown in Table 3.1.

3.3.2 Stellar spectral library

The new ingredient of the SSP models presented in this paper is the XSL, which covers the spectral range from 3100 to 10200 Å at a resolution of $R \sim 7000$.

We have removed all stars with flux losses (see Chen et al. 2013a), carbon stars, and stars with incomplete spectral ranges (mostly low signal-to-noise ratio in the UVB arm, i.e. $\lambda < 5600$ Å). The remaining 155 stars which are used for building the SSP models are shown in Figure 3.2. With this sample of XSL stars, we can build SSP models over the entire wavelength range simultaneously with good flux calibration. The physical parameter coverage of the present sample is: $2400 \leq T_{\text{eff}} \leq 22192$ K, $0.18 \leq \log g \leq 4.93$, and $-2.0 \leq [\text{Fe}/\text{H}] \leq 0.5$. From this Figure 3.2 we can see that the metallicity range $-0.7 \leq [\text{Fe}/\text{H}] \leq 0.0$ is relatively well sampled given the available data; the lowest metallicity $[\text{Fe}/\text{H}] \leq -1.0$ and highest metallicity $[\text{Fe}/\text{H}] \geq 0.2$ ranges are not well sampled, so the models will not be trustable significantly far away from solar metallicity. Moreover, since we are missing low temperature ($T_{\text{eff}} \leq 5500$ K) main sequence stars, it will be difficult to model stellar systems older than ~ 10 Gyrs. We will improve our models when XSL has a wider parameter coverage.

Instead of carbon stars, we use long-period-variable stars for the AGB and TP-AGB phases (Lançon & Mouhcine 2002). The idea is that in the future we plan to make models with a range in C/O ratio. For the moment we have only made the oxygen-rich models. Cool M stars (M7 – M9, $T_{\text{eff}} \sim 2400 - 2700$ K) are also included. By using a well-sampled stellar library, we are able to make model predictions as not only the warm stars but also cool stars at all wavelength more accurately.

We set a homogeneous gap for all the spectra between 5460 and 5800 Å due to the

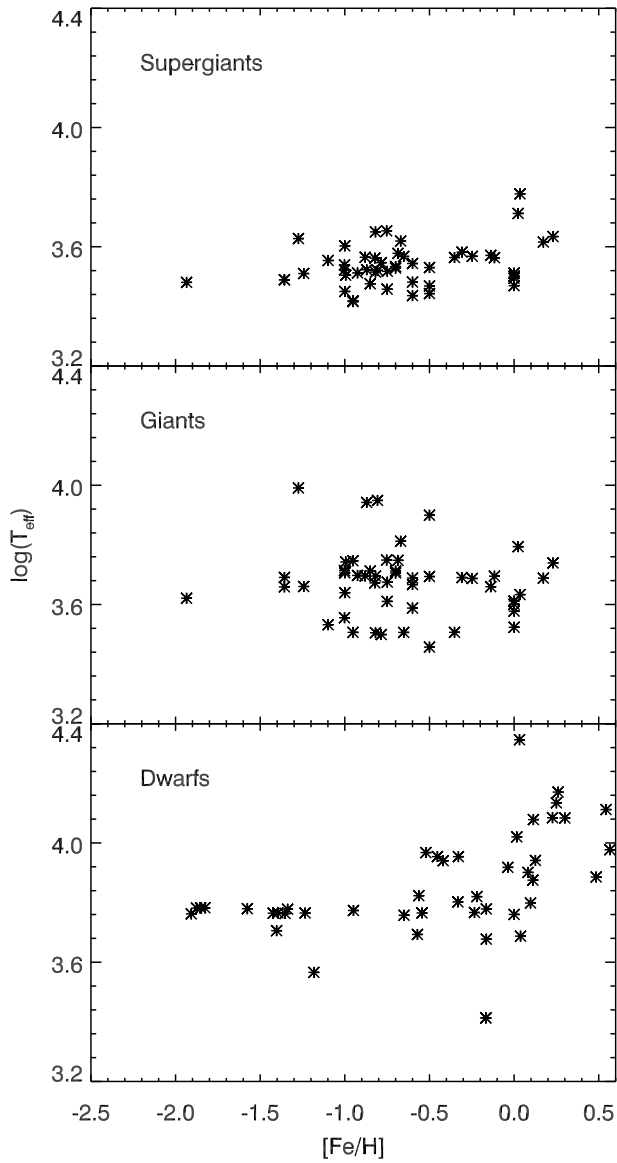


Figure 3.2: Atmospheric parameter coverage of the first release of XSL sorted by luminosity class, where supergiants are defined with $\log g < 1.0$, giants with $1.0 \leq \log g < 3.5$, and dwarfs with $\log g \geq 3.5$

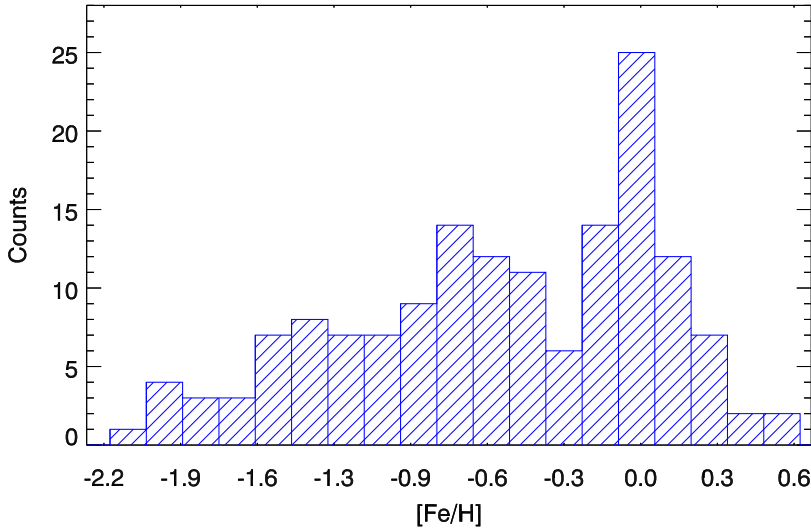


Figure 3.3: Metallicity distribution of the XSL stars used to build the SSP models.

strong dichroic feature at the end of the UVB arm and at the beginning of the VIS arm of the XSL spectra. This causes problems in the flux calibration of those wavelengths (see Chen et al. 2013a for details).

3.3.3 The initial mass function

An initial mass function (IMF) is required to populate an isochrone with the proper number of stars before integrating their spectra to produce the spectral energy distribution of the total composite stellar population. The effect of IMF on stellar population models has been a popular topic recently due to the observational evidence that the previous assumption of a universal IMF is not adequate to describe the detailed spectra of massive early-type galaxies (van Dokkum & Conroy 2010; Conroy & van Dokkum 2012a; Spiniello et al. 2012). In this work we adopt the Salpeter IMF (Salpeter 1955) $dN/dm \propto m^{-2.35}$ as a reference and the Kroupa (2001) IMF two often-used IMF prescriptions (see Chapter 4 for a detailed description). For both IMFs, we use a mass range of 0.1–100 M_{\odot} for Marigo models.

3.3.4 Isochrones

We use theoretical isochrones from Marigo et al. (2008) and Pietrinferni et al. (2004) (BaSTI) to predict the evolutionary sequences of the stellar interiors. The Marigo et al. (2008) isochrones include stellar phases from the zero-age main sequence (ZAMS) to

the onset of the thermally-pulsing asymptotic giant branch phase (TP-AGB). The range of initial mass in this set of isochrones is $0.15 \leq m \leq 60 M_{\odot}$, with available metallicities $Z = 0.0001, 0.0003, 0.0008, 0.0038, 0.0076, 0.019, 0.023$, and 0.03 ($Z_{\odot} = 0.019$).

The BaSTI isochrones have high resolution along their tracks, which enables one to investigate various stellar phases in more detail. We adopt the AGB extended, non-canonical solar scaled tracks for this work. Similar to the Marigo isochrones, the tracks run from the ZAMS to the first few thermal pulses. The initial mass cut off is slightly higher, with stellar masses beginning at $m = 0.5 M_{\odot}$. Available metallicities are $Z = 0.0001, 0.0003, 0.0006, 0.001, 0.002, 0.004, 0.008, 0.01, 0.0198, 0.03$, and 0.04 ($Z_{\odot} = 0.0198$).

In this work, rather than using the V-band luminosities given by the Marigo et al. (2008) and BaSTI isochrones, we use luminosities determined in the way presented by Meneses-Goytia et al. (2013b), who use the metal-dependent bolometric corrections of Alonso et al. (1996, 1999).

3.4 Results

3.4.1 Spectral energy distributions

We show SEDs of the XMSa form of our SSP models at different ages and metallicities in Figure 3.4. The spectra change as a function of both age and metallicity. This plot shows the well known age-metallicity degeneracy, i.e. the metal-poor models in the bottom panel have similar shapes as the younger models in the upper panel. With the higher resolution of the XSL data, we can analyze the line behavior in detail. We show a sequence of SEDs at solar metallicity as a function of age in more detail in Figure 3.5. The Balmer series becomes weaker as the age increases. Metal lines such as the Ca line at 3933 \AA , the Ca triplet around 8600 \AA , and Mg 5170 show strong evolution especially at younger ages ($t \leq 5 \text{ Gyr}$).

In Figure 3.6, we show how spectral lines evolve at 5 Gyr as a function of metallicity for the XMSa model. Fe lines such as those at $4383, 4405, 4415$, and 4668 are clearly stronger with increasing metallicity. Similar behavior is found for Mg 5170 . Metal-rich models have stronger metal-line strengths. Ca lines show a strong dependence with metallicity.

Since SSP models from different authors may have variety of input ingredients, (i.e., stellar evolution models or isochrones, stellar libraries and IMFs), it is interesting to compare their predictions. We take literature models from Maraston (2005); Le Borgne et al. (2004); Vazdekis et al. (2012) and Conroy & van Dokkum (2012a) for the spectral comparison. In Figures 3.7 to 3.10, we show XMSa versus the literature SEDs assuming a Salpeter IMF for all models. Figures 3.7 and 3.9 show the overall shape for 10 Gyr and 3 Gyr SSP in XMSa at solar metallicity, respectively. We note that because the lack of cool stars around solar metallicity, our model for 10 Gyr is bluer compared with other models. Models from different authors for the same age, metallicity and IMF show considerable differences especially at red wavelengths ($\lambda \geq 6500 \text{ \AA}$). Similar trends are found for 3 Gyr XMSa models. XMSa is closer to the models by Maraston (2005) for

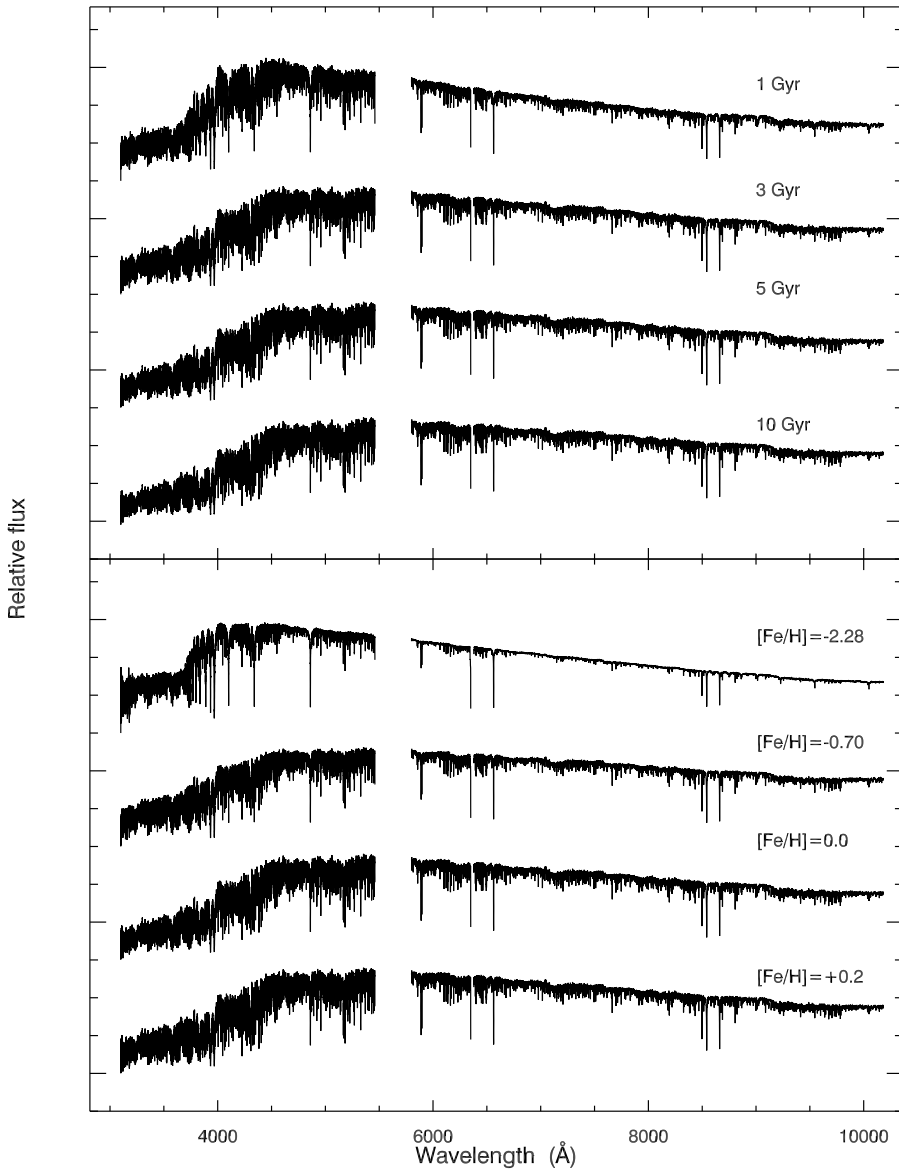


Figure 3.4: SSP spectra of the XMSa model (Marigo isochrones + Salpeter IMF). Upper panel: solar metallicity models at different ages. Bottom panel: 5 Gyr XMSa models at different metallicities.

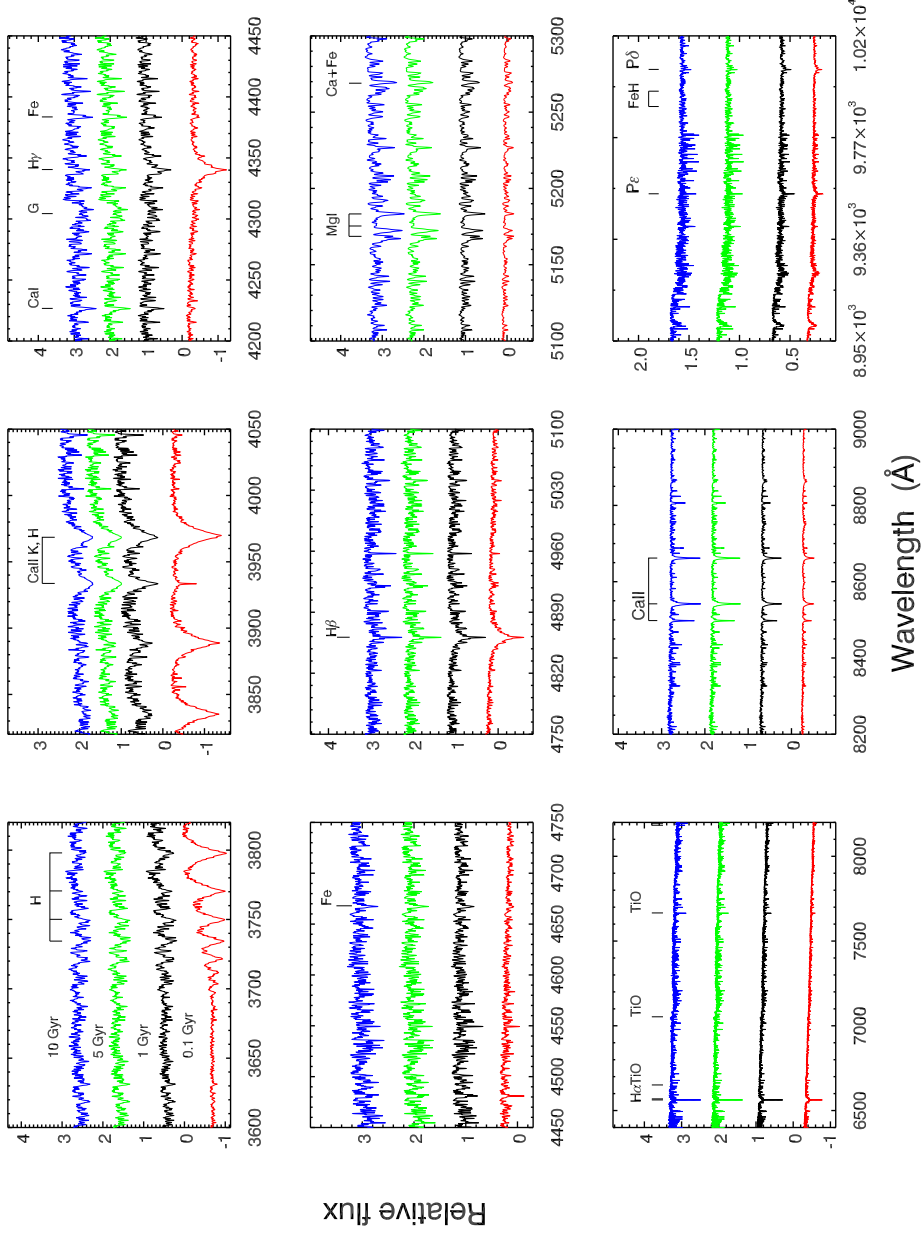


Figure 3.5: Detailed evolution of selected spectral lines as a function of age in the XMSa models at solar metallicity. Models are normalized at 5000 Å and shifted for clarity.

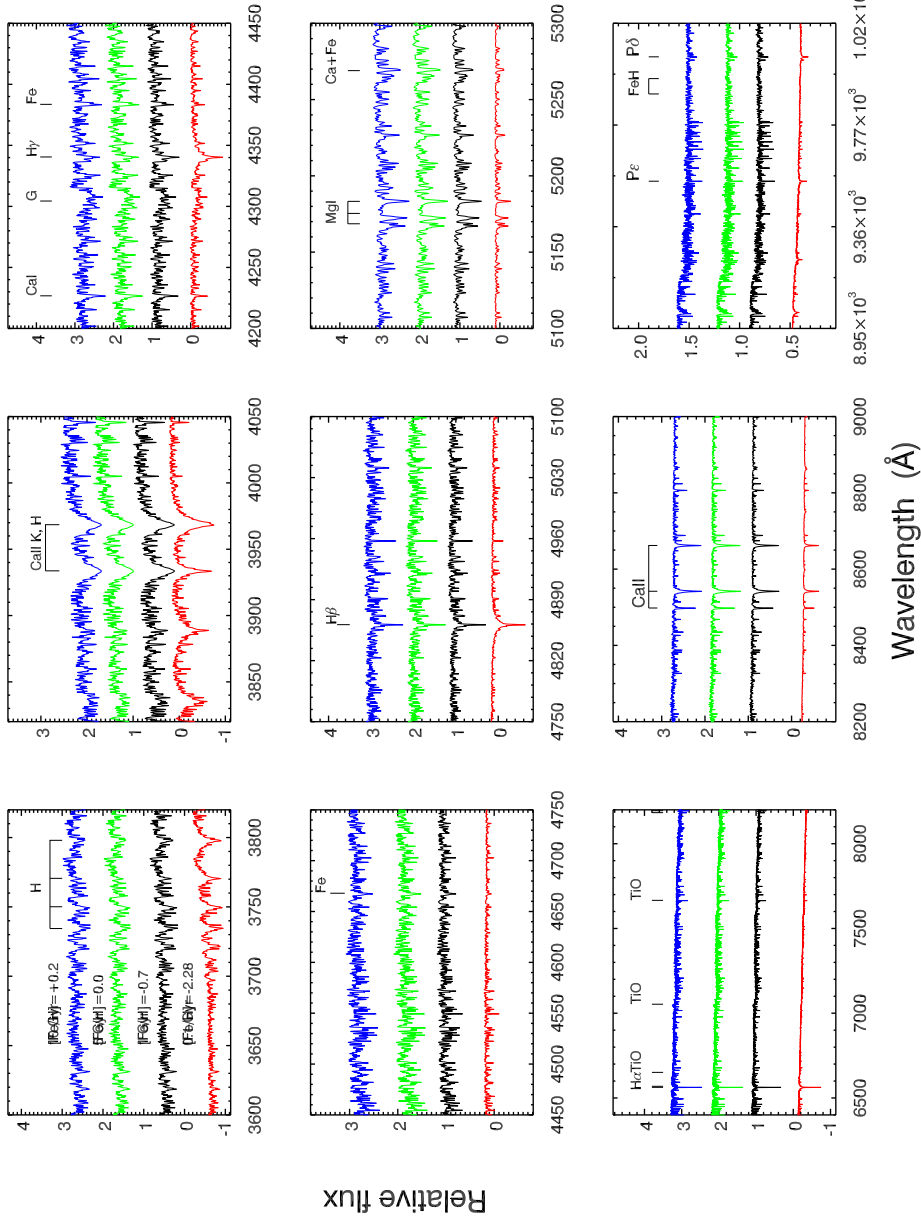


Figure 3.6: Detailed evolution of selected spectral lines as a function of metallicity in the XMSa models at 5 Gyr. Models are normalized at 5000 Å and shifted for clarity.

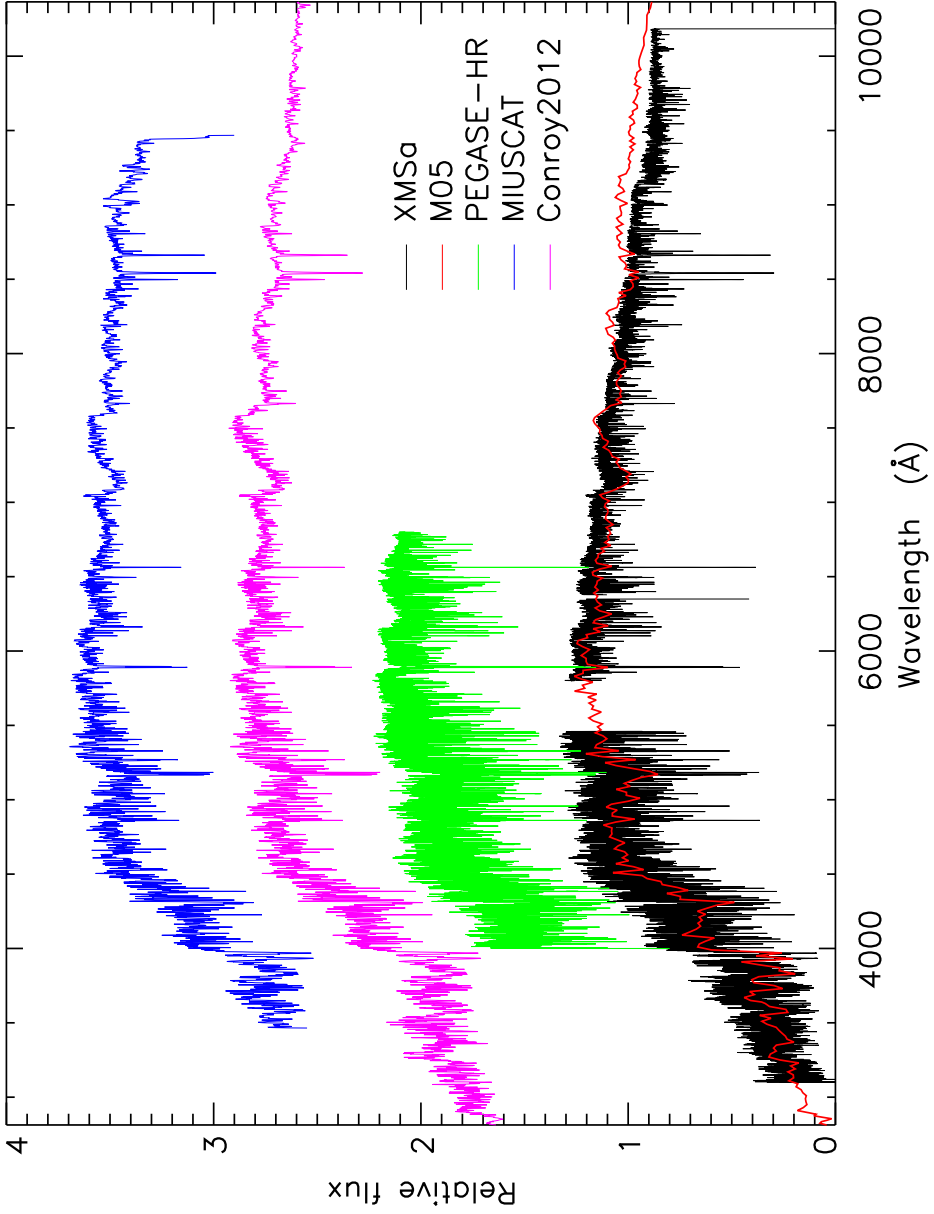


Figure 3.7: XMSa models at 10 Gyr and solar metallicity compared with literature models at the same age and metallicity: Maraston (2005) (M05, red), Le Borgne et al. (2004) (PEGASE-HR, green), Vazdekis et al. (2012) (MIUSCAT, blue) and Conroy & van Dokkum (2012a) (Conroy2012, magenta). All model spectra are normalized at 5000 Å and shifted for clarity.

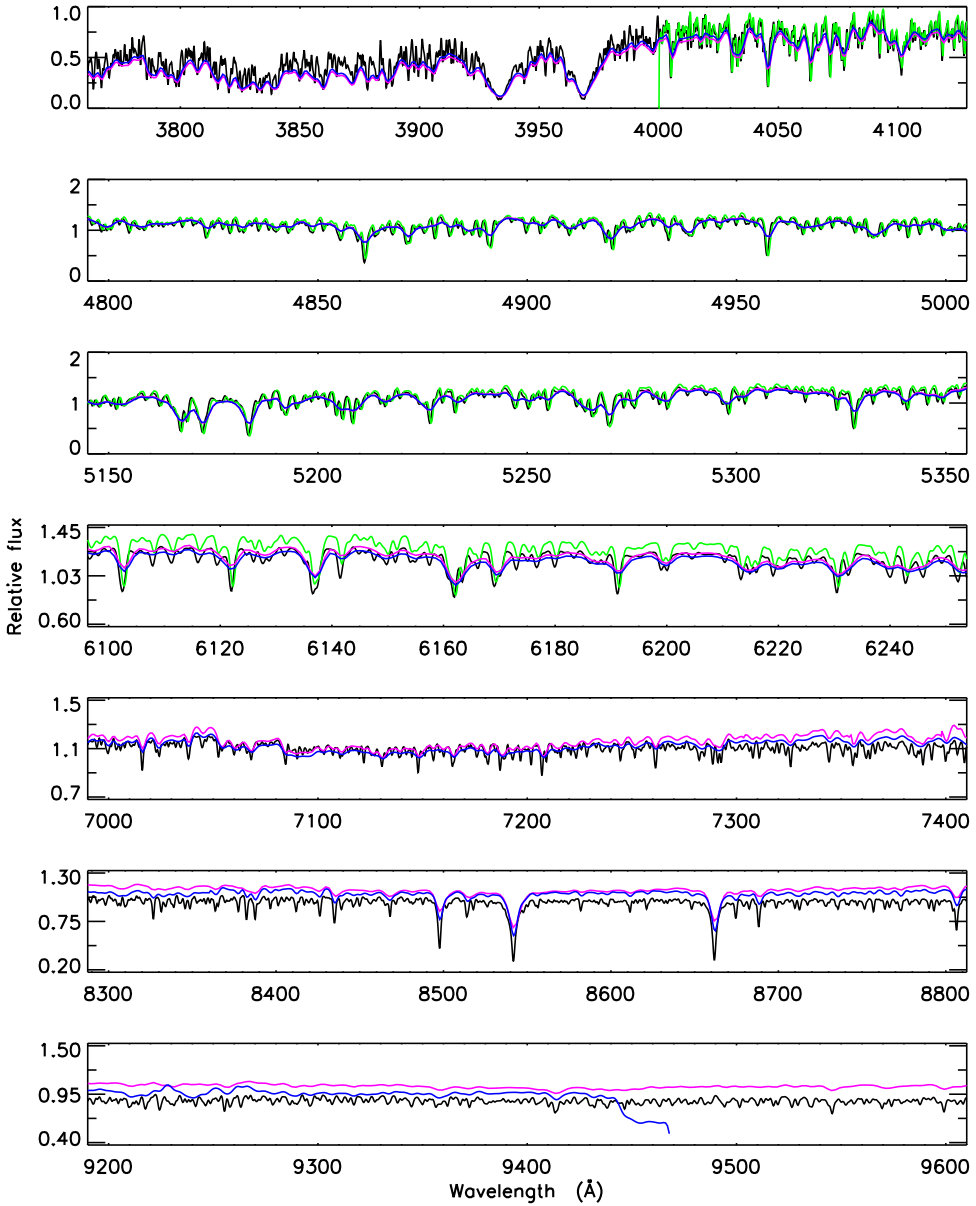


Figure 3.8: Detailed spectral line comparison of the 10 Gyr, solar-metallicity XMSa model and the literature models shown in Figure 3.7. Line colors are the same as in Figure 3.7.

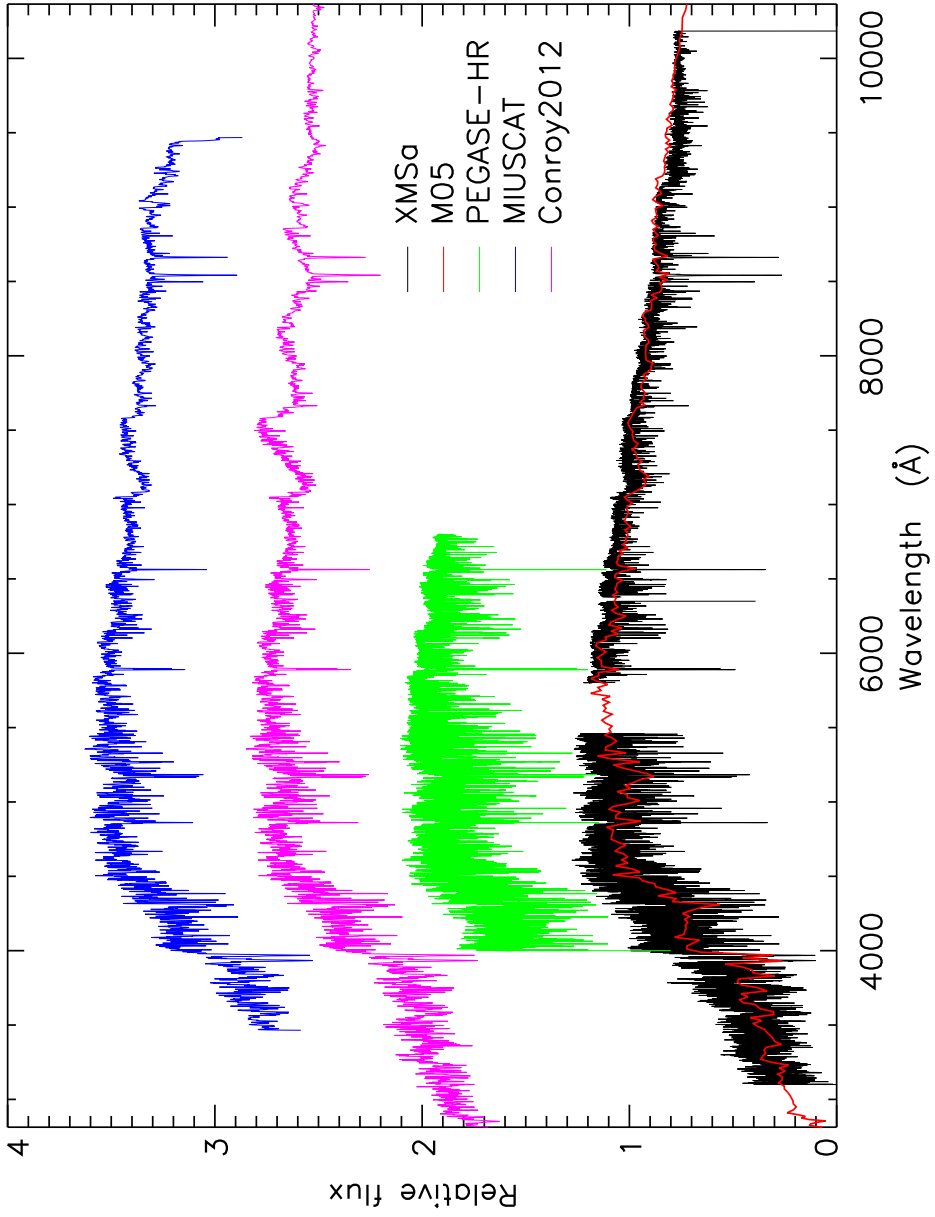


Figure 3.9: As in Figure 3.7, for 3 Gyr old, solar-metallicity models.

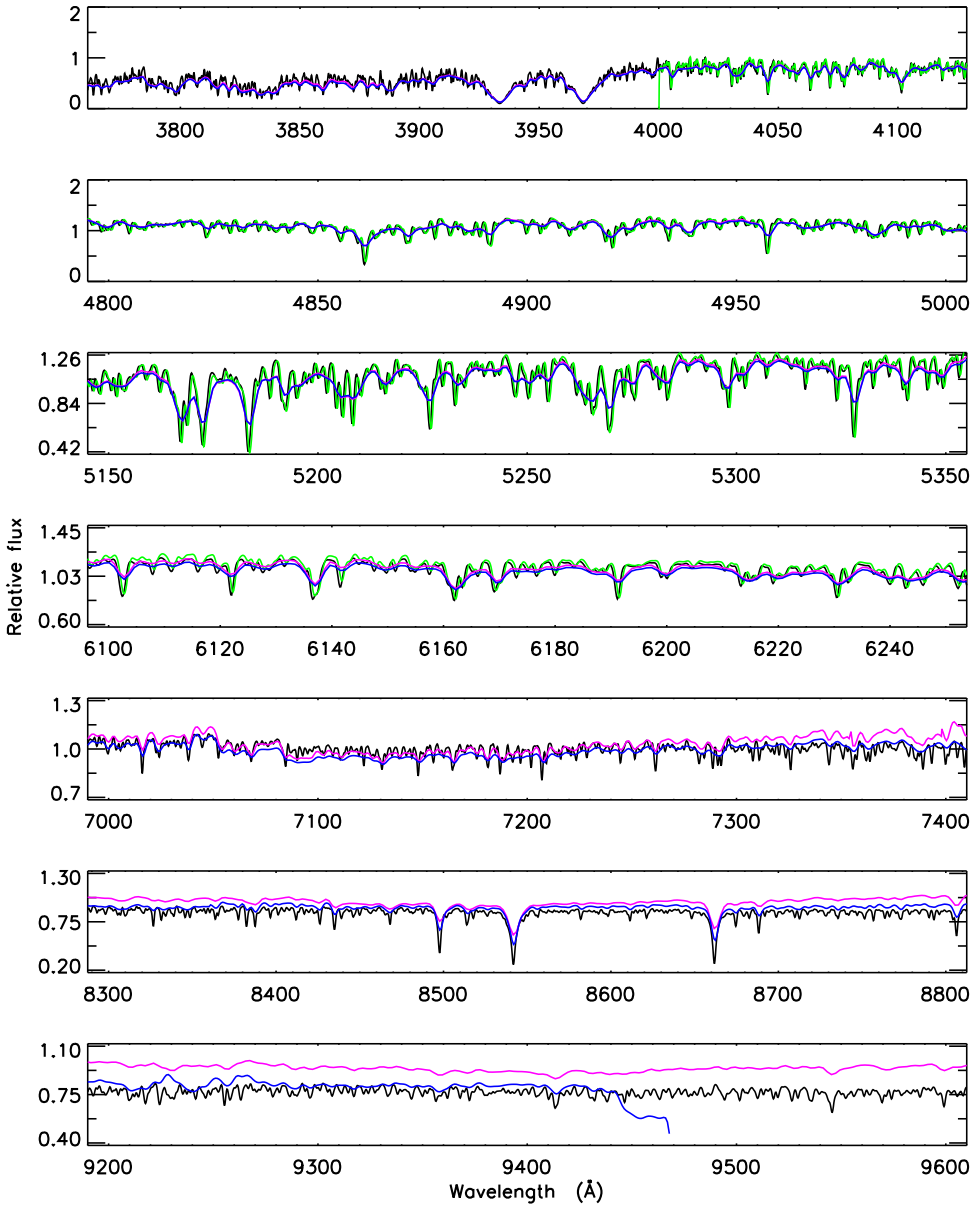


Figure 3.10: As in Figure 3.9, for 3 Gyr old, solar-metallicity models. Line colors are the same as in Figure 3.9.

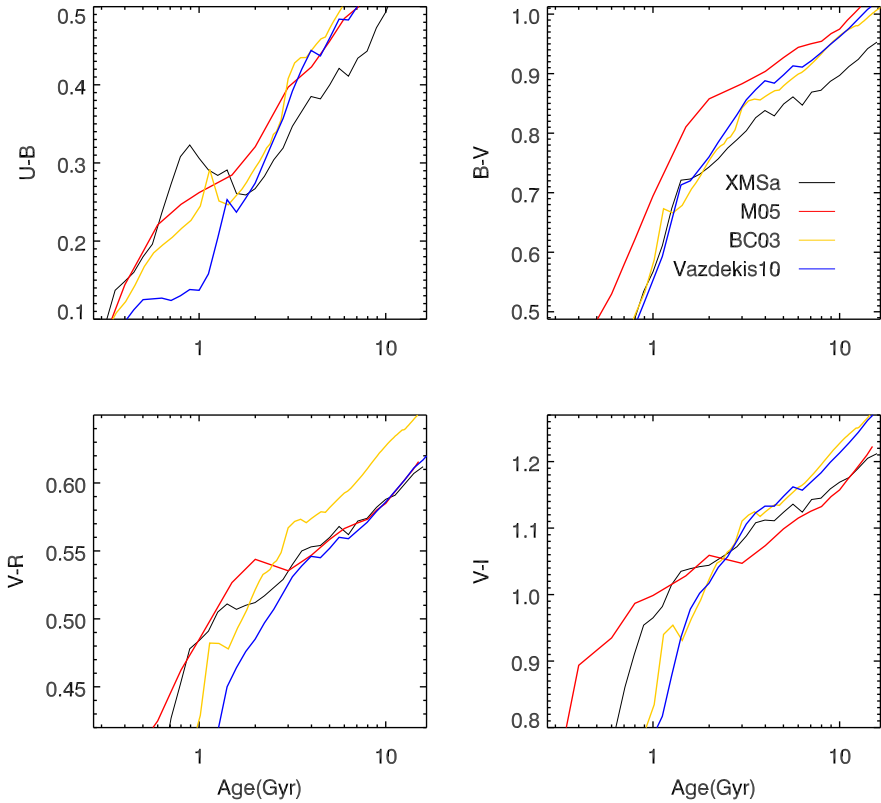


Figure 3.11: Integrated broad band colors of the XMSa model as a function of age at solar metallicity ($[\text{Fe}/\text{H}] = 0.0$), compared with SSP models of Maraston (2005) (M05, red), Bruzual & Charlot (2003) (BC03, orange) and Vazdekis et al. (2010) (Vazdekis10, blue).

solar metallicity at 3 Gyr. Detailed spectral comparisons are shown in Figures 3.8 and 3.10, where Le Borgne et al. (2004) models are degraded to the same resolution as our XSL models. At bluer wavelengths, our model (XMSa) agrees well with the similar resolution model of PEGASE-HR (Le Borgne et al. 2004), especially below 5350 \AA . In the red, our model has a higher resolution and our model spectra match literature model spectra (i.e. Vazdekis et al. 2012; Conroy & van Dokkum 2012a) even on a line-by-line basis. This will allow us to investigate faint lines in the red to reveal the ages and abundances of small stellar systems, e.g., galaxies or clusters with small velocity dispersions.

3.4.2 Broad-band colors

We calculate the broad-band colors from the SEDs on the Johnson–Cousins system. To test our results, we compare our results with literature colors and data from Magellanic Cloud GCs.

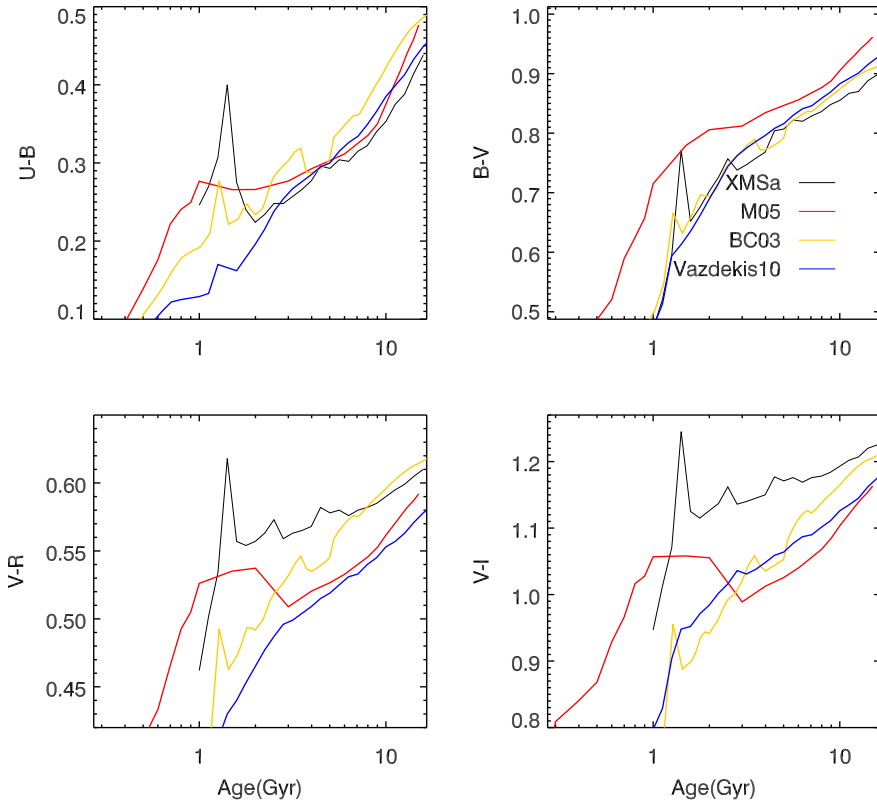


Figure 3.12: Integrated broad band color for XMSa as a function of age at metallicity $[\text{Fe}/\text{H}] = -0.4$, compared with SSP models by Maraston (2005) (M05, red), Bruzual & Charlot (2003) (BC03, orange) and Vazdekis et al. (2010) (Vazdekis10, blue).

Figure 3.11 shows the evolution of $(U - B)$, $(B - V)$, $(V - R)$ and $(V - I)$ at solar metallicity of our XMSa models compared with colors from other models, i.e. Bruzual & Charlot (2003); Maraston (2005) and Vazdekis et al. (2010). Our XMSa models are bluer than other models in $(U - B)$ and $(B - V)$. This is due to the fact that some important giants are lacking at the metallicity, which have a stronger contribution to the resulting SSP SEDs in the colors. Missing those important giants at solar metallicity affects not only blue colors but also red colors, because the spectral interpolator searches for the closest stars for a given point along the isochrone. When those stars are not available in the parameter space, the interpolator will (likely) take cooler giants to fill the gap along the isochrone. When the cooler giants are used with the same weight as the warmer giants (missing stars) in the integrated light, the SED color will show more cool giant features. In the blue, the spectrum is dominated by main sequence stars, so therefore the blue colours are too blue. In the red, the situation is opposite.

Color evolution at lower metallicity of $[\text{Fe}/\text{H}] = -0.4$ is presented in Figure 3.12.

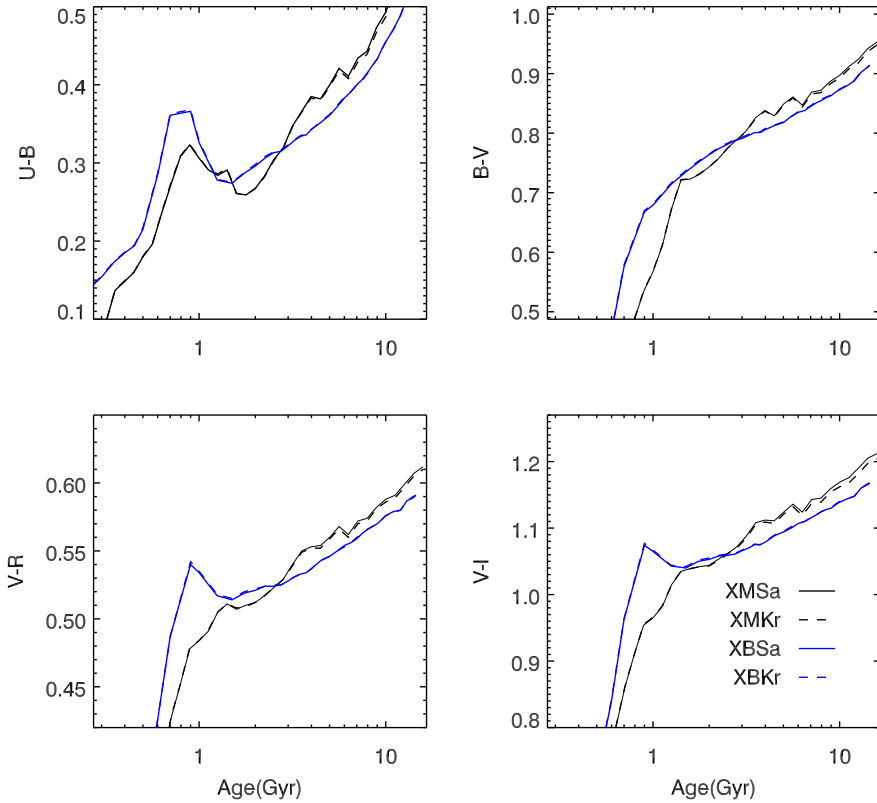


Figure 3.13: Evolution of integrated broad band color for models XMSa, XMKr, XBSa and XBKr at solar metallicity.

XSL’s parameter coverage is best at this metallicity, and we can therefore make a fairer comparison to literature models. The sharp feature from the asymptotic-giant-branch (AGB) phase change around one to two Gyr (Renzini & Voli 1981) is clearly seen in all of the four colors. ($U-B$) and ($B-V$) colors are consistent with other models (e.g. Bruzual & Charlot 2003; Vazdekis et al. 2010) after ~ 2 Gyr. The ($V-R$) and ($V-I$) colors show the biggest differences: our models are in general redder than the others, especially at young ages, during the phase influenced by the AGB stars. This is due to the current (and temporary) limitations of the XSL parameter space, which mainly contains giants and supergiants, as shown in Figure 3.2.

In Figure 3.13 we show the time evolution of colors for our four models at solar metallicity. Here we can trace the color difference caused by the input stellar evolutionary tracks (i.e. isochrones) directly. We see the AGB bump shifts between the models with different input isochrones. Furthermore, the overall color difference between XMSa and XBSa varies by 0.05–0.1 mag. It is understandable that the color difference given by different authors in Figure 3.11 may be partly due to the input isochrones.

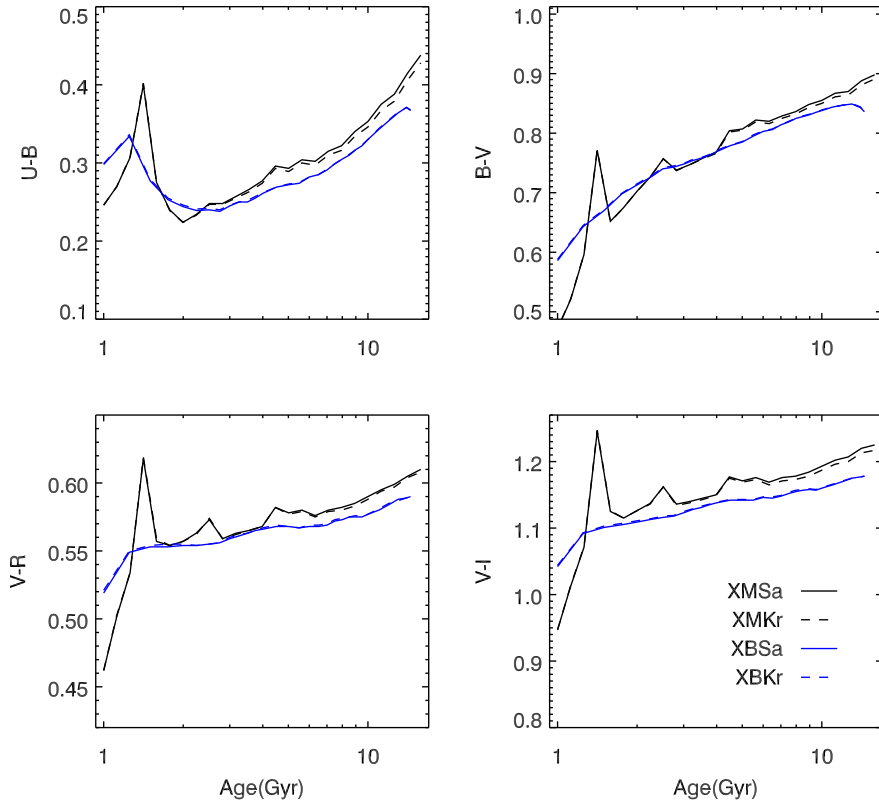


Figure 3.14: Evolution of integrated broad band color for models XMSa, XMKr, XBSa and XBKr at metallicity $[\text{Fe}/\text{H}] = -0.4$.

For example, model SEDs by Maraston (2005) employ the tracks and isochrones from Cassisi et al. (1997a,b) and Cassisi et al. (2000) while Vazdekis et al. (2010) employ the Padova 2000 isochrones (Girardi et al. 2000); our XMSa models use isochrones by Marigo et al. (2008), which are the improved version of Girardi's.

Color evolution at $[\text{Fe}/\text{H}] = -0.4$ for our four models is shown in Figure 3.14. Models based on BaSTI (Pietrinferni et al. 2004) isochrones XBSa and XBKr are in general bluer than their counterparts XMSa and XMKr. Furthermore, the RGB and AGB tracks clearly have different prescriptions from these two set of isochrones as seen in the color evolution of $(B - V)$, $(V - R)$ and $(V - I)$.

In Figure 3.15, we show the color-color diagrams of XMSa at three metallicities ($[\text{Fe}/\text{H}] = -0.7, -0.4$ and 0.0) for young ages ($t \leq 2.5$ Gyr), compared with Magellanic Cloud GC data, which are good candidates in the age range relevant to the TP-AGB (Maraston 2005). We collect the $(U - B)$ and $(B - V)$ colors from Bica et al. (1996); and the $(V - R)$ and $(V - I)$ colors from Goudfrooij et al. (2006) which matches the apertures sizes given by Bica et al. (1996). We carefully select the data with $[\text{Fe}/\text{H}] > -1.0$

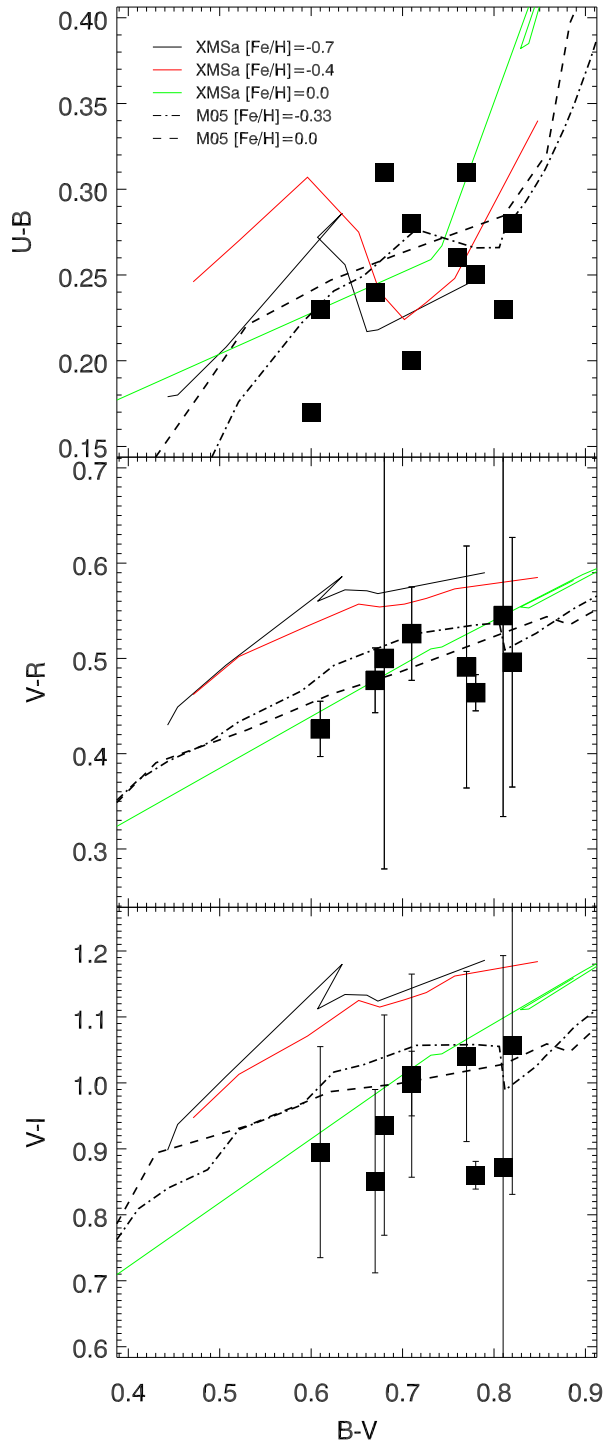


Figure 3.15: Color-color plots of XMSa below 2.5 Gyr with data of Magellanic Cloud GCs (filled squares). Magellanic Cloud data are selected to have $[\text{Fe}/\text{H}] > -1.0$ and intermediate ages around 1–3 Gyr according to Asa'd & Hanson (2012).

to match our model capabilities. The colors of data are well reproduced by our model, with only two outliers in the $(V - I)$ panel. To further check our models' behavior, we put the models by Maraston (2005) in the same plot (dashed and dash-dotted lines).

3.4.3 Line-strength indices

We measure absorption-line strength indices directly from our SSP SEDs, keeping the original resolution of $R = 7000$ using our IDL routine `cal_index`. The standard Lick/IDS index definitions, (Worthey et al. 1994; Trager et al. 1998) and CaT^* (Cenarro et al. 2001) are adopted. A new gravity-sensitive index $\text{TiO}+\text{CaH}$ (discussed in Chapter 4) is also considered here. We show the evolution of the line strengths of H_β , $H_{\gamma A}$, $H_{\gamma F}$, $H_{\delta A}$, $H_{\delta F}$, CN1, CN2, Fe4383, Fe4668, G4300, Mgb, Fe5335, TiO1, TiO2, CaT^* and $\text{TiO}+\text{CaH}$ in Figure 3.16 for the XMSa and XMKr models at $[\text{Fe}/\text{H}] = 0$ and -0.4 . This figure shows that the line strength differences caused by IMF changes in general are smaller than those caused by metallicity changes. Some indices, such as Fe4668, Fe5335, TiO1, TiO2 and CaT^* , show a bump around 1 Gyr, which is likely to be influenced by the AGB phase. In addition, index strengths as a function of metallicity show that Balmer lines and metal lines evolve in a different direction with metallicity (e.g. Tinsley & Gunn 1976; Rabin & Moore 1980; Rabin 1982; Worthey et al. 1994; Buzzoni 1989; Vazdekis et al. 2010). Gravity sensitive indices (potential IMF indicators) such as TiO1, TiO2, $\text{TiO}+\text{CaH}$, and CaT^* show more complicated evolution as a function of metallicity and age. If one wishes to extract IMF information from the SSP indices, careful separation of age and metallicity (and probably also individual element abundances: Conroy & van Dokkum 2012b, Spiniello et al. 2013, in prep.) is necessary and crucial. We leave detailed discussion about IMF influences on index strengths to Chapter 4.

Interpretation of integrated spectra based on absorption line indices varies with the applied stellar population models (e.g. Trager et al. 2008; Vazdekis et al. 2010). In order to check this effect, we degrade our models to the same resolution as MILES and measure the indices on the lower resolution models. We show the comparison in Figure 3.17. In general, our models agree with the model predictions from MIUSCAT with some variations. The variation in Balmer lines is smaller than in iron lines. This may be due to the different atmospheric parameter space coverage of T_{eff} , $\log g$, and $[\text{Fe}/\text{H}]$, where metal lines are more sensitive to the metallicity $[\text{Fe}/\text{H}]$ space.

Given by the relatively high resolution of our models, we can investigate line indices strength in remarkable detail. New indices which separate lines that are contaminated by adjacent lines at low resolution can be defined and analyzed in the future for galaxies with small velocity dispersion broadening.

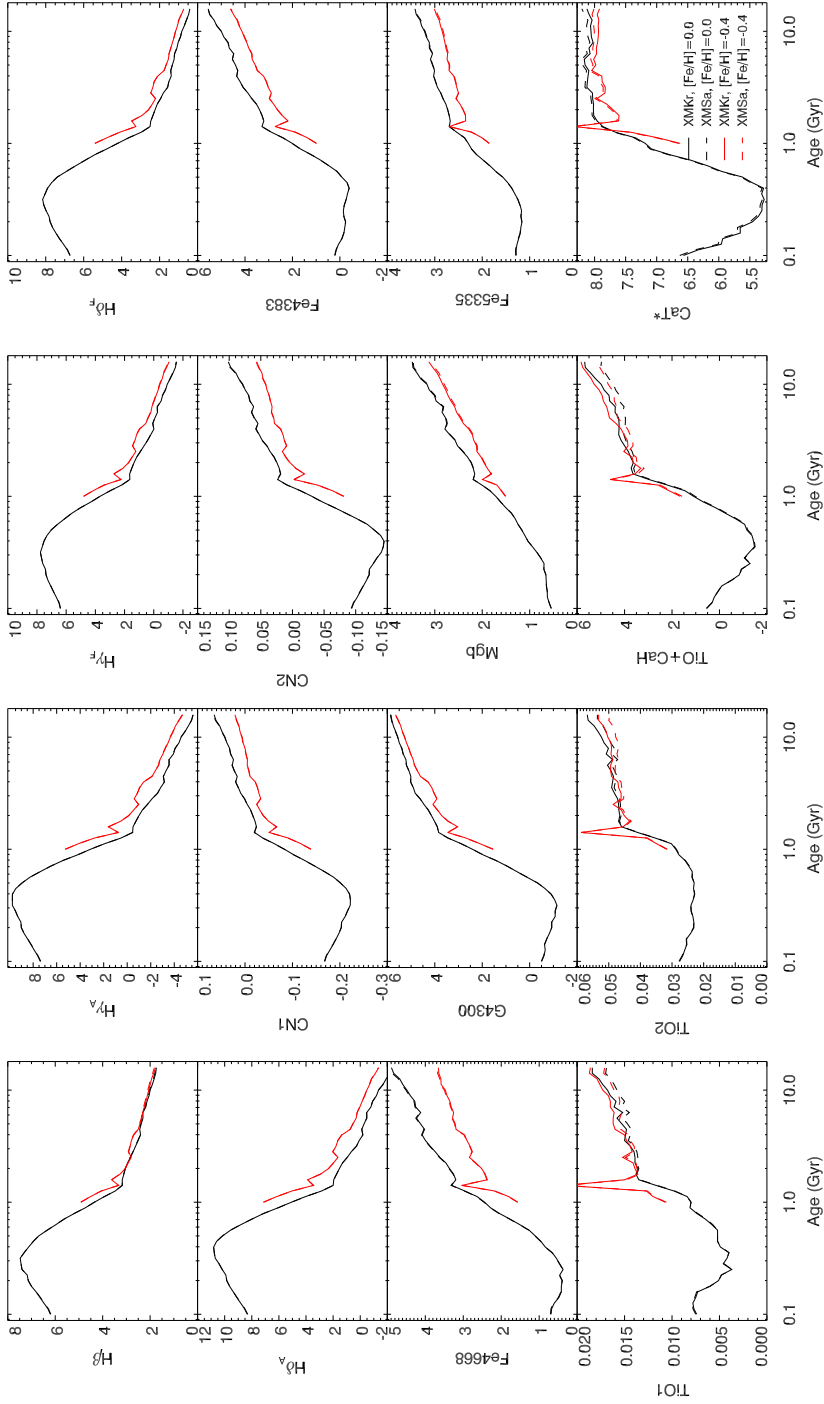


Figure 3.16: Line-strength evolution of several Lick indices, and the CaT^* and $\text{TiO}+\text{CaH}$ indices at solar metallicity (black) and $[\text{Fe}/\text{H}] = -0.4$ (red). XMSa (dashed lines) and XMKr (solid lines) models at resolution of $R = 7000$ are presented. Due to the lack of data in the metal poor range, no models with ages $t < 1$ Gyr are shown at $[\text{Fe}/\text{H}] = -0.4$.

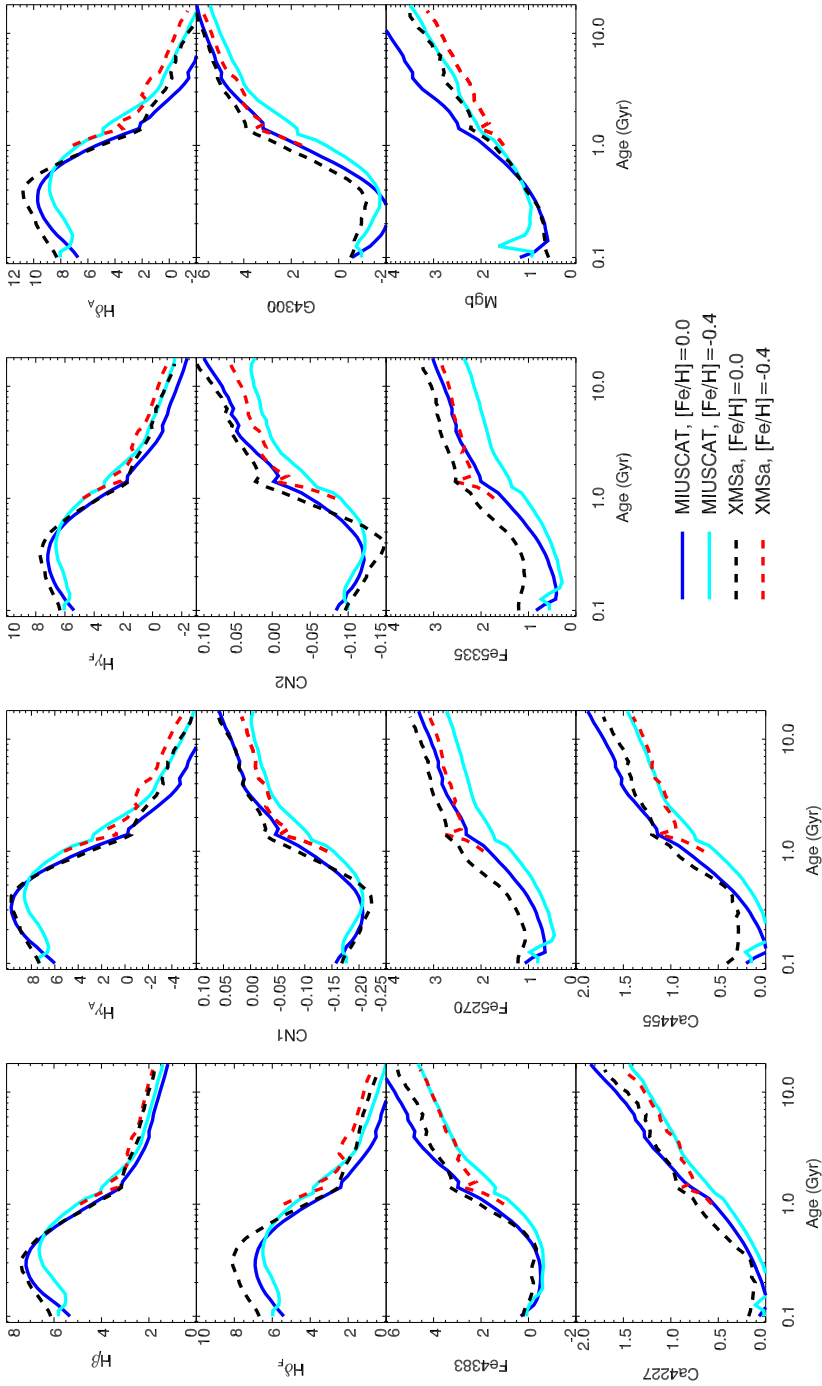


Figure 3.17: Line-strength evolution of several Lick indices at solar metallicity (black) and $[Fe/H] = -0.4$ (red) compared with MIUSCAT models. Spectra of XMSa (dashed lines) are degraded to the same resolution as MIUSCAT (solid lines).

3.5 IMF effects on the SEDs

Although the influence of IMF shape on the SSP SEDs is not as drastic as the impact of the input isochrones, spectral library, or the metallicities, they show a non-negligible effect on the line strengths (e.g. Vazdekis et al. 2003, 2010; Conroy & van Dokkum 2012a). Here we present the variation of model SEDs with changing IMF shape, between Salpeter (1955) and Kroupa (2001). Here we consider only two representative IMFs to illustrate the influence of the dwarf to giant ratio on the spectral evolution. We refer readers to Vazdekis et al. (2010) for a detailed discussion on impact of IMF shape and slope on line strengths.

Figure 3.18 shows the ratio of model fluxes between Salpeter (1955) and Kroupa (2001) IMFs at $[\text{Fe}/\text{H}] = -0.4$ and 10 Gyr, based on the Marigo et al. (2008) isochrones. We see that, besides the traditional Lick indices TiO1 and TiO2, there are a number of other gravity-sensitive features. It is worth noting that TiO and CaH molecular features are promising IMF indicators (e.g. features around 6000–7500 Å), since they are broad and are almost not affected by low resolution. However, the possible difficulty when investigating those features may arise from the telluric contamination in ground-based observations, and one has to be very careful when dealing with those features. Na and Ca features, on the other hand, are also possible candidate for IMF slope indicators, as shown by the negative and positive ratio features, respectively. A number of studies have noticed that the Na features, especially NaI 8200, are sensitive to the dwarf-to-giant ratio in old populations (e.g., van Dokkum & Conroy 2010; Spiniello et al. 2012; Ferreras et al. 2013). The gravity-dependent Ca features, as shown by the work of Vazdekis et al. (2003); Cenarro et al. (2003); Falcón-Barroso et al. (2003), can also be used to trace the shape of the IMF. However, Na features may not be straightforward IMF indicators. Work by Spiniello et al. (2012) shows that Na lines are likely to be contaminated by TiO lines or interstellar medium (ISM) and are influenced by the $[\text{Na}/\text{Fe}]$ elemental abundance ratio.

We have presented the SEDs based on the Marigo isochrones for two different sets of IMFs to show the possible application on determining the dwarf-to-giant ratio in old stellar populations. The models XBSa and XBKr are not suitable for the IMF investigation yet, because of the higher cut-off mass in the isochrones. To be able to constrain the IMF shape or slope in a population, low mass stars ($0.1 \leq m \leq 0.5 M_{\odot}$) are required in both the isochrones and the input spectral library.

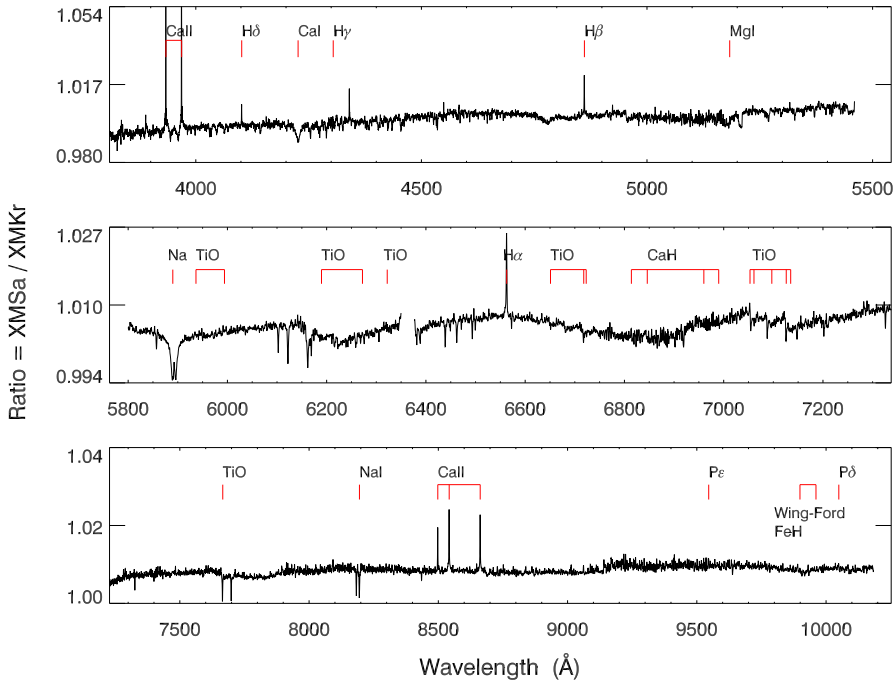


Figure 3.18: Flux ratio between models with Salpeter (1955) and Kroupa (2001) IMFs at $[\text{Fe}/\text{H}] = -0.4$ and an age of 10 Gyr, with some absorption features labeled. The ratio spectrum is normalized at 5000 Å for display purpose.

3.6 Fitting Globular Cluster spectra

We now compare our model SEDs with globular clusters (GCs), which are excellent calibrators for stellar population models, as they are (nearly) SSPs and their ages and metallicities are known from their resolved stellar populations. The GC data are selected from the library of Schiavon et al. (2005). These authors obtained integrated spectra with a long-slit spectrograph at a resolution of $\text{FWHM} = 3.1 \text{ \AA}$. The spectra cover the range $\lambda\lambda 3350 - 6430 \text{ \AA}$, with high signal-to-noise ratio ($S/N \sim 50-240$). We refer readers to Schiavon et al. (2005) for details of the observations and data reduction.

Three GCs are considered here: NGC 2808, NGC 6304 and NGC 6553. We perform full spectrum fitting using pPXF taking XBK models one by one as templates, the age and metallicity of a GC is obtained by the fit which has the single template with the lowest χ^2 .

We perform the fit on flux-calibrated spectra over the wavelength range 3360–5450 Å. Figures 3.19, 3.21, and 3.23 show our SSP analysis on NGC 2808, NGC 6304 and NGC 6553, respectively. Our derived ages and metallicities are presented in Table 3.2, and

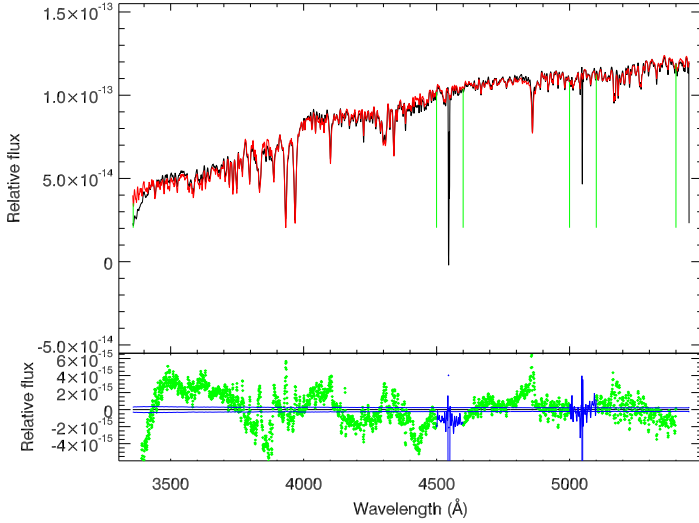


Figure 3.19: Full spectral fitting of NGC 2808. The top panel shows the spectrum of NGC 2808 in black and the best fit in red by our model XBKt. The bottom panel shows the residual between the GC spectrum and the best fit in green, where the blue regions indicate the bad pixels, which are also seen in the top panel; the continuous blue lines mark the $1\text{-}\sigma$ deviation as expected by the input S/N.

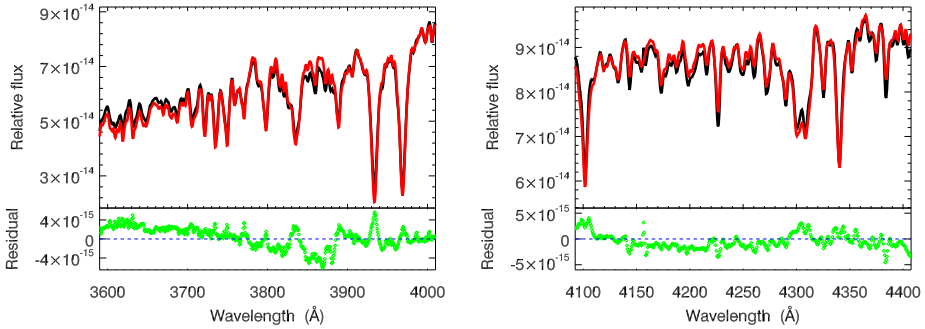


Figure 3.20: Full spectral fitting of NGC 2808, zoomed in two wavelength ranges.

Table 3.2: SSP fitting for GCs

GC name	t_{SSP} (Gyr)	$[\text{Fe}/\text{H}]_{SSP}$	t_{litter} (Gyr)	$[\text{Fe}/\text{H}]_{litter1}$	$[\text{Fe}/\text{H}]_{litter2}$
NGC 2808	10.00	-1.3	10.0 ± 2.2^f	-1.29^a	-1.18 ± 0.04^e
NGC 6304	13.00	-0.4	13.5 ± 2.8^b	-0.66^a	-0.37 ± 0.07^e
NGC 6553	13.00	-0.3	13.0 ± 2.5^d	-0.20^a	-0.16 ± 0.06^e

References: (a) Schiavon et al. (2005); (b) Marín-Franch et al. (2009); (c) Momany et al. (2003); (d) Beaulieu et al. (2001); (e) Carretta et al. (2009); (f) De Angeli et al. (2005).

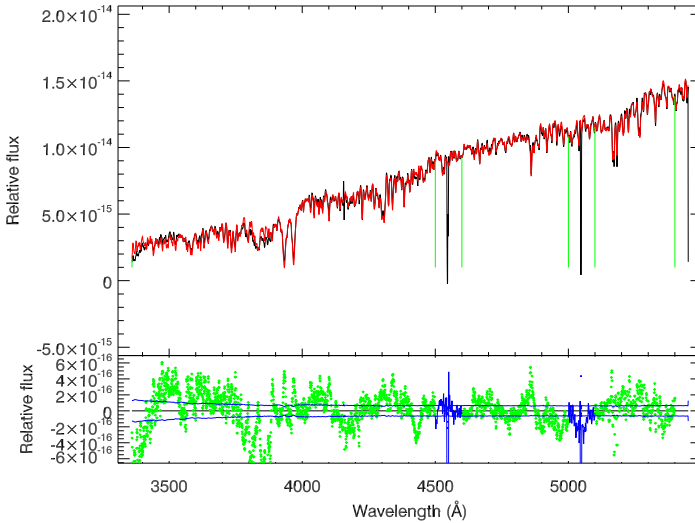


Figure 3.21: Same as Figure 3.19 but for NGC 6304.

they are in reasonable agreement with literature CMD-based estimations. We show two zoomed-in regions to show the fits in detail in Figures 3.20, 3.22, and 3.24 for NGC 2808, NGC 6304, and NGC 6553, respectively. The model reproduces the main stellar absorption features of each GCs fairly well, except for the CN features at ~ 3860 Å and the Ca H and K lines. The mismatch of the CN features was reported by e.g., Burstein et al. (1984); Rose & Tripicco (1986); Trager (2004); Cenarro et al. (2007); Vazdekis et al. (2010). CN-strong stars are used to correct for the model predictions by Schiavon et al. (2002a,b), α -enhanced stellar evolutionary isochrones and stellar spectra have been suggested (Vazdekis et al. 2010) to give a better fit to the strong CN features in the GC spectra.

On the other hand, the Ca H and K features are over-estimated by the models,

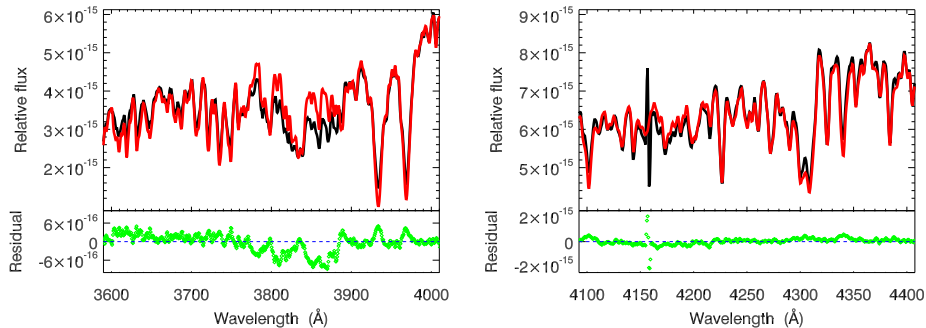


Figure 3.22: Full spectral fitting of NGC 6304, zoomed in two wavelength ranges.

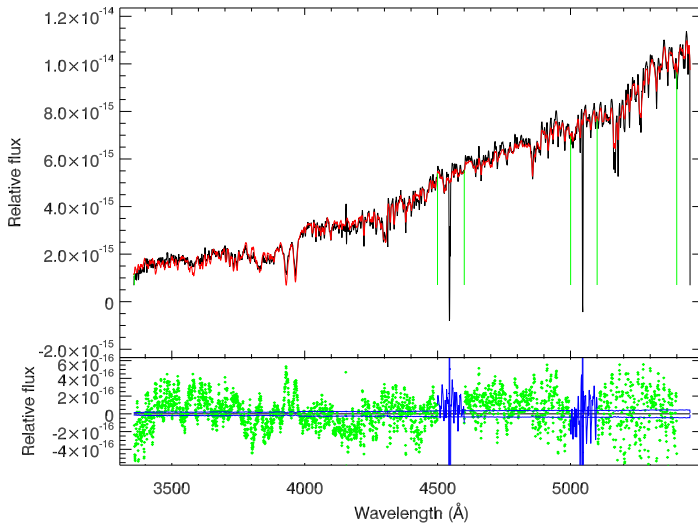


Figure 3.23: Same as *Figure 3.19* but for NGC 6553.

which may also require non-solar abundance patterns in the models.

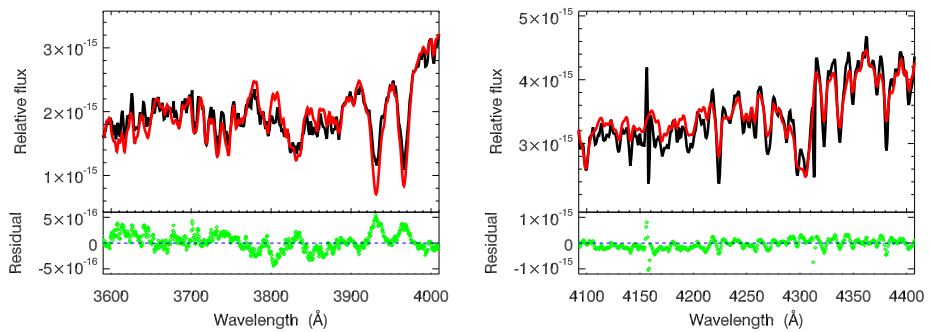


Figure 3.24: Full spectral fitting of NGC 6553, zoomed in two wavelength ranges.

3.7 Summary

We have presented new SSP SEDs based on the first year sample of the X-shooter Spectral Library (XSL, Chen et al. 2013a), which covers a wide wavelength range from 3100 to 10200 Å at a resolution of $R = 7000$. The atmospheric parameter coverage of XSL DRI allows us to construct SSP SEDs with metallicities from $[\text{Fe}/\text{H}] = -0.7$ to $[\text{Fe}/\text{H}] = 0.2$ and ages from 0.1 to 15.8 Gyr, where SEDs with ages below 1 Gyr are only available for $0.0 \leq [\text{Fe}/\text{H}] < +0.2$. Two set of isochrones, Marigo et al. (2008) and BaSTI (Pietrinferni et al. 2004), and two IMFs Kroupa (2001) and Salpeter (1955) are available in the new models.

Our models are constructed from a single input spectral library, which reduces the possible uncertainties from either a spliced spectral wavelength range or spliced spectral libraries. We have shown that the SSP SEDs reproduce well the observed spectra of Galactic GCs and colors of AGB-dominated Magellanic Cloud GCs. Because of the large collection of AGB stars in XSL, our models are an excellent tool for studying the evolutionary history of the Magellanic Cloud GCs (Maraston 2005). The intermediate resolution of our models make them well suited for the analysis of stellar populations of small stellar systems.

Acknowledgements

Appendix 3.A Stellar atmospheric parameters of XSL

We present the adopted atmospheric parameters for 218 XSL stars in Table 3.3. In this table, the first column is the star name; the second column is the spectral type from the SIMBAD database.

Table 3.3: *Adopted atmospheric parameters for 218 XSL stars from the first-year sample*

Star name	Sp. type	T_{eff} (K)	$\log g$	$[\text{Fe}/\text{H}]$
HD194453	A0	10477	3.77	0.02
HD164257	A0	9794	3.34	0.50
HD204041	A1IV	8998	4.33	-0.45
HD72968	A1spe...	9492	3.65	0.57
HD174240	A1V	9284	3.71	-0.52
HD2857	A2	7931	2.56	-1.52
HD193281	A2III	8717	3.97	-0.42
HD190073	A2IVe	9000	2.53	-2.13
HD28978	A2Vs	8997	3.51	-0.33
HD163346	A3	7502	4.05	0.11
HD174966	A3	7968	4.13	0.08
HD38237	A3	8284	4.13	-0.04
HD18769	A3m	8738	4.37	0.13

Table 3.3 – Continued

Star name	Sp. type	T_{eff} (K)	$\log g$	[Fe/H]
HD19445	A4p	5783	4.14	-1.91
HD172230	A5	7689	3.55	0.49
HD34816	B0.5IV	28963	3.87	-0.17
HD96446	B2IIIp	22193	3.71	0.03
HD224926	B7III-IV	14816	3.78	0.26
HD34797	B8/B9IV:	12941	4.34	0.54
HD196426	B8IIIp	13628	3.92	0.25
HD358	B8IVmnp...	13932	4.16	0.32
HD128801	B9	8893	2.72	-1.88
HD163641	B9III	12154	3.94	0.23
HD175640	B9III	12127	3.92	0.30
HD27295	B9IV	11978	4.07	0.11
HD147550	B9V	8754	2.85	-0.43
HD16031	F0V	6044	4.06	-1.88
HD29391	F0V	7316	4.00	-0.04
HD284248	F2	6061	4.10	-1.83
HD167278	F2	6607	4.31	-0.22
HD205202	F2	6654	4.11	-0.56
HD170756	F4Ibvp	5530	2.86	-0.80
G029-023	F5	6053	4.05	-1.85
HD160365	F6III	6222	3.06	-0.07
HD61064	F6III	6490	3.16	0.15
HD196892	F6V	5935	3.94	-0.95
HD4813	F7IV-V	6151	4.32	-0.17
G188-22	F8	5996	4.07	-1.34
HD19019	F8	6007	4.38	-0.16
G20-15	F8	6019	4.06	-1.58
HD175805	F8	6288	4.20	0.10
HD217877	F8V	5845	4.22	-0.23
HD52298	F8V	6342	4.27	-0.33
HD157089	F9V	5824	4.19	-0.54
HD45282	G0	5171	2.89	-1.51
HD200081	G0	5610	3.33	0.15
G187-40	G0	5799	4.22	-1.35
HD161770	G0	5815	3.84	-1.42
HD188262	G0	4983	2.52	0.07
HD52973	G0Ibv	5599	1.01	0.07
HD216219	G0IIp	5576	3.10	-0.41
HD39587	G0VCH+M	5871	4.43	-0.11
HD345957	G0Vw	5829	3.81	-1.40
HD13043	G2V	5758	4.09	0.00
HD17072	G2w...	5486	2.74	-0.95
G169-28	G3V	5823	4.22	-1.24

Table 3.3 – Continued

Star name	Sp. type	T_{eff} (K)	$\log g$	[Fe/H]
HD8724	G5	4902	2.21	-1.44
HD204155	G5	5722	4.07	-0.65
HD179821	G5Ia	5990	0.18	0.04
HD193896	G5IIIa	5153	2.20	-0.10
HD6229	G5IIIw	5155	2.47	-1.20
HD18907	G5IV	5078	3.49	-0.66
HD44007	G5IV:w...	4961	2.56	-1.49
HD99648	G8Iab	4941	2.32	-0.03
HD83212	G8IIIw...	4643	1.28	-1.45
HD201626	G9p	4960	2.09	-1.63
PHS2008-RGB522	K	4270	1.54	-0.42
PHS2008-RGB533	K	4289	1.39	-0.52
PHS2008-RGB512	K	4197	1.02	-0.90
HD37828	K0	4703	1.84	-1.14
HD173158	K0	5149	0.90	0.02
HD93813	K0/K1III	4388	2.16	-0.10
HD179870	K0IIb	4906	2.23	0.20
HD82734	K0III	4884	2.44	0.36
HD170820	K0III	4955	2.00	0.22
HD33299	K1Ib	4731	1.11	0.11
HD1638	K1III	4297	1.64	-0.61
HD165438	K1IV	4880	3.41	0.06
HD190404	K1V	4933	4.64	-0.57
HD25329	K1V...	5077	4.52	-1.40
HD50877	K2.5Iab	4102	0.43	0.20
HD63302	K2Iab	4308	0.32	0.23
HD37763	K2III	4574	3.19	0.25
HD175545	K2III	4560	2.99	0.16
HD19787	K2III	4834	2.69	0.12
HD31421	K2IIIb	4459	2.29	-0.17
BS4432	K3.5III	3989	1.80	-0.19
HD81797	K3II-III	4139	1.67	0.04
HD65354	K3III	4148	1.42	0.11
HD232078	K3IIp	4241	0.60	-1.27
HD165195	K3p	4566	1.15	-2.07
HD16160	K3V	4757	4.49	-0.16
HD160346	K3V	4868	4.57	0.04
HD52005	K4Iab	4128	0.82	0.17
HD74088	K4III	3996	1.94	-0.27
BS4104	K4III	4089	1.75	-0.17
BS3923	K5III	3781	1.54	0.01
HD114960	K5III	4130	2.36	0.15
SMC052334	K7	4008	0.02	-1.00

Table 3.3 – Continued

Star name	Sp. type	T_{eff} (K)	$\log g$	[Fe/H]
HD79349	K7IV	3871	1.66	0.04
BUL-SC17-1595	LPV	2429	1.16	0.00
BUL-SC13-1542	LPV	2441	1.14	0.00
BUL-SC04-1709	LPV	2465	0.81	0.00
BUL-SC36-2158	LPV	2543	1.02	0.00
BUL-SC41-3304	LPV	2560	1.32	0.00
BUL-SC33-4149	LPV	2562	1.18	0.00
BUL-SC19-2948	LPV	2605	1.29	0.00
BUL-SC06-2525	LPV	2606	1.29	0.00
BUL-SC41-3443	LPV	2640	1.23	0.00
BUL-SC16-1428	LPV	2673	1.83	0.00
BUL-SC22-1319	LPV	3000	1.31	0.00
BUL-SC08-1687	LPV	3007	1.47	0.00
BUL-SC19-2332	LPV	3029	1.42	0.00
BUL-SC30-0707	LPV	3037	1.59	0.00
BUL-SC06-1799	LPV	3068	0.91	0.00
BUL-SC24-0989	LPV	3068	0.93	0.00
BUL-SC19-2302	LPV	3074	1.06	0.00
BUL-SC15-2106	LPV	3079	0.92	0.00
BUL-SC06-2997	LPV	3095	0.72	0.00
BUL-SC33-0357	LPV	3105	0.99	0.00
BUL-SC15-1379	LPV	3116	0.98	0.00
BUL-SC03-1890	LPV	3122	0.91	0.00
BUL-SC01-0235	LPV	3156	1.21	0.00
BUL-SC26-0532	LPV	3173	0.96	0.00
BUL-SC03-3941	LPV	3197	0.94	0.00
BUL-SC04-4628	LPV	3208	1.04	0.00
BUL-SC13-0324	LPV	3211	1.06	0.00
BUL-SC04-9008	LPV	3248	0.77	0.00
BUL-SC03-8195	LPV	4868	1.37	0.00
SHV0506368	M	2691	1.07	-0.74
SHV0506368	M	2600	0.76	-0.60
SgrI55	M	2600	0.64	0.48
SHV0533015	M	2604	0.56	-0.75
J005714.4-730121	M	2605	0.50	-0.95
SgrI117	M	2614	1.76	0.05
SgrI11	M	2626	0.56	0.14
SHV0523357	M	2632	0.58	-1.85
SHV0515461	M	2725	0.93	-1.50
SHV0525543	M	2773	0.69	-0.50
J005314.8-730601	M	3367	0.60	-0.70
J005059.4-731914	M	3377	0.85	-0.70
SHV0526364	M	3390	0.59	-0.50

Table 3.3 – Continued

Star name	Sp. type	T_{eff} (K)	$\log g$	[Fe/H]
J004950.3-731116	M	3415	0.71	-0.70
SHV0503595	M	3031	0.89	-0.60
SHV0503595	M	3498	0.78	-0.60
J005622.2-730334	M	4077	1.21	-1.20
OGLE-650C2	M	4160	0.77	-0.67
Arp4329	M	4178	1.31	-1.02
OGLE-433669	M	4254	1.77	-0.13
OGLE-3733C3	M	4297	1.18	-0.19
J005304.7-730409	M	4300	0.50	-0.70
OGLE-3267C3	M	4361	1.07	0.01
J005332.4-730501	M	4465	0.62	-0.82
J005101.9-731607	M	4501	0.53	-0.75
OGLE-3690C7	M	5082	1.52	-1.48
HD209290	M0.5V	3681	3.53	-1.18
UCrt	M0e	3300	1.42	0.00
SMC046662	M0I	3581	0.69	-1.10
N371R20	M0I	3782	0.63	-0.69
CD-603636	M0Iab	3694	0.78	-0.65
LMC170452	M1.5I	3404	1.01	-0.66
HD35601	M1.5Ia0-Ia...	3724	0.73	-0.14
CPD-573502	M1.5Iab	3664	0.62	-0.35
CD-603621	M1.5Iab	3698	0.77	-0.25
LMC162635	M1I	3671	0.79	-0.88
HD98817	M1Iab	3658	0.70	-0.12
BS4517	M1III	3593	1.21	-1.48
LMC148035	M2.5I	3294	0.70	-0.75
CD-314916	M2.5Iab	3462	0.71	-1.00
CD-314916	M2.5Iab	3520	0.67	-0.79
CMCar	M2e	3200	2.06	-0.76
SMC083593	M2I	3392	1.02	-1.60
LMC158646	M2I	3648	0.76	-0.82
HV2360	M2Ia	3252	0.94	-0.93
HD39801	M2Iab:	3443	0.81	0.00
LMC150040	M3-M4	3237	0.35	-1.24
LMC168757	M3?m4I...	3328	0.53	-1.00
SMC055188	M3.5I	2818	0.75	-1.00
HD101712	M3Iab	3317	0.53	-0.81
HD101712	M3Iab	3334	0.45	-0.87
BS4463	M3III	3339	1.20	-1.34
SHV0549503	M4	2689	0.94	-2.66
B86-133	M4	3024	0.86	-1.94
HV2255	M4	3083	0.37	-1.36
HV2255	M4	3083	0.37	-1.36

Table 3.3 – Continued

Star name	Sp. type	T_{eff} (K)	$\log g$	[Fe/H]
RCha	M4.5e	2557	1.24	-1.11
EVCar	M4.5Ia	3274	0.40	-0.82
LMC143035	M4I	2941	0.66	-0.50
J18040638-3010497	M5	3192	1.04	-0.21
J18025277-2954335	M5	3278	1.20	-0.21
HV2446	M5e	2532	1.26	-0.97
SHV0518570	M6	2547	0.66	-0.65
SHV0543367	M6	2870	0.53	-0.75
SHV0452361	M6	2892	1.14	-0.80
SHV0452361	M6	2892	1.14	-0.80
J18042244-3000534	M6	2897	0.90	-0.21
SHV0510004	M6	2729	0.70	-0.60
SHV0510004	M6	2905	0.30	-0.60
BUL-SC01-1821	M6	2948	0.57	0.00
SHV0501215	M6	2991	0.44	-0.85
SHV0501215	M6	2991	0.44	-0.85
J18032525-2959483	M6	3008	0.80	-0.21
J18024611-3004509	M6.5	2881	0.81	-0.21
J18034305-3007541	M6.5	2928	0.66	-0.21
J18042719-3002575	M6.5	3210	1.03	-0.21
GL866	M6(M7e?)	2940	4.39	-0.24
J18024572-3001120	M7	2477	0.61	-0.51
SHV0606101	M7	2622	0.81	-0.95
GL644C	M7V	2715	4.58	-0.35
J18042265-2954518	M9	2427	0.63	-0.21
LHS2065	M9.0V	2589	4.93	-0.17
LHS2065	M9.0V	2589	4.93	-0.17
IRAS15060+0947	M9III	2626	1.80	-0.52
IRAS14303-1042	Me	2864	1.28	-1.76
SHV0529467	Ms	2719	1.04	-0.50
SHV0522380	Ms	3819	0.97	-0.31
HD57060	O7e...	36129	2.93	0.42
HD64332	S	3195	0.40	-1.00

Bibliography

Allard, F., Homeier, D., & Freytag, B. 2011, in *Astronomical Society of the Pacific Conference Series*, Vol. 448, 16th Cambridge Workshop on Cool Stars, Stellar Systems, and the Sun, ed. C. Johns-Krull, M. K. Browning, & A. A. West, 91

- Alonso, A., Arribas, S., & Martínez-Roger, C. 1996, *A&AS*, 117, 227
- Alonso, A., Arribas, S., & Martínez-Roger, C. 1999, *A&AS*, 140, 261
- Armandroff, T. E. & Zinn, R. 1988, *AJ*, 96, 92
- Asa'd, R. S. & Hanson, M. M. 2012, *MNRAS*, 419, 2116
- Beaulieu, S. F., Gilmore, G., Elson, R. A. W., et al. 2001, *AJ*, 121, 2618
- Bica, E., Claria, J. J., Dottori, H., Santos, Jr., J. F. C., & Piatti, A. E. 1996, *ApJS*, 102, 57
- Bonnefoy, M., Chauvin, G., Lagrange, A.-M., et al. 2013, *ArXiv e-prints*
- Bruzual, G. & Charlot, S. 2003, *MNRAS*, 344, 1000
- Burstein, D., Faber, S. M., Gaskell, C. M., & Krumm, N. 1984, *ApJ*, 287, 586
- Buzzoni, A. 1989, *ApJS*, 71, 817
- Buzzoni, A., Mantegazza, L., & Gariboldi, G. 1994, *AJ*, 107, 513
- Cappellari, M. & Emsellem, E. 2004, *PASP*, 116, 138
- Carretta, E., Bragaglia, A., Gratton, R., D'Orazi, V., & Lucatello, S. 2009, *A&A*, 508, 695
- Cassisi, S., Castellani, M., & Castellani, V. 1997a, *A&A*, 317, 108
- Cassisi, S., Castellani, V., Ciarcelluti, P., Piotto, G., & Zoccali, M. 2000, *MNRAS*, 315, 679
- Cassisi, S., degl'Innocenti, S., & Salaris, M. 1997b, *MNRAS*, 290, 515
- Cenarro, A. J., Beasley, M. A., Strader, J., Brodie, J. P., & Forbes, D. A. 2007, *AJ*, 134, 391
- Cenarro, A. J., Cardiel, N., Gorgas, J., et al. 2001, *MNRAS*, 326, 959
- Cenarro, A. J., Cervantes, J. L., Beasley, M. A., Marín-Franch, A., & Vazdekis, A. 2008, *ApJ*, 689, L29
- Cenarro, A. J., Gorgas, J., Vazdekis, A., Cardiel, N., & Peletier, R. F. 2003, *MNRAS*, 339, L12
- Conroy, C. & van Dokkum, P. 2012a, *ApJ*, 747, 69
- Conroy, C. & van Dokkum, P. G. 2012b, *ApJ*, 760, 71
- De Angeli, F., Piotto, G., Cassisi, S., et al. 2005, *AJ*, 130, 116
- Faber, S. M. & French, H. B. 1980, *ApJ*, 235, 405
- Falcón-Barroso, J., Balcells, M., Peletier, R. F., & Vazdekis, A. 2003, *A&A*, 405, 455
- Ferreras, I., La Barbera, F., de la Rosa, I. G., et al. 2013, *MNRAS*, 429, L15
- Fioc, M. & Rocca-Volmerange, B. 1997, *A&A*, 326, 950
- Foster, C., Proctor, R. N., Forbes, D. A., et al. 2009, *MNRAS*, 400, 2135

- Geisler, D., Bica, E., Dottori, H., et al. 1997, *AJ*, 114, 1920
- Geisler, D. & Sarajedini, A. 1999, *AJ*, 117, 308
- Girardi, L., Bressan, A., Bertelli, G., & Chiosi, C. 2000, *A&AS*, 141, 371
- González Delgado, R. M., Cerviño, M., Martins, L. P., Leitherer, C., & Hauschildt, P. H. 2005, *MNRAS*, 357, 945
- Goudfrooij, P., Gilmore, D., Kissler-Patig, M., & Maraston, C. 2006, *MNRAS*, 369, 697
- Guiderdoni, B. & Rocca-Volmerange, B. 1987, *A&A*, 186, 1
- Koleva, M., Prugniel, P., Bouchard, A., & Wu, Y. 2009, *A&A*, 501, 1269
- Koleva, M. & Vazdekis, A. 2012, *A&A*, 538, A143
- Kroupa, P. 2001, *MNRAS*, 322, 231
- Lançon, A. & Mouhcine, M. 2002, *A&A*, 393, 167
- Le Borgne, D., Rocca-Volmerange, B., Prugniel, P., et al. 2004, *A&A*, 425, 881
- Leggett, S. K., Allard, F., Geballe, T. R., Hauschildt, P. H., & Schweitzer, A. 2001, *ApJ*, 548, 908
- Leitherer, C., Alloin, D., Fritze-v. Alvensleben, U., et al. 1996, *PASP*, 108, 996
- Leitherer, C., Schaerer, D., Goldader, J. D., et al. 1999, *ApJS*, 123, 3
- Maraston, C. 2005, *MNRAS*, 362, 799
- Marigo, P., Girardi, L., Bressan, A., et al. 2008, *A&A*, 482, 883
- Marín-Franch, A., Aparicio, A., Piotto, G., et al. 2009, *ApJ*, 694, 1498
- Momany, Y., Ortolani, S., Held, E. V., et al. 2003, *A&A*, 402, 607
- Piatti, A. E. 2012, *MNRAS*, 422, 1109
- Piatti, A. E., Geisler, D., & Mateluna, R. 2012, *AJ*, 144, 100
- Pietrinferni, A., Cassisi, S., Salaris, M., & Castelli, F. 2004, *ApJ*, 612, 168
- Prugniel, P. & Soubiran, C. 2001, *A&A*, 369, 1048
- Prugniel, P., Vauglin, I., & Koleva, M. 2011, *A&A*, 531, A165
- Rabin, D. 1982, *ApJ*, 261, 85
- Rabin, D. & Moore, R. L. 1980, *ApJ*, 241, 394
- Ramírez, S. V., Stephens, A. W., Frogel, J. A., & DePoy, D. L. 2000, *AJ*, 120, 833
- Rayner, J. T., Cushing, M. C., & Vacca, W. D. 2009, *ApJS*, 185, 289
- Renzini, A. & Voli, M. 1981, *A&A*, 94, 175

- Rice, E. L., Barman, T., Mclean, I. S., Prato, L., & Kirkpatrick, J. D. 2010, *ApJS*, 186, 63
- Rose, J. A. & Tripicco, M. J. 1986, *AJ*, 92, 610
- Salpeter, E. E. 1955, *ApJ*, 121, 161
- Sánchez-Blázquez, P., Peletier, R. F., Jiménez-Vicente, J., et al. 2006, *MNRAS*, 371, 703
- Schiavon, R. P., Faber, S. M., Castilho, B. V., & Rose, J. A. 2002a, *ApJ*, 580, 850
- Schiavon, R. P., Faber, S. M., Rose, J. A., & Castilho, B. V. 2002b, *ApJ*, 580, 873
- Schiavon, R. P., Rose, J. A., Courteau, S., & MacArthur, L. A. 2005, *ApJS*, 160, 163
- Spiniello, C., Trager, S. C., Koopmans, L. V. E., & Chen, Y. P. 2012, *ApJ*, 753, L32
- Tinsley, B. M. 1978, *ApJ*, 222, 14
- Tinsley, B. M. & Gunn, J. E. 1976, *ApJ*, 203, 52
- Trager, S. C. 2004, in *Carnegie Observatories Astrophysics Series, Vol. 4, Origin and Evolution of the Elements*, ed. A. McWilliam & M. Rauch, 388
- Trager, S. C., Faber, S. M., & Dressler, A. 2008, *MNRAS*, 386, 715
- Trager, S. C., Worthey, G., Faber, S. M., Burstein, D., & González, J. J. 1998, *ApJS*, 116, 1
- Valdes, E., Gupta, R., Rose, J. A., Singh, H. P., & Bell, D. J. 2004, *ApJS*, 152, 251
- van Dokkum, P. G. & Conroy, C. 2010, *Nature*, 468, 940
- Vazdekis, A. 1999, *ApJ*, 513, 224
- Vazdekis, A., Cenarro, A. J., Gorgas, J., Cardiel, N., & Peletier, R. F. 2003, *MNRAS*, 340, 1317
- Vazdekis, A., Ricciardelli, E., Cenarro, A. J., et al. 2012, *MNRAS*, 424, 157
- Vazdekis, A., Sánchez-Blázquez, P., Falcón-Barroso, J., et al. 2010, *MNRAS*, 404, 1639
- Worthey, G. 1994, *ApJS*, 95, 107
- Worthey, G., Faber, S. M., González, J. J., & Burstein, D. 1994, *ApJS*, 94, 687
- Wu, Y., Singh, H. P., Prugniel, P., Gupta, R., & Koleva, M. 2011, *A&A*, 525, A71

THE INITIAL MASS FUNCTION OF INTERMEDIATE-MASS EARLY-TYPE GALAXIES

Yan-Ping Chen, Scott C. Trager, Reynier F. Peletier and Alexandre Vazdekis

To be submitted to MNRAS

Abstract

Gravity-sensitive absorption lines in integrated light allow for a determination of the slope of the initial mass function (IMF) in old stellar populations. We define a new gravity-sensitive index and measure its strength in the spectra of seven intermediate-mass early-type galaxies (ETGs) obtained with the X-Shooter spectrograph. Our new TiO+CaH index proves to be a good IMF slope indicator, providing results that are similar to results obtained using the Lick TiO1 and TiO2 indices. For the five galaxies with velocity dispersions below 200km s^{-1} we find that the IMF slope cannot be steeper than Salpeter. The two most massive galaxies in the sample may have a slightly more dwarf-enhanced IMF

4.1 Introduction

Understanding the ages and chemical compositions of stellar populations that make up galaxies provide valuable clues to their formation and evolution through cosmic time. A fundamental assumption in stellar population models is the initial mass function (IMF) of stars. An IMF is required to populate an isochrone with the proper number of stars before integrating their spectra to produce the proper spectral energy distribution of the total composite stellar population.

The IMF has long been thought to be universal. In our Galaxy the IMF can be measured by counting stars, and correcting this number for stars that have died since they

were formed (Miller & Scalo 1979; Scalo 1986; Kroupa 2001). At high masses ($M \geq 1M_{\odot}$) it has a power-law shape $dN/dm \propto m^{-(1+x)}$, with $x = 1.3$ for the Salpeter (1955) IMF. At lower masses, it is either flat or turns over to have a deficiency of low mass stars (e.g. Kroupa 2001; Chabrier 2003), at least in the solar neighbourhood.

In galaxies beyond the Local Group, counting individual (low mass) stars is not yet possible, and the IMF has to be constrained using stellar population synthesis. Deriving the IMF slope in an old stellar population is equivalent to finding the relative number of dwarfs and giants. In general, this can be done using colours or line strengths in the integrated light that are sensitive to gravity. A number of studies have suggested that the IMF may vary with environment or even redshift (Rieke et al. 1993; McCrady et al. 2003; van Dokkum 2008; Davé 2008). There are a number of strong gravity-sensitive absorption lines such as the Wing-Ford band at $\lambda\lambda 9910$ and NaI doublet at 8183–8195, TiO features at $\lambda\lambda 8430$ and 8880 and CO at $2.3 \mu m$. The Wing-Ford and NaI are found to be strong in dwarfs, and van Dokkum & Conroy (2010) have used these features to suggest that a “bottom-heavy” IMF ($x \geq 2$) is necessary to match the near-infrared lines of stacked spectra of Virgo and Coma early-type galaxies. The TiO and CO features are found to be strong in giants (Whitford 1977; Conroy & van Dokkum 2012a). The CaII triplet has also been proposed to trace power-like IMF shapes. In fact Vazdekis et al. (2003); Cenarro et al. (2003); Falcón-Barroso et al. (2003) found a $\text{CaT}^* - \sigma$ anti-correlation which might be understood if the IMF is steeper for massive galaxies. More recently, the Lick index (Burstein et al. 1984; Worthey et al. 1994; Trager et al. 1998) TiO2 has been used by Spiniello et al. (2012) to trace the IMF slope of early-type gravitational-lens galaxies.

Deriving the IMF slope from absorption line indices from integrated light, however, is not easy, because indices are also affected by the age of the stellar population and the abundance mix of its stars. One has to compare the indices with stellar population models which may be inadequate for the intended purpose. For instance, the models may have only solar abundance ratios, which can be different from the abundance ratios in the galaxy; or models have non-solar abundance ratios but were constructed with few stars in the temperature and surface gravity range of interest, which may result in biased stellar population models (e.g. Trager et al. 2000b). The effect of the IMF and elemental abundance can be separated by combining indices in the blue, which are relatively insensitive to IMF slope, with indices in the red, which depends more on the dwarf to giant ratios, especially the features dominated by the same element (Conroy & van Dokkum 2012a). This means that a wide wavelength coverage from both the data and the models is required. It is dangerous to use only a single feature as the absolute indicator of some physical parameter (e.g. IMF slope, age, metallicity etc), since it may yield results inconsistent with other absorption features. As an example, in the work of Cenarro et al. (2003), the red CaII triplet is combined with the metallicity-sensitive sTiO index, observed in the same region. The IMF slope is constrained by the CaT^* index, however effects due to non-solar abundance patterns are hard to rule out (Cenarro et al. 2003; Conroy & van Dokkum 2012a). In general, up to recently, it has been very difficult to measure good spectra in the infrared region beyond 7000 \AA , due to low sensitivity detectors, strong fringing in the CCDs, etc. This has led workers to stack spectra to get higher signal-to-noise ratios (e.g. van Dokkum & Conroy 2010;

Spiniello et al. 2012). However, stacked spectra may contain one or more outliers with different properties, which makes them difficult to interpret.

Recently the situation has improved. New near-infrared spectrographs with better detectors are making the wavelength region beyond 7000 Å more accessible. An example of such a spectrograph is the new X-Shooter instrument on ESO's VLT (Vernet et al. 2011), which obtains spectra simultaneously between 3000 – 25000 Å at moderate resolution ($R \geq 5000$). We retrieved spectra taken with the X-Shooter spectrograph of seven intermediate-mass ETGs from the ESO archive.

In this work we compare IMF-sensitive absorption-line indices measured from these X-Shooter spectra with predictions from modern stellar population synthesis models. We therefore require stellar population models with IMF slopes as a free parameter as well as varying ages, metallicities and, if possible, abundance ratios. There are several stellar population models which take into account the IMF slope, such as the CvD (Conroy & van Dokkum 2012a) and the MIUSCAT models (Vazdekis et al. 2012). As the CvD models do not allow for a large variation in metallicity, we use the new, more flexible MIUSCAT models, to probe the IMF slope as well as resolve the degeneracy between age, metallicity and IMF-slope. We do this by defining the new index TiO+CaH around 6700 Å, and use two Lick indices, TiO1 and TiO2. In this paper we use [MgFe] (González 1993) as a metallicity indicator. Based on the TiO indices, we find that the IMF of those seven ETGs are constrained to have a slope no steeper than the Salpeter value, except possibly for NGC 4365.

We begin with a description of the X-Shooter data of the ETGs, and the steps required to reduce this data to indices, in Section 4.2. We present a full description of the behaviour of the IMF-sensitive absorption-line indices and other indices used in this work in Section 4.3. We compare the line strengths of the ETGs with our model predictions in Section 4.4. We discuss other gravity-sensitive indices that may be useful for probing the IMF slope in Section 4.5. We conclude with a summary in Section 4.6.

4.2 Data

4.2.1 The Galaxy Sample

We have selected seven ETGs from the ESO archive to examine the possible variation of IMF slope in intermediate-mass ETGs. The spectra were collected with the X-Shooter spectrograph on ESO's VLT telescope between 2009 October 18 and 2010 March 13¹. Four objects are typed as 'E' and three as 'S0' in de Vaucouleurs et al. (1991, RC3), and the galaxies have absolute magnitudes with absolute B-band magnitude $-21 < M_B < -18$ (Table 4.1). They were observed with a $1.''0 \times 11''$ slit in the UVB arm (3000–6000 Å) and a $0.''9 \times 11''$ slit in the VIS arm (6000–10200 Å). We measure resolutions of $R = 5100$ in the UVB arm and $R = 8800$ in the VIS arm from the widths of bright night-sky emission lines. The typical exposure time was 2×76 seconds in the UVB and 2×70 in

¹These observations were taken as part of ESO observing program 384.B-1029, PI: Clemens. Ten galaxies were taken in this program, but the VIS arm spectra of three were corrupted by electronic noise, yielding them unusable for this study.

Table 4.1: Galaxies used in this work

Name	RA (J2000)	Dec (J2000)	Morphology	Centre Distance(″)	cz (km s^{-1})	σ_v (km s^{-1})	PA ($^\circ$)	S/N^a (\AA^{-1})	S/N^b (\AA^{-1})	R_e (″)
NGC 1389	03:37:11.6	-35:44:45.3	SAB0	5.40	966.2 ± 7.7	137.1 ± 10.8	75	69	66	15.0
NGC 1426	03:42:49.0	-22:06:28.7	E4	5.36	1448.0 ± 2.1	165.6 ± 6.8	109	67	70	25.0
NGC 3818	11:41:57.4	-06:09:20.9	E5	5.52	1681.7 ± 7.4	213.4 ± 4.5	-150	50	59	22.2
NGC 4339	12:23:34.8	+06:04:54.9	E0	5.52	1257.0 ± 3.4	139.1 ± 7.4	24	42	49	32.1
NGC 4365	12:24:28.3	+07:19:03.8	E3	5.40	1201.3 ± 0.2	279.6 ± 5.9	-162	82	94	49.8
NGC 4371	12:24:55.3	+11:42:16.5	SB(r)0	5.44	910.3 ± 4.8	137.9 ± 6.6	28	51	57	23.3
NGC 4377	12:25:12.2	+14:45:44.7	SA0	5.44	1341.6 ± 3.7	159.2 ± 7.4	29	71	78	13.1

Column 1: Galaxy name. Column 4: Morphology from the RC3 (de Vaucouleurs et al. 1991). Column 5: Distance of the galaxy centre from the edge of the slit. Column 6 and 7: Radial velocity and velocity dispersion measured in this work. Column 8: Position angle of the observation. Column 9 and 10: Median signal to noise ratio (S/N) per \AA , a in the UVB arm over the wavelength range 5000–5400 \AA and b in the VIS arm over the wavelength range 5800–8300 \AA . Column 11: Effective radius from the RC3.

the VIS arm, respectively. We leave the NIR data of these galaxies to a future paper. Basic observational parameters are listed in Table 4.1.

4.2.2 Data Reduction

The data reduction was performed using the X-Shooter pipeline (Modigliani et al. 2010) version 1.3.7, following the steps described in the X-Shooter pipeline manual² as far as producing two-dimensional spectra. Sky subtraction was performed using the sky frames observed in the offset mode in the order ‘Object–Sky–Sky–Object’. After the pipeline reduction we extracted the one-dimensional spectra using our own IDL optimal extraction code, following the prescription of Horne (1986).

The spectra in the VIS arm are strongly affected by absorption lines of the Earth’s atmosphere. We performed telluric correction using the full-spectral-fitting program pPXF (Cappellari & Emsellem 2004) with a collection of telluric atmosphere spectra prepared for the reduction of the X-Shooter library (XSL, Chen et al. 2011). We fit the spectrum of a galaxy with a linear combination of the spectra in the (normalized) telluric library in the atmospheric absorption regions, fitting at the same time the line-broadening of the science spectra, and multiplying the result with a polynomial which mimics the continuum of the galaxy spectrum. The telluric corrected spectra are then obtained by dividing the one-dimensional spectra by the best fit templates.

The one-dimensional spectra were flux calibrated using the XSL response curve and the Paranal extinction curve from Patat et al. (2011). Although the slit-widths of the XSL standard stars and these galaxies are different, the result is good enough for measuring the line-strength indices. Figure 4.1 shows the flux-calibrated galaxy spectra smoothed to $\sigma_v = 300 \text{ km s}^{-1}$ in the rest frame, where the UVB arm spectra are zoomed in between 5000–5500Å and the VIS arm spectra are shown between 5800–9200Å. We show a typical telluric template at the bottom of the right panel shifted to a radial velocity of $\sim 1000 \text{ km s}^{-1}$ to demonstrate the rough positions of the atmospheric absorption features in the galaxy spectra.

²See <http://www.eso.org/sci/software/pipelines/>

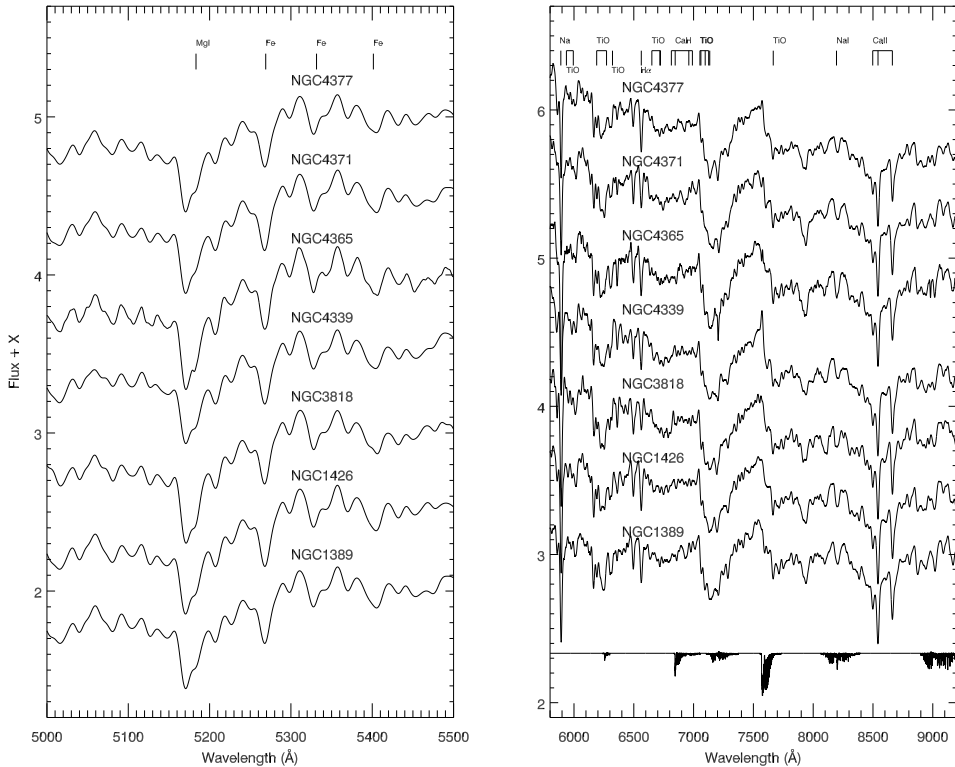


Figure 4.1: Flux calibrated X-Shooter spectra in the rest frame, smoothed to $\sigma_v = 300 \text{ km s}^{-1}$. The UVB arm is normalized at 5300 \AA , and the VIS arm is normalized at 6400 \AA .

4.3 Absorption line indices

To assess the impact of the IMF on absorption-line strengths inferred from stellar population models, we use the extended MILES models (MIUSCAT: Vazdekis et al. 2012) grids. These models are based on a stellar library constructed from MILES in the wavelength range $3525\text{--}7500 \text{ \AA}$ (Sánchez-Blázquez et al. 2006), the CaT triplet library in the wavelength range $\lambda\lambda 8350\text{--}9020 \text{ \AA}$ (Cenarro et al. 2001), and the Indo-US library in the wavelength range $3465\text{--}9469 \text{ \AA}$ (Valdes et al. 2004), which are smoothed to a uniform resolution of $\text{FWHM}=2.51 \text{ \AA}$. These models cover the following safe parameter ranges: metallicities of $-0.71 \leq [Z/H] \leq 0.22$, ages of $0.063 \leq t \leq 17.8 \text{ Gyr}$, and IMF slopes of $0.3 \leq x \leq 2.3$ in the form of Unimodal, Bimodal, Kroupa Universal and Kroupa Revised IMFs (see Vazdekis et al. 2003, for details). Recall that the Salpeter (1955) IMF in the unimodal case has an IMF slope of $x = 1.3$. We show the IMFs considered in this work in Figure 4.2. The lower and upper mass-cutoff of the IMF adopted here are 0.1 and $100 M_\odot$, respectively. Note that these models do not allow for a variation of element abundance ratios, although one can infer abundance ratios by examining variations of different indices.

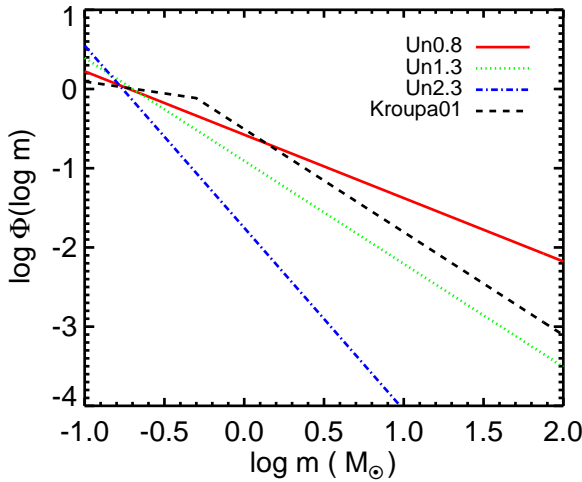


Figure 4.2: *IMFs used for the SSP models considered in this work.*

4.3.1 Variations of the model spectra with changing IMF

In Figure 4.3 we show unimodal models at solar metallicity ($[Z/H] = 0.0$) with IMF slopes of $x = 0.8$ (in black) and $x = 2.3$ (in red) normalized by a fourth-order polynomial. By taking the ratio of model fluxes with unimodal IMFs with slopes of $x = 0.8$ and $x = 2.3$, one can see the IMF-sensitive features.

In this plot, there are a number of gravity-sensitive TiO features to be seen. These include the traditional Lick indices TiO1 and TiO2 around 5900–6200 Å, the prominent feature between 6600–6800 Å and 7000–7200 Å, and the feature around 7700 Å. The prominent feature at 6600–6800 Å, is also clearly seen in the upper panel of Figure 4.3. This feature increases rapidly with increasing IMF slope. The last one at ~ 7700 Å is close to a region heavily affected by telluric absorption; further, it is in the part the spectrum where the MILES and Indo-US libraries have been joined to construct the MIUSCAT models, and it is likely that the models may be less reliable here. For these reasons we did not use it in our analysis. The broad feature at 7000–7200 Å is the strongest TiO feature; however, its interpretation might not be reliable because of atmospheric absorption. In the future, these indices can be studied, when e.g. stellar populations based on space-based spectra are available, for example, the NGSL library (Gregg et al. 2006). For the same reason we use only the beginning part of the feature at 6600–6800 Å, and we define this index as “TiO+CaH”. This feature is a blend of TiO and CaH molecular lines prominent in cool M dwarfs (see Reid et al. 1995). In this paper we will also consider two other features: the Lick indices TiO1 and TiO2, which become stronger with increasing IMF slope. We note that the sodium features NaD $\lambda 5895$ and NaI $\lambda 8190$ also show strong dependence on the IMF slope. As discussed in Cenarro et al. (2003); Conroy & van Dokkum (2012a); Vazdekis et al. (2012), the CaII triplet at 8498–8662 Å behaves in the opposite manner to the sodium features, becoming weaker with steeper IMF slope. Here we concentrate on the TiO indices in this work.

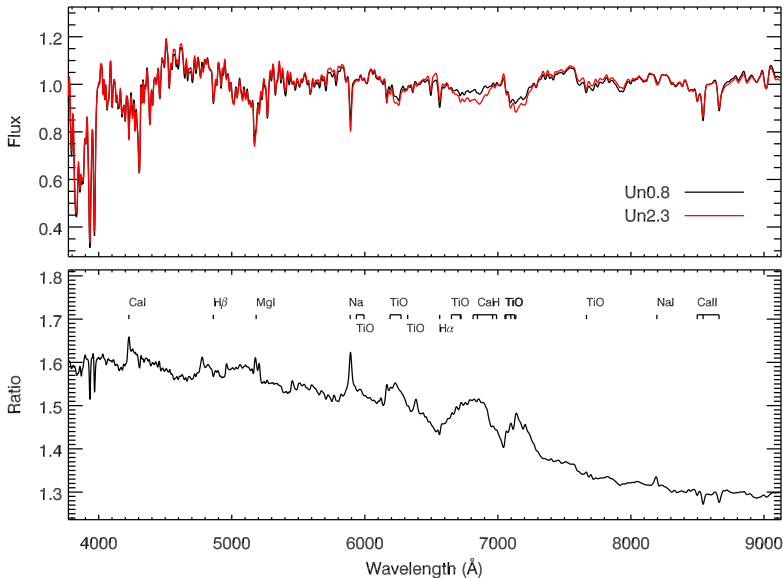


Figure 4.3: *MIUSCAT model spectra convolved to $\sigma_v = 300\text{km s}^{-1}$ at solar metallicity and an age of 10 Gyr with unimodal IMFs. Upper panel: models with IMF slopes $x = 0.8$ and $x = 2.3$ normalized by a fourth order polynomial; bottom panel: direct flux ratio between models with $x = 0.8$ and $x = 2.3$, with some absorption features labelled.*

4.3.2 Index definitions

In this paper we rely on spectral indices to investigate the behaviour of spectral absorption-line features as a function of age, metallicity, and IMF. We measure the line-strengths of *Mgb*, *Fe5270*, *Fe5335*, *TiO1* and *TiO2* using the standard Lick index definitions (Worthey et al. 1994; Trager et al. 1998). The reader should note that we do not put these indices on the zero point of the Lick index system, but use flux-calibrated spectra. We do, however, use the same definitions of the feature bands and pseudo-continua. All indices used in this work are given as equivalent widths (EWs) in units of Å, except *TiO1* and *TiO2*, which are in magnitudes. We also define new index *TiO+CaH* described above, which is sensitive to the IMF slopes. The *TiO+CaH* was defined carefully to avoid significant telluric absorption regions. The definition of the new index is illustrated in Figure 4.4. A 5 Gyr old, solar-metallicity MIUSCAT single-stellar-population (SSP) model smoothed to 300km s^{-1} with unimodal IMF slope of $x = 1.3$ is taken as an example. To identify the relative contribution of *TiO* and *CaH* in this index, we define two extra sub-indices with the same pseudo-continua “*TiO3*” and “*CaH*” according to Reid et al. (1995). These two sub-indices are marked on the same plot to clarify the comparison

Table 4.2: *Spectral indices used in this work*

Index	Central feature (Å)	Blue Pseudo-continua (Å)	Red Pseudo-continua (Å)	Notes
Mgb	5160.125–5192.625	5142.625–5161.375	5191.375–5206.375	Lick
Fe5270	5245.650–5285.650	5233.150–5248.150	5285.650–5318.150	Lick
Fe5335	5312.125–5352.125	5304.625–5315.875	5353.375–5363.375	Lick
TiO1	5936.625–5994.125	5816.625–5849.125	6038.625–6103.625	Lick, mag
TiO2	6189.625–6272.125	6066.625–6141.625	6372.625–6415.125	Lick, mag
TiO+CaH	6600.000–6817.000	6520.000–6545.000	7035.000–7050.000	this work
TiO3	6600.000–6723.000	6520.000 6545.000	7035.000–7050.000	this work
CaH	6775.000–6817.000	6520.000 6545.000	7035.000–7050.000	this work

with TiO+CaH (Reid et al. 1995). The central feature and pseudo-continua of indices used in this work are listed in Table 4.2.

We use the unimodal MIUSCAT models with IMF slopes of $x = 0.8, 1.3, 2.3$ in this work. We also include the multi-part power-law IMF proposed by Kroupa (2001) to examine the influence of the low-mass part of the IMF on the spectra.

4.3.3 Correction for velocity dispersion broadening

A galaxy spectrum is the integrated spectrum of the light from all of its stars convolved with the galaxy’s line-of-sight velocity distribution (LOSVD). To compare the galaxies and the predictions from stellar population models, both the galaxies and the models are required to have the same resolution, which means that the galaxies will have to be corrected for the broadening effect of their LOSVD. To do this, we determine the velocity dispersion of the galaxies by fitting them to a library of X-Shooter stars using pPXF (Cappellari & Emsellem 2004), which gives the radial velocity cz and velocity dispersion σ_v simultaneously. In each fit six stellar spectra from XSL (Chen et al. 2011) with different stellar types HD217877 (F8V), HD13043 (G2V), HD18907 (K2V), HD170820 (K0III), HD175545 (K2III) and HD114960 (K5III) are used as templates. We list the measured cz and σ_v of the sample galaxies in Table 4.1, which are consistent with previously published work (e.g. HyperLeda, Paturel et al. 2003). To avoid the systematic differences between indices at different spectral resolution, we convolve all the model spectra and galaxy spectra to a fixed velocity dispersion of $\sigma_v = 300 \text{ km s}^{-1}$ (the upper limit of our galaxy sample) using a Gaussian kernel. The indices listed in Table 4.2 are then measured on the convolved galaxy spectra.

We obtain the errors of the indices using the following procedure: For a given galaxy spectrum, we generate 1000 Monte Carlo random spectra based on a Gaussian distribution using its error spectrum. We then calculate the indices of the original galaxy spectrum modified by the 1000 error spectra. The final indices are taken to be the mean value of the indices measured from the Monte Carlo simulations, and the errors are obtained from the standard deviations of these measured indices.

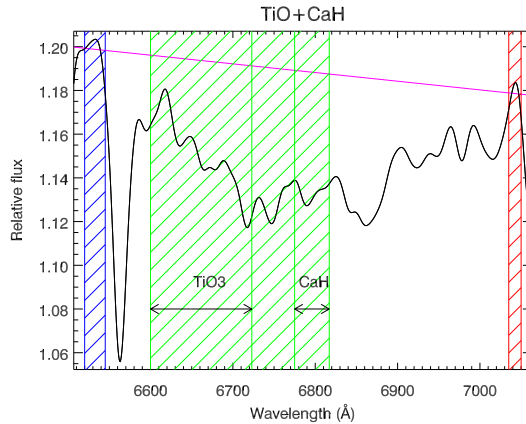


Figure 4.4: Index definition for TiO+CaH on a MIUSCAT SSP model of solar metallicity, 5 Gyr and unimodal IMF with $x = 1.3$. The SSP model spectrum has been smoothed to $\sigma_v = 300 \text{ km s}^{-1}$. The central feature bandpass is shown in green. Pseudo-continua are indicated in blue for the left continua bandpass and in red for the right continua bandpass, which defines the continuum level indicated by magenta line. Sub-indices TiO3 and CaH are marked with the same pseudo-continua to clarify the contribution of TiO and CaH (see text for details).

4.3.4 Comparison with the literature

We compare the indices measured in this paper with values from the literature. There are five galaxies in common between our sample and Trager et al. (1998): NGC 1426, NGC 3818, NGC 4339, NGC 4365 and NGC 4377. Two galaxies are in common with the sample of Rampazzo et al. (2005): NGC 1389 and NGC 1426. Three galaxies are in common with the sample of Ogando et al. (2008): NGC 1426, NGC 3818 and NGC 4339. Two galaxies are in common with the sample of Yamada et al. (2008): NGC 4339 and NGC 4365. In Figure 4.5 we show the comparison in detail. The literature indices from Trager et al. (1998) are measured through aperture slits of $1.''4 \times 4.''$; indices from Rampazzo et al. (2005) are measured through aperture slits of $2.'' \times 10.''$; indices from Ogando et al. (2008) are measured through aperture slits of $2.''5 \times 4.''1$; and indices from Yamada et al. (2008) are measured through aperture slits of $0.''6 \times 3.''2$ for NGC 4339 and $1.''6 \times 8.''$ for NGC 4365 (i.e., within $R_e/10$ for these two galaxies). We extracted our data according to the appropriate slit lengths for a fair comparison.

Along with the velocity dispersion correction, the data have to be put onto the same instrumental resolution to compare samples. We decide here to convolve our data (which have much higher spectral resolution than any of the literature data) to the resolution of the various samples. To compare with the data of Trager et al. (1998), we convolve our galaxies using the formulae in Trager et al. (2008) and Worthey & Ottaviani (1997), and correct for velocity dispersion broadening using the polynomial coefficients from Table 5 of Trager et al. (1998). Galaxies in common with Rampazzo

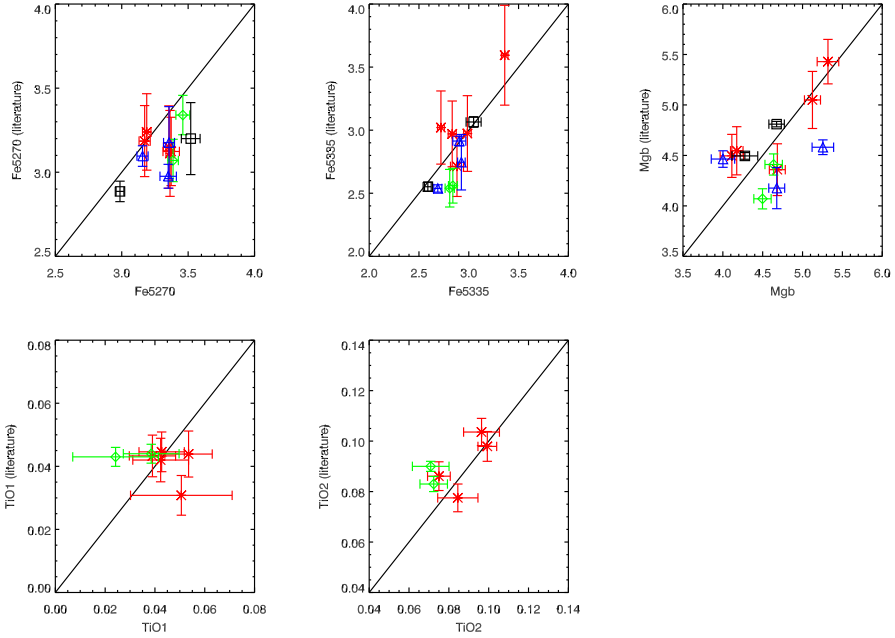


Figure 4.5: Comparison of our measured indices with literature values. Comparisons with Trager et al. (1998) are given as red crosses, with Rampazzo et al. (2005) as green diamonds, with Ogando et al. (2008) as blue triangles, and with Yamada et al. (2008) as black squares. The one-to-one relation is shown as a solid black line.

et al. (2005) are convolved to the Lick resolution as described in their paper. Derived line indices are transformed to the Lick-system, by using the fitting function $EW_{\text{Lick}} = \beta + \alpha \times EW_{\text{Ram}}$, (see their Table 8 for α and β). Since the galaxy indices in Ogando et al. (2008) were observed with $\text{FWHM} = 3\text{\AA}$ and $\text{FWHM} = 6\text{\AA}$ and then transferred to the Lick resolution; we convolve our data to the Lick resolution directly and calculate the indices for comparison. We have determine correction factors for the effect of velocity dispersion on the Ogando et al. (2008) line strengths from their Figure 6 and applied them to our data. For the galaxies in common with Yamada et al. (2008), we convolve our data for NGC 4365 to 300 km s^{-1} and NGC 4339 to 150 km s^{-1} for correcting the velocity dispersion effects and measure the indices directly. No offsets are applied to the Lick system as mentioned in their paper. Five of the Lick indices are compared and presented in Figure 4.5. The comparison with the literature is summarized in Table 4.3. We calculate the offset using the error-weighted mean residual. As shown in here, our measured indices are in good agreement with those available in the literature, with the possible exception of Fe5270, which is slightly ($\approx 1.3\sigma$) stronger in the X-Shooter data than in the literature.

Table 4.3: Comparison with the literature indices

Index	Mgb	Fe5270	Fe5335	TiO1	TiO2
Units	(Å)	(Å)	(Å)	mag	mag
Offset	0.06	0.16	0.07	-0.003	-0.007
Dispersion	0.37	0.13	0.18	0.011	0.009

Offsets and 1σ scatter dispersions of the residuals between our data and the literature.

4.4 Results

Table 4.4 lists the velocity-dispersion-corrected indices and rms errors for all galaxies observed through the $1''.0 \times 11''$ slit in the UVB arm and $0''.9 \times 11''$ slit in the VIS arm.

The goal of the paper is to find indices that are insensitive to age, metallicity and abundance ratios. We begin by establishing whether the galaxies in this sample show non-solar abundance ratios. Figure 4.6 shows the distribution of $\langle \text{Fe} \rangle^3$ as a function of Mgb. Unimodal models with four IMF slopes are presented. The α -enhancement can be traced by the plot $\langle \text{Fe} \rangle$ -Mgb, in which $\langle \text{Fe} \rangle$ is an indicator of iron abundance and Mgb is affected by α -enhancement. In this plot, we see that the model grids do not cover the full range of the data, since the MIUSCAT models only have the solar abundance pattern. Most of the galaxies fall on the model grids, while two galaxies, NGC 3818 and NGC 4365, fall outside of the model predictions. These two galaxies are therefore likely to be α -enhanced.

To establish the dependence of an index on the IMF, we adopt the combined index [MgFe] suggested by González (1993)⁴ as a metallicity indicator insensitive to $[\alpha/\text{Fe}]$ effects. The possible variation of the IMF slope is traced by the various TiO indices. We plot TiO+CaH, TiO1, and TiO2 as a function of [MgFe] in Figure 4.7. When examining TiO+CaH, it is interesting to note that all galaxies are fit best by models of Salpeter IMF or flatter IMF slopes. The [MgFe] values imply that all these galaxies have about the solar metallicity or slightly higher. It is worth noting that TiO+CaH is almost insensitive to age for the flatter IMFs. We note that the well-known metallicity-velocity dispersion relation is clearly seen in this plot, with velocity dispersion rising from left to the right.

We show the Lick index TiO1 as function of [MgFe] in the middle panel of Figure 4.7. This plot is consistent with the upper panel. Again, TiO1 grows with increasing IMF slope. The galaxy data within their error bars are well fitted by the models with IMF slopes of $x \leq 1.3$. The most massive galaxy in the sample, NGC 4365, has the highest TiO1 strength and may also be fitted by a steeper IMF. The large uncertainty in this index is likely due to the fact that TiO1 lies very near the blue limit of X-Shooter VIS arm for these galaxies, where the signal-to-noise ratio is always lower than in the central part of the wavelength range of this arm.

The Lick index TiO2 as a function of [MgFe] is shown in the bottom panel of Figure

³ $\langle \text{Fe} \rangle = (\text{Fe}5270 + \text{Fe}5335)/2$

⁴ $[\text{MgFe}] = \sqrt{(\text{Fe}5270 + \text{Fe}5335)/2 \times \text{Mgb}}$

Table 4.4: Line indices

Name	Mgb $\sigma(\text{Mgb})$	Fe5270 $\sigma(\text{Fe5270})$	Fe5335 $\sigma(\text{Fe5335})$	TiO1 $\sigma(\text{TiO1})$	TiO2 $\sigma(\text{TiO2})$	TiO+CaH $\sigma(\text{TiO+CaH})$	TiO3 $\sigma(\text{TiO3})$	CaH $\sigma(\text{CaH})$
NGC 1389	3.77 0.10	2.74 0.04	2.19 0.04	0.020 0.017	0.074 0.007	8.9 1.5	4.5 1.3	1.97 0.08
NGC 1426	3.95 0.10	2.86 0.05	2.24 0.04	0.035 0.011	0.072 0.009	9.3 1.4	5.0 1.2	1.82 0.10
NGC 3818	4.71 0.17	2.71 0.05	2.16 0.06	0.032 0.010	0.105 0.012	9.5 1.5	4.2 1.3	2.37 0.11
NGC 4339	3.60 0.15	2.88 0.09	2.22 0.08	0.032 0.021	0.085 0.012	9.3 2.1	4.5 1.9	2.05 0.11
NGC 4365	4.74 0.11	2.98 0.04	2.58 0.04	0.039 0.010	0.084 0.005	10.5 1.0	5.3 0.9	2.31 0.05
NGC 4371	3.71 0.15	3.05 0.08	2.22 0.06	0.027 0.022	0.079 0.008	11.7 1.9	6.2 1.7	2.22 0.08
NGC 4377	3.70 0.09	2.83 0.04	2.15 0.04	0.034 0.011	0.069 0.008	9.5 1.2	5.0 1.1	1.89 0.06

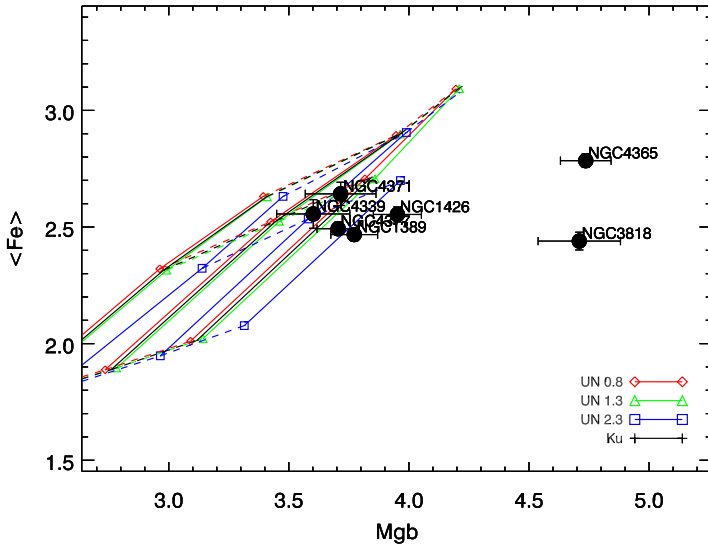


Figure 4.6: MIUSCAT unimodal models with IMF slopes of $x = 0.8$, 1.3, 2.3 and Kroupa IMF are presented. IMF slope $x = 0.8$ is shown by red diamonds; Salpeter IMF slope $x = 1.3$ is shown by green triangles; steeper IMF slope models with $x = 2.3$ is shown by blue squares and Kroupa IMF models is shown by black crosses. Within each set of IMF slopes, solid lines show the same ages, and dashed lines show the same metallicities. Model ages are 5.0, 10.0, 17.0 Gyr, and metallicities are $[Z/H] = -0.4, 0.0$ (solar metallicity), $+0.22$. Galaxies are marked by black filled circles with their names labeled.

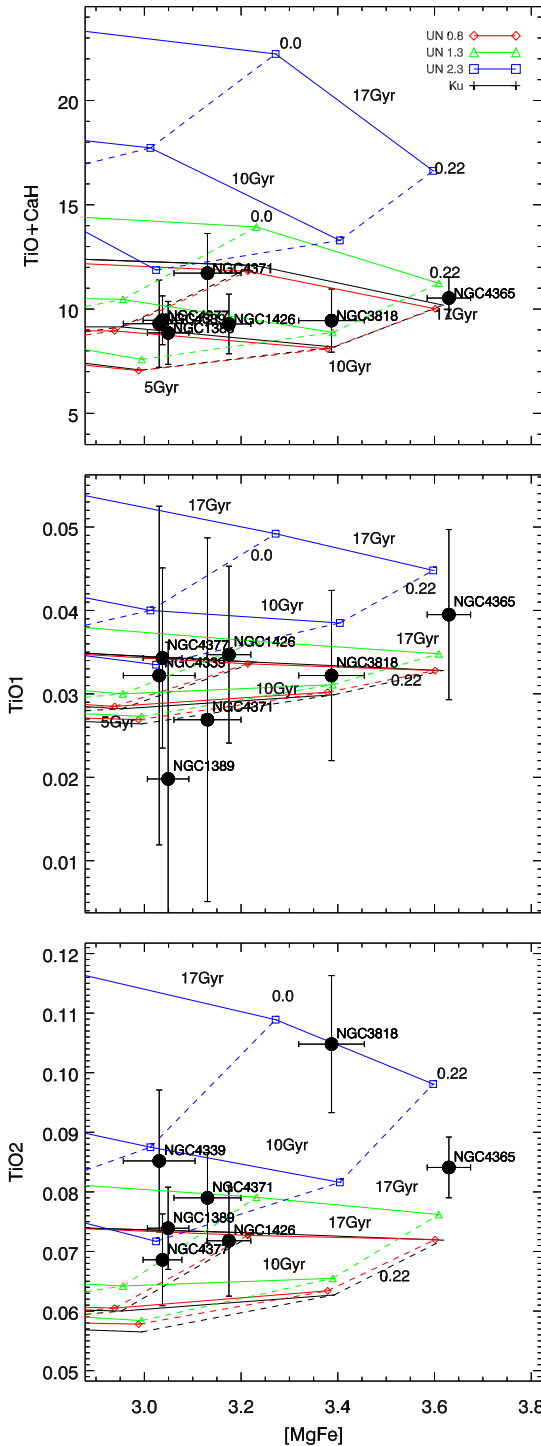


Figure 4.7: Index–index grids for the IMF sensitive features, models and symbols are the same as Figure 4.6. Top panel: SSP model predictions versus data, $TiO+CaH$ as a function of $[MgFe]$, with ages and metallicities labelled. Middle panel: $TiO1$ as a function of $[MgFe]$. Bottom panel: $TiO2$ as a function of $[MgFe]$.

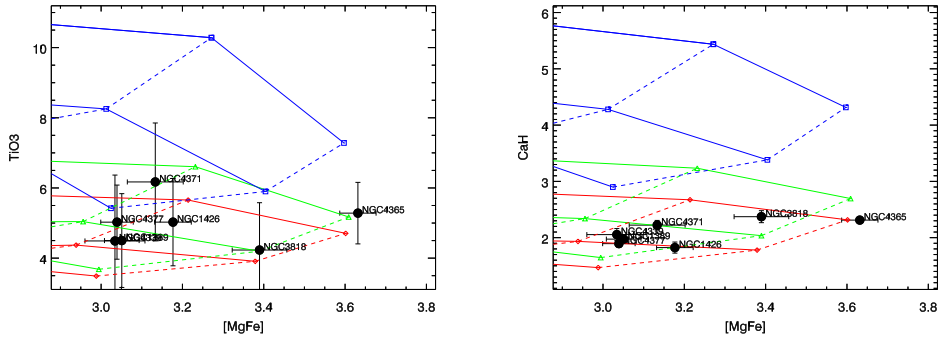


Figure 4.8: Same as the top panel of Figure 4.7, with the sub-indices $TiO3$ and CaH .

4.7. $TiO2$ clearly grows with increasing IMF slope. We find that six galaxies fall within the region of Salpeter or flatter IMF slope, while NGC 3818 appears to show a different behavior. Given the results of Figure 4.7, it is clear that there is no galaxy in our sample with an IMF slope steeper than Salpeter, except possibly for NGC 4365.

When the number of the low-mass stars is reduced, such as in the Kroupa IMF (Kroupa 2001), $TiO+CaH$ becomes smaller. As shown in Figure 4.7, model grids with a Kroupa IMF behave similarly to the flatter unimodal model with $x = 0.8$. We recall that the difference between Salpeter IMF and Kroupa IMF is the low mass part, i.e. $M \leq 0.5M_{\odot}$. This trend is found in all the three panels of $TiO+CaH$ versus $[MgFe]$, $TiO1$ versus $[MgFe]$ and the relation between $TiO2$ versus $[MgFe]$.

Because $TiO+CaH$ is an index composed of both TiO and CaH , we show their separate model predictions as well as the data in Figure 4.8. Clearly $TiO3$ shows a similar behaviour as $TiO1$ and $TiO2$, and its strength increases with increasing IMF slope. It is consistent with the model predictions made for $TiO+CaH$. The red part of the $TiO+CaH$ index, CaH , is shown as a function of $[MgFe]$ in the right panel. The spread in the CaH index is small, 1 \AA , and this index strongly supports the conclusion that a Salpeter or flatter IMF fits these intermediate-mass galaxies' line strengths best.

4.5 Discussion

In the preceding we have attempted to determine the slope of the low-mass IMF of seven mostly intermediate-mass ETGs from their integrated spectra. Unlike some previous studies (e.g., van Dokkum & Conroy 2010; Ferreras et al. 2013), the observed spectra are not stacked to improve the signal-to-noise, allowing us to examine the (quite small) galaxy-to-galaxy dispersion of the inferred IMF slopes. We have used a set of gravity-sensitive indicators, primarily dominated by TiO features, in the spectra and compared these with the MIUSCAT SSP models of Vazdekis et al. (2012). These TiO indices, when combined with metallicity-sensitive indices, allow us to decouple IMF effects on the features from age and metallicity effects. All of these indices point to towards these galaxies having nearly the same low-mass IMF, with the Salpeter IMF

consistent with being the steepest permissible IMF for these intermediate-mass ETGs.

The molecular bands of TiO are promising tracers of the IMF, as they are the dominant spectral characteristic of M dwarf stars in the red (Reid et al. 1995). TiO dominates the optical opacity of low mass dwarfs' cool atmospheres (Bochanski et al. 2007), and the strengths of the TiO features are used to define the M spectral sub type classification scheme (Reid et al. 1995; Bochanski et al. 2007). However, abundance ratio effects may play a significant role in the strengths of the TiO features. As discussed in Conroy & van Dokkum (2012a), both varying abundance ratios and giant-to-dwarf ratios can change the strength of the gravity-sensitive lines in composite populations. We use the $\langle \text{Fe} \rangle$ - Mgb diagram to separate the α -enhancement effects from the effect of low-mass IMF slope on the strengths of the TiO features. The excessive strength of TiO1 and TiO2 of NGC 4365 and NGC 3818 is likely at least partly due to α -enhancement, given that Ti is an α -element and both of these galaxies have very high Mgb strengths for their $\langle \text{Fe} \rangle$ strengths (Figure 4.6), suggesting strong α -element enhancement in these two objects (commensurate with their velocity dispersions; see, e.g. Trager et al. 2000a; Thomas et al. 2005). However, because the MIUSCAT models do not include abundance ratio variations, we cannot investigate the elemental abundances here quantitatively. Recent models by Thomas et al. (2011a) suggest that TiO1 and TiO2 depend weakly on $[\alpha/\text{Fe}]$, implying that these indices may be even better IMF indicators than we suppose here.

The TiO+CaH appears to be a promising feature to trace the IMF. It is quite a broad feature covering $\sim 200 \text{ \AA}$ and is therefore almost insensitive to velocity dispersion effects. The entire feature spans $\sim 6600 \text{ \AA}$ to $\sim 7000 \text{ \AA}$. We only use part of this feature because of possible atmospheric absorption, but it is clearly a powerful IMF indicator. We have used it to infer that low-mass IMF slope has an upper limit consistent with a Salpeter IMF in the intermediate-mass galaxies examined here. This is consistent with recent results based on gravitational lensing, which gives an upper limit on the stellar mass, and rules out the most extreme "bottom-heavy" IMFs (Spiniello et al. 2012).

To explore this new index in detail, we have defined two sub-indices, TiO3 and CaH. As shown in Figure 4.4 and 4.8, we define TiO3 and CaH carefully avoid overlapping region so that their independent contribution can be traced. We find their model predictions are slightly different, for example, NGC 4365 appears to have a Salpeter IMF when compared with the model in a plot of TiO3- $[\text{MgFe}]$, while it appears to have a flatter IMF in a plot of CaH- $[\text{MgFe}]$. Within the error bars, however, these two sub-indices give consistent results for these galaxies.

The behavior of CaH as a function of IMF deserves further, future investigation. The main contribution of CaH in the prominent gravity-sensitive band around $6600\text{--}7000 \text{ \AA}$ is at wavelengths redder than 6800 \AA (Reid et al. 1995), which are buried in the atmospheric absorption lines in the current spectra. Indeed, the red region beyond 6800 \AA contains several features that appear to have the potential to yield rich information on the low-mass IMF. However, some of those regions suffer from strong atmospheric absorption in both our data and the SSP models derived from ground-based stellar spectra, especially the redder TiO features that we would like to investigate. Space-based spectra (like those of Gregg et al. 2006) or better correction of telluric contamination are required.

IMF slopes flatter than Salpeter below $1 M_{\odot}$ are hard to distinguish with these indices using the current data and models. If we reduce the number of low-mass stars, for example using the Kroupa IMF, the features have strengths similar to those in the bottom-light case ($x = 0.8$). An IMF slope of $x = 0.8$ increases the number of high-mass stars, which mimics the effect of purely reducing the number of low-mass stars while keeping the high-mass stars as in the Salpeter IMF. The difference between Kroupa IMF and unimodal with $x = 1.3$ is in the low-mass region as shown in Figure 4.2, i.e., $M \leq 0.5 M_{\odot}$. The TiO+CaH index strengths of a model with a Kroupa IMF are about ~ 15 – 17% lower than a model with a Salpeter IMF, because the TiO+CaH is primarily sensitive to the dwarfs. It may be possible to constrain even the low-mass IMF shape (Faber & French 1980; Conroy & van Dokkum 2012a); however, the current MIUSCAT models do not yet have this capability.

Our result is consistent with the result of Dutton et al. (2012), who determined the mass-to-light ratios for high-density ETGs in the local Universe and ruled out “bottom-heavy” IMFs, and with the work of Grillo & Gobat (2010), who claimed that massive lens and non-lens early-type galaxies favour a Salpeter IMF. Lensing results by Thomas et al. (2011b) have showed a similar trend to the one found here that galaxies with velocity dispersions around 200 km s^{-1} are consistent with a Kroupa IMF, while those more massive objects could be explained with a Salpeter IMF.

We do not find significant trend between the IMF slope and velocity dispersion of these galaxies. This may be the reality, that the IMF slopes of the intermediate-mass ETGs tend to be universal. On the other hand, we only have seven objects, and more data on intermediate-mass ETGs would be very helpful to look for clearer trends.

4.6 Summary and Conclusion

We have investigated the low-mass IMF slopes of seven ETGs observed with the X-Shooter spectrograph. We have defined the new index TiO+CaH, based on spectra smoothed to 300 km s^{-1} , and we have measured it along with five Lick indices *Mgb*, Fe5270, Fe5335, TiO1, and TiO2. By comparing the model predictions and the indices measured from the galaxies, we obtain the following results:

1. TiO indices are promising features to distinguish the IMF from age, metallicity and abundance patterns in a stellar population, in combination with metallicity-dependent indices and α -enrichment-sensitive indices.
2. The Salpeter IMF slope is the upper limit of the IMF slope for nearly all of these ETGs. Since the grids overlap, it is hard to tell if one galaxy precisely follows in the Salpeter IMF or a flatter IMF slope ($x = 0.8$ or the Kroupa IMF). Only in two cases, NGC 3818 (and then only in the TiO2 index) and NGC 4365, is there a hint of a slightly steeper low-mass IMF; however, we argue that this could be due to the clear α -enhancement in both of these galaxies.

In this paper, we have demonstrated the power of using the gravity-sensitive TiO features in old stellar populations to probe the low-mass end of the IMF in ETGs. A full

study that combines these indices with other gravity-sensitive features (like NaI λ 8200, the Wing-Ford band, and the CaII triplet, cf. Conroy & van Dokkum 2012a,b) for these intermediate-mass ETGs is now required to test the results of this and other recent studies. When coupled with dynamical studies of these objects (as in, e.g., Cappellari et al. 2012), the true total stellar mass and therefore the low-mass end of the IMF of these galaxies can be determined.

Acknowledgments

We thank L. V. E. Koopmans, C. Spiniello and J. Falc3n-Barroso for helpful discussions. We are grateful to M. Koleva for providing SSP models based on NGSL before publication to check the behaviour of the extended MILES models in telluric-contaminated spectral regions. A. Vazdekis acknowledges financial support from the Programa Nacional de Astronomía y Astrofísica of the Spanish Ministry of Science and Innovation under grant AYA2010-21322-C03-02. We acknowledge financial support to the DAGAL network from the People Programme (Marie Curie Actions) of the European Union's Seventh Framework Programme FP7/2007-2013/ under REA grant agreement number PITN-GA-2011-289313.

Bibliography

- Bochanski, J. J., West, A. A., Hawley, S. L., & Covey, K. R. 2007, *AJ*, 133, 531
- Burstein, D., Faber, S. M., Gaskell, C. M., & Krumm, N. 1984, *ApJ*, 287, 586
- Cappellari, M. & Emsellem, E. 2004, *PASP*, 116, 138
- Cappellari, M., McDermid, R. M., Alatalo, K., et al. 2012, *Nature*, 484, 485
- Cenarro, A. J., Cardiel, N., Gorgas, J., et al. 2001, *MNRAS*, 326, 959
- Cenarro, A. J., Gorgas, J., Vazdekis, A., Cardiel, N., & Peletier, R. F. 2003, *MNRAS*, 339, L12
- Chabrier, G. 2003, *PASP*, 115, 763
- Chen, Y., Trager, S., Peletier, R., & Lançon, A. 2011, *Journal of Physics Conference Series*, 328, 012023
- Conroy, C. & van Dokkum, P. 2012a, *ApJ*, 747, 69
- Conroy, C. & van Dokkum, P. G. 2012b, *ApJ*, 760, 71
- Davé, R. 2008, *MNRAS*, 385, 147
- de Vaucouleurs, G., de Vaucouleurs, A., Corwin, Jr., H. G., et al. 1991, *S&T*, 82, 621
- Dutton, A. A., Mendel, J. T., & Simard, L. 2012, *MNRAS*, 422, L33

- Faber, S. M. & French, H. B. 1980, *ApJ*, 235, 405
- Falcón-Barroso, J., Balcells, M., Peletier, R. F., & Vazdekis, A. 2003, *A&A*, 405, 455
- Ferreras, I., La Barbera, F., de la Rosa, I. G., et al. 2013, *MNRAS*, 429, L15
- González, J. J. 1993, PhD thesis, Thesis (PH.D.)—UNIVERSITY OF CALIFORNIA, SANTA CRUZ, 1993. Source: Dissertation Abstracts International, Volume: 54-05, Section: B, page: 2551.
- Gregg, M. D., Silva, D., Rayner, J., et al. 2006, in *The 2005 HST Calibration Workshop: Hubble After the Transition to Two-Gyro Mode*, ed. A. M. Koekemoer, P. Goudfrooij, & L. L. Dressel, 209
- Grillo, C. & Gobat, R. 2010, *MNRAS*, 402, L67
- Horne, K. 1986, *PASP*, 98, 609
- Kroupa, P. 2001, *MNRAS*, 322, 231
- McCraday, N., Gilbert, A. M., & Graham, J. R. 2003, *ApJ*, 596, 240
- Miller, G. E. & Scalo, J. M. 1979, *ApJS*, 41, 513
- Modigliani, A., Goldoni, P., Royer, F., et al. 2010, in *Society of Photo-Optical Instrumentation Engineers (SPIE) Conference Series*, Vol. 7737, *Society of Photo-Optical Instrumentation Engineers (SPIE) Conference Series*
- Ogando, R. L. C., Maia, M. A. G., Pellegrini, P. S., & da Costa, L. N. 2008, *AJ*, 135, 2424
- Patat, F., Moehler, S., O'Brien, K., et al. 2011, *A&A*, 527, A91
- Paturel, G., Petit, C., Prugniel, P., et al. 2003, *A&A*, 412, 45
- Rampazzo, R., Annibali, F., Bressan, A., et al. 2005, *A&A*, 433, 497
- Reid, I. N., Hawley, S. L., & Gizis, J. E. 1995, *AJ*, 110, 1838
- Rieke, G. H., Loken, K., Rieke, M. J., & Tamblyn, P. 1993, *ApJ*, 412, 99
- Salpeter, E. E. 1955, *ApJ*, 121, 161
- Sánchez-Blázquez, P., Peletier, R. F., Jiménez-Vicente, J., et al. 2006, *MNRAS*, 371, 703
- Scalo, J. M. 1986, in *IAU Symposium*, Vol. 116, *Luminous Stars and Associations in Galaxies*, ed. C. W. H. De Loore, A. J. Willis, & P. Laskarides, 451–466
- Spiniello, C., Trager, S. C., Koopmans, L. V. E., & Chen, Y. P. 2012, *ApJ*, 753, L32
- Thomas, D., Maraston, C., Bender, R., & Mendes de Oliveira, C. 2005, *ApJ*, 621, 673
- Thomas, D., Maraston, C., & Johansson, J. 2011a, *MNRAS*, 412, 2183
- Thomas, J., Saglia, R. P., Bender, R., et al. 2011b, *MNRAS*, 415, 545
- Trager, S. C., Faber, S. M., & Dressler, A. 2008, *MNRAS*, 386, 715

- Trager, S. C., Faber, S. M., Worthey, G., & González, J. J. 2000a, *AJ*, 120, 165
- Trager, S. C., Faber, S. M., Worthey, G., & González, J. J. 2000b, *AJ*, 119, 1645
- Trager, S. C., Worthey, G., Faber, S. M., Burstein, D., & González, J. J. 1998, *ApJS*, 116, 1
- Valdes, E., Gupta, R., Rose, J. A., Singh, H. P., & Bell, D. J. 2004, *ApJS*, 152, 251
- van Dokkum, P. G. 2008, *ApJ*, 674, 29
- van Dokkum, P. G. & Conroy, C. 2010, *Nature*, 468, 940
- Vazdekis, A., Cenarro, A. J., Gorgas, J., Cardiel, N., & Peletier, R. F. 2003, *MNRAS*, 340, 1317
- Vazdekis, A., Ricciardelli, E., Cenarro, A. J., et al. 2012, *MNRAS*, 424, 157
- Vernet, J., Dekker, H., D'Odorico, S., et al. 2011, *A&A*, 536, A105
- Whitford, A. E. 1977, *ApJ*, 211, 527
- Worthey, G., Faber, S. M., González, J. J., & Burstein, D. 1994, *ApJS*, 94, 687
- Worthey, G. & Ottaviani, D. L. 1997, *ApJS*, 111, 377
- Yamada, Y., Arimoto, N., Vazdekis, A., & Peletier, R. F. 2008, *ApJ*, 674, 612

CONCLUSIONS AND OUTLOOK

In this thesis, we present the pilot survey of the new X-Shooter spectral library (XSL) covering the wavelength range from 3100 Å to 10200 Å at a moderate resolution of $R \sim 10000$. This pilot release contains 237 unique stars with excellent flux calibration and telluric correction, which makes the library well suited for stellar population synthesis of galaxies and star clusters, kinematic investigation of stellar systems and studying the physics of cool stars. Four sets of stellar population models based on the pilot release of XSL are constructed: XMSa, XBSa, XMKr and XBKr, which provide flexible tools for various investigations of stellar populations. We have tested our models on spectra of Galactic globular clusters to extract their evolutionary histories. Our inferred ages and metallicities of these clusters agree well with the published values. Gravity-sensitive spectral features as potential tracers of dwarf-to-giant ratio in stellar systems are identified in our models. We define a new gravity-sensitive index, TiO+CaH, and use this index to constrain the slope of the initial mass function in distant intermediate-mass early-type galaxies (ETGs).

5.1 Summary of main results

5.1.1 The new X-Shooter stellar spectral library

In Chapter 2 we present the first release of XSL, the X-Shooter Spectral Library. Features of the pilot survey are described. We show a promising principal component analysis (PCA)-based method which we developed and used to perform the telluric correction on XSL.

- Features of XSL

This release contains 237 stars spanning the wavelengths 3000–10200 Å observed at a resolving power $R \equiv \lambda/\Delta\lambda \sim 10000$. The sample contains O – M, long-period variable (LPV), C and S stars. We emphasize that our library has a large collection of M stars (more than 40% in the sample of the pilot survey), which contribute a non-negligible fraction of the light to the stellar populations in the red

and are interesting by themselves to study. In addition, thanks to the unique broad-band coverage of X-Shooter, we are able to observe variable stars from the near-ultraviolet to near-infrared simultaneously. Our library has been carefully corrected for telluric absorption, flux-calibrated, shifted to the rest frame, and combined into single, broad-band (UV and optical) spectra.

- The telluric library and the telluric correction applied to XSL

A telluric library is constructed from 152 early type stars to perform the telluric correction on XSL in the optical ($\lambda\lambda \sim 5300 - 10200\text{\AA}$). The telluric library contains two A-type and 150 B-type stars sharing the same resolution as XSL in the VIS arm ($R = 10986$). We have developed a principal component analysis (PCA)-based method that can quickly and precisely perform the telluric corrections on the XSL data for the warm stars. We find that the first two primary components of our telluric library have clear physical meaning: the first component presents the mean spectrum of the telluric library; the second component tends to separate the transmission contribution of most of the water vapour features from O_2 features. Telluric correction of the spectra of cool stars is challenging. Because the continua of cool stars are dominated by complicated molecular features, we recommend using instead stellar telluric templates taken close in time to the observation of the cool star.

- Careful flux calibration

Flux calibration is important to a spectral library. In XSL, most stars have both narrow-slit observations to achieve high resolution and a wide-slit observation to preserve the total flux. We derive the extinction curve of X-Shooter in Periods 84 and 85 in the UVB and VIS arm, respectively, using a number of flux-standard stars. Averaged response curves in the UVB and VIS arm of X-Shooter are presented in this work. For some stars, manual compensation for possible flux losses had to be performed, due to the failure of Atmospheric Dispersion Compensator (ADC) occurring in some of our observations. We suggest a boxcar-smoothing method to generate the compensation curve for stars affected by the ADC effect.

5.1.2 Stellar population models with XSL in the optical

In Chapter 3 we present our stellar population models built from the stars observed in the first-year pilot survey of XSL. The behavior of our models is described, and the models are tested with Galactic globular clusters.

- Model ingredients and behaviour

Our stellar population models are constructed from the stellar isochrones of Marigo (Marigo et al. 2008) or BaSTI (Pietrinferni et al. 2004); the initial mass functions (IMFs) of Kroupa (2001) or Salpeter (1955); and the X-Shooter stellar library with stars covering a large parameter space of effective temperature, T_{eff} , gravity, $\log g$, and metallicity, $[\text{Fe}/\text{H}]$. The spectral energy distributions (SEDs) of

our model span the wavelength range from 3100 Å to 10200 Å. In order to make the stellar population models more easily useable, we have degraded the original XSL spectra to a uniform lower resolution of $R \equiv \lambda/\Delta\lambda \sim 7000$, because the resolved power of XSL in the UVB arm is a function of wavelength ($R = 9584 - 7033$), while it tends to be a constant value in the VIS arm ($R = 10986$). Stellar population models are available at ages ranging from 0.1 to 15.8 Gyr, with metallicities from $[\text{Fe}/\text{H}] = -0.7$ to $[\text{Fe}/\text{H}] = 0.2$. In particular, our models are well suited to study small stellar systems.

- Effect of initial mass function on the SEDs

We find that the initial mass function does not influence the colors of the stellar population models as much as the input isochrones do. However, their influence on line strengths is non-negligible. We show gravity-sensitive spectral features in our models which can be used as tracers of the dwarf-to-giant ratio in stellar populations. To constrain the IMF shape or slope of a population, low-mass stars are required in both the isochrones and the input spectral library.

- Interpretation of the integrated light of Galactic GCs

Globular clusters (GCs) are excellent calibrators for stellar population models, as they are nearly single-stellar populations, and their ages and metallicities are known from their resolved stellar populations. We have tested our models against three globular clusters. Our model predictions of ages and metallicities are consistent with other literature values based on color-magnitude diagram (CMD) estimates. In order to interpret the CN and Ca H and K features in the GCs, non-solar abundance patterns in the models are required.

5.1.3 Determining the masses of distant galaxies

We expand our discussion of the IMF in Chapter 4. We evaluate gravity-sensitive absorption-line indices as potential IMF slope indicators. We highlight the new index TiO+CaH, which together with several traditional Lick/IDS indices, is used to constrain the IMF slopes in seven low-to-intermediate mass early type galaxies.

- Behaviour of TiO-related line features in SEDs

TiO dominates the optical opacity of low-mass dwarfs' cool atmospheres, and the strengths of the TiO features are used to define the M spectral subtype classification scheme. Therefore the molecular bands of TiO are promising tracers of the IMF. Stellar population models which include low-mass ($m \leq 0.5 M_{\odot}$) stars in both isochrones and the input library present a good opportunity to investigate the effects of the IMF on the integrated light. A direct ratio of SEDs with different IMFs clearly shows a deviation in TiO-related line features.

- TiO+CaH as a tracer of the IMF slope

We define a new index TiO+CaH on spectra smoothed to 300 km s^{-1} , where possible significant telluric contamination is carefully avoided. This broad index

covers $\sim 200 \text{ \AA}$, and is almost insensitive to velocity dispersion effects. Index-index plots show separated sequences for SEDs with various IMFs. Comparing model grids with our galaxy data gives us hints of how to constrain the IMFs in stellar populations. We find that the IMF slope cannot be steeper than Salpeter for early-type galaxies with velocity dispersion below $\sim 200 \text{ km s}^{-1}$.

- α -enhancement in galaxies

Although TiO features are sensitive to the dwarf-to-giant ratios, chemical abundance-ratio effects may play a significant role in determining their strengths. The chemical abundance distribution, for example the α -enhancement, must be taken into account to obtain a better constraint on the slope and shape of the IMF in galaxies. Stellar population models including α -enhancement are therefore required.

5.2 Future outlook

5.2.1 Fundamental parameters of nuclear clusters

Our stellar population models constructed with XSL are ideal for population analysis of small stellar systems. One possible application of these models is to estimate the ages, metallicities and masses of nuclear clusters (NCs), since their fundamental parameters still remain largely unknown (Walcher et al. 2005). Reliable estimates of the above parameters will reveal the kinship among NCs, globular clusters (GCs), super star clusters (SSCs), and the nuclei of dwarf elliptical (dE) galaxies.

We measure velocity dispersions, ages and metallicities of four NCs: NGC 300, NGC 428, NGC 1042 and NGC 1493, observed with UVES on VLT using our XMKr models as templates. Flux-calibrated one-dimensional spectra were kindly provided by C. Jakob Walcher. Instead of degrading the original spectral resolution of the observations with a Gaussian of 3 \AA FWHM (Walcher et al. 2006), our models allow the preservation of more information in the fit due to the higher resolution. We derive the fundamental parameters using full-spectrum fitting. A blue wavelength range ($3650\text{--}4700 \text{ \AA}$) is used to perform the fit, with strong emission lines or bad pixels masked when necessary. Single stellar population (SSP) synthesis has been performed on each NC. Age, metallicity and velocity dispersion of each NC are obtained from the fit of the SSP model with minimum χ^2 .

We list the best fit ages, metallicities and velocity dispersion as well as χ^2 in Table 5.1. The small values of χ^2 indicate that the error spectrum may be overestimated (Walcher et al. 2006). To check our results, we also list literature values (Walcher et al. 2006) estimated from two different methods, i.e. SSP full-spectrum fitting and absorption line indices. We find reasonable agreement between our estimates and the literature ages and metallicities for NGC 300 and NGC 428. In NGC 300, the age we derived is a bit older and metallicity is lower than the literature values. This is not surprising because the metallicity expected is almost at the limit of our models. Therefore a slightly older age is compensated by a lower metallicity in the fit of NGC 300. Because our

Table 5.1: SSP ages, metallicities, and velocity dispersions of nuclear clusters

NC name	t_{SSP} (Myr)	[Fe/H] SSP	σ_v (km s ⁻¹)	χ^2	S/N (Å ⁻¹)	t_1^* (Myr)	[Fe/H] ₁ [*]	t_2^* (Myr)	[Fe/H] ₂ [*]	σ_v^* (km s ⁻¹)
NGC 300	2142	-0.96	18.9 ± 1.8	0.85	37	1000	-0.69	1288	-0.69	13.3 ± 2.0
NGC 428	2136	-0.61	27.8 ± 3.9	0.36	16	1000	0.39	2291	-0.69 - 0.00	24.4 ± 3.7
NGC 1042	-	-	42.2 ± 2.8	1.23	24	30	-0.69	100	-0.69 - 0.39	32.0 ± 4.8
NGC 1493	-	-	29.6 ± 1.4	4.64	20	30	-0.40	55	-0.69	25.0 ± 3.8

Note: The values of S/N are taken from the work done by Walcher et al. (2005) to show the spectral quality. The last five columns are literature values taken from Walcher et al. (2005) and Walcher et al. (2006), where t_1 and [Fe/H]₁ are the SSP estimates, t_2 and [Fe/H]₂ are the ages and metallicities from absorption-line indices.

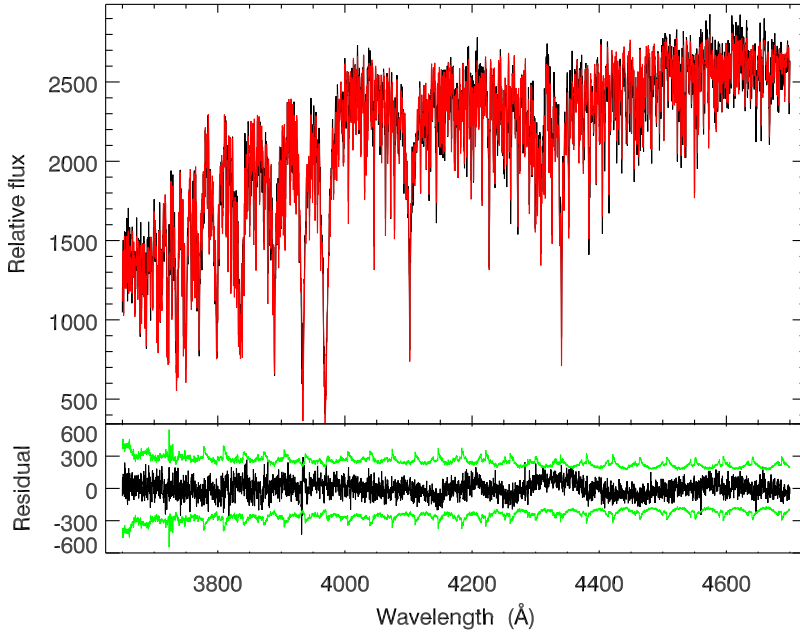


Figure 5.1: Full-spectrum fitting of NGC 300. The top panel shows the spectrum of NGC 300 in black and the best fit in red by our model XMKr. The bottom panel shows the residual between the GC spectrum and the best fit in black; the continuous green lines mark the $1\text{-}\sigma$ deviation as expected by the input S/N.

models are not yet available for very young ages at sub-solar metallicity, no estimates for NGC 1042 and NGC1493 are presented.

Figure 5.1 shows the overall best fit of the spectrum of NGC 300, which has the highest S/N of the three considered NCs. The spectrum is zoomed into three regions in Figure 5.2, with a small amount of overlap in wavelength. The model reproduces the spectral lines very well. Similar SSP fits on the other three NCs are shown in Figures 5.3, 5.4, 5.5, 5.6, 5.7 and 5.8. We find that our model in general reproduces well the spectral features in NCs. NCs with emission lines, e.g., NGC 1402 are quite well reproduced. Balmer emission lines, even weak ones, are clearly seen in Figure 5.6. Fits of NCs with low S/N are also successful, with the exception of the Ca K line at 3934 Å in NGC 1493.

To briefly summarize our result: the young ages of NCs in late-type spiral galaxies (Walcher et al. 2006) are confirmed by our SSP analysis. Better estimates of age and metallicity in NCs could be achieved by performing a composite stellar populations analysis. On the other hand, improving the stellar population models, especially metal-poor ($[\text{Fe}/\text{H}] \leq -0.7$) models, will help to achieve reliable age and metallicity determinations in these small stellar systems.

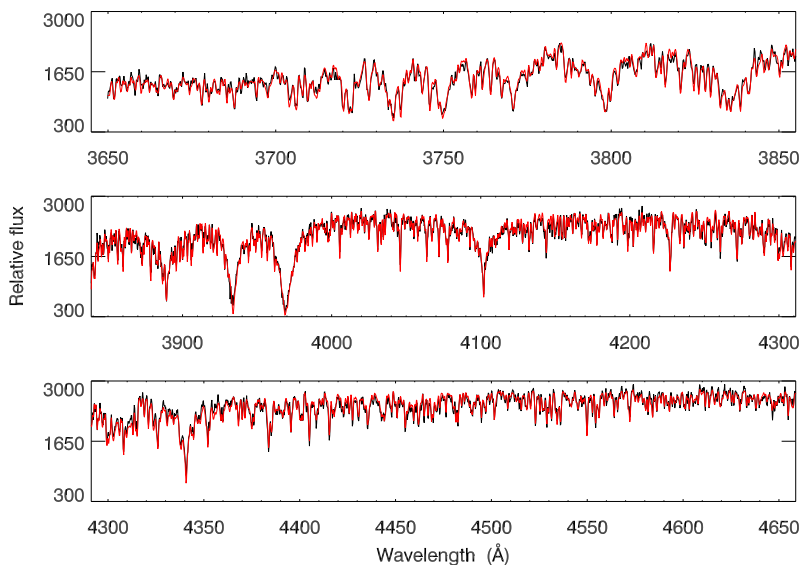


Figure 5.2: Best SSP fit for NGC 300 (red) compared with the observed data (black). Note that almost every single line is well reproduced by the model.

5.2.2 XSL and stellar population models with XSL

XSL is still under construction. The final database will contain 600 – 700 stars with complete atmospheric parameter coverage along the Hertzsprung-Russell diagram at a wide range of metallicities. The wide wavelength coverage at intermediate resolution will make it a vital tool for extragalactic astronomers to extract even more information from their observations than previously possible. Spectral features in the near-infrared will be investigated in remarkable detail, leading to new knowledge about cool stars in galaxies. XSL will provide stellar astronomers with a world-leading panchromatic spectral library for further studies of a wide range of stellar types.

We have shown that our stellar population models built from only one-third of the data provide reasonable results. When the complete XSL is available, our models will be extended to $2.5 \mu\text{m}$ with a wider metallicity distribution. We will also construct α -enhanced stellar population models which will be able to study non-solar-abundance-ratio systems. With our improved stellar population models, stellar features in the entire wavelength range can be analyzed simultaneously, which will make it possible to study more details in the star formation histories of galaxies. Finally, the large coverage in the infrared will make it possible to much better study the role of asymptotic-giant-branch stars in the evolution of galaxies.

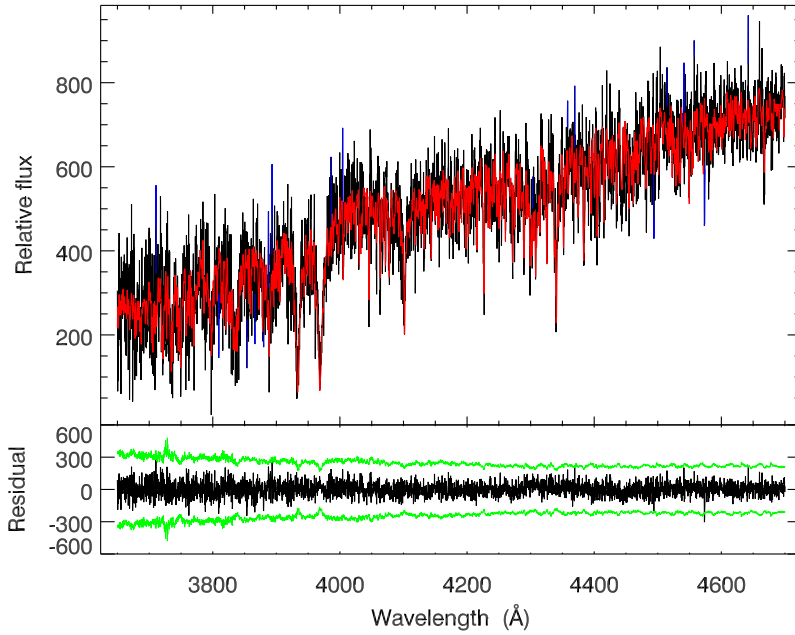


Figure 5.3: Same as Figure 5.1 but for NGC 428. Pixels masked out in the fit are marked in blue.

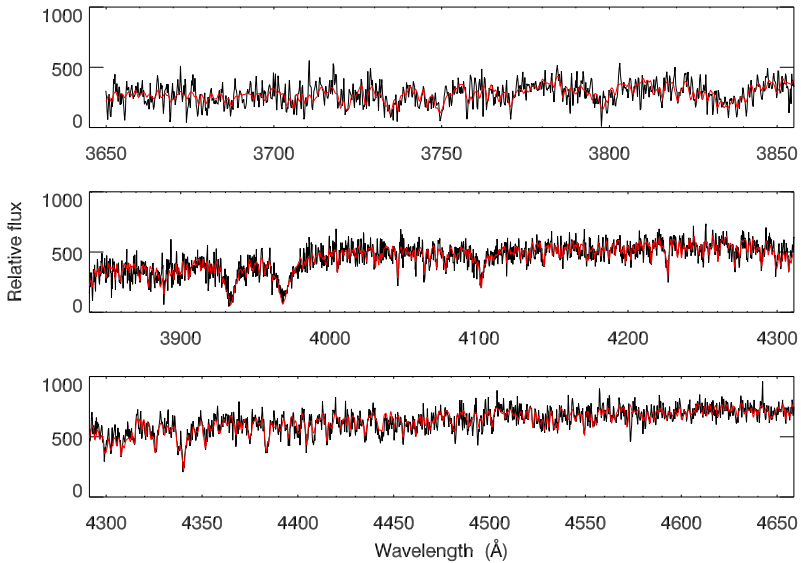


Figure 5.4: Best SSP fit for NGC 428 (red) compared with the observed data (black).

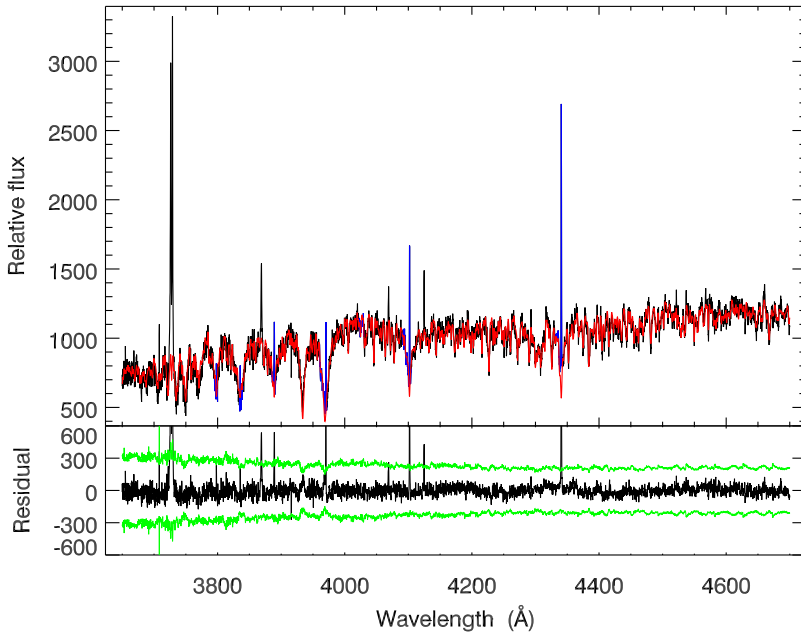


Figure 5.5: Same as Figure 5.3 but for NGC 1042.

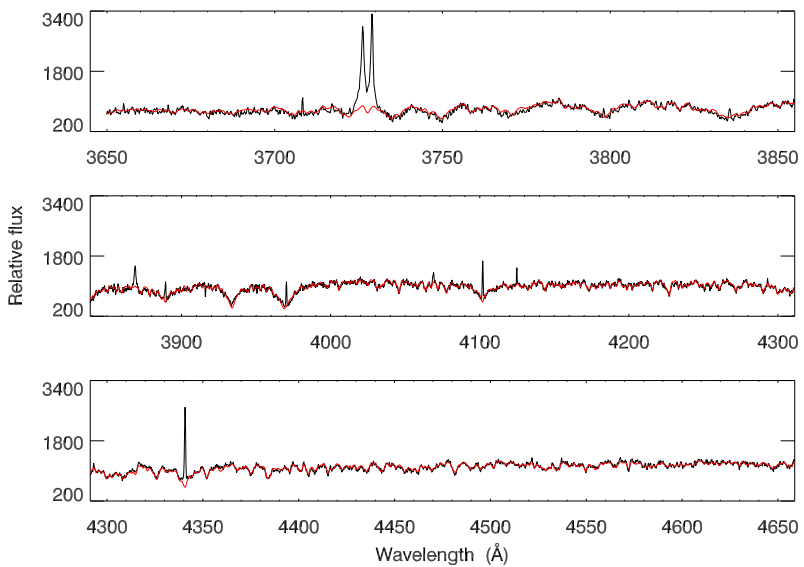


Figure 5.6: Best SSP fit for NGC 1402 (red) compared with the observed data (black).

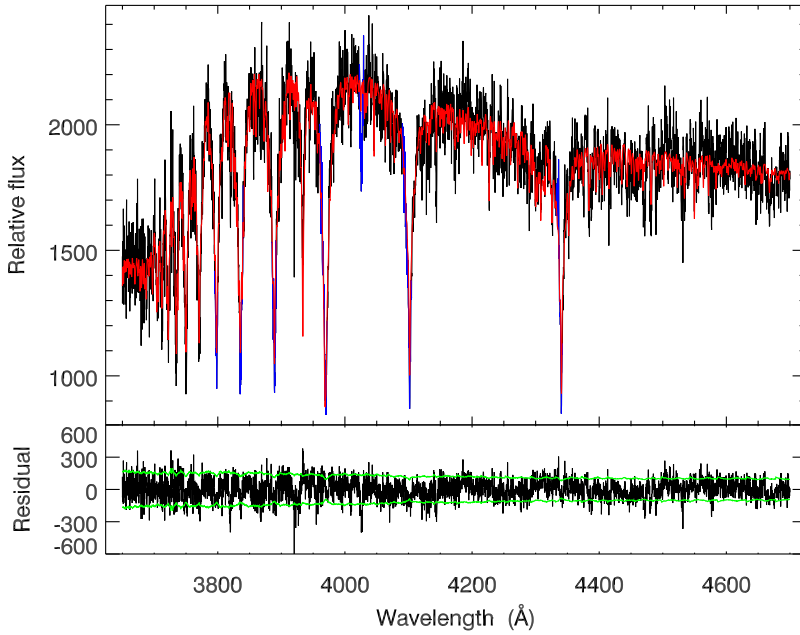


Figure 5.7: Same as Figure 5.3 but for NGC 1493.

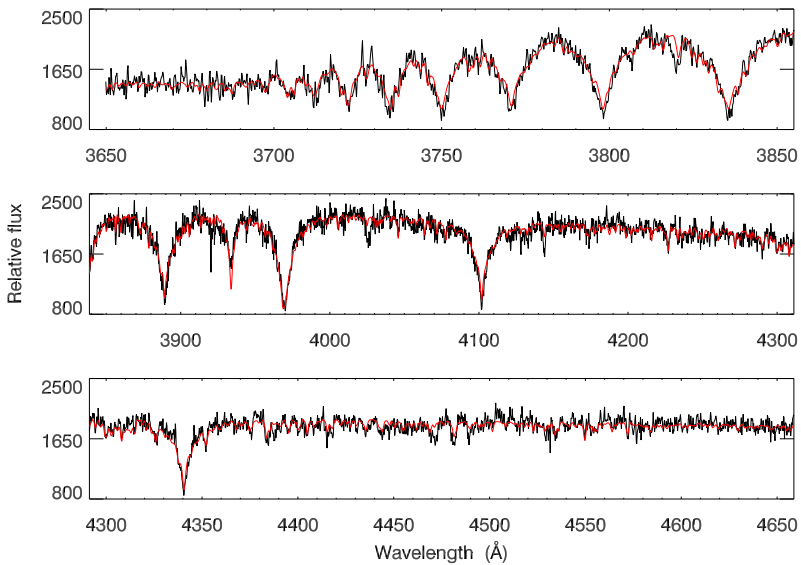


Figure 5.8: Best SSP fit for NGC 1493 (red) compared with the observed data (black).

Nederlandse Samenvatting

In dit proefschrift hebben we de evolutie van stersystemen onderzocht, in het bijzonder bolhopen en sterrenstelsels. De volgende vragen zijn hierbij behandeld: “Hoe oud zijn deze systemen?”, “Wat voor chemische samenstelling kunnen ze hebben?”, “Wat zijn de massa’s van de sterren in melkwegstelsels?” en “Hoe zijn deze sterrenstelsels en bolhopen ontstaan?”. Als we de individuele sterren van sterrenstelsels of bolhopen niet meer kunnen onderscheiden, dan kunnen we alleen iets over deze objecten leren door hun geïntegreerde licht te bestuderen. Het synthetiseren van de sterpopulaties is een goede methode om informatie te vergaren die bevat is in het geïntegreerde licht. Bij deze techniek wordt de evolutionaire geschiedenis bepaald door het geïntegreerde licht te reproduceren met gesynthetiseerde modellen van sterpopulaties.

Moderne sterpopulatiemodellen hebben drie essentiële ingrediënten (e.g. Vazdekis et al. 2010): sterisochronen; deze representeren eigenschappen van sterren van verschillende massa’s, die met dezelfde chemische samenstelling op hetzelfde moment zijn ontstaan; een initiële massaverdeling (IMF, initial mass function) die het aantal sterren per massa interval bepaalt; en een bibliotheek van standaardsterren, met sterren van elke temperatuur (T_{eff}), zwaartekracht ($\log g$), en metalliciteit ($[\text{Fe}/\text{H}]$).

Bibliotheken met stellaire spectra zijn belangrijk in verscheidene onderzoeksgebieden van de sterrenkunde. In het bijzonder vormen deze bibliotheken de basis voor het modelleren van sterpopulaties om de evolutie van sterrenstelsels te bestuderen. De meeste bestaande bibliotheken van experimenteel waargenomen spectra hebben echter beperkingen waardoor het moeilijk is om de spectra van sterrenstelsels, in het bijzonder het rode deel, volledig te reproduceren. Deze bibliotheken hebben ofwel een te lage resolutie, zijn niet te gebruiken voor moderne spectroscopische surveys, of beperken zich tot een klein aantal golflengtegebieden.

Sinds kort kunnen deze beperkingen worden overkomen met behulp van de X-Shooter spectrograaf op de Very Large Telescope (VLT) van de Europese Zuidelijke Sterrenwacht (ESO, European Southern Observatory). Met zijn hoge efficiëntie, het grote golflengtebereik, en de hoge spectrale resolutie van deze spectrograaf kunnen we een bibliotheek maken die, met meer dan 700 sterren, het hele Hertzsprung-Russel diagram beslaat bij alle golflengtes van 300 nm tot 2048 nm. Dit proefschrift presenteert een nieuwe empirische bibliotheek van sterspectra, de X-Shooter bibliotheek (XSL, X-Shooter library).

In totaal worden er met de ESO VST in zes periodes waarnemingen verricht voor het XSL project. De data van de eerste twee waarneemperiodes (de “pilot survey”) zijn verwerkt binnen het kader van dit proefschrift. Deze pilot survey bevat de spectra van 237 individuele sterren, met golflengtes van 3100 Å tot 10182 Å en een resolutie van

$R \sim 10000$. Het is nodig om de datareductie heel secuur uit te voeren om er voor te zorgen dat we de strenge eisen die we aan de bibliotheek stellen ook daadwerkelijk halen. Alle avonturen die werden beleefd bij het reduceren van de X-Shooter data zijn bijgehouden in Hoofdstuk 2, samen met de technische details van X-Shooter. De openbaar beschikbare software om X-Shooter gegevens te verwerken is verre van perfect omdat X-Shooter een relatief nieuw instrument is. We hebben een aantal problemen in versie 1.5.0 van deze software blootgelegd en de oplossingen die we hebben aangedragen zijn overgenomen door ESO. Daarbovenop heb ik ook zelf software geschreven voor data visualisatie, verkrijgen van eendimensionale spectra, detecteren van verzadiging, berekenen van indices en fluxcalibratie. Deze programma's zorgden voor een dramatische verbetering in de efficiëntie van de dataverwerking en in de precisie van het eindproduct. Omdat we met zo'n grote dataset werkten, konden we belangrijke kennis van het instrument terugkoppelen naar ESO, bijvoorbeeld hoe de efficiëntie-curven en resolutie afhangen van de golflengte. De resolutie van de XSL spectra worden in detail besproken in Hoofdstuk 2. X-Shooter heeft drie aparte 'armen' (UVB, VIS en NIR) voor de verschillende golflengtegebieden die het omvat en het blijkt dat deze zich verschillend gedragen. Het oplossend vermogen in de UVB arm hangt af van de golflengte, terwijl het over het algemeen gelijk blijft in de VIS arm.

Spectra die genomen zijn met telescopen op de grond worden beïnvloed door de atmosfeer van de Aarde. In de zichtbare en nabij-infrarode delen van het spectrum wordt het licht gedeeltelijk geabsorbeerd door waterdamp, moleculair zuurstof, koolstofdioxide en methaan. De specifieke kenmerken van een spectra die veroorzaakt worden door de atmosfeer van de Aarde noemen we tellurische kenmerken. Het corrigeren voor tellurische vervuiling is cruciaal voor de XSL spectra in de VIS en NIR armen. We hebben een bibliotheek samengesteld met 152 experimenteel bepaalde transmissiecurves zodat we een zeer precieze correctie hebben kunnen ontwikkelen voor de XSL waarnemingen. Deze bibliotheek kan ook op zichzelf staand gebruikt worden.

Om een bibliotheek van spectra te kunnen maken moet de flux op iedere golflengte precies gekalibreerd worden. Voor de eerste twee waarnemingsperiodes hebben we een globale extinctiecurve bepaald en een specifieke responscurve voor elke individuele waarneming. De kwaliteit van de fluxcalibratie werd gewaarborgd door vergelijkingen te maken met breedband kleuren uit de literatuur. Verder is er een absolute golflengtecalibratie toegepast op elk eendimensionaal spectrum en op het gecombineerde eindproduct. Hierbij vormde het combineren van spectra van verschillende armen van het instrument de grootste uitdaging: bepaalde eigenschappen van de UVB en VIS armen zijn van sterke invloed op de vorm van de spectraallijnen. We hebben ernaar gestreefd om de flux en spectraallijnen van de gecombineerde spectra zo nauwkeurig mogelijk te maken. Al is XSL nog in ontwikkeling, het is al wel een essentieel hulpmiddel voor sterrenkundigen om nog meer informatie uit hun waarnemingen te halen dan voorheen mogelijk was.

Stellaire spectrale bibliotheken worden vooral gebruikt bij het synthetiseren van sterpopulaties. Hierbij wordt de spectrale energieverdeling (SED, spectral energy distribution) van stellaire systemen (bv. Melkwegstelsels) gemodelleerd. De spectra van sterren in de bibliotheek worden gebruikt om de spectrale eigenschappen in deze modellen te reproduceren. Deze modellen stellen ons in staat om de evolutionaire ge-

schiedenis van verre, onopgeloste sterrenstelsels en bolhopen te achterhalen. De ingrediënten van sterpopulatiemodellen zijn: de isochronen van sterren, de IMF, en de bibliotheek met spectra. Hoofdstuk 3 is gewijd aan het verhaal van de sterpopulatiemodellen en hun bestanddelen.

We construeren SEDs voor enkelvoudige sterpopulaties (SSP, single stellar population, d.w.z. Sterpopulaties met een enkele leeftijd en metalliciteit) met behulp van de XSL, twee sets van isochronen, en twee IMFs. Hiermee onderzoeken we de invloed van de individuele ingrediënten. Binnen het kader van dit proefschrift variëren we alleen de gebruikte isochronen en de IMFs; de XSL blijft steeds de gebruikte bibliotheek. Derhalve zijn er vier SSP SEDs gemaakt en vergeleken. Om het gebruiksgemak van de sterpopulatiemodellen te vergroten hebben de resolutie van de XSL spectra verlaagd naar een uniforme resolutie van $R = 7000$. Voor het maken van zinvolle modellen is het nodig om de atmosferische parameters van elke ster in de gebruikte spectraalbibliotheek goed te kennen. Deze parameters zijn bepaald door het volledige spectra van de sterren te fitten met een set sterren met bekende parameters. Voor de hete sterren blijken deze gefitte parameters overeen te komen met de literatuur. Voor koudere sterren (M-sterren en variabele sterren met een lange periode) zijn er helaas geen waarden beschikbaar in de literatuur om mee te vergelijken. Desalniettemin hebben we ook voor deze sterren de atmosferische parameters bepaald omdat ze wel een belangrijke bijdrage leveren aan het rode deel van het spectrum. Onze modellen geven een compleet beeld van sterpopulatiesynthese, want ze hebben de unieke eigenschap dat elk model een groot golflengtebereik van 3100 Å tot 10185 Å beslaat.

In Hoofdstuk 3 hebben we laten zien dat het variëren van de gebruikte isochronen een grotere invloed heeft op de kleuren in de SEDs dan het variëren van de IMFs. Verder kunnen we ook de invloed van de volledigheid van de spectraalbibliotheek niet verwaarlozen bij het maken van SEDs. Al hebben de IMFs dan wel een kleine invloed op de kleuren van de SEDs, ze leveren wel belangrijke aanwijzingen over de verhouding tussen het aantal dwergsterren en het aantal reuzensterren binnen sterpopulaties. Het effect van IMF-keuze kan pas worden opgemerkt als men de eigenschappen van de spectra in detail bekijkt. Deze effecten worden beïnvloed door de massaondergrens van de isochronen. Onze modellen zijn geschikt om de IMF te onderzoeken omdat ze met behulp van Marigo isochronen zijn gemaakt en die hebben een massabereik tot $0.15M_{\odot}$.

Sterrenkundigen kunnen de evolutionaire geschiedenis bepalen uit het geïntegreerde licht door ofwel alleen de spectraallijnen te gebruiken of het hele spectrum te fitten. We hebben onze enkelvoudige sterpopulatiemodellen getest door de tweede methode toe te passen op bolvormige sterrenhopen in ons sterrenstelsel. We concluderen dat de spectraallijnen netjes gereproduceerd worden door onze modellen, en dat de afgeleide leeftijden en metalliciteiten goed overeen komen met de literatuurwaarden.

Spectraallijnen die gevoelig zijn voor de zwaartekracht kunnen dienen als indicator voor de IMF. We hebben een aantal van deze spectraallijnen gevonden in onze SSP SEDs en kunnen deze mogelijk gebruiken om de verhouding tussen de het aantal dwergsterren en reuzensterren te achterhalen. In Hoofdstuk 4 gaan we verder op dit onderwerp in, en onderzoeken we door middel van een aantal IMF-tracers de mogelijke helling van de IMF in verre sterrenstelsels. In plaats van onze eigen modellen,

gebruiken we de MIUSCAT modellen om zeven vroeg type stelsels te onderzoeken met massa van $10^9 - 10^{10}$ zonsmassa's. Aan de hand van tellurisch gecorrigeerde spectra van sterrenstelsels, definiëren we een nieuwe coëfficiënt die gevoelig is voor de zwaartekracht als mogelijke indicator van de helling van de IMF. Deze nieuwe coëfficiënt, TiO+CaH, gebruiken we samen met de traditionele Lick/IDS coëfficiënten om de helling van de IMF van onze zeven sterrenstelsels te bepalen. Onze bevindingen zijn als volgt:

- TiO-gerelateerde spectraallijnen zijn potentiële IMF indicatoren.
- TiO+CaH is een goede tracer voor de helling van de IMF.
- Voor vroegtype sterrenstelsels met een snelheidsdispersie onder de $\sim 200 \text{ km s}^{-1}$ kan de helling van de IMF niet steiler zijn dan Salpeter.
- De verdeling van zwaardere elementen, zoals een verhoging van α -elementen, moet meegenomen worden om de helling en vorm van de IMF beter te kunnen bepalen.

In dit proefschrift hebben we een de ingrediënten van sterpopulatiemodellen beschreven, het gedrag van onze modellen bestudeerd, en ze toegepast op onopgeloste stersystemen. We presenteren nieuwe hulpmiddelen voor spectroscopisch onderzoek in de sterrenkunde, in het bijzonder voor het onderzoeken van het geïntegreerde licht van sterrenstelsels en bolhopen. De X-Shooter spectraalbibliotheek, XSL, zal een belangrijk hulpmiddel zijn voor onderzoek binnen een groot aantal vakgebieden binnen de sterrenkunde. XSL gaat vergezeld door onze tellurische spectraalbibliotheek, die nuttig zal zijn voor meer dan alleen het uitvoeren van tellurische correcties voor de XSL. Voor dit proefschrift zijn de door ons ontwikkelde hulpmiddelen gebruikt om de evolutionaire geschiedenis van zowel nabije als verre stersystemen te ontrafelen. Verder stellen we gevoelige tracers voor om de verhouding in de aantallen dwergen en reuzensterren in verre sterrenstelsels ($d \geq 17 \text{ Mpc}$) te bepalen. Naar verwachting zullen er meer belangrijke sterrenkundige resultaten worden gerealiseerd met de hulpmiddelen die in dit proefschrift worden aangedragen.

Summary

In this thesis we had a tour probing the evolutionary histories of stellar systems, namely star clusters and galaxies. The questions we addressed were the following: “How old are these systems?”, “What are their possible chemical compositions?”, “What are the masses of the stars in galaxies?” and “How did these galaxies and clusters form?”. When galaxies or clusters cannot be resolved into single stars, everything that we can learn from these objects is contained in their integrated light. Stellar population synthesis has been shown to be a powerful tool for decoding the information hidden within the integrated light. The basic concept of this technique is to extract the evolutionary history information from the integrated light by reproducing the colors or spectra with synthesized stellar population models.

To construct modern stellar population models, three primary ingredients are used (e.g. Vazdekis et al. 2010): stellar isochrones that represent the properties of stars with different masses but sharing the same initial chemical composition and age; an initial mass function (IMF) to populate the isochrones with a sensible number of stars; and a stellar library with stars covering the parameter space of effective temperature, T_{eff} , gravity, $\log g$, and metallicity, $[\text{Fe}/\text{H}]$.

Spectral libraries play an important role in different fields of astrophysics. In particular, they serve as a fundamental ingredient for models of stellar populations used to study the evolution of galaxies. However, most of the existing empirical libraries are either low resolution, not suitable for modern spectroscopic galaxy surveys, or limited to one or several narrow wavelength ranges that makes it difficult to reproduce the whole spectral features of galaxies, especially in the red. With the high efficiency, broad wavelength coverage, and intermediate/high resolution of the X-Shooter spectrograph at ESO’s VLT, we can build a spectral library with ≥ 700 stars covering the entire Hertzsprung-Russell diagram in the full wavelength range from 300 nm to 2048 nm. This thesis presents a new empirical stellar spectral library, the X-Shooter library (XSL).

The XSL project has six periods of observations in total on the ESO VLT and data from the first two periods (the “pilot survey”) have been processed in this thesis. This pilot survey contains 237 unique stars covering the spectral range of 3100 Å to 10182 Å at a resolution of $R \sim 10000$. Very careful data reduction must be performed in order to satisfy the stringent requirements of a spectral library. All the adventure in X-Shooter data reduction and the technical parameters of X-Shooter have been recorded in Chapter 2. As X-Shooter is still a relatively new instrument, the publicly available pipeline is far from perfect. We identified a number of issues with version 1.5.0 of the pipeline and possible solutions we suggested have been adopted by ESO. In addition, I have also

written my own scripts for data visualization, automatic grouping, one-dimensional spectrum extraction, saturation reporting, index calculation and flux calibration, all of which dramatically improved the efficiency of the data reduction process and the precision of the final product. Working with a large data set has allowed us to report back to ESO on important instrumental profiles such as the response curves and resolution as a function of wavelength. Details of the resolution of XSL spectra are discussed in Chapter 2, which shows that the resolved power in the UVB arm is a function of wavelength, while it tends to be a constant value in the VIS arm.

Ground-based spectroscopy is subject to contamination from the Earth's atmosphere. In the visible and NIR portions of the spectrum, water vapour, molecular oxygen, carbon dioxide and methane generate strong absorption features. Absorption features that originate in the Earth's atmosphere are referred to as telluric features. Correction for telluric contamination is therefore crucial for the XSL spectra in the VIS and NIR arms (the X-Shooter has three arms for different spectral ranges: UVB, VIS and NIR). In order to perform the telluric correction on our data, in particular in the optical, we have built a telluric library that contains 152 empirical atmospheric transmissions. The telluric library is used to develop a principal component analysis (PCA)-based method that can quickly and precisely perform the telluric corrections on the XSL data. It can also be used as a stand-alone library.

Precise flux calibrations must be performed in order to generate a spectral library. We have generated the overall extinction curve for the first two periods of data acquisition and individual response curves for each observation. The quality of the flux calibration has been confirmed by making comparisons with published broad-band colors. Extra absolute wavelength calibration has been carefully performed on each one-dimensional spectrum and the merged final product, where combining spectra from different arms for the same object presents the biggest challenge: strong dichroic features between the UVB and VIS arms severely affect line features and spectral shape. We have endeavoured to make the flux and spectral lines of the arm-combined spectra as precise as possible. XSL is still under construction, but already provides a vital tool for extragalactic astronomers to extract even more information from their observations than previously possible.

One of the important uses for a spectral library is in stellar population synthesis, where the individual spectrum of various stars from the stellar library are used as crucial input to create the spectral features for the model SEDs. With this powerful tool, we can reveal the evolutionary history of galaxies and clusters, in particular the remote, unresolved ones. The ingredients of stellar population models include the stellar tracks (isochrones), IMF and the spectral library. Chapter 3 is dedicated to telling the story of stellar population models and their constituents.

We build single stellar population (SSP) SEDs with XSL, two sets of isochrones and two IMFs to investigate the influence of each input ingredient. In this thesis, we keep XSL as the input library, and allow the isochrones and IMFs to change. Four sets of SSP SEDs have therefore been generated and compared. In order to make the stellar population models more easily useable, we have degraded the original XSL spectra to a uniform lower resolution of $R = 7000$. To build sensible stellar population models, proper atmospheric parameters are strongly desired for each star in the input spectral

library. Delicate atmospheric parameters are determined with a full-spectrum-fitting technique for the warm stars and are shown to be consistent with literature values. We also obtain the stellar parameters for M stars and long-period variable stars, for which literature parameters are not available, but that still make important contributions to the integrated light in the red. Our models, with the unique capability of simultaneously covering a wide wavelength range from 3100 Å to 10185 Å at a moderate resolution, open up a more complete view of stellar population synthesis.

We have shown in Chapter 3 that varying the input isochrones can have a stronger impact on the broad-band colors of SEDs than the IMFs. In addition, stellar parameter coverage of the input spectral library also plays a non-negligible role in the SEDs. The IMFs, although not showing an obvious impact on the color of SEDs, provide important hints on the dwarf-to-giant ratios of stellar populations. Their effects can only be noticed when one takes a close look at the spectral features, while their effects on the SEDs also depends on the low-mass cut in the isochrones. Our models, which are made using Marigo isochrones, for example, are appropriate for the IMF analysis because of the complete mass coverage ($m \geq 0.15M_{\odot}$) over the isochrones.

Astronomers extract evolutionary histories from integrated light either by evaluating the spectral line indices (called the “fitting function”) or by full-spectrum fitting. We have tested our models with the latter method on Galactic globular clusters using single stellar population synthesis. We find that the spectral lines are reproduced well by our models, and that the extracted ages and metallicities agree well with published literature values.

A number of gravity-sensitive spectral lines (IMF tracers) that may reveal the dwarf-to-giant ratio in stellar systems have been identified in our SSP SEDs based on Marigo isochrones. To understand the possible IMF slope in remote galaxies and IMF tracers better, we expand on this topic in Chapter 4. Instead of using our own models, we adopted MIUSCAT models to do the analysis on seven low to intermediate-mass early-type galaxies. We define a new gravity-sensitive index (potential IMF slope indicator) on telluric corrected integrated galaxy spectra. This new index, TiO+CaH, together with several traditional Lick/IDS indices, is used to constrain the IMF slopes in our seven galaxies. We find the following:

- TiO-related line features are potential IMF indicators.
- TiO+CaH is a good tracer of the IMF slope.
- The IMF slope cannot be steeper than Salpeter for early-type galaxies with velocity dispersion below $\sim 200 \text{ km s}^{-1}$.
- Chemical abundance distribution, for example α -enhancement, must be taken into account in order to obtain a better constraint on the slope and shape of IMF for galaxies.

In this thesis, we have toured through the ingredients of stellar population models, inspected the behavior of our models, and described their application on unresolved stellar systems. We present new tools for spectroscopic research in astronomy, especially for investigating the integrated light of galaxies and clusters. The X-Shooter

spectral library, XSL, will be an important tool for research over a wide range of astrophysical fields. XSL is also accompanied by our telluric spectral library, which will be useful to astronomers beyond simply performing telluric corrections for the XSL. For this particular thesis, the tools we have developed have been used to extract the evolutionary histories of both nearby and remote stellar systems. We also suggested sensitive tracers that reveal the dwarf-to-giant ratio in distant galaxies ($d \geq 17$ Mpc). More great astronomical results are expected to be achieved with the tools presented in this thesis.

Acknowledgements

In these last few pages, I would like to express my appreciation to all the people I met during my staying in this beautiful cloudy and green country. Life is full of adventures and it brought me to this nice city and institute. For the first time in my life, I started learning and using English seriously to communicate with people and even doing science. Before I had spent more than a decade memorising words, grammar and tenses, however, I was only a mute English user. When I lost the fear of opening my mouth and making mistakes, I felt so wonderful that now I can do something that I never thought possible before! Thank you Mariano! It was you who gave me this first important lecture in my life. This actually had a great effect both in my research and in my daily life, and will continue to have a long-lasting effect.

Scott and Reynier, thank you for offering me this great opportunity to work with you. Thank you for your patience and enthusiasm during the past years. Scott, you are a walking encyclopedia! I appreciate all the small lectures that you gave and your extraordinary memory of so many references that you talked about, which helped me a lot with my research. You are a great scientist, chief and father. Sorry that I might not use the correct word here, but in some moments, your way of talking to me has been like a father :) Thank you for your guidance and for training me to think carefully in doing my research, although sometimes I am still “stubborn”. I appreciate the support and help you have given me over the years. Thanks for everything!

Reynier, I didn't know how bad a student I was to begin with but I am happy to note that I seem to have become a better student in the end. Thank you for your scientific insights, efficient help and frankness. I learned a lot from you! Sometimes Guobao jokes to me that I am becoming you. I have to admit that at the beginning of this project I was very scared of you. If something went wrong or you didn't understand me well, you used to express that immediately on your face and tell me outright. I still remember our observations in La Palma, it was wonderful! You showed me the beautiful Milky Way and the shining stars, which brought me into a wonderland. As time went on, I found out that you were an enthusiastic person. And I cannot count how many pens you have brought me, some of which I returned to you. Thank you for your support and supervision, which helped me a lot in having a clear timeline for my research and for finishing this thesis.

I would like to thank Ariane for all the interesting collaborations and discussion that we had over the years. You are such a sweet lady that you make me feel jealous of Anaïs. I am impressed at your attitude towards solving problems and searching for collaborations. It has been a very pleasant experience to work with you. You are a considerably open-minded, critical and patient scientist. I have seen how you guide a

student and explain the necessary background in a gentle and clear way. I am looking forward to keeping this collaboration in the future.

Thanks to all the past and present PBC members of the Kapteyn Institute: Inga, Rein, Saleem, Marc, Peter, Amina and Eline. I was nervous at the beginning PBC meetings, that made me feel like I was waiting for a court's decision. Thank you for all the nice conversations and support!

I am grateful to my reading committee members: Prof. dr. J.M. van der Hulst, Prof. dr. M. Salaris, and Dr. Ph. Prugniel. Thank you for the useful discussions, which helped me to think more deeply about my work.

Lucia, thank you for all your help. From the beginning to the end, I cannot imagine how it would have been without you. You found me a private English teacher, you helped me with all the bureaucratic documents, you encouraged me to be brave during my hard times, you even shared with me some good skills to help me survive in academic life. Hennie, thank you for taking care of the travel forms and sometimes my Dutch bills. I really enjoyed the annual Kapteyn outing, thank you so much for organizing them. Jackie, thank you for being so enthusiastic. Whenever I had a question about living in this country, I would think, "Jackie knows everything". I was sad when I heard that you would stop working at this institute. But I happily found you are on facebook! I would also like to thank Gineke and Christa: "hartelijk bedankt"!

Thanks to the system managers, Martin, Eite and Wim. You have been so friendly to me and you were willing to help anytime when I had problems with my machine or software. Wim, thank you for helping me out every time I stepped into your office or stopped you in the corridor saying "Wim, help!". You always assisted me immediately. Also thank you for the warm hugs and nice conversations. I will miss you when I'm gone.

Special thanks go to Hugo for helping me with the Dutch translation and Aladin scripts. You are my guardian angel, who always helped me out whenever I had a question or requested for emergency help, even though you were not familiar with my research. I am grateful to all your kind words, suggestions and encouragement for me and my life. Thank you also for the birthday parties where I met your girl friend, Wieke. It was very nice to talk to her and good luck for you both being parents soon :)

I would like to thank Maarten, who helped me with my \LaTeX skills in the last few months. Thank you for your patience and understanding. Even when I sometimes caught you in other offices, you never made any excuses and helped me immediately.

Koshy, it was nice meeting you and being friends with you. Your positive attitude can easily make people be happy and relaxed. We started almost the same time, so if I had to point out the person who knew me best in my work and life in Groningen, it must be you. Thank you for your random visits to my office and for your chocolates when both of us were working till late. I won't say much about how you encouraged me and supported me because that will bring me to tears. The "Life of Ping" continues with your blessing. Thank you, Macha!

Chiara, Gergö and Wouter, thank you for the interesting discussions in our group meetings. Gergö and Wouter, I am grateful for your corrections on my Dutch summary. Chiara, Dr. Spiniello, thank you for your bitter Italian coffee, even though it was too strong for me. Thank you for all your help with the X-Shooter pipeline, our scientific

discussions, my first IDL script, and your experience in dealing with the bureaucratic steps in order to get to the point of a thesis defense. I wonder how such big energy comes from your not-very-big body?

My thanks also go to Esra and Parisa, with whom I spent some great time chatting and having dinners and drinks. I am sorry that my house is far away from the center, which made you both get lost in the evening when we had the house warming-party. It was a lot of fun being with you in the same institute and joining some ACLO courses together.

Zsofia, we got to know each other in the “wadlopen” Kapteyn outing, when we had to change our clothes behind dunes. You love cats crazily while cats run away from your passion. Thank you for the tea breaks and Hungarian alcohol. I should have visited your home town a long time ago but I haven't yet made it. Hopefully I can find some time after my PhD to see this beautiful place. Thank you for telling me a quicker solution of printing out my thesis, which provided timely help!

Anaïs, you are not a Kapteyner yet, but you will be soon. I appreciated your hospitality when I visited Strasbourg. Thank you for teaching me the French song “Un deux trois nous irons au bois. . .” It is always enjoyable talking to you. You are an attractive French girl! I wish you a very successful PhD both in Strasbourg and in Groningen.

I would like to thank Sofia and Thomas, you are great friends. I felt very lucky to meet you in Kapteyn. Thank you for your invitation to the wedding party, house warming-party, birthday party, dinners and many more. I enjoyed chatting with you, learning from you, and sharing great moments with you. I especially thank Sofia, you are not only my good friend, but also an excellent collaborator! Thank you for the warm words and positive suggestions for my life and my research. I will never ever forget your words “Never give up”.

My dear Yunhee, I am so grateful for being your officemate. Your desk is always clean, while mine is incredibly messy. There were a few times that I cleaned my desk, after which it looked nicer. But usually after at maximum 10 minutes, it became messy again. Thank you for tolerating me occupying a small part of your desk for our tea, candies and maybe sometimes my papers, pens, etc.. Thank you for teaching me so many IDL skills, thank you for sharing with me my bad moments and good moments, thank you for the small gifts every time when you came back from some traveling.

Teresa, Oscar, Burcu, Andera, Beike, Diego, Germán, Anto and Facu, Stefania, Stéphanie, Katinka, Lelli, Robyn, Rosina, Stefano, Beth, Antonino, Tjitske, Harish, Marius, thank you for the nice lunch times.

I would like to thank Kyle, who also trained and guided me in my work. Thank you for the useful comments and discussions.

Sanaz, you are very a good friend, and a smart girl! Do you still remember you sent me your manuscript to me that should have gone to Sarod? I was astonished by that and thought: did she really want me comment on her draft? Sarod, thank you for your special greeting of “What do you want” whenever you saw me.

Hi Pratyush, you amazing Indian boy! You are so talkative and you make friends everywhere. You always have adventures everywhere in the world, incredible!

Evgenia, Maja, Anastasia and Nadine, I feel lucky to hav met you all. It was not as long as with other people in the institute, but we had a lot of pleasant conversations.

Gert, mushroom-prince! I am happy that you are still here after your PhD. I had told you that I hoped I could be as good as you at your defense reception, and I am still looking forward to that. Thank you for the invitations to your birthday parties and funny stories you've told me.

Ciao Macio, thank you for showing up in the last days of my stay in Groingen. I am so happy to meet you again here. We shared the same office for one year during which I was quite impressed by your humor and intelligence.

Most of my weekends and holidays cannot be without you two: Xia & Lin. I enjoyed all the days we spent together: from Prague to Rome, from Cairo to Alexandria, from Barcelona to Brussels, from Lisbon to Porto. Where will be our next trip? I am looking forward to it! I also thank Wei & Mengsu – thank you for the chats, weekend dinners and all your support. Mengsu – I appreciated our chats about how we can keep ourselves looking young and all the online shopping tricks you have taught me.

I would also like to thank Jenny, my little friend. Thank you for keeping me company during the times when Guobao was absent. Thank you for your visits and for being my photographic model, which always makes me happy. I have never met such a polite friend, saying “Miao~” every time when you leave.

Shoko, my sweet sister. Thank you for your precious help and encouragement of my English writing. You are a ray of warm sunshine who threw light on my darkest last few months during my PhD. Thank you for sharing berries, chocolates, tea, cookies and nice conversations on the balcony with me. I really appreciate the time with you, so calm and natural. You have trained me not only in English, but also in my science. I wish I had known you earlier.

To my family: I am grateful to my parents who devoted much of their life to my growth. Thank you Papa, thank you Mama. Thank you my grandma in heaven, with whom I had spent most of my childhood and teenage years. I hope you will be proud of me when I get my PhD.

Guobao, my husband, thank you for showing me different views of the world. We have been lucky to have been together everywhere since the beginning and we always will be. Thank you for tolerating my bad temper that I seldom show to other people, and for tolerating me shouting to you at home! Thank you for being with me and your support that make me feel safe. I love you!

Yanping Chen
October 11, 2013